Durability of solid oxide cells : an experimental and modelling investigation based on synchrotron X-ray nano-tomography characterization

Maxime Hubert

Communauté
UNIVERSITÉ Grenoble Alpes

THÈSE

Pour obtenir le grade de

DOCTEUR DE LA COMMUNAUTE UNIVERSITE GRENOBLE ALPES

Spécialité : **Matériaux, Mécanique, Génie civil, Electrochimie**

Arrêté ministériel : 25 mai 2016

Présentée par

Maxime HUBERT

Thèse co-dirigée par **Florence LEFEBVRE-JOUD** et **Jérôme LAURENCIN** et encadré par **Peter CLOETENS**

préparée au sein du **CEA² LITEN** et de **l'ESRF**
dans **l'École Doctorale I-MEP²**

Durability of Solid Oxide Cells: an experimental and modelling investigation based on synchrotron X-ray nano-tomography characterization

Thèse soutenue publiquement le **« 24 mai 2017 »**,
devant le jury composé de :

Mme. Elisabeth SIEBERT
Directeur de recherche, LEPMI Grenoble, Présidente du jury
M. Jean-Marc BASSAT
Directeur de recherche, ICMCB Bordeaux, Rapporteur
M. Jean-Yves BUFFIERE
Professeur, MATEIS INSA Lyon, Rapporteur
M. Jan VAN HERLE
Professeur, EPFL Lausanne, Examinateur
Mme. Florence LEFEBVRE-JOUD
Docteur, CEA LITEN Grenoble, Co-directrice de thèse, invitée
M. Jérôme LAURENCIN
Docteur, CEA LITEN Grenoble, Co-directeur de thèse
M. Peter CLOETENS
Docteur, ESRF Grenoble, Co-encadrant de thèse

« S’il n’y a pas de solution, c’est qu’il n’y a pas de problème »
Jacques Rouxel / Les Shadoks

Remerciements

Ces travaux se sont déroulés conjointement au sein du Laboratoire de Production d'Hydrogène (LPH) du commissariat à l'énergie atomique et aux énergies alternatives (CEA^2) et sur la ligne de lumière ID16A à l'ESRF de Grenoble. Je remercie à ce titre Julie Mougin de m'avoir permis de réaliser ce travail de thèse au sein de son service.

Je remercie vivement Jean-Yves Buffières, professeur à l'INSA de Lyon et Jean-Marc Bassat, Directeur de recherche à l'ICMCB de Bordeaux d'avoir accepté d'être rapporteurs de ce travail. Je tiens également à remercier Jan Van Herle, professeur à l'EPFL Lausanne, d'avoir participé au jury en tant qu'examinateur malgré les difficultés de transport et Elisabeth Siebert, directrice de recherche au LEPMI de Grenoble, d'avoir présidé le jury et d'avoir contribué à l'avancé de mes travaux de thèse au court de discussions scientifiques toujours intéressantes.

Je tiens à exprimer ma reconnaissance envers Florence Lefebvre-Joud, directrice de thèse, pour sa vision globale du sujet qui a évité de s'éparpiller sur les nombreuses problématiques envisageables. J'adresse également mes chaleureux remerciements à Jérôme Laurencin, co-directeur de cette thèse, qui a su me guider au quotidien. Les mécanismes réactionnels des MIEC auront hanté quelques-unes de ses nuits. Enfin, je remercie Peter Cloetens, encadrant de thèse à l'ESRF, qui a pris le temps de me former alors que la nouvelle ligne était en plein démarrage. Je n'oublierai pas son émerveillement devant mes différents vélos.

Mes sincères remerciements à mes collègues du LPH pour la bonne ambiance qui règne au sein du laboratoire, ce qui permet d'accomplir des miracles ! Merci au groupe de joueur de badminton Lionel, Philipe, Guilhem, Bertrand et Michel. Ils m'auront fait courir après les volants les jeudi midi. Merci à Pascal que j'ai fait travailler pour du nano comme pour du macro et qui a toujours su répondre à ma demande. Je souhaite le meilleur à Albin, André, Benoit, Charlotte, Denis, Fabien, Georges, Karine, Magali, Marie, Nathalie, Olivier, Patrick, Stéphane et Thomas. J'ai une pensée particulière pour Lucile qui a été ma co-bureau tout au long de ma thèse au CEA et un soutien lorsque les manip' ne marchaient pas. Je souhaite bonne continuation à ceux que j'ai eu le plaisir de croiser Jérôme A., François, Luca, Myriam, Serguii, Sophie et pleins de courage pour ceux qui sont en pleins dans leur thèse ou post-doc Alexandra F., Federico, Hamza, Rakesh. Merci à Sarah qui est toujours d'une aide précieuse pour tous les problèmes administratifs et d'organisations.

Je remercie également les collègues d'autres laboratoires du CEA qui m'ont aidé pendant ma thèse. Je pense particulièrement à Pierre Bleuet et son dynamisme infini qui m'a permis de « bien monter » mes échantillons. Je remercie aussi Guillaume pour ses conseils lorsque la situation était mal embarquée au PFIB. Je remercie également Gérard Delette qui dans la dernière ligne droite de ma thèse a su me donner quelques références bibliographiques pour finaliser mes travaux sur l'agglomération du Nickel.

Du côté de l'ESRF, je remercie tout d'abord les membres de la ligne ID16A qui ont toujours été disponibles pour m'aider. Un grand merci à Alexandra, Yang, Julio, Murielle. J'ai une

pensée pour Lorène la plus petite des Daltons du bureau d'ID16, Valentin et Florin complétant la troupe. Je remercie également Julie qui avait ouvert la voie de la nanotomographie avec ses travaux de thèse. Merci à Lionel, Rémi, Damien, Woult, JP, Sylvain B. Sylvain L., toujours partant pour un gâteau dans la cuisine d'ID16.

Et parce qu'entre les tests de vieillissement, la modélisation au CEA et la tomo à l'ESRF, il y avait quand même un peu de temps pour profiter des amis. Je tiens particulièrement à remercier les Mactans, toujours prêts à tester un nouveau restaurant quand ils étaient sur Grenoble. Un grand merci également à Xavier et Aurélia qui m'ont permis de tester la gestion de crise pour le choix des couleurs de leur appartement. Je remercie aussi Florent et Dani pour les soirées brésiliennes, Hortense, Chris, Romain, Selim, Emi, Pauline toujours partants pour boire une bière ou plus sur Grenoble. Merci à tous les 400 grammes répartis partout en France : Thomas G, Guigui, Syssy, Doudou, Gaetan, Jerem', Paul, Cyril ; ou alors très loin jusqu'en Australie pour Thomas B ; c'est toujours un bon moment de se retrouver.

Je remercie bien sûr ma famille pour leur soutien même si les convertisseurs électrochimiques à oxyde solide restent un mystère pour eux, ils ont su me changer les idées. Je remercie également la belle famille qui est toujours prête à partir faire du géocaching.

Enfin, j'adresse ma profonde affection à Mélissa qui m'a supporté au quotidien et n'a pas hésité à se lever la nuit pour venir me chercher lorsque mes vélos avaient rendu l'âme. La réussite de ce travail est aussi la tienne.

Contents

List of Figures

Introduction

Chapter I: Context of high temperature Solid Oxide Cells

Chapter II: State-of-the-art in synchrotron X-ray imaging by phase contrast

Chapter III: Enhancement of the X-ray nano-holotomography protocol

Chapter IV: Long-term electrochemical tests and post-mortem characterizations

Chapter V: Numerical tools for degradation study

Chapter VI: Discussion

List of Tables

Chapter I: Context of high temperature Solid Oxide Cells

Chapter III: Enhancement of the X-ray nano-holotomography protocol

Chapter IV: Long-term electrochemical tests and post-mortem characterizations

Chapter V: Numerical tools for degradation study

List of abbreviations and symbols

Abbreviations

ASR	Area Specific Resistance
CGM	Conjugate Gradient Method
DGM	Dusty Gas Model
EIS	Electrochemical Impedance Spectroscopy
FIB / PFIB	Focused Ion Beam / Plasma Focused Ion Beam
GDC	Gadolinium Doped Ceria
LSC	Lanthanum Strontium Cobaltite
LSCF	Lanthanum Strontium Cobalte Ferrite
MIEC	Mixed Ionic Electronic conductor
OCV	Open Circuit Voltage
PSD	Particle Size Distribution
PSF	Point Spread Function
RVE	Representative Volume Element
SEM	Scanning Electron Microscopy
SNR	Signal to Noise Ratio
SOC	Solid oxide Cell
SOEC	Solid Oxide Electrolysis Cell
SOFC	Solid Oxide Fuel Cell
TPB	Triple Phase Boundary
YSZ	Yttria Stabilized Zirconia

Parameters for electrochemistry

D_i	Diffusion coefficient of specie *i*	$mol.s^{-1}$
N_i	Molar flux of specie *i*	$mol.s^{-1}.m^{-2}$
P_i	Partial pressure of specie *i*	atm
a_i	Activity of specie *i*	-
ε_i	Volume fraction of specie *i*	-
ζ_{TPB}	Density of TPB	μm^{-2}
τ_i	Tortuosity factor of specie *i*	-
$\mathcal{F}$	Faraday constant	96483 $C.mol^{-1}$
R	Gas constant	8.314 $J.mol^{-1}.K^{-1}$
T	Temperature	K
U	Voltage	V
i	Current density	$A.m^{-2}$
α, β, γ	Exponents for exchange current density laws	-
η	Overpotential	V

Parameters for tomography

$\mathcal{F}$	Fourier transform	
$\mathcal{F}^{-1}$	Inverse Fourier transform	
N_i	Number of element *i*	
$P_i(x)$	Propagation function at distance *i*	
$u_i(x)$	Wave function at distance *i*	
z_1	Distance focus-sample	m
z_2	Distance sample-detector	m
$B(x)$	Projection of absorption index	
D	Distance of beam propagation	m
$I(x)$	Intensity of the beam	
$T(x)$	Transmission function	
n	Complex refractive index	
s	Source size	m
β	Absorption index	
δ	Refractive index decrement	
λ	wavelength	m
μ	Linear coefficient attenuation	m^{-1}
$\varphi(x)$	Projection of refractive index decrement	

Résumé étendu en français

L'objet de ce travail est l'étude de la dégradation des convertisseurs électrochimiques haute température à oxydes solides. C'est une approche expérimentale et de modélisation qui se base sur des reconstructions obtenues par nanotomographie des rayons X au synchrotron.

De nos jours, la réponse à la forte demande énergétique mondiale est principalement assurée par des énergies fossiles comme le charbon, le pétrole ou le gaz naturel. Mais l'utilisation massive de ces sources d'énergies émet d'importantes quantités de gaz à effet de serre, ce qui affecte le climat. La communauté internationale en a pris conscience et des accords ont été conclus pour réduire l'impact de l'activité humaine sur le changement climatique. Dans ce cadre, l'Union Européenne a fixé des objectifs ambitieux de réduction d'émissions polluantes d'ici 2050. Le domaine de la production d'énergie est considéré comme ayant le plus gros potentiel pour réduire les émissions voire les éliminer totalement d'ici 2050. Cette objectif pourrait être atteint notamment grâce au développement des énergies renouvelables comme le solaire, l'éolien, la biomasse ou encore l'hydroélectricité. Ces sources d'énergies étant intermittentes, il apparait nécessaire de développer un nouveau vecteur énergétique capable de stocker cette énergie lorsqu'elle est produite et de la restituer lorsque la demande est forte. Il faut bien-sûr que ce vecteur énergétique soit à faible emprunte carbone pour rentrer dans les objectifs de diminutions de gaz à effet de serre.

L'hydrogène ressort comme un candidat intéressant avec son fort ratio énergie sur masse (et malgré son faible ratio énergie sur volume). Actuellement, il est principalement produit à partir du pétrole par des procédés qui émettent beaucoup de gaz à effet de serre. Il existe pourtant des procédés moins polluants comme l'électrolyse de l'eau. Le développement d'une filière de production d'hydrogène propre se révèle indispensable pour envisager le déploiement de ce vecteur énergétique à plus large échelle. Le procédé d'électrolyse de l'eau, qui a été découvert au XIXème siècle par Sir W. Grove, consiste en la dissociation de la molécule d'eau en hydrogène et oxygène gazeux. Plusieurs technologies ont été développées ces dernières années comme l'électrolyse alcaline, celle utilisant des membranes polymères échangeuses de protons ou encore les électrolyseurs à oxydes solides. Cette dernière technologie fonctionnant à haute température n'est pas encore mature mais présente des perspectives prometteuses pour ce qui est du rendement et du coût. De plus, sa flexibilité qui permet soit de produire de l'hydrogène ou bien de produire de l'électricité à partir du même objet, est particulièrement intéressante pour le couplage avec des sources d'énergie renouvelable.

Un gros effort a été réalisé ces dernières années pour le développement de la technologie des convertisseurs électrochimiques haute température à oxydes solides. Cependant, la durée de vie de ces objets reste encore trop limitée pour envisager leur déploiement à plus large échelle. Le problème de durabilité est dû au fonctionnement à haute température qui favorise les évolutions microstructurales, le dépôt de polluants ou bien encore la réactivité des matériaux entre eux. Une meilleure compréhension de ces mécanismes de dégradation est nécessaire afin

de développer des solutions permettant de les éviter ou bien de choisir des conditions opératoires limitant leurs effets.

Ce travail de thèse cherche à améliorer la compréhension des mécanismes de dégradation en mode pile à combustible et électrolyse. Cette étude se focalise principalement sur le lien entre les évolutions microstructurales dans les électrodes et la perte de performance dans le temps mesurée dans différentes conditions opératoires. Une approche complète, qui va des tests de durabilité longue durée jusqu'à la modélisation des performances en passant par la caractérisation fine des microstructures d'électrodes, est utilisée dans ce travail.

Le premier chapitre est dédié à la présentation du contexte des convertisseurs électrochimiques haute température à oxydes solides. Les principes de base du fonctionnement de ces objets sont rappelés dans les deux polarisations (pile à combustible et électrolyse). Une revue des principales architectures et des matériaux classiquement utilisés pour les cellules est proposée. Les différents phénomènes physiques se produisant dans les électrodes sont détaillés ainsi que les mécanismes réactionnels généralement considérés dans les couches actives des électrodes. Un état de l'art des approches de modélisation est proposé en insistant sur les différentes échelles de description qu'on retrouve dans la littérature. Il faut noter que les modèles sont principalement développés en mode pile à combustible. Il y a beaucoup moins d'études dédiées au fonctionnement en électrolyse. Ensuite, un état de l'art sur les performances et la durabilité des convertisseurs électrochimiques à oxydes solides est présenté. On remarque que les performances données dans la littérature sont difficilement comparables du fait des différentes conditions opératoires sélectionnées. Il apparait que les hautes températures permettent d'atteindre de meilleures performances car les conductivités et les réactions sont thermiquement activées. Le choix des matériaux d'électrodes semble également influer sur l'efficacité des cellules. Enfin, la microstructure des électrodes est très certainement déterminante sur les performances de la cellule au vue de la divergence des résultats obtenus dans la littérature pour des cellules constituées des mêmes matériaux testées dans des conditions similaires. La durabilité d'une cellule est caractérisée par l'évolution de sa tension rapportée à une durée de vieillissement de 1000h ($mV.kh^{-1}$). Il existe de nombreuses études de durabilité réalisées dans différentes conditions opératoires sur des cellules simples ou sur des empilements (stack). Les taux de dégradation mesurés sont de plus en plus faibles pour les deux polarisations mais ils restent encore trop élevés pour être économiquement viables. Cette baisse de performance des cellules est due à des mécanismes de dégradation impactant ses différentes couches. On trouve notamment dans la littérature pour l'électrode à oxygène que la ségrégation, la diffusion et la réactivité des cations pourraient avoir un effet non négligeable sur les pertes de performance. La délamination des électrodes à base de LSM est également possible. L'empoisonnement au chrome est le dernier mécanisme de dégradation affectant cette électrode qui est couramment reporté. Ce problème peut être évité en utilisant des revêtements spéciaux pour les inter-connecteurs métalliques et en introduisant des gaz secs dans l'électrode. Pour l'électrolyte dense, les principaux mécanismes de dégradation sont la transformation de phase, qui devrait avoir un effet limité, l'électro-réduction due à de mauvaises conditions opératoires et la formation de nano-porosités, dont la contribution à la dégradation est plus difficilement quantifiable. Enfin, deux mécanismes de dégradation sont principalement

discutés dans la littérature pour l'électrode à hydrogène. Il s'agit de l'empoisonnement par des impuretés, qui peuvent provenir des matériaux bruts, du joint de verre assurant l'étanchéité ou encore des gaz. Le deuxième mécanisme est l'agglomération du Nickel de l'électrode. La réorganisation de la phase Nickel implique un changement de densité des sites actifs pour les réactions électrochimiques ce qui affecte les performances de la cellule. De cet état de l'art, il ressort un intérêt à étudier l'agglomération du Nickel dans l'électrode à hydrogène. Afin d'approfondir la compréhension de ce mécanisme de dégradation, une approche triangulaire basée sur des tests électrochimiques longue durée, de la caractérisation fine par nanotomographie et de la modélisation semble pertinente. Cette étude est réalisée sur une cellule utilisant des matériaux classiques pour les différentes couches.

Le deuxième chapitre présente l'état de l'art pour l'imagerie rayons X synchrotron par nano-holotomographie. Une première partie est dédiée à la présentation des différentes techniques d'imagerie en 3D pour caractériser les électrodes de convertisseurs électrochimiques à oxydes solides. Une brève description des 3 techniques majeures est donnée ainsi que leurs avantages et inconvénients majeurs. Le FIB-SEM est une méthode destructive qui permet d'obtenir de très bonne résolutions mais pour des volumes de taille limitée. On retrouve ensuite deux techniques utilisant les rayons X. La première est basée sur la tomographie d'absorption. Les matériaux des électrodes étant fortement absorbant, il est difficile d'obtenir de grand volume et la taille des voxels (pixels en 3D) est intermédiaire. La dernière technique qu'on retrouve dans la littérature est l'holotomographie. Avec cette méthode, la taille des voxels est relativement petite tout en ayant un large champ de vue ce qui permet d'être représentatif de la microstructure de l'électrode. C'est cette technique qui est utilisée dans ce travail de thèse. Une deuxième section du chapitre présente la base de la physique des rayons X utilisée pour cette technique de caractérisation. Il s'agit notamment de présenter succinctement le principe d'un synchrotron, les propriétés du faisceau de rayons X obtenu, son interaction avec la matière ainsi que l'enregistrement du faisceau transmis sur un détecteur. Ensuite, la méthode d'holotomographie, qui prend avantage du contraste de phase, est présentée en détail ainsi que les méthodes itératives spécifiques utilisées pour obtenir des reconstructions de bonne qualité des électrodes. La dernière partie est dédiée à la présentation de la méthode de reconstruction tomographique une fois l'information de phase obtenue. L'ensemble de ces outils permet d'obtenir des volumes représentatifs des microstructures des électrodes avec une bonne résolution spatiale.

Le troisième chapitre expose les adaptations du protocole expérimental de nano-holotomographie pour améliorer la fiabilité des reconstructions ainsi que la résolution spatiale dans les volumes 3D. Une première section décrit la nouvelle ligne de lumière ID16A pour la nano-imagerie à l'ESRF en insistant sur les évolutions permettant une amélioration de la qualité des reconstructions. Un faisceau haute énergie (33.6 keV) est disponible après 185 mètres de propagation, ce qui permet une meilleure cohérence des rayons X (propriété importante pour le contraste de phase). Le faisceau est nano-focalisé à l'aide de miroirs KB (Kirkpatrick-Baez) donnant accès à une très bonne résolution spatiale dans le volume 3D final. Des moteurs piézo-électriques de haute précision sont utilisés pour le positionnement de l'échantillon afin de limiter la perte de résolution due aux problèmes de stabilité ou de vibrations. Enfin, un

détecteur d'imagerie haute résolution permet l'enregistrement des projections. Afin d'améliorer la fiabilité du procédé de caractérisation, une nouvelle méthode de préparation des échantillons a été développée. La préparation est maintenant assurée à l'aide d'un équipement spécifique : un Plasma-FIB utilisant des ions Xénon. Cet outil permet de choisir précisément la localisation de l'échantillon et il assure un parfait contrôle de sa taille et de sa forme finale. L'acquisition des données a également été améliorée. Tout d'abord grâce à l'utilisation d'une méthode itérative dont les résultats pour une électrode à hydrogène sont présentés. Ensuite grâce à une nouvelle méthode d'acquisition lors des scans tomographiques basée sur le déplacement aléatoire de l'échantillon. Ce nouveau procédé permet de supprimer les artefacts en forme d'anneaux qui rendaient impossible l'analyse des volumes 3D (notamment la segmentation des différentes phases). Les reconstructions de l'électrode à oxygène et à hydrogène dans leur état de référence ont été obtenues. La résolution spatiale a été mesurée directement dans les volumes 3D en regardant l'évolution du niveau de gris à la frontière entre deux phases. Celle-ci a été caractérisée à 50 nm ce qui apparait comme une valeur minimale pour permettre une bonne analyse des fines microstructures des électrodes de la cellule étudiée. Enfin, les principales propriétés microstructurales nécessaires à la modélisation ont été extraites à partir de programmes présentés de manière concise. Ces données de microstructure sont regroupées dans deux tableaux bilans.

Le quatrième chapitre est dédié à la présentation des tests électrochimiques de longue durée menés lors de la thèse ainsi qu'aux caractérisations post-mortem réalisées sur ces cellules. Le montage expérimental ainsi que l'ensemble de la procédure de démarrage d'un essai et de la mesure des performances initiales sont détaillés dans une première section. Les courbes de vieillissement sont dévoilées dans une deuxième partie du chapitre qui contient également les conditions opératoires choisies pour les vieillissements. Une première analyse sur la dégradation apparente est réalisée à partir de ces résultats expérimentaux. Il est notamment observé qu'une plus forte densité de courant entraine une dégradation apparente plus importante. Dans des conditions opératoires similaires, le taux de dégradation est moins important pour un vieillissement réalisé en mode pile à combustible qu'un test réalisé en électrolyse. Un essai effectué à plus basse température sous hydrogène sec pendant 9000h (plus d'un an de vieillissement) permet de montrer qu'il n'y a pas d'évolution critique de la tension de cellule pendant cette durée. On remarque également que la dégradation apparente semble plus importante bien que la température soit plus faible dans ce cas. Les courbes de polarisation et les spectres d'impédance enregistrés régulièrement au cours du vieillissement des cellules sont difficilement exploitables du fait du montage expérimental qui utilise un bulleur pour l'alimentation en vapeur. Des caractérisations post-mortem ont été réalisées sur ces même cellules. Ces résultats sont présentés dans une troisième section de ce chapitre. Les premières observations de l'électrode à hydrogène par microscopie électronique à balayage (MEB) permettent de constater une évolution de la phase Nickel. Cependant, cette évolution reste limitée, ce qui confirme la nécessité d'utiliser un outil comme la nano-tomographie qui est sensible aux faibles modifications microstructurales. De plus, l'observation fine de l'interface entre l'électrolyte et l'électrode H_2 par MEB n'a pas révélé une déplétion significative du Nickel pour les vieillissements réalisés. Une caractérisation par nano-tomographie a été réalisée sur ces cellules en prélevant des échantillons à différentes positions (entré/sortie gaz,

volume/interface de l'électrode H_2). L'ensemble de ces reconstructions permet de disposer d'une grande quantité de données avec différentes conditions opératoires. Il ressort de l'analyse de ces données qu'un certain nombre de paramètres peuvent être considérés comme étant secondaire pour l'agglomération du Nickel (densité de courant, pression partiel de vapeur, polarisation). En revanche, le temps et la température semblent jouer un rôle primordial sur l'évolution microstructurale de la phase Nickel. Une réorganisation des petites particules vers des plus grosses a été identifiée à partir de l'analyse de la distribution de taille des particules (PSD). Une augmentation de 30% de la taille des particules de Nickel a été observée après 2000h de vieillissement à 850°C tandis qu'elle est seulement de 13% après 9000h à 750°C. Cette évolution de la phase Nickel affecte également sa surface spécifique. L'extraction des propriétés microstructurales a notamment permis de mettre en évidence l'effet inhibitif du squelette en zircone sur l'agglomération du Nickel. Enfin, la densité de sites actifs diminue également, ce qui devrait affecter directement les performances de la cellule.

Le cinquième chapitre décrit les outils numériques qui ont été utilisés pour l'étude de la dégradation due à l'agglomération du Nickel. Une première section est dédiée à la présentation de la structure de modélisation multi-échelle utilisée dans ce travail. Le lien unissant le macro-modèle développé à l'échelle de la cellule avec les micro-modèles décrivant le fonctionnement de chacune des électrodes est particulièrement détaillé. Une calibration de l'approche de modélisation est nécessaire afin d'avoir une cohérence entre la simulation et les courbes expérimentales. Les constantes cinétiques des réactions étant les seules inconnues dans notre approche, elles sont ajustées sur une courbe expérimentale obtenue à 800°C sous hydrogène sec. Le modèle est ensuite validé dans des conditions opératoires différentes (changement de composition, flux des gaz, changement de polarisation et de température). Le modèle permet notamment de comprendre la dissymétrie des courbes entre le mode pile à combustible et électrolyse. Celle-ci est principalement due à la diffusion Knudsen dans l'électrode à hydrogène. La dernière section de ce chapitre est consacrée à la modélisation de l'agglomération du Nickel afin de quantifier sa contribution sur les pertes de performances. Deux lois, qu'on retrouve classiquement dans la littérature, ont été utilisées sur les données expérimentales complétées avec d'autres données issues de la littérature sur des cellules similaires. Il apparait que la loi de type « Capacitor » peut être considérée comme une limite basse pour l'agglomération tandis que la loi « Puissance » serait sa limite haute. Une loi « Puissance » est également utilisée pour décrire la baisse de densité des sites actifs. En rentrant cette loi dans l'approche de modélisation, il est possible de quantifier la contribution de l'agglomération du Nickel sur les baisses de performances mesurées expérimentalement. Il apparait que ce mécanisme de dégradation explique environ 30% des baisses de performances entre 1000h et 2000h lors d'un vieillissement en mode pile à combustible à 850°C alors que c'est seulement 20-25% en mode électrolyse pour des mêmes temps.

Le dernier chapitre discute des résultats obtenus au cours de ce travail et les met en perspectives de travaux récents. Il est notamment discuté dans une première partie des évolutions potentielles des techniques d'imagerie pour encore améliorer la résolution spatiale et réussir à imager des matériaux avec des contrastes proches. Les aspects de modélisation se sont avérés pertinents pour décrire les performances des cellules. Cependant, des perfectionnements sont

possibles, par exemple en détaillant les mécanismes réactionnels se produisant dans l'électrode H_2. Néanmoins, ces améliorations ne devraient pas changer l'évolution générale obtenue avec le modèle. Pour ce qui est de la modélisation de la dégradation, l'approche utilisée dans ce travail a permis d'améliorer la compréhension de l'agglomération du Nickel en mesurant sa contribution sur la perte des performances. Une amélioration de la description de la baisse de la densité de sites actifs en identifiant une loi morphologique permettrait de mieux décrire cette évolution. L'utilisation de ces lois d'agglomération permet de quantifier la part due à ce mécanisme de dégradation. La contribution de l'agglomération du Nickel a été quantifiée à un peu moins d'un tiers de la baisse de performance mesurée expérimentalement à 850°C après 2000h de vieillissement. Le modèle peut également être utilisé pour faire des extrapolations dans d'autres conditions opératoires ou d'autres durées de vieillissement. Des résultats surprenants de la littérature ont notamment pu être expliqués grâce à cette approche. Enfin, des pistes sont avancées pour les contributions qui peuvent expliquer les deux autres tiers de la perte de performance de la cellule. Il a notamment été observé de la réactivité entre les matériaux d'électrolyte et d'électrode à oxygène pour les cellules vieillies en mode électrolyse. Cette approche triangulaire complète s'avère donc pertinente pour l'étude de la dégradation des convertisseurs électrochimiques à oxydes solides. Cette méthodologie pourrait être étendue à d'autres microstructures d'électrodes, à d'autres matériaux ou encore à d'autres conditions opératoires.

Introduction

Nowadays, the energy demand is mainly ensured by fossil energies such as coal, oil and natural gas. As shown on Figure 0.1, their contributions to the world energy supply are exceeding 80% of the total[1]. The massive use of such resources is affecting the climate due to greenhouse gas emissions. A significant global warming has been noticed by the experts of Intergovernmental Panel on Climate Change (IPCC) in their last report[2]. The international community has recognized the need to limit greenhouse gas emissions.

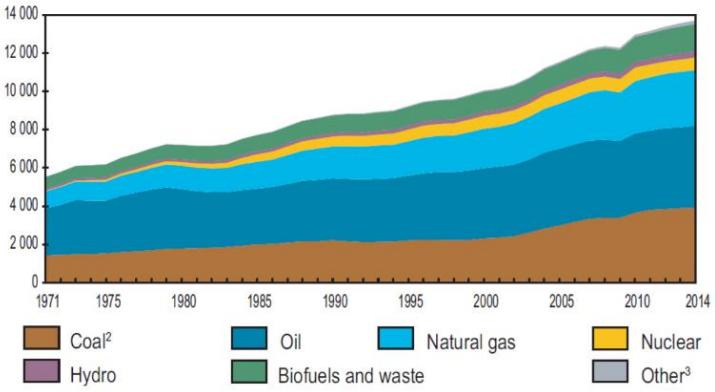

Figure 0.1 – World total primary energy supply from 1971 to 2014 by fuel (Mtoe)[1]

In this context, the European Union (EU) has fixed targets to cut the emissions to 80% below 1990 level by 2050[3]. Knowing that the power sector, in other words the electricity production, is considered as the biggest potential for cutting emissions as shown on Figure 0.2, the massive deployment of renewable energy production technologies such as wind turbines, solar panels, biomass digesters or hydroelectricity is required. However, many of these clean energy sources being intermittent by nature, a new flexible energetic vector for storing energy when produced and non-consumed has to be developed.

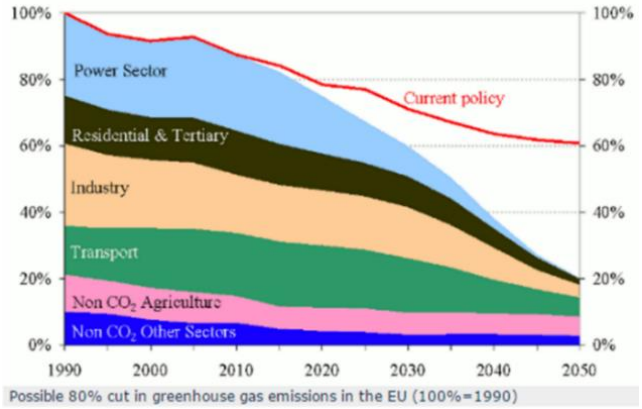

Figure 0.2 – Emissions cuts by sector up to 2050[3].

[1] International Energy Agency, Key world energy statistics 2016, https://www.iea.org/publications/freepublications/publication/KeyWorld2016.pdf
[2] Intergovernmental Panel on Climate Change, http://www.ipcc.ch/report/ar5/wg1/
[3] European Commission, Climate action, https://ec.europa.eu/clima/policies/strategies/2050_en

In that frame, hydrogen appears as a relevant energy vector. Indeed, the H_2 molecule presents a high ratio of energy to mass[4] of about 120 $MJ.kg^{-1}$ well above coal (29 $MJ.kg^{-1}$), oil (43 $MJ.kg^{-1}$) or natural gas (50 $MJ.kg^{-1}$). Nowadays, the dominating process to produce hydrogen is steam reforming of hydrocarbons that is emitting greenhouse gas. Therefore, there is a need to promote cleaner technologies with a low carbon footprint such as steam reforming of biogases or water electrolysis. The electrolysis process, which was discovered during the 19th century by Sir W. Grove [5], consists in the dissociation of the water molecule into H_2 and O_2 gaseous molecule. Several contributions during the last century allowed the development of different electrolysis technologies such as Alkaline electrolysis, Polymer Electrolyte Membrane electrolysis (PEM) or Solid Oxide Electrolysis (SOE).

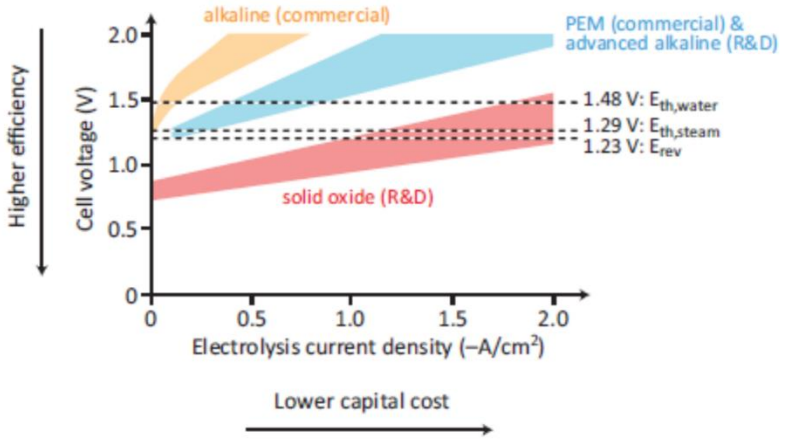

Figure 0.3 - Typical ranges of polarization curves for different types of state-of-the-art water electrolysis cells [6].

From the different technologies available for the hydrogen production, the high temperature solution is considered as the less mature but also the most promising in terms of efficiency and cost. Indeed, this process exhibits the higher electrical efficiency compared to the other solutions as shown on Figure 0.3 at the scale of a single cell. In other words, for a given electrical consumption, the hydrogen production is higher when using Solid Oxide Cells (SOCs). Indeed, in the case of the high-temperature electrolysis, a part of the required energy for the reaction is assumed to be provided by "free" heat. It is thus necessary to combine high-temperature electrolysers with available sources of heat (such as nuclear plants, incinerators, or any industrial furnace).

SOCs are made of ceramic and ceramic-metallic materials without any expensive catalyst. Their operating temperatures are comprised between 600-900°C. Among all these advantages, it is worth noting that SOCs are reversible devices contrary to the low temperature solutions that require specific catalysts for each reaction. It means that the same object can be used to produce hydrogen or to produce electricity. This flexibility is especially interesting for the application to renewable energy storage. Indeed, the electricity can be used to produce

[4] It should be noted that the comparison based on the ratio energy to volume is not so impressive for H_2 that suffers poor compressibility.
[5] W. R. Grove, "LXXII. On a gaseous voltaic battery." Philos. Mag. (1842) 417-420
[6] C. Graves, S. D. Ebbesen, M. Mogensen, K. S. Lackner, "Sustainable hydrocarbon fuels by recycling CO 2 and H 2 O with renewable or nuclear energy", Renewable and Sustainable Energy Reviews 15(1) (2011) 1-23

hydrogen when there is a low electrical demand (electrolysis mode). Then, this hydrogen can be used to fulfil the electrical demand during the peaks of consumption (fuel cell mode).

During the last decade, a huge effort has been paid to develop the high temperature SOC technology. Nevertheless, the lifetime of SOCs still remains insufficient for their industrial deployment and their durability is nowadays considered as the main issue of the technology. Indeed, the operation at high temperature is strongly affecting the material and interfacial stabilities by promoting interdiffusion, chemical decompositions, generation of pollutants or microstructural evolutions. It is thus still necessary to acquire a deep understanding of these degradation mechanisms to be able either to develop solution for avoiding them or to select operating conditions minimizing their effects. It means that the links between the electrode microstructure with the cell performances and the degradation should be examined. This is the context of the present study.

Objectives of the study

This work aims at better understanding the degradation mechanisms of SOCs in fuel cell and electrolysis operations. It will mainly focus on the relationships between the microstructural evolutions and the loss of performances in different operating conditions over time. To reach this goal, a coupled experimental and modelling approach has been used as depicted on Figure 0.4. It is important to carry out long-term durability tests on elementary cells for the experimental investigation of the degradation processes. These tests must be performed with well controlled operating conditions and regular electrochemical characterizations. The effects of polarisation, current density, temperature or gas compositions will be considered in this work.

It has been shown by several previous studies [7] that the electrode microstructure tends to evolve upon operation. Nickel agglomeration is known to occur in the hydrogen electrode. Nevertheless, despite a strong impact on the electrochemistry, the rate of these morphological changes can be rather low especially when considering the state-of-the-art cells. In order to observe such fine evolutions, a highly sensitive characterization method has to be employed. In this work, X-ray nano-holotomography will be used to study the electrodes microstructures. The improvement of the spatial resolution as well as the enhancement of the procedure reliability are two main objectives of this thesis. Morphological and microstructural parameters will be extracted from the obtained 3D volumes of pristine and aged cells.

The data acquired with the characterization methods will be introduced in a multi-scale and multi-physics modelling approach to compare experimental and theoretical performances. In this framework, a model dedicated to new oxygen electrode materials showing Mixed Ionic and Electronic Conduction (MIEC) must be developed to complete the available simulation

[7] E. Lay-Grindler, J. Laurencin, J. Villanova, P. Cloetens, P. Bleuet, A. Mansuy, J. Mougin, G. Delette, "Degradation study by 3D reconstruction of a nickel–yttria stabilized zirconia cathode after high temperature steam electrolysis operation", Journal of Power Sources 269 (2014) 927-936

software. The model takes into account the elementary processes occurring in the electrodes and allows the scale-up to the cell macroscopic behaviour. Comparison of the degradation measured during durability tests and the results of simulations will allow the global contribution of each degradation mechanism to be evaluated.

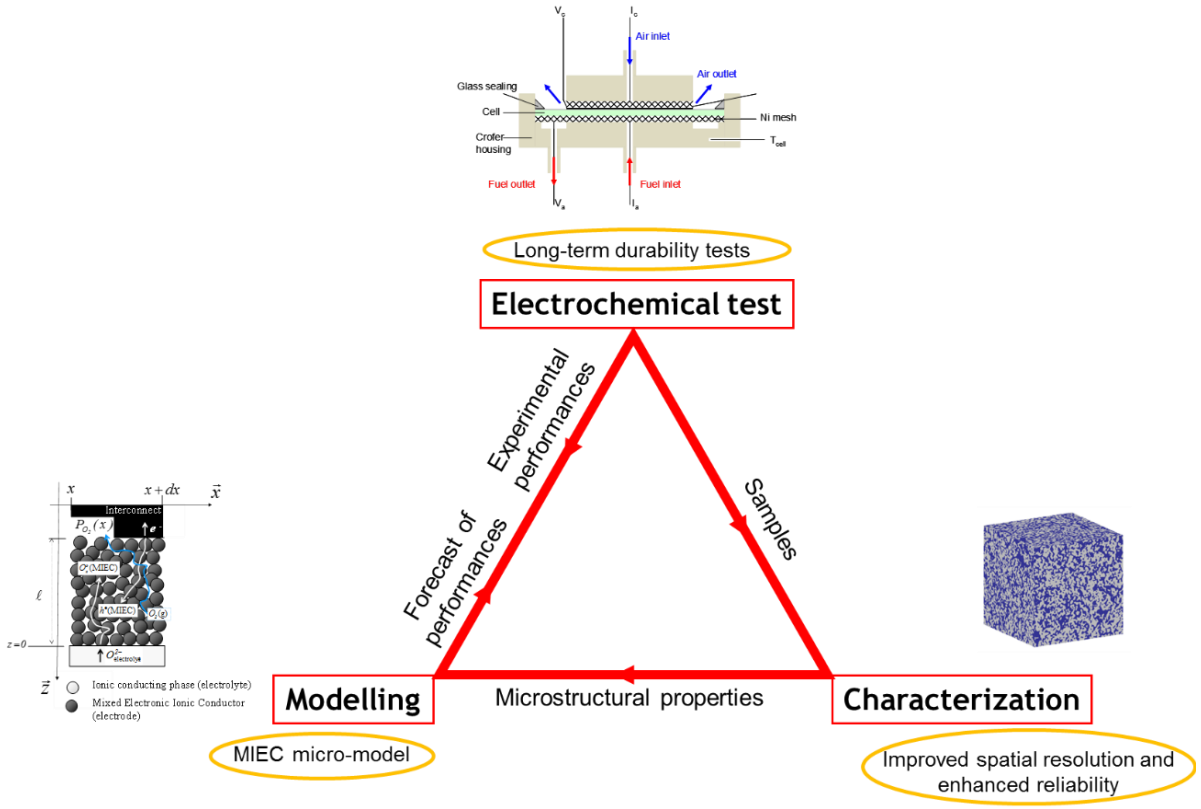

Figure 0.4 - Schematic representation of the triangular approach used in this work. The circled elements are the milestones to be reached before the use of the approach.

Layout of the manuscript

The first chapter is dedicated to the presentation of the context of high temperature Solid Oxide Cells. Firstly, both performance and durability of the state-of-the-art SOCs are provided. Then, a special effort has been given to detail and to rank as far as possible the importance of the main expected degradation mechanisms. In the light of this literature review, the choices and the strategy adopted in the present study are presented.

The second chapter presents the state-of-the-art in synchrotron X-ray imaging by phase contrast. A special discussion has been added to highlight the advantages and drawbacks of nano-holotomography compared to other 3D characterization techniques available for SOCs. The specific method used for the SOCs electrode reconstruction is presented in detail.

The third chapter shows the adaptations of the X-ray nano-holotomography experimental protocol to reach higher spatial resolution and to enhance the reconstruction reliability. In

particular, the new ID16A Nano-Imaging beamline is presented as well as the new sample preparation and data acquisition process. The morphological properties extracted from the 3D volume of pristine O_2 and H_2 electrodes are detailed in this chapter.

The long-term electrochemical tests and post-mortem characterizations are described in the chapter IV. The degradation rates obtained with the test bench are discussed regarding the selected operating conditions. Post-mortem characterizations of every aged cell are also presented to highlight the operating parameters affecting the Nickel agglomeration in the hydrogen electrode.

These microstructural properties are used as input data for the modelling approach presented in the chapter V. The multi-scale modelling approach is validated and used to discuss the degradation effects. The nickel agglomeration contribution on the experimental degradations is detailed in this chapter.

The last chapter is dedicated to an overview of all the results obtained in this study. They are discussed together in the light of recent published literature in the objective to make a synthesis and propose some outlooks to the present work.

Chapter I:

Context of high temperature Solid Oxide Cells

In this chapter, the context of high temperature Solid Oxide Cells (SOCs) is introduced. In particular, the architecture, the materials and the fundamentals of solid-state electrochemistry in SOCs are presented. The basic reactive mechanisms occurring in the electrodes are discussed according to the fuel cell or the electrolysis mode. The SOCs performances and the long-term tests available in the literature are reported and analysed to estimate the most impacting operating parameters on the cell degradation rate. A section is finally dedicated to the underlying mechanisms of material ageing upon operation which are liable to explain the durability tests. From that introduction, a summary and justification of the chosen approach is done.

1. Introduction to SOCs

On Figure I.1, a schematic representation [Lefebvre-Joud2010] of a high temperature SOC operated in electrolysis is shown. The basics of SOCs are given in this first section. The operation principles as well as the common architectures and materials are presented hereafter.

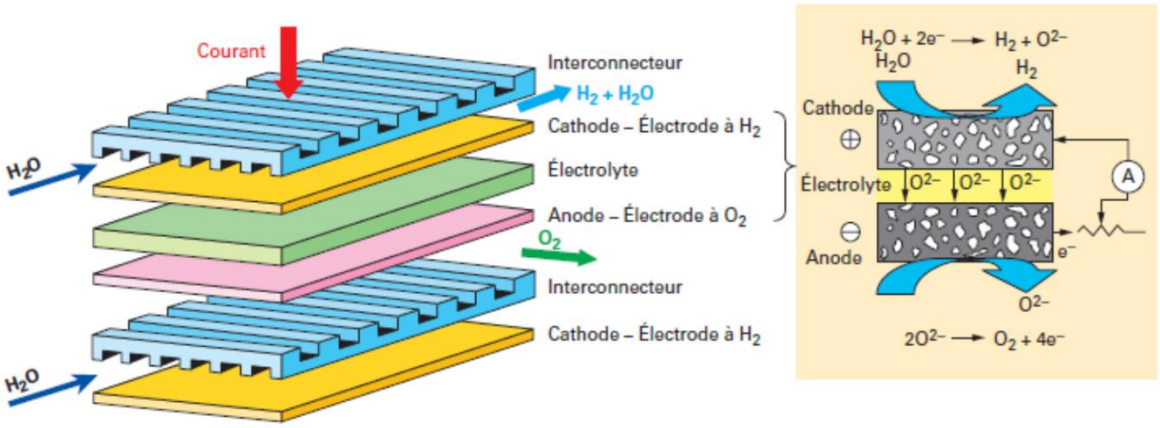

Figure I.1 – Schematic representation of a planar high temperature SOC operated in electrolysis [Lefebvre-Joud2010]

1.1 Operation principles

The SOCs are high temperature electrochemical devices composed of ceramic and metallic components. They can be operated in Solid Oxide Fuel Cell (SOFC) mode to produce electricity by electrochemical oxidation of hydrogen. The same device can be used in the opposite way, in the Solid Oxide Electrolysis Cell (SOEC) mode to produce hydrogen from the reduction of steam under an electrical current. The global equation of the reaction is described in (I.1).

$$H_2O \underset{produce\ electricity}{\overset{consume\ electricity}{\rightleftharpoons}} H_2 + \frac{1}{2}O_2 \qquad (I.1)$$

A SOC consists of three layers made of a dense electrolyte sandwiched between two porous electrodes. The so-called hydrogen electrode is the cell layer in which hydrogen is oxidized in

fuel cell mode or produced from steam in electrolysis mode according to the half reactions (I.2) and (I.3) respectively. The electro-oxidation or reduction of O_2 takes place in the so-called oxygen electrode according to the half reactions (I.4) and (I.5) respectively.

	SOFC mode	**SOEC mode**
H_2 electrode	Anode (I.2) $H_2 + O^{2-} \rightarrow H_2O + 2e^-$	Cathode (I.3) $H_2O + 2e^- \rightarrow H_2 + O^{2-}$
O_2 electrode	Cathode (I.4) $\frac{1}{2}O_2 + 2e^- \rightarrow O^{2-}$	Anode (I.5) $O^{2-} \rightarrow \frac{1}{2}O_2 + 2e^-$

The electrolyte ensures the conduction of the oxygen ions produced by electrochemical reactions from one electrode to the other. In fuel cell mode, gaseous oxygen molecules are reduced at the oxygen electrode into O^{2-} ions that migrate through the dense electrolyte to react spontaneously with gaseous hydrogen at the hydrogen electrode and to produce steam and electrons. In electrolysis, the water molecules are dissociated to form hydrogen gas and oxygen ions. These ions diffuse through the dense electrolyte and are oxidised at the O_2 electrode [Ni2008]. The schematic operation principle of SOFC and SOEC are shown on the Figure I.2.

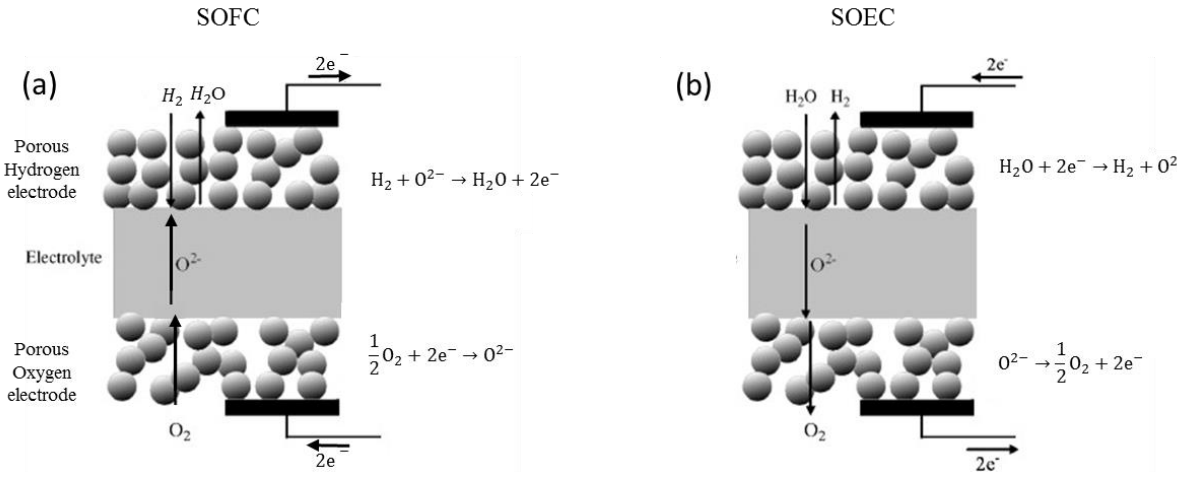

Figure I.2 – Schematic operation principle in (a) SOFC and (b) SOEC modes respectively with the half equations for each electrode.

The high operating temperature of SOCs (between 600°C and 1000°C) allows flexibility on the nature of the inlet gas. In fuel cell mode, internal reforming of hydrocarbons such as methane is thus possible to produce hydrogen into the H_2 electrode [Vernoux2000, Zhu2003, Tu2004, Morel2005, Laurencin2008]. In electrolysis mode, carbon dioxide and steam can be simultaneously co-electrolysed to produce a syngas of carbon monoxide and hydrogen [O'Brien2008, Aicart2014].

Working at high temperature has other interesting advantages. First of all, no expensive catalysts such as Platinum are required for the activation of the electrochemical reactions conversely to the low temperature technologies (polymer electrolyte membrane fuel cells for instance) [Kiburakaran2009, Mekhilef2012]. In addition, from a pure thermodynamic point of view, working at high temperature can also allow reducing the cost of the produced hydrogen if the electrolyser can be connected to a free or cheap available heat source. Indeed, the electrical demand for the water splitting (ΔG) is reduced when increasing the operating temperature. As depicted in Figure I.3, the decrease in ΔG is then balanced by an increase in the thermal need ($T\Delta S$) while the enthalpy is only slightly affected by the operating temperature [Hino2004, Ni2008, Laguna2012].

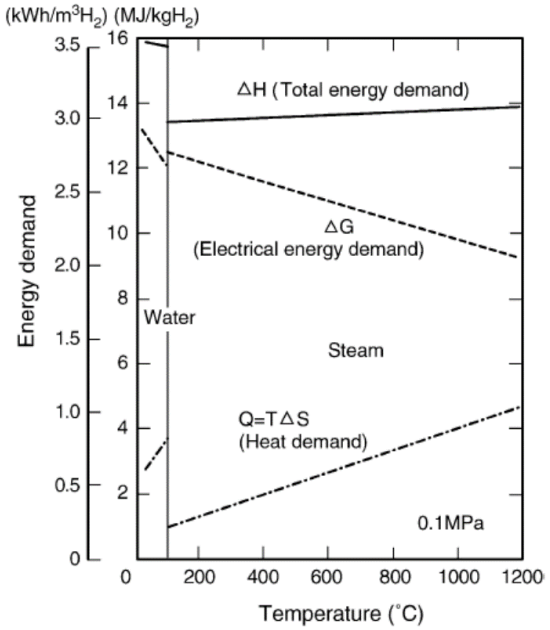

Figure I.3 – Energy demand for water electrolysis as a function of temperature [Hino2004]

1.2 SOC architecture

Several designs have been proposed for the SOC geometry in the literature. The first architecture was initially developed by Siemens-Westinghouse [Hassmann2001] with tubular cells assembled into a bundle. Each cell is composed of a thick O_2 electrode substrate manufactured by extrusion and sintering on which the thin electrolyte and H_2 electrode layers are deposited. In the first tubular concept, cells were 1.8 m long with a thickness of about 2 mm and an external diameter of 22 mm [Blum2005]. The main advantage of the tubular design is its mechanical robustness. It has been shown that this architecture is able to withstand many thermal cycles without degradation. However, the performances of tubular cells are quite low because of high ohmic losses and the compactness of the bundle remains rather poor with a ratio of the active surface on volume of 1 $cm^2.cm^{-3}$ [Déportes1994, Stevens2000].

The tubular design can be favourably replaced by the planar architecture that presents several advantages. Indeed, this design is easier to manufacture. It exhibits much higher performances by limiting the cell ohmic losses and by ensuring a better gas distribution onto the electrodes [Hino2004, Ni2008]. Nowadays, the use of the planar design is widespread and can be

considered as the classical architecture for the high temperature technology. Planar cells are assembled with metallic interconnects to form a stack of high power density. The interconnect plates are designed to ensure the gas distribution and to collect the current. The main drawback of this configuration lies in the management of the gas tightness. Several architectures have been proposed to ensure the structural resistance of the cell (Figure I.4).

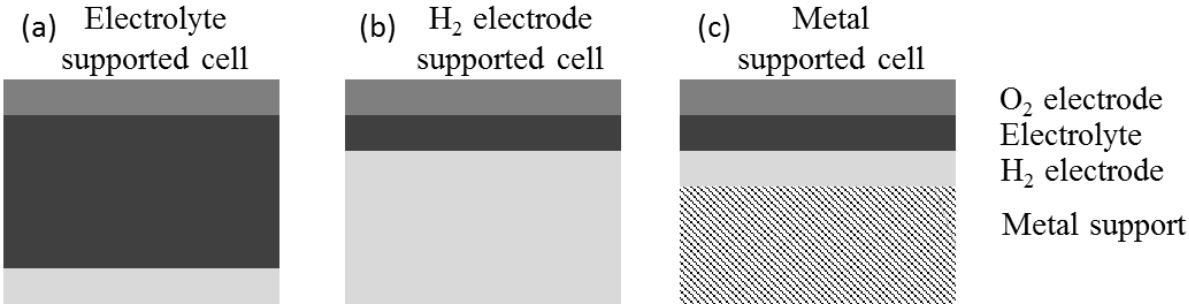

Figure I.4 – Schematic classical architectures of planar cells. (a) electrolyte supported cell, (b) electrode supported cell and (c) metal supported cell

The mechanical strength is obtained by increasing the thickness of one layer that is used as support for the other cell components. A first solution is to deposit thin electrodes on a thick dense electrolyte (Figure I.4a). In this configuration, the ionic conductivity is limiting the performances and high temperatures are necessary to reach high enough conductivity values for the electrolyte. A second solution is to use the H_2 electrode as the cell mechanical support (Figure I.4b). Thanks to the thin electrolyte, the ohmic resistance is reduced and the temperature can be decreased down to 700°C. In this case, the performances can be limited by the gas diffusion across the electrode substrate. In order to increase the cell mechanical reliability, some authors have proposed to use porous metallic interconnects as support for both electrodes and the electrolyte [Villareal2003, Brandon2004, Tucker2010] (Figure I.4c). The main advantage of this variant is its capability to withstand many thermal cycles without any degradation but it raises drastic corrosion issues. The architecture that is the most commonly used nowadays is the hydrogen electrode support concept.

1.3 Materials in SOC

The selection of materials is decisive for the cell performances and durability. They must fulfil several constraints. Regarding the cell mechanical stability, the Thermal Expansion Coefficients (TECs) of the electrodes should match with the electrolyte one. As general features, the electrode materials must also exhibit a high electro-activity regarding the electrochemical reactions and a high electronic conductivity. They should be stable at high temperature either under oxidising atmosphere at the O_2 electrode or under reducing condition at the H_2 electrode. The electrolyte material must exhibit a good ionic conduction whereas its electronic conductivity must be negligible to prevent short circuit. Moreover, the material should be also chemically stable under a large range of oxygen partial pressure at high

temperature. The most classical components for the electrolyte and electrodes are presented in the following parts.

1.3.1 Electrolyte

Stabilized zirconia are the most common materials for SOC electrolyte. Several dopants such as Yb_2O_3, Sc_2O_3 or Y_2O_3 can be used to improve the ionic conductivity and the stability of zirconia. Yttria Stabilized Zirconia (YSZ) is the most classical compound which exhibits the best compromise between mechanical and conduction properties [Ni2008]. The doping ratio has a huge impact on the ionic conductivity of the electrolyte as it stabilizes the cubic zirconia. The ionic conductivity evolves between 0.05 $S.cm^{-1}$ and 0.14 $S.cm^{-1}$ at 1000°C for a doping ratio comprised between 5%mol and 12%mol [Yamamoto2000]. The electrolyte is often doped with 8%mol Y_2O_3 even if a 3%mol can also be used for a better mechanical stability. The ionic conductivity is thermally activated, even with a thin electrolyte, the operating temperature cannot be decreased below 650-700°C to limit reasonably the ohmic losses. Stabilized zirconia are now rather well understood and optimized for operation around 800°C in combination with a number of known electrode materials. To decrease the operating temperature, several alternative materials are being studied such as Gadolinium Doped Ceria (GDC) [Kreuer2003, Ni2008].

1.3.2 Hydrogen electrode

Since Nickel is a good electronic conductor and presents a very high electrochemical activity towards hydrogen, it is nowadays used as the standard material for the H_2 electrode. Nevertheless, it is worth mentioning that the active sites for the reaction (I.2) or (I.3) are limited to the vicinity of Triple Phase Boundary (TPB) lines where the oxygen ions coming from the electrolyte, the electrons transported in the Ni and the gaseous molecules can meet. To extend the TPB lines in the volume of the electrode, a porous cermet of Ni and YSZ (Ni-YSZ) is realized. This architecture allows the electrochemical reaction to be delocalised in the thickness of the electrode. The ratio of Ni to YSZ is directly impacting the performances of the electrode as well as its mechanical robustness [Zhu2003]. Indeed, the thermal expansion coefficient of the cermet is varying with the Ni content [Ni2008]. Moreover, the electronic conductivity strongly depends on this ratio. It has been shown in [Aruna1998] that a content of Ni comprised between 30%vol and 50%vol presents the best properties. It should be noticed that the microstructure of this electrode (especially the TPB density) has a huge impact on the cell performances.

1.3.3 Oxygen electrode

The materials of this electrode are working under a highly oxidising atmosphere at high temperature. As a consequence, pure oxide ceramics are usually used there. Several designs have been developed for this electrode. The first one consists of a composite electrode composed of a good electronic conductor mixed with electrolyte material for the ionic conduction. The architecture of such electrode is similar to the hydrogen electrode with electrochemical reaction taking place at TPB lines (Figure I.5a). By choosing an adapted ratio between the two materials, it is possible to obtain a TEC closed to the electrolyte. A classical composite used for the oxygen electrode is $La_{1-x}Sr_xMnO_3$ – YSZ (LSM-YSZ) where LSM ensures the electronic conductivity and YSZ the ionic one.

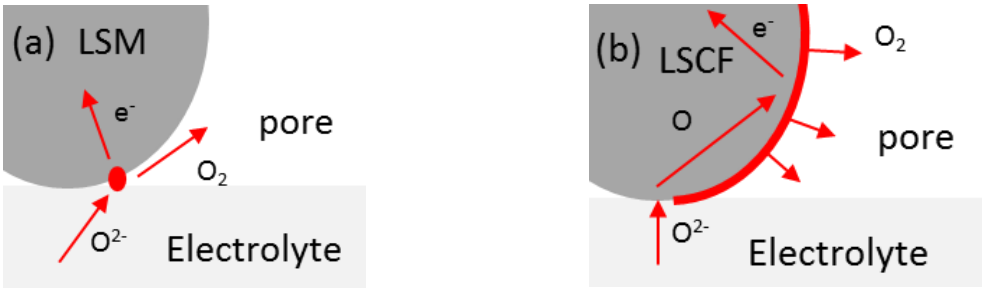

Figure I.5 – Schematic representation of the electrochemically active area (red). (a) case of a LSM-YSZ electrode where the reaction is limited to TPB lines and (b) case of a MIEC (LSCF) electrode where the reaction occurs on the whole surface of the material.

A second class of materials presenting a Mixed Ionic and Electronic Conduction (MIEC) is getting more and more used as oxygen electrodes. In this case, the same material ensures the conduction of electrons and ions. Moreover, the electrochemical reaction is no longer limited to TPB lines but is able to extend onto the whole material surface (Figure I.5b). $La_{1-x}Sr_xCoO_3$ (LSC) or $La_{1-x}Sr_xCo_yFe_{1-y}O_3$ (LSCF) perovskites are the most common MIEC materials used as oxygen electrodes. These compounds allow the electrochemical performances to be improved compared to the LSM-YSZ composite [Tietz2006]. However, the chemical instability of LSC or LSCF and their reactivity with YSZ are major drawbacks that limit the cell durability. To mitigate this issue, a thin barrier layer of GDC is classically added between the electrolyte and the electrode. Moreover, composite electrode made of LSCF and GDC has been also proposed to adapt the electrode TEC to the electrolyte one [Gao2016].

2. Physical phenomena in SOCs

Many physical phenomena are involved in the SOCs operation [Singhal2003, US2004, Kendall2015]. They affect the cell performances which are characterised by the polarisation curve. This curve plots the evolution of the cell voltage U_{cell} as a function of the current density i. As depicted in Figure I.6, the cell voltage varies non-linearly with the current density and

depending if its value is small or big, the mechanisms controlling the cell behaviour are different. All these different elementary mechanisms are detailed in the following parts.

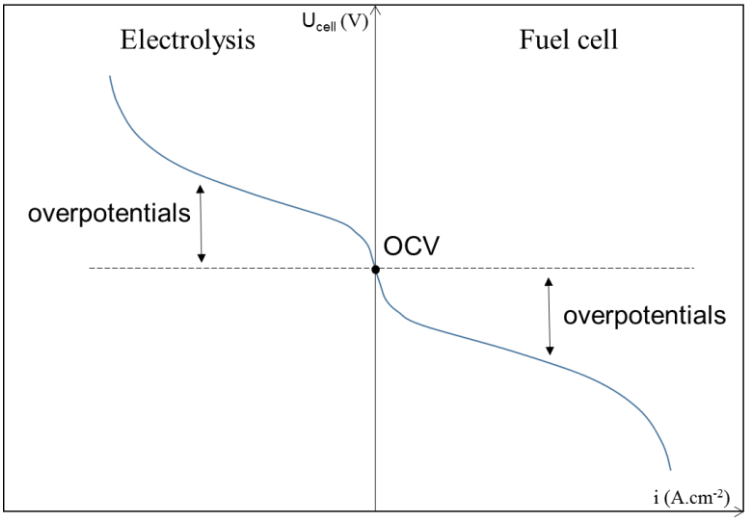

Figure I.6 –Polarisation curve of a SOC in electrolysis and fuel cell modes.

2.1 Open Circuit Voltage (OCV)

The difference of oxygen partial pressure across the electrolyte leads to an electrical voltage. In open circuit condition, the potential $U_{i=0}$ can be expressed thanks to the Nernst law (Eq. (I.6)) [US2004, Kendall2015]. It depends on the gas conditions as well as the temperature as follows:

$$U_{i=0} = U^0(T) + \frac{RT}{2\mathcal{F}} \ln\left(\frac{a_{H_2}^{interface,i=0} \times \left(a_{O_2}^{interface,i=0}\right)^{0.5}}{a_{H_2O}^{interface,i=0}}\right) \quad \text{(I.6)}$$

where U^0 is the standard potential of the reaction and $a_x^{interface,i=0}$ the activity of the element x taken at the interface with the electrolyte under a nil current. $\mathcal{F}$ is related to the Faraday's constant and R is the gas constant ($R = 8.314$ J.mol^{-1}.K^{-1}). Upon operation, several overpotentials are generated that modify the cell voltage.

2.2 Ohmic overpotential

The ohmic overpotential includes the material resistance to the flow of electrons and ions as well as the contact resistance grouped under R_Ω expressed in ohm.cm^2. This overpotential is proportional to the current density and obeys the classical Ohm's law (Eq. (I.7)).

$$\eta_{ohmic} = R_\Omega \times i \quad \text{(I.7)}$$

The resistance of the dense electrolyte represents the main part of the ohmic overpotential. The second contribution is due to the contact between cells and current collectors. A grid is usually used in test set-up to limit this resistance as much as possible.

2.3 Concentration overpotential

The concentration overpotential η_{conc} arises in operation because of the electrode inability to maintain the fluid initial composition in the neighbourhood of the electro-active sites. It can be expressed as the sum of the gas conversion losses ΔU_{rev} and the diffusion overpotential η_{diff}:

$$\eta_{conc} = \Delta U_{rev} + \eta_{diff} \tag{I.8}$$

2.3.1 Gas conversion losses

Even if the system is considered as ideal (i.e. the thermodynamic conditions are fulfilled), the cell potential remains impacted by a reversible contribution due to the change in the gas composition with the current [Laurencin2015]. These conversion overpotentials can be deduced from the Nernst equation when it is applied under current assuming a steady state situation. They are expressed as follows for each electrode (Eq. (I.9) and (I.10)):

$$\Delta U_{rev}^{H_2} = \frac{RT}{2\mathcal{F}} ln\left(\frac{a_{H_2}^{canal,i=0} \times a_{H_2O}^{canal,i\neq0}}{a_{H_2}^{canal,i\neq0} \times a_{H_2O}^{canal,i=0}}\right) \tag{I.9}$$

$$\Delta U_{rev}^{O_2} = \frac{RT}{4\mathcal{F}} ln\left(\frac{a_{O_2}^{canal,i\neq0}}{a_{O_2}^{canal,i=0}}\right) \tag{I.10}$$

where $a_x^{canal,i=0}$ and $a_x^{canal,i\neq0}$ are the activity of the species x taken in the canal of gas distribution at a current density $i = 0$ and $i \neq 0$ respectively. These expressions do not consider the mass transfer in the electrode porous thickness. It only expresses the gas conversion limitation on the cell voltage. They reflect the fact that the cell current density reaches a limiting value when all the reactant has been consumed.

It is worth mentioning that the gas conversion losses depend only on the operating conditions defined by the current density and the gas feeding conditions. These 'thermodynamic' contributions are thus 'unavoidable' and will be the same whatever the SOC materials. In these conditions, cell polarisation curves can be compared only if the contributions $\Delta U_{rev}^{H_2}$ and $\Delta U_{rev}^{O_2}$ are identical. In other words, assessment in performances of different cells is relevant only if the *i-U* curves are compared for identical conditions of inlet gas fluxes N_{gas}^{inlet} that lead to the same steam conversion and oxygen production rates. The gas conversion rates are usually defined as follows for fuel cell and for steam electrolysis respectively:

$$Fuel\ Utilisation = \frac{i}{2\mathcal{F}N_{H_2}^{inlet}} \text{ and } Steam\ Conversion = \frac{i}{2\mathcal{F}N_{H_2O}^{inlet}} \tag{I.11}$$

where the ratio $i/2\mathcal{F}$ represents the hydrogen or steam consumed by the electrochemical reaction according to Faraday's law.

2.3.2 Gas diffusion overpotential

The porous electrodes constitute a barrier to the gas transfer from the gas channel to the electrode active sites. This limitation on the gas transport induces a partial pressure gradient across the electrode thickness resulting in the so-called diffusion overpotentials:

$$\eta_{diff}^{H_2} = \frac{RT}{2\mathcal{F}} ln\left(\frac{a_{H_2}^{canal,i\neq 0} \times a_{H_2O}^{TPB,i\neq 0}}{a_{H_2}^{TPB,i\neq 0} \times a_{H_2O}^{canal,i\neq 0}}\right) \quad \text{(I.12)}$$

$$\eta_{diff}^{O_2} = \frac{RT}{4\mathcal{F}} ln\left(\frac{a_{O_2}^{TPB,i\neq 0}}{a_{O_2}^{canal,i\neq 0}}\right) \quad \text{(I.13)}$$

The activities are considered under current in the canal or in the electrochemical active area noted TPB.

2.4 Activation overpotential

The activation overpotential takes into account the irreversible phenomena associated to the electrochemical reactions. They include all the elementary reactive mechanisms taking place within the active part of the electrodes in which the reactions extend such as the charge transfer or diffusion around the TPBs. At the cell level, they are simply modelled according to a Butler-Volmer formalism [Ni2007, Udagawa2007]. It should be noticed that it is a purely phenomenological approach as this equation only considers a charge transfer at the electrode/electrolyte interface [Laurencin2015]. The activation overpotential for both electrodes are given in Eq. (I.14) and (I.15).

$$\eta_{act}^{H_2} = \frac{RT}{\mathcal{F}} sinh^{-1}\left(\frac{i}{2i_0^{H_2}}\right) \quad \text{(I.14)}$$

$$\eta_{act}^{O_2} = \frac{RT}{\mathcal{F}} sinh^{-1}\left(\frac{i}{2i_0^{O_2}}\right) \quad \text{(I.15)}$$

where i_0 is an "apparent" exchange current density that characterizes the electrochemical reactions. This parameter is mainly dependent on the microstructure and the temperature but also on the gas composition. It should be noticed that the microstructure of the electrode active part plays a major role on the activation overpotential [Virkar2000].

2.5 Reactive mechanisms

The determination of the elementary reactive mechanisms occurring in the electrodes is complex and requires fine analysis and characterisations. The modelling approach is generally used to compare experimental data with simulated ones assuming precise hypothesis in the objective to identify a relevant reactive pathway. It should be noticed that the reactive

mechanism may differ according to the polarisation or the test conditions. Moreover, the microstructure of the electrodes affects directly the mechanisms since the kinetic rates depends on the morphological properties. An overview of the reactive mechanisms considered in the literature for the hydrogen and oxygen electrodes is proposed hereafter.

2.5.1 Hydrogen electrode

The reactive mechanisms in the classical Ni-YSZ electrode have been studied in many works [Mizusaki1994, Mogensen1996, Bessler2007, Vogler2009, Goodwin2009, Grondin2011, Dasari2013]. A major part has been dedicated to the fuel cell mode. With this polarisation, a multi-step reactive pathway is generally considered in the studies. The first elementary step is the hydrogen adsorption on the Ni surface. In parallel, the oxygen ions are excorporated from the YSZ bulk to its surface. The charge transfer reaction takes place at the TPB. Complex surface reactions referred to hydrogen spillover have been proposed in the literature [Bessler2007]. The water is finally desorbed from the surface to give steam. In this series of reactive steps, there is a large concordance to consider the charge transfer reaction at TPBs as the limiting step of the global mechanism in that polarisation.

In electrolysis mode, the multi-step reactions could be different. Some experiments tend to show a limitation by the water partial pressure suggesting that an adsorption reaction could be the limiting step [Grondin2011, Laurencin2015]. The global reactive pathway is thus expected to be different from the fuel cell mode. However, at the time of writing, there is no clear consensus on the elementary reaction pathway in electrolysis mode on the Ni-YSZ electrode.

2.5.2 Oxygen electrode

For a composite oxygen electrode made of LSM-YSZ, it is generally admitted that the reduction reaction in fuel cell mode is the reverse of the oxidation reaction occurring in electrolysis polarisation. The proposed reactive mechanism is usually based on two main steps [Lay2013, Shin2013]. In SOFC, the first step is the oxygen adsorption on the surface of LSM. Then, a charge transfer reaction takes place at the TPB to give an oxygen ion into the YSZ phase. The reverse mechanism would occur in electrolysis. There would be firstly a charge transfer reaction at TPBs. The oxygen is then desorbed to give an O_2 gas molecule. Some authors propose a more complex pathway on surface of the LSM by adding other steps [Jorgensen2001, Kim2001, Chen2003]. All these models show that the surface diffusion of the adsorbed oxygen or its desorption have a huge impact on the cell performance.

Mixed ionic and electronic conductors have the advantage to extend the electrochemically active area on the whole surface of the solid phase. It can be easily understood that the reactive pathway will be different from the LSM-YSZ electrode. In fuel cell mode, the reactive mechanisms are generally described by a three steps mechanism. The first reaction is the oxygen adsorption on the MIEC surface. The adsorbed molecules are then reduced by charge transfer and incorporation into the lattice of the MIEC material. Finally, the oxygen ions flow

by solid-state diffusion and are transferred into the electrolyte by a second charge transfer reaction. It is generally admitted that this reaction pathway, which is called the "bulk path", controls the global reactive mechanism of MIECs operated in fuel cell mode [Adler1996, Deseure2005, Fleig2007, Rueger2007, Carraro2012]. Nevertheless, some authors have pointed out that the direct reduction at the electrolyte/MIEC/gas TPB lines could be also involved in the mechanism [Liu1998, Liu1998b, Coffey2003, Simrick2012, Enrico2014, Gong2014]. Moreover, it is expected that the direct charge transfer at TPB lines could become non-negligible for some operation conditions or materials compositions. For example, in the case of a composite MIEC-GDC, the density of TPB is substantially increased as the active sites extend in the whole electrode thickness. In this composite a reactive mechanism limited to the bulk path could appear too restrictive. Contrarily to the fuel cell mode, very few studies have been dedicated to analyse the reactive mechanisms in electrolysis mode [Coffey2003, Wiemhoefer2002]. They suggested the contribution of TPBs in the electrode performances. The reaction pathway activated under anodic polarisation for O_2 production remains almost unknown.

3. State of the art of modelling

The development of numerical tool to understand the SOC response is of high interest. These approaches can be used to allow the interpretation of experimental results or to find the reactive mechanisms of an electrode. There is a lot of approach to model the physical phenomena in SOC as illustrated on Figure 1.I.7. They can be differentiated in several categories such as the state (transient or steady state) or the dimension (from 0D to 3D). There is also different scale level to model SOCs [Andersson2010, Stempien2013]. Some numerical tools proposed in the literature are dedicated to the understanding of the electrochemical mechanisms in the electrodes whereas others describe the cell or stack response. The main goals of models developed from the atomistic to the macroscopic scale are reminded hereafter.

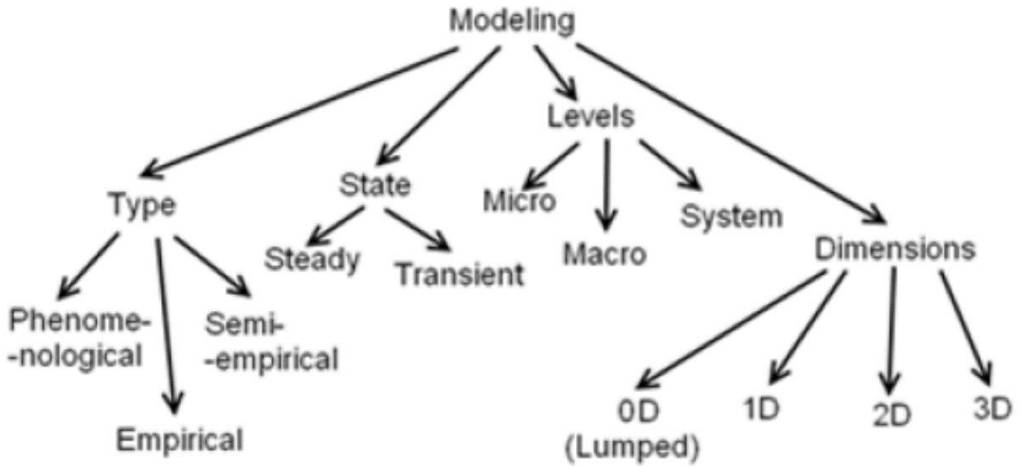

Figure 1.I.7 – Categories of model of physical phenomena [Stempien2013]

3.1 Atomic nano-scale modelling

Some studies have been dedicated to a better understanding of the processes occurring at the atomic scale. These models are especially interesting to identify some properties required for the upper scale modelling. There are different approaches based for example on density functional theory, molecular mechanics or kinetic Monte-Carlo simulations. There are few works for SOFC to describe electrode reactions [Anderson2006, Mukherjee2007, Rossmeisl2008, Shishkin2009]. These models are not yet able to give access to macroscopic information as polarisation curve or impedance spectra.

3.2 Electrode micro-scale modelling

A lot of studies have been dedicated to the modelling of the elementary kinetics in the oxygen and hydrogen electrodes. The main goal of these simulations is to investigate the possible reactive mechanisms and their delocalisation in the electrode thickness. A review of the main models for cathode and anode is proposed in [Adler2010]. In these simulations, the reactions occurring at the solid/gas and solid/solid interfaces are taken into account. The different species transports are also considered in these models. The electrode response can be calculated with these numerical tools in different operating conditions. The limiting step in the global electrochemical reaction can be determined with the simulation. Some models are dedicated to steady-state simulations whereas others are dealing with the electrochemical impedance spectra. There is not a consensus on the reaction pathways, intermediate species and rate-limiting steps for both electrodes [Bessler2007]. For the cathode (O_2 electrode), the mechanism in MIEC have been modelled by successive steps as proposed in [Adler1996, Liu1998, Coffey2003, Deseure2005, Fleig2007, Rueger2007, Gong2014, Yurkiv2014]. For the anode (H_2 electrode), the reactive pathway is divided into successive elementary steps or limited to a simple charge transfer at TPBs for simplification of simulations [Mizusaki1994, Mogensen1996, Costamagna1998, Bieberle2002, Bessler2005, Goodwin2009]. At this scale, the transport in the gas channel is usually neglected. They can be taken into account in more general simulation tools developed at the cell level.

3.3 Cell macro-scale modelling

Several groups have developed models allowing the prediction of the complete cell performances. The simulations are used to explain the experimental polarisation curve recorded in different operating conditions. These approaches are generally based on the calculation of the Nernst potential at equilibrium. Then, the overpotentials are subtracted to this value. In these models, the activation overpotential is generally calculated by using a Butler-Volmer type equation to describe the electrochemical kinetic. It means that the possible complex reactive mechanisms occurring in the electrodes is simplified by a single charge transfer reaction. This approach is widely used as it is computationally cheap and the cell response is rather well described. Several review articles are available in the literature to have an overview of existing

models [Kakac2007, Hajimolana2011, Wang2011]. The simulations are based either on in-house numerical tools [Ferguson1996, Iwata2000, Aguiar2002, Costamagna2004, Morel2005, Leonide2009] or Complex Fluid Dynamic (CFD) approaches [Yakabe2001, Ackmann2003, Pasaogullari2003, Recknagle2003, Autissier2004]. The micro and macro scale models can be linked each other to enhance the SOC electrochemical response obtained by the simulation. There is also models considering the system level [Winkler2002, Leucht2011]. They are mainly used for basic feasibility studies as big simplifications are generally assumed.

3.4 Modelling of the electrolysis mode

Most of the models have been developed for the fuel cell mode. There is less literature dedicated to the simulation of the electrolysis polarisation. A review of articles devoted to this mode can be found in [Stempien2013]. It appears that some numerical tools developed for the fuel cell mode have simply been used to simulate the operation in electrolysis. However, this polarisation presents some specificities. Some models have been developed at the electrode scale to describe this operating condition [Grondin2011, Lay2013]. There are also simulations to describe the cell response in electrolysis mode. In-house and CFD approaches are found in the literature [Ni2007, Udagawa2007, Ni2009, Laurencin2011]. It appears that there is still a lack in the understanding of the reactive mechanism in electrolysis. More researches are needed on this specific polarisation.

4. State of the art of SOC performances and durability

A deep understanding of the physical processes involved in the SOCs operation is essential to improve the cell performances and durability all together. Well defined protocols are also of major importance to evaluate both the initial performances and the degradation rates in relevant experimental conditions. In this context classical measurements are proposed in the literature in an attempt to compare the performances and the degradation between different cells. Despite these efforts, it is worth noting that a direct comparison between the data reported in the literature is somewhat complicated due to differences in the test conditions (temperature, gas composition, flow rates …). However, in this section, typical cell performances and degradation rates are reported. The underlying mechanisms, which are assumed to be involved in the cell performance degradation, are also reported.

4.1 SOC performances

One of the best performances reported up to now on both modes is illustrated on Figure I.8 where a typical polarisation curve in both modes for a H_2 electrode supported cell made of Ni-YSZ//YSZ//GDC//LSCF is shown. The complete test conditions can be found in [Schefold2012]. In fuel cell mode, with a ratio H_2/H_2O of 92/8, a current density of 1 $A.cm^{-2}$ is reached at 0.78 V, T=776°C and a Fuel Utilisation (FU) rate of 63%. In electrolysis mode,

with a ratio $H_2/H_2O/N_2$ of 9/80/11, a current density of -1 A.cm^{-2} is reached at 1.08 V, T=772°C and a Steam Conversion (SC) rate of 36%.

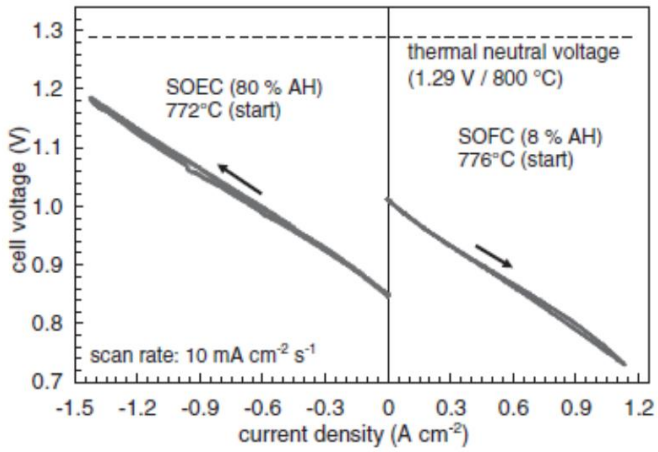

Figure I.8 – Typical polarisation curves measured in both SOFC and SOEC modes for a H_2 electrode supported cell made of Ni-YSZ//YSZ//GDC//LSCF [Schefold2012].

Table I.1- Some initial performances from the literature highlighting the effects of operating temperature, cell materials and manufacturers.

Mode	T (°C)	O_2 electrode materials	U (V)	i (A.cm^{-2})	ASR (Ω.cm^2)	Reference
SOFC	750	LSM-YSZ	0.72	0.5	0.44	[Hauch2006]
		LSCF-ScSZ	0.71	0.35		[Tomoshige2013]
		LSCF	0.76	0.35		[Mori2015]
	780	LSCF	0.78	1		[Schefold2012]
	800	LSM-YSZ			0.93	[Laguna2010]
		LSCF			0.79	[Laguna2010]
		LSCF (1)	0.72	0.3		[Zhang2013]
		LSCF (2)	0.81	0.3		[Zhang2013]
	850	LSM-YSZ	0.82	0.5	0.21	[Hauch2006]
		LSCF (3)	0.82	0.3		[Zhang2013]
		LSM-YSZ (3)	0.8	0.3		[Zhang2013]
SOEC	750	LSM-YSZ	1.26	-0.5	0.65	[Hauch2006]
	770	LSCF	1.08	-1		[Schefold2012]
	800	LSCF (1)	1.04	-0.3		[Zhang2013]
		LSCF (2)	0.95	-0.3		[Zhang2013]
		LSM-YSZ			0.83	[Laguna2010]
		LSCF			0.70	[Laguna2010]
	850	LSM-YSZ	1.06	-0.5	0.27	[Hauch2006]
		LSCF (3)	0.95	-0.3		[Zhang2013]
		LSM-YSZ (3)	0.99	-0.3		[Zhang2013]

Cell Manufacturer: (1) SOFCPower Inc., (2) Ceramatec Inc., Materials and Systems Research Inc., (3) Saint Gobain Advanced Materials.

In Table I.1, the performances of different Ni-YSZ cermet supported cells are reported in terms of current density and Area Specific Resistance (ASR). As expected, higher temperature leads

to better performances since the conductivities and the reactions are thermally activated [Hauch2006]. Knowing that the activation losses at the O_2 electrode are reckoned to be significant [Leonide2010], the cell efficiency is also strongly dependent on the choice of the O_2 electrode material. As already discussed, MIECs such as LSCF or LSC perovskites allow the activation losses to be significantly reduced, and hence, to improve the global cell efficiency [Laguna2010, Tomoshige2013, Zhang2013, Mori2015].

Nevertheless, even for the same materials tested in the same conditions, a large discrepancy in the cell performances is found when testing cells from different manufacturer [Zhang2013]. It tends to mean that the electrodes microstructures play a major role on the performances and constitute key parameters that govern the cell efficiency. More specifically, the microstructure of the cell support can be expected to be crucial for the gas diffusion whereas the microstructure of the electrode active layer would favour the electrochemical reactions (for example, by increasing the density of TPBs).

4.2 SOC durability

The long-term tests are commonly performed in galvanostatic conditions (i.e. the current density is imposed) whereas the cell voltage is recorded over time. The degradation rate is then defined as the voltage loss divided by the test duration Δt as shown in Eq. (I.16):

$$r_{deg} = \frac{U_t - U_0}{\Delta t} \tag{I.16}$$

The degradation rate r_{deg} is usually expressed for 1000h of operation. Note that the rate is sometimes expressed in percentage of voltage loss during 1000h. A typical curve measured during a durability test of 9000h [Schefold2012] is shown on Figure I.9. The cell voltage evolution is noisy due to experimental instability (gas flows, power failure…).

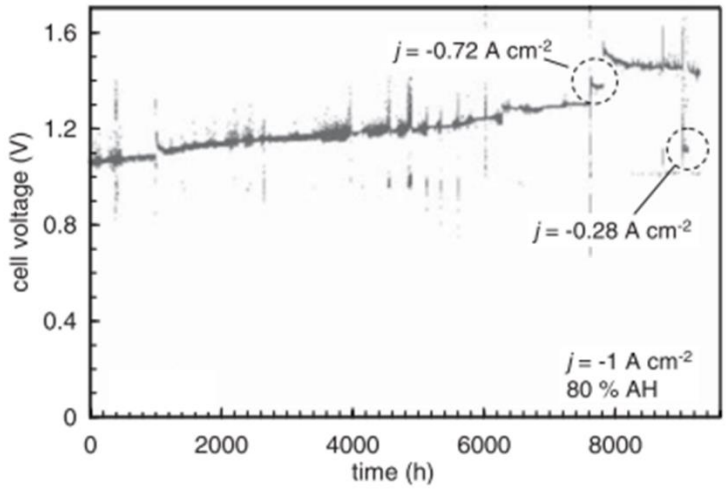

Figure I.9 – Cell voltage evolution over time for a cell operated in electrolysis mode at -1 A.cm^{-2} [Schefold2012]

The durability of SOCs is nowadays the main issue of the technology. Indeed, a lot of data are available in the literature on the cell degradation in different test conditions from individual button cell to stacks. On Figure I.10, degradation rates reported in the literature are plotted as

a function of operation time for tests performed on stack or cells in different conditions (temperature, polarisation, gas composition, current density,…) [Skafte2016].

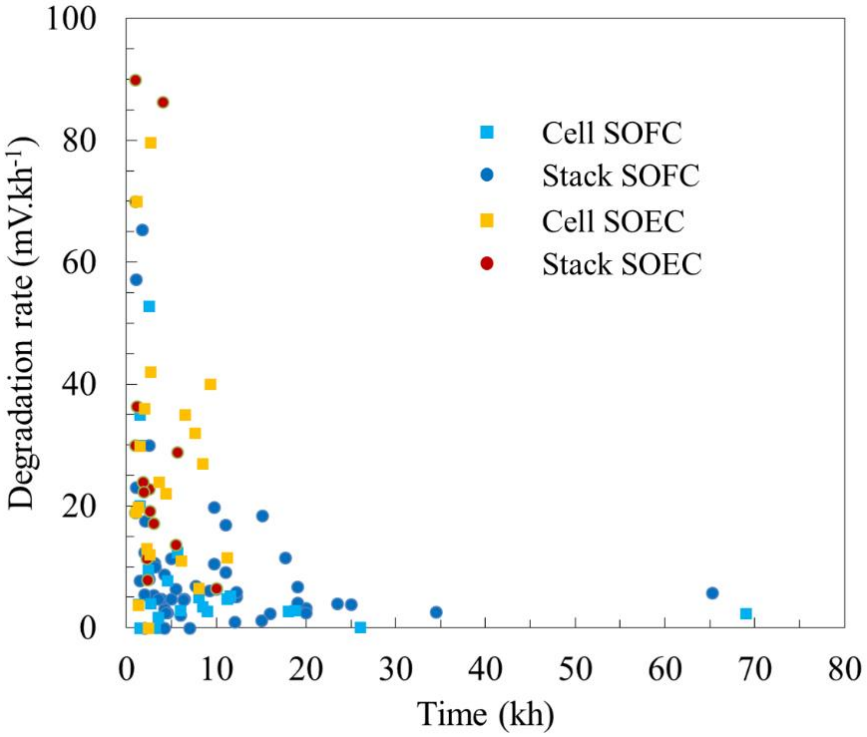

Figure I.10 – Degradation rates for single-cell (square) and stack (circle) long-term tests in both fuel cell (blue) and electrolysis (red) modes (data from [Skafte2016]).

In fuel cell mode, one of the longest ageing tests reported in the literature measured a degradation rate of 0.32 mV.kh^{-1} after 19000h on a planar cell [Torabi2016]. The durability of planar SOCs in fuel cell mode ranges currently around few millivolts per 1000h (i.e. around 1-0.5 %.kh^{-1}) [Tietz2006, Orui2008, Ghezel2013, Borglum2015, Hatae2015, Noponen2015, Trofimenko2015]. In electrolysis mode, the degradation rates are found to be higher. The order of magnitude is about 10 mV.kh^{-1} (i.e. 1-5 %.kh^{-1}) [Brisse2008, Hauch2008, Schefold2013]. In one of the longest tests, performed during 9300h, a degradation rate of 40 mV.kh^{-1} was measured [Schefold2012]. Better durability has been obtained in [Schefold2015] with a degradation rate of about 7 mV.kh^{-1} after 11000h or in [The2015] with a value below 1 %.kh^{-1} after 6100h. Despite this quite low values, the degradation rates are still too high. Indeed, to be economically viable, the cell degradation rates should not exceed 0.25 %.kh^{-1} in fuel cell mode [Blum2013] and 1-3 %.kh^{-1} in electrolysis mode [Relhy].

In fuel cell mode, several studies have been dedicated to identify the operating parameters that affect the degradation rates. As a general rule, it is well accepted that the inlet gas composition and flow, and the current density have a major impact on the durability curve. For example, Hagen et al. [Hagen2006] have shown that the degradation is significantly accelerated by any increase of the current density (35 mV.kh^{-1} at 0.41 A.cm² and 125 mV.kh^{-1} at 0.75 A.cm²). Surprisingly, many authors reported that the degradation rate is lowered at higher temperature [Hagen2006, Hauch2006, Diethelm2013, Fang2015, Kotisaari2016]. As an illustration,

[Hagen2006] have measured a rate of 125 $mV.kh^{-1}$ at 750°C and 20 $mV.kh^{-1}$ at 850°C. There are much less studies devoted to the durability in electrolysis mode [Hauch2006, Knibbe2010, Sun2015]. The operating parameters influencing the degradation are not precisely determined. In addition, the degradation rates seem to be higher under electrolysis mode compared to fuel cell mode.

4.3 Degradation mechanisms

The degradation rate reflects the material ageing of SOC components upon operation. The cell ohmic losses and/or the electrode overpotentials are increased over time because of pollutions or of microstructural evolution such as phase coarsening or material destabilisation at high temperature. These evolutions are different according to the operating conditions or the cell materials. Nowadays, despite several efforts, the underlying mechanisms of degradation are not fully understood. In practise, advanced post-test characterizations are required to analyse the change in electrode microstructure or in physico-chemical properties of the materials. In the literature several degradation mechanisms are proposed for the SOC components, which are presented hereafter.

4.3.1 Oxygen electrode

A lot of studies exist on the degradation occurring at the oxygen electrode in fuel cell and electrolysis mode. The main mechanisms that have been highlighted in the literature are related to the cation diffusion, the materials reactivity with the electrolyte or the delamination of the electrode. Numerous articles are also dedicated to Chromium poisoning coming from the metallic interconnects.

4.3.1.1 Segregation, diffusion and reactivity of cations

The oxide materials used in the oxygen electrode are subject to an electrochemical potential gradient. It induces the mobility of chemical or charged elements inside the electrode. In practise, with classical oxygen electrode components (LSM-YSZ or MIEC), reactivity of cations with the electrolyte has been observed after cell operation. The new phases $SrZrO_3$ and $La_2Zr_2O_7$ have been detected by many authors [Setoguchi1990, Jiang1999, Mai2005, Yokokawa2008, Adijanto2011, The2015]. They are mainly localised at the electrode-electrolyte interface as shown by [Simner2006].

The mechanism for the reactivity of these materials is still unclear, but some experimental works allow proposing hypothesis. A Strontium segregation at the surface of LSCF has been observed in several articles [Simner2006, Oh2012, Pan2015, Wang2016]. A SrO passivation film has been clearly identified after heat treatment by [Oh2012]. A hydroxide strontium species $Sr(OH)_2$ has even been found on a LSCF surface by [Cai2012]. As suggested by F. Tietz et al. [Tietz2008], the Strontium transport from the electrode to the interface with the

electrolyte probably occurs in the gas phase due to the $Sr(OH)_2$ volatile species. The effects of operating parameters as temperature or polarisation on this degradation mechanism are unclear as contradictory results can be found in literature. Nevertheless, the water content in the gas at the oxygen electrode seems to be an impacting parameter [Hjalmarson2008, Bucher2011].

The new phases created at the interface with the electrolyte have a low conductivity and will not be electrochemically active. Their localisation could favour the delamination of the oxygen electrode [Jiang1999]. As already mentioned, a thin GDC barrier layer is generally added between the electrode and the electrolyte [Mai2006, Uhlenbruck2009, Adijanto2011] to limit the material reactivity. Nevertheless, the Strontium segregation at the LSCF surface and the precipitation of a SrO passivation film is suspected to affect the reaction kinetics and to degrade the electrode performances [Simner2006, Oh2012]. Therefore, even if $SrZrO_3$ formation is avoided, the electrode performances could be impacted. This degradation mechanism could be non-negligible in the overall cell performance decay.

4.3.1.2 Delamination

At the oxygen electrode side, the delamination at the interface with the electrolyte is another impacting degradation. Few studies observed a delamination of the oxygen electrode in fuel cell mode [Hagen2006, Virkar2007, Park2010], which were attributed to a TEC mismatch between the electrode and electrolyte materials [Park2010]. More studies have highlighted a delamination upon electrolysis operation [Knibbe2010, Laguna2011, Hjalmarsson2013, Kim2013, Tietz2013].

For a composite LSM-YSZ oxygen electrode, a degradation mechanism has been proposed to explain the delamination in electrolysis mode [Chen2011, Keane2012]. The cations reactivity with zirconia is creating the new phases $La_2Zr_2O_7$ and $SrZrO_3$ [Keane2012] that could induce a mechanical stress in the particle leading to micro cracks [Chen2011]. The repetition of such micro-cracking all along the interface could result in the complete delamination of the electrode. This degradation would be favoured in electrolysis mode as the internal oxygen pressure in the electrolyte is high under anodic polarisation [Virkar2007, Knibbe2010, Virkar2010, Zhang2012]. A higher temperature could also enhance this degradation mechanism as the cations mobility would be favoured [Rashkeev2012, Zhang2012]. However, it is specific of LSM-YSZ electrodes.

4.3.1.3 Chromium poisoning

The metallic interconnects are often made in ferritic steel containing a large amount of Chromium. Many studies have demonstrated that the Chromium can be released from interconnects under oxidizing atmosphere at high temperature and react with the O_2 electrode material [Matsuzaki2001, Simner2005, Konysheva2006, Jiang2014]. The Cr poisoning is a well-documented degradation mechanism. In the literature this pollution has been mainly observed in fuel cell mode even if it also happens in electrolysis mode [Sharma2010]. A

significant amount of $SrCrO_4$ is usually observed in the area directly in contact with the interconnect [Jiang2006, Ardigo2011]. In this case, solid state diffusion would be the main transport mechanism. However, many studies have shown that Chromium is transferred from the interconnect into the electrode by volatilisation and re-deposition [Hilpert1996, Simner2005, Chen2010]. The gaseous molecules react with the LSM, LSC or LSCF to form $SrCrO_4$ particles, which are mainly observed within the electrode current collecting layer [Sharma2010, Schuler2012, Jiang2014, Park2014b, Wei2015]. The most classical volatile species would be CrO_3 under dry atmosphere and $CrO_2(OH)_2$ under humid atmosphere.

From that point of view, the gas humidity appears like a strongly impacting parameter [Hilpert1996, Chen2010]. The higher the steam content in the gas, the higher the volatilisation and the reactivity in the electrode. Moreover, high temperature has been found as another operating parameter increasing the Chromium poisoning [Tucker2006, Wei2015]. In fuel cell mode, Park et al. [Park2014] studied the effect of the electrode polarisation. It seems that the Cr deposition is favoured for high polarisation whereas the current density would have no effect on this degradation. The segregation of cations at the surface of oxygen electrode material seems to assist the Chromium poisoning [Park2014, Park2014b].

Nowadays, appropriate protective coatings are usually layered on the interconnects to avoid the Cr poisoning. Moreover, even without protection, the Cr volatilization is slowed down thanks to the use of dry gas. This degradation should not affect the electrochemical reactions before a very long time of operation [Schuler2012].

4.3.2 Electrolyte

The dense electrolyte is sensitive to some degradation mechanisms such as phase transformation or electro-reduction of the stabilised zirconia. A short presentation of the mechanisms affecting the yttria stabilised zirconia is given in the following sections.

4.3.2.1 Phase transformation

As shown previously, yttria stabilised zirconia (YSZ) is the most classical material for SOC electrolyte. However, a loss in ionic conductivity has been spotlighted by some studies under reducing atmosphere at the hydrogen electrode [Linderoth2001, Haering2005, Kishimoto2012, Shimonosono2012]. Raman spectroscopy has been carried out periodically to follow the phase evolution of YSZ at 900°C over time and reported in [Kishimoto2012]. A phase transformation from cubic to tetragonal, which is less conducting, has been observed after 20h in these operating conditions. This crystallographic transformation was observed to start from the Ni-YSZ interface and to spread to half of the electrolyte thickness.

A mechanism has been proposed in [Linderoth2001] that is based on the initial Nickel diffusion into the electrolyte layer during the cell layer co-sintering at high temperature [Lefarth2011, Priebe2016]. An exsolution of Ni from YSZ is then suspected to occur in operation under reducing atmosphere and should create the conditions of a phase transformation from cubic to

tetragonal. A high doping level of zirconia would limit this problem [Linderoth2001, Haering2005, Delaforce2007]. It should be noticed that other studies claim that the electrolyte phase transformation is limited over time [Aarberg1998, Liu2012]. The effect of this degradation on the cell performance are expected to remain limited.

4.3.2.2 Electro-reduction

The electro-reduction of the electrolyte is a potential degradation mechanism for cells tested in electrolysis mode. This degradation occurs locally for steam conversion exceeding 100%. This condition can happen at very high current density or in case of heterogeneous gas distribution in the cell. This phenomenon has been reported in several articles [Laguna2011, Laguna2011b]. It results in the reduction of YSZ giving rise to a non-negligible electronic conductivity in the electrolyte. The induced current short-circuit leads to a saturating potential in the polarisation curve, the value of which changes according to the experimental conditions. It has been estimated around 1.5 V and 2.2 V for YSZ at 800-1000°C [Weppner1977, Schouler1981, Schefold2009]. To avoid this degradation, the operating conditions are generally restricted to steam conversion rates below 80% for cells operated in electrolysis mode.

4.3.2.3 Nano-porosities

Some authors have observed the presence of nano-porosities at the grain boundaries after long-term operation in electrolysis mode as shown on Figure I.11 [Knibbe2010, Tietz2013]. The porosities formation mechanism remains unclear. It could be related to the reactivity of LSCF or LSC with YSZ leading to the precipitation of $SrZrO_3$ at the interface with the electrolyte. The diffusion of Zr^{4+} cations in the YSZ would create nano-porosities when passing through the grains boundaries [The2015].

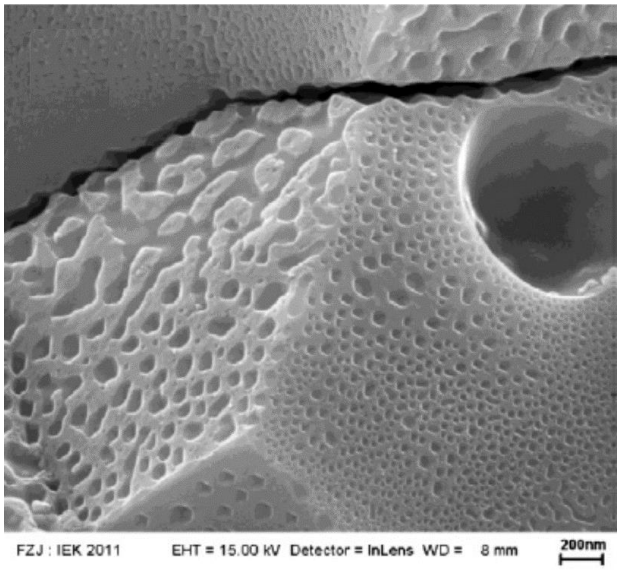

Figure I.11 – Images of a 8YSZ grain surface with fractured grain boundary after 9000h of operation in SOEC mode [Tietz2013]

4.3.3 Hydrogen electrode

A significant part of the cell performance loss is caused by the degradation of the H_2 electrode [Minh1993, Iwata1996, Knibbe2011, Moçoteguy2013]. Two main mechanisms are reported in the literature. The first one corresponds to the electrode poisoning with impurities coming from the glass seal or even from the raw materials before manufacturing. The second reason is attributed to the Nickel morphological evolution over time. These mechanisms are detailed hereafter.

4.3.3.1 Impurities

Impurities are a possible reason for the hydrogen electrode degradation. The presence of undesirable materials has especially been studied by the Risoe laboratory [Jensen2001, Mogensen2002, Jensen2003, Liu2003, Liu2005, Hauch2008, Ebbesen2010]. The impurities can mainly come from the glass seal ensuring the gas tightness or even from the raw material used for the cell manufacturing. The studies, which have been dedicated to the characterisation of impurities, have been mainly performed on samples at open circuit voltage or under fuel cell polarisation [Jensen2001, Mogensen2002, Jensen2003, Liu2005, Utz2011]. The pollutants are usually detected at the TPBs near the interface between H_2 electrode and electrolyte. Their presence at the electrochemically active sites affects the cell performances.

The glass seal containing silica appears to be an important source for this degradation. Indeed, SiO_2 phase is often detected at TPBs. The steam content tends to accelerate the electrode poisoning as Si is transported under hydroxide $Si(OH)_4$ species in the gas phase [Jacobson2005]. In electrolysis mode, Hauch et al. [Hauch2008] tested different sealings. Low impurity quantities have been found in the hydrogen electrode of cells using a metallic seal. However, SiO_2 pollution has been already observed after 68h at 950°C when using a glass seal. The use of clean raw materials and a pre-treatment of the glass seal should be sufficient to limit the degradation.

4.3.3.2 Nickel agglomeration

Nickel agglomeration and volatilisation is reckoned as a major mechanism of the H_2 electrode ageing [Iwata1996, Iosolevitch1997, Hagen2006, Hauch2008, Jiao2012, Lee2014]. Indeed, the microstructural change over time has been highlighted by post-test characterisations of cells (Figure I.12). The Ni coarsening has been initially characterised by simple 2D image analysis obtained with a Scanning Electron Microscope (SEM) [Simwonis2000, Jiang2003, Tanasini2009]. Because of the three dimensional complex microstructure of the cermet, tomographic techniques have been employed to reconstruct the electrode before and after operation [Wilson2006, Shearing2009, Cronin2011, Jiao2012, Lay2014]. The analysis of the 3D volumes allows to quantify the evolution of morphological parameters such as the TPBs,

Ni tortuosity and specific surface area. These studies have revealed that the Ni agglomeration results in an increase in the mean particle diameter and a significant decrease in Nickel percolation and density of TPBs [Matsui2010, Cronin2011, Lay2014]. Introducing the morphological parameters in models allows evaluating the effect of the Nickel evolution on the electrode and cell electrochemical behaviour. By a modelling approach, it has been shown by Faes et al. [Faes2009] that Ni coarsening is responsible of a substantial loss in the electrode and cell performances ranging between 18% and 41% of the total degradation.

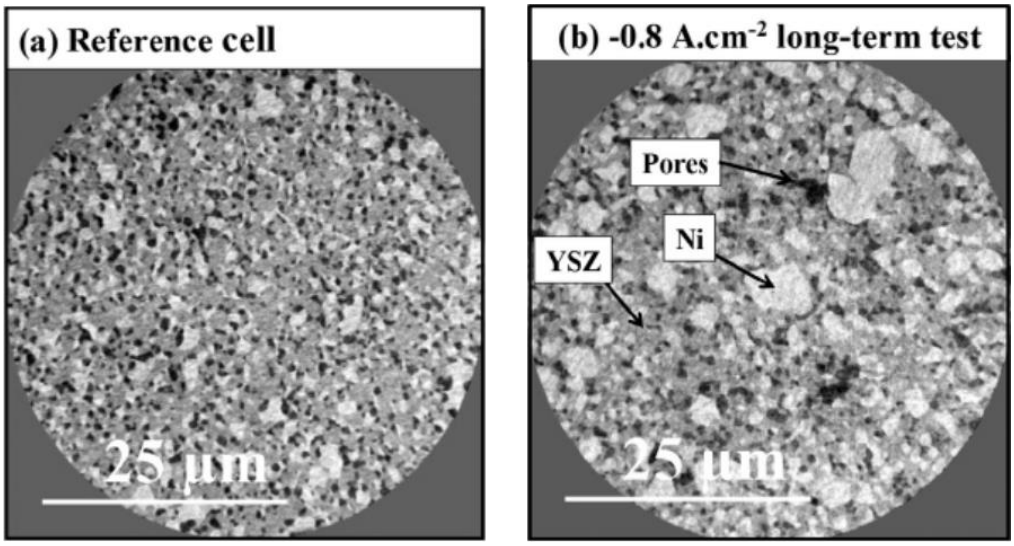

Figure I.12 – Slices extracted from 3D reconstructions obtained by X-ray nano-holotomography (a) on a pristine cell and (b) on a 1000h aged cell at 800°C in electrolysis mode showing pronounced Nickel agglomeration [Lay2014]

The Ni agglomeration is clearly due to the sintering of the metallic particles at high temperatures. However, the precise mechanism is not yet established. [Gao2014, Lee2014] have proposed that the Ni coarsening could be controlled by the Nickel surface diffusion whereas the bulk transport is generally neglected [Chen2011b]. Other works have shown that the Ni evaporation under $Ni(OH)_2$ gaseous specie and re-deposition in the cermet could be the major mechanism of Ni agglomeration [Hagen2006, Hauch2008, Jiao2011]. This last mechanism would explain an inhomogeneous distribution of Ni after test with a depletion observed at the electrolyte interface [Matsui2012, The2015, Mogensen2016]. Nevertheless, this mechanism has not been observed systematically and this could indicate that the underlying mechanism of Ni evolution is strongly dependent on both electrode microstructure and operating conditions.

As expected, the temperature plays a major role on the Ni agglomeration [Sehested2006, Yokokawa2008, Pihlatie2011, Lee2014]. An increase of this operating parameter results in larger particle size as shown in [Lee2014]. Several studies have also reported the effect of humidity contained in the gas phase on the particle growth [Jiang2003, Yokokawa2008, Holzer2011, Pihlatie2011, Lee2014]. It has been shown by [Sehested2006] that the presence of water enhances the diffusion of Ni_2-OH complex at the particles surface. It could also favour the formation of Ni volatile species in the vaporisation mechanism [Hauch2008, Jiao2011].

The potential effect of the cell polarisation, current density or FU/SC rates on the Ni agglomeration have not been decorrelated from the other operating parameters. In [Hagen2006], the Nickel particle sizes are found to be larger after a long-term test performed in fuel cell mode with a higher current density and temperature. In [Lay2014], the Nickel mean diameter increases with the current density and SC rate for tests performed in electrolysis mode at 800°C.

There is an interest to develop microstructural evolution laws depending on the operating conditions to better understand the Ni agglomeration. As the coarsening proceeds slowly, it requires long-term experiments with different test conditions that are difficult to complete. In the literature, few studies proposed evolution laws for microstructural properties. Most of them are based on 2D image analysis and proposed laws for the growth of the Nickel particle diameter [Simwonis2000, Vassen2001, Tanasini2009, Nelson2012]. Much less works are dedicated to the decrease of electrochemical active sites. Faes et al. [Faes2009] fitted the density of TPBs estimated on SEM cross sections with an equivalent unloading capacitor model. In [Nelson2012], the TPBs have been measured on 3D reconstructions to determine an evolution over time. However, there is a clear lack of data in the literature of large 3D microstructural characterisations of long-term aged cells.

5. Conclusions of this chapter

This chapter proposed the context of high temperature Solid Oxide Cells (SOCs). The operating principles have been reminded as well as the classical materials and architecture. The effects of physical phenomena on the cell performances have been shown. These contributions are generally understood thanks to modelling approaches developed at different scales. An overview on the state-of-the-art of SOC performances is reported in this chapter. The strong effect of operating conditions and the electrodes microstructures have been highlighted. Data on durability are also proposed. While the degradation rates are lower and lower, they are still too high to be economically viable. To improve the durability, the degradation mechanisms must be better understood. The main mechanisms affecting the electrolyte and the both electrodes have been presented and their criticality on the SOC performances are summarized in Table I.2.

Table I.2 – Criticality of degradation mechanisms.

Degradation mechanism	O_2 electrode	Electrolyte	H_2 electrode
Cation segregation and nano-porosities	***	?	
Delamination	*		
Cr poisoning	*		
Phase transformation		*	
Electro-reduction		*	
Pollutant poisoning			**
Ni agglomeration			***

* : low, ** : medium, *** : high, ? : non-rated

Two degradation mechanisms appear severe for the SOC durability. It is known that the Nickel agglomeration is responsible of a significant part of the degradation rates measured during long-term tests. This work aims at better understanding the Nickel coarsening contribution on the SOC degradation by using the triangular approach (electrochemical tests, characterizations and modelling). To reach this goal, a typical single-cell has been used for the electrochemical long-term tests. It is made of classical materials in both electrodes. This cell presents good performances and a high robustness. It is thus important to carry out long-term durability tests with well controlled operating conditions and regular electrochemical characterizations. Moreover, a highly sensitive characterization method should be employed since the microstructural evolutions could be limited. In this work, X-ray nano-holotomography will be used to study the Nickel agglomeration in the hydrogen electrode. This technique is described in the following chapter.

Chapter II:

State-of-the-art in synchrotron X-ray imaging by phase contrast

In this chapter we focus on methods able to characterize the electrode microstructure in three dimensions (3D). Indeed, a fine description of the microstructure is requested to establish the links between the electrodes properties and the SOC performances. The electrodes microstructural evolutions, which are an important topic in the literature, are suspected to explain a major part of the electrochemical degradation. Several techniques have been developed to obtain the electrode morphological properties. Among these existing methods, the synchrotron X-ray tomography techniques appear as interesting solutions as they are non-destructive and they allow a sufficient high spatial resolution and field of view to be reached. A specific attention is paid to the synchrotron X-ray nano-holotomography method developed at the ESRF and used as main 3D characterisation technique in this work. An exhaustive description, going from the X-ray interaction to the volume reconstruction, is proposed. In particular, the phase contrast imaging principle is detailed step by step.

1. The 3D characterisation techniques

For a fine description of SOCs microstructure, several techniques have been used to get the main morphological properties. Historically, before the development of 3D characterisation techniques, 2D images obtained by scanning electron microscopy were used. Thanks to stereological assumptions, it is possible to have a rough estimate of some important properties of the cell such as volume fractions, particle sizes or specific surface area [Lee2002, Song2006, Shikazono2009, Faes2009]. Nevertheless, 3D electrode reconstruction is the most relevant way to quantify without prior model important properties, such as the percolation rate, the tortuosity factor [Holm2006] or the density of triple phase boundaries. As these last properties can have a huge impact on the cell performance and can evolve in operation, there is a great interest to develop 3D characterisation techniques. However, because of the features of the SOC electrode microstructure (characteristic length scale, multiphase materials, etc.), the reconstructions must combine a high spatial resolution in the nanometre range with a large analysed volume of few tens of micrometres. To fulfil these specifications, three techniques are usually employed for the microstructure 3D imaging. They are described in the following sections.

1.1 FIB-SEM

This is a destructive method for the 3D imaging of SOCs consisting of a Focused Ion Beam coupled with a Scanning Electron Microscope (FIB-SEM). The FIB is used to cut away the material slice by slice and the SEM allows the imaging (cf. Figure II.1). An advantage of this technique is the high lateral resolution obtained on the 2D images acquired with the SEM. However, the cutting with the FIB introduces a lower resolution in the third space direction. The stack of images is then aligned to obtain a 3D volume of the sample. This tool has been used for the first time by Wilson et al. [Wilson2006] for the characterisation of a SOC hydrogen electrode made of Ni-YSZ. A volume of 105 μm^3 is analysed in this paper with a voxel size of 50 nm. The size of the 3D volume was insufficient to obtain good statistics on the electrode properties. In other words, the size of the reconstruction was not large enough to reach the

Representative Volume Element (RVE) of the studied microstructure that is required to quantify accurately the properties. After this first work, a lot of improvements have been made to enlarge the analysed volume and to reduce the processing time. Some published volumes associated to their voxel size are plotted on the Figure II.4 (blue dot and blue continuous circle). Nowadays, the typical domain size is still limited below 15 µm whereas the voxel dimensions range between 10 nm and 40 nm.

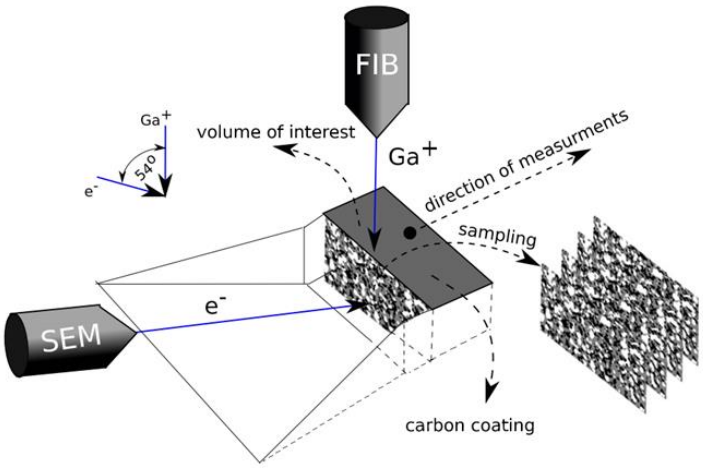

Figure II.1 - Schematic view of FIB–SEM settings and the measuring procedure [Brus2014]

1.2 Synchrotron X-ray absorption tomography

The possibility to use X-ray laboratory computed tomography for SOC electrode characterization has been investigated by some authors [Izzo2008, Shearing2010b] (Figure II.2). Because of the low X-ray flux and energy, the authors have shown that the laboratory technique is not suitable to distinguish the solid phases. This system can be used as an investigation equipment for the porosity or as a pre-qualification experiment for more advanced synchrotron investigations.

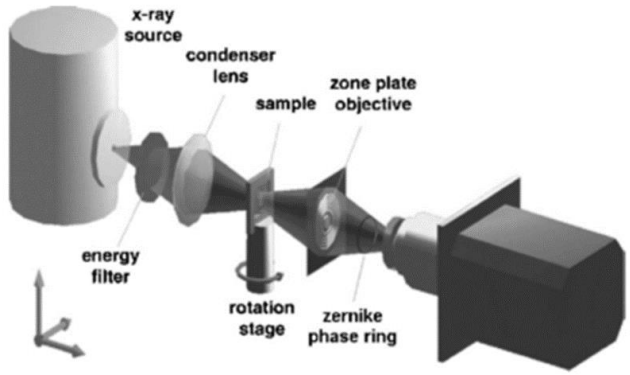

Figure II.2 - Schematic view of absorption tomography settings [Izzo2008]

Synchrotron X-ray absorption and X-ray near-edge absorption tomographies are conventional techniques that have been widely used in other scientific domains [Ketcham2001, Maire2001, Salvo2003]. Compared to the FIB-SEM, this process is interesting as it is a non-destructive method. Simple X-ray absorption tomography works well to distinguish a solid phase from the

porosity in an electrode. For more complex microstructures with multiple phases such as the Ni-YSZ cermet, it is necessary to scan twice the sample at two energies located under/above the absorption edge of one phase of the sample. For example, Shearing et al. [Shearing2010] obtained a volume of 680 μm^3 with a 22 nm voxel size for a Ni-YSZ porous electrode by imaging above and below the Ni absorption edge. The main drawback of this technique is the long process time as two scans have to be recorded for a composite. Moreover, since the energies of the absorption edge are generally low, the sample size has to be reduced to obtain enough transmitted X-ray photons on the detector placed behind the specimen. As a result, the characteristic sizes of these reconstructions are quite low even by using high flux synchrotron X-ray radiation. As shown in the Figure II.4 (red square and red dot circle), the volumes have typically the same sizes than the FIB-SEM reconstructions, except for a few studies carried out at the Advanced Light Source (ALS) located in Argonne [Shearing2010b, Cronin2013, Guan2016]. In this last case, the authors succeeded to reach a 3D volume as large as ~30x30x30 μm^3. It can be noticed that the voxel size is generally around 25-60 nm and thus larger than in FIB-SEM studies.

1.3 Synchrotron X-ray holotomography

Synchrotron X-ray nano-holotomography is a more recent technique for the characterisation of SOCs. This is also a non-destructive technique which has been developed at the ESRF [Cloetens1999b, Mokso2007]. It has been applied to the SOCs electrodes in collaboration with CEA [Laurencin2012, Quey2013, Villanova2013, Usseglio2014]. The method is based on the optical phase contrast that arises between the electrode materials. The sensitivity of the measure allows separating the different solid phases in the sample also at higher X-ray energies, well above the absorption edges. In practice, the phase contrast is recorded on a detector placed at different distances from the sample (Figure II.3). The 3D reconstruction presents a large field of view and a medium voxel size. The main characteristics of the volume and voxel size are presented in Figure II.4 (green triangle and green dash circle).

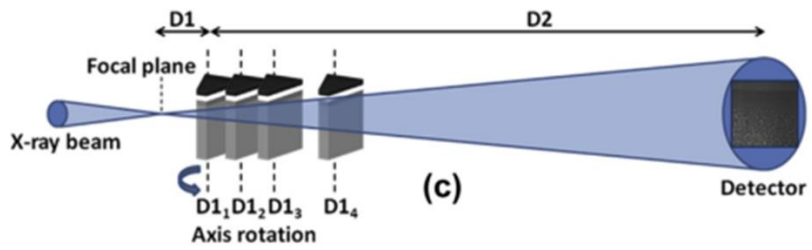

Figure II.3 - Schematic view of holotomography settings [Villanova2013]

The description of the electrode microstructure requires a sufficiently large volume to be representative. This RVE has been estimated at 35x35x35 μm^3 by Laurencin et al. [Laurencin2012] for a Ni-YSZ substrate. It is 13x13x13 μm^3 for a functional layer which has a finer microstructure [Usseglio2014]. The required spatial resolution of the 3D volume is another essential parameter of the reconstructions. It depends on the electrode characteristic length. Joos et al. [Joos2012] have shown that around 10-15 voxels on the particle diameter are

needed to determine accurately the electrode specific surface area. With the usual SOC microstructure, the spatial resolution requested is about 50-100 nm. It can be seen on Figure II.4 that the FIB-SEM and absorption tomography present small volume sizes compared to the RVE. On the contrary, holotomography has a sufficiently large volume size. On the other hand, the spatial resolution in the 3D reconstruction has been estimated at 80 nm [Villanova2013], which can be too coarse for fine microstructures.

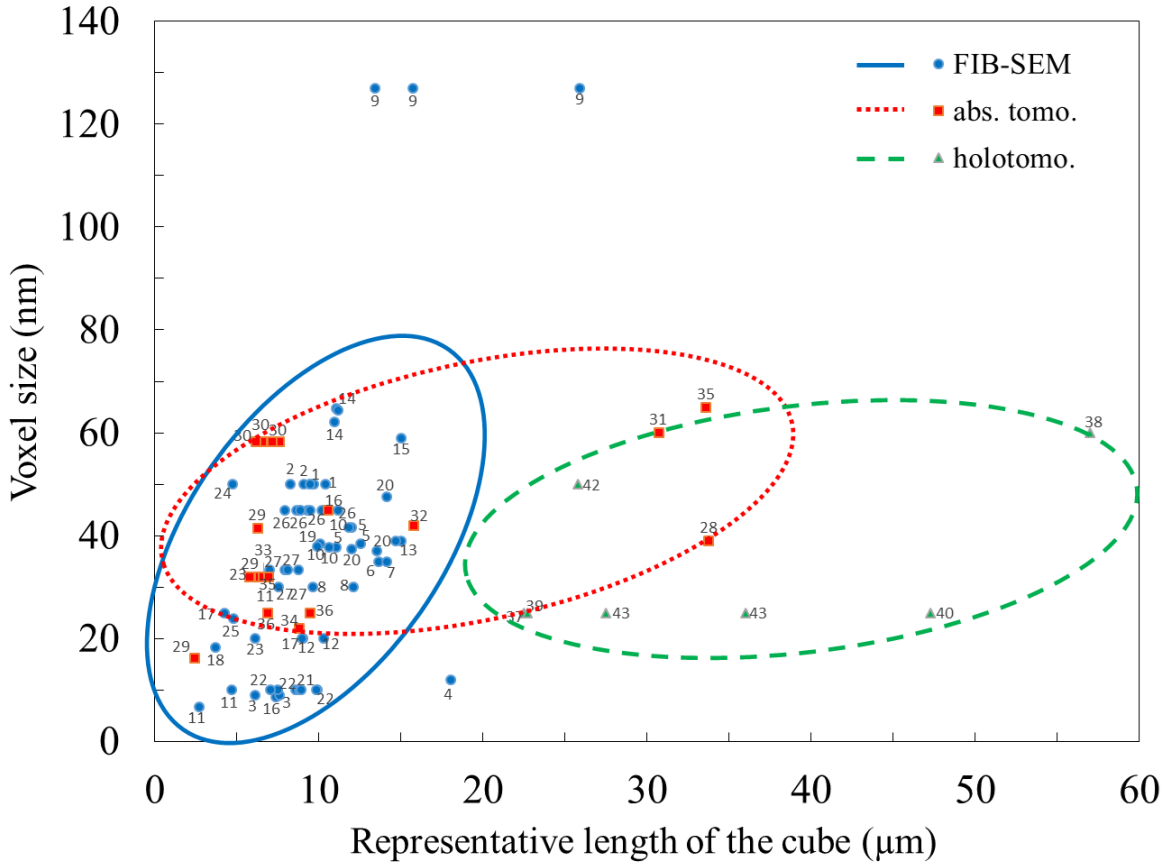

Figure II.4 – Voxel size as a function of the representative size of the 3D volume for data obtained by the three characterization techniques. The blue points and circle correspond to FIB-SEM, red squares and circle are related to absorption tomography and the green triangles and circle to holotomography. A reference number is written near each point. The list is given in the bibliography.

In this work, the nano-holotomography technique has been chosen for SOC characterization. The state-of-the-art for the characterisation by synchrotron X-ray nano-holotomography is presented hereafter. A reminder of the X-ray physics used for synchrotron imaging is provided. Then, the detailed steps of the image formation process (direct problem) and the phase retrieval process (inverse problem) are given. Finally, the standard analytical algorithm used for the 3D tomographic reconstruction is detailed.

2. X-ray physics

The discovery of X-rays has been done in 1895 by Wilhelm Roentgen [Roentgen1896]. The first radiography was performed on the hand of his wife with a ring (Figure II.5). Quickly, researchers found an interest for these new rays. They were especially used for medical diagnostics by Marie Curie during the First World War. In the 1940s, first studies on synchrotron radiation were realised. The radiation obtained from accelerated relativistic electrons is described by Schwinger [Schwinger1949]. It was not until the 1980s that dedicated equipment for synchrotron radiation was built. Nowadays, the X-rays produced by this way are used in numerous fields such as medicine, chemistry, materials or art restoration. In the next section, a more precise explanation of synchrotron radiation is given as well as its main characteristics. Then, the interaction between X-rays and matter is described. Finally, we describe the specific instrumentation required for the detection of the X-rays after the sample.

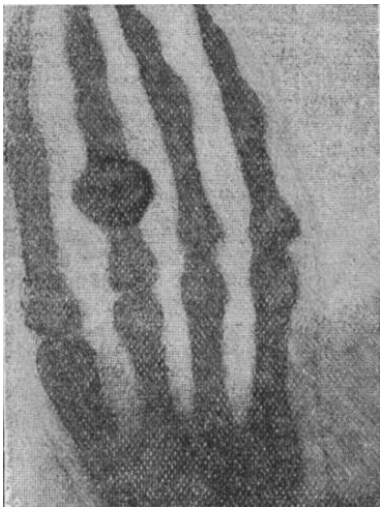

Figure II.5 – X-ray radiography of a human hand with a ring on the central finger [Roentgen1896]

2.1 Synchrotron radiation

In this work, X-ray synchrotron radiation is used for the study of SOCs. The X-ray beam obtained with this equipment has interesting properties for the materials analysis. The main advantages are presented hereafter.

2.1.1 Principle

It is reminded that charged particles emit a radiation when they are accelerated to nearly the light speed. Therefore, because of its radial acceleration, an electron guided in a magnetic field at a relativistic speed is emitting so-called synchrotron radiation in the tangential direction (Figure II.6). As depicted in Figure II.6b, the radiation is emitted in a narrow cone, with an aperture that depends on the velocity of the particle. The European Synchrotron Radiation

Facility (ESRF) is a third generation synchrotron dedicated to the emission and the use of the synchrotron radiation.

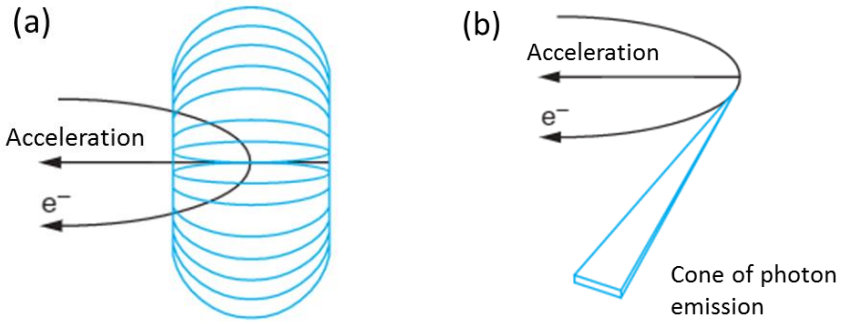

Figure II.6 – Scheme representing the photon emission from an accelerated electron on a circular orbit (a) at non-relativistic and (b) at relativistic speed [Doucet2011]

The electrons used in the machine are produced from an electron gun, which consists of a heated cathode. Then, the electrons are pre-accelerated on a linear section ("LINAC") before being injected in a small ring. This ring is called booster as it increases the electron's energy until the desired value. At the ESRF, this energy is 6 GeV. The electrons are then injected in an 844 meters circumference storage ring. The electrons' orbit and frequency are monitored thanks to different control systems such as bending magnets and radiofrequency cavities. The complete ring is under ultra-high vacuum ($<10^{-8}$ mbar) to reduce the probability of collision between the electrons and residual gas.

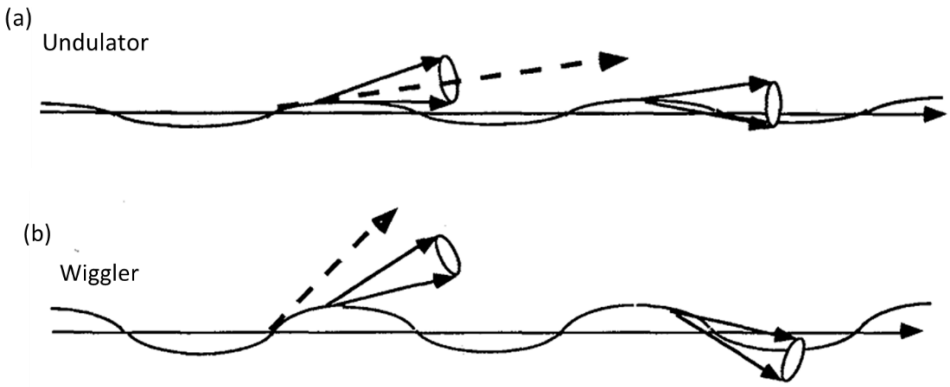

Figure II.7 – Schematic representation of the X-ray emission from (a) an undulator and (b) a wiggler. The difference in the photon emission angle involves different spectra according to the insertion device. [Bessiere1996]

There are two types of beamlines at the ESRF. The first type uses Bending Magnets (BM), which produce a continuous spectrum in energy (Figure II.8). The second type uses Insertion Devices (ID), which produce a more brilliant beam. These devices are located in the straight sections of the ring, located in between the bending magnets. Two kinds of device, either wigglers or undulators, are used for the X-ray emission. They both consist of a sequence of

dipole magnets of alternative polarisation inducing the oscillation of the electrons. In the case of a wiggler, the radiation cone induced by the oscillation is larger angle than the photon divergence (cf. Figure II.7b). No interference occurs between the radiations emitted by the successive poles giving rise to a broad energy spectrum (Figure II.8). In the case of an undulator, the radiations emitted by the different poles interfere with each other resulting in a spectrum with peaks at a specific energy and its harmonics (Figure II.8). The choice of the energy is tuneable especially by changing the gap of the undulator.

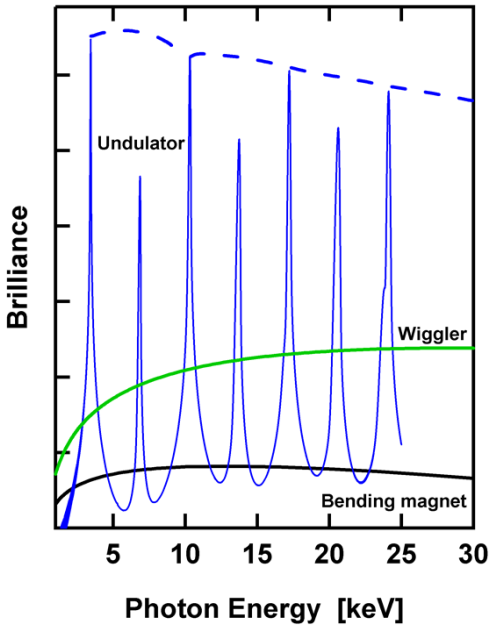

Figure II.8 – Spectra obtained with a bending magnet (black), a wiggler (green) and an undulator (blue) (from photon-science.desy.de)

2.1.2 Brightness

Synchrotron radiation has interesting properties compared to classical X-ray sources. One of the most important is the brightness. Its units are given in the following expression:

$$Brightness = \frac{Photons}{s.mm^2.mrad^2.(0.1\%BW)} \quad \text{(II.1)}$$

This parameter expresses the photon flux as a function of angular divergence, source size and 0.1% bandwidth of the central wavelength. A high brightness means a lot of photons of a given energy in a small surface. This allows to scan faster or more absorbing materials. It can be noticed that the brightness at the ESRF is about twice the one of the sun.

2.1.3 Coherence

Another important characteristic of synchrotron radiation is the coherence. This is an essential property for the tomographic phase contrast imaging that has been employed in this work.

Indeed, the ability to create interference fringes with good optical contrast is controlled by the coherence of the incident beam [Margaritondo2001]. There are two types of coherence. The first one is the temporal or longitudinal coherence, which is related to the monochromaticity of the beam (cf. Figure II.9).

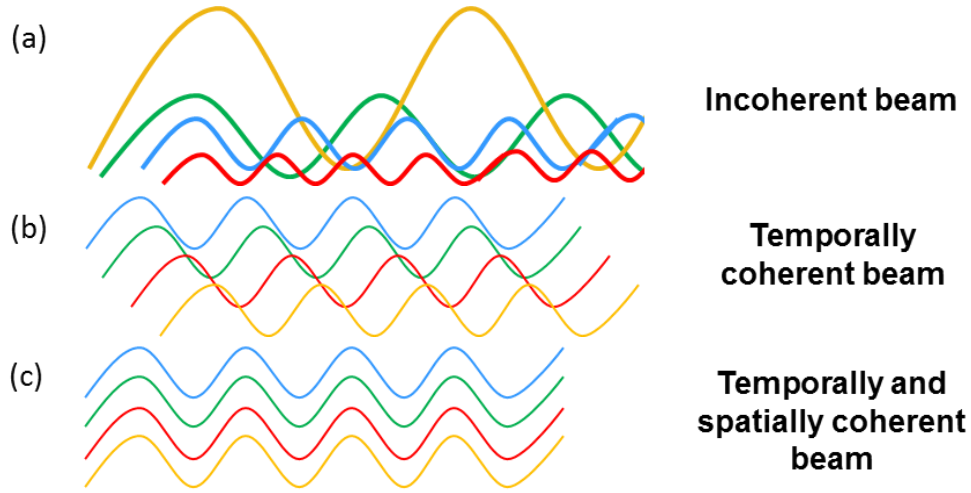

Figure II.9 - Schematic representation of the coherence. (a) represents an incoherent beam, (b) is a monochromatic but not spatially coherent beam, (c) is a temporally and spatially coherent beam. These properties allow the observation of interference patterns.

The temporal coherence corresponds to the length l_t for which two waves with a slight difference in the wavelength ($\Delta\lambda$) are in phase opposition. By doing the approximation that the difference in wavelength is small, the temporal coherence length can be expressed as follows:

$$l_t = \frac{\lambda^2}{\Delta\lambda} \tag{II.2}$$

The second type of coherence is the spatial or transverse coherence. It describes the correlation between two points taken in the transverse plane of the wave propagation. When two points separated of a distance l_s are in phase opposition, their contribution to the fringe visibility cancels out. In the case of an incoherent source, this characteristic length is related to the wavelength λ, the beamline length L and the source size s as expressed in equation (II.3). With the long beamline used in this work, the spatial coherence is about 155 µm at 33.6 keV in the vertical direction.

$$l_s = \frac{\lambda\, L}{2\, s} \tag{II.3}$$

2.2 X-ray interaction with matter

The X-ray imaging techniques are taking advantage of the X-ray interaction with matter. Indeed, the X-ray beam passing through a sample can be affected by two contributions (Figure II.10). One is the effect on the amplitude of the wave, it corresponds to the attenuation

described by the absorption index β. The second one is related to the phase shift of the wave, which is described by the refractive index decrement δ. These two effects are brought together in the complex refractive index n which is expressed as:

$$n = 1 - \delta + i\beta \tag{II.4}$$

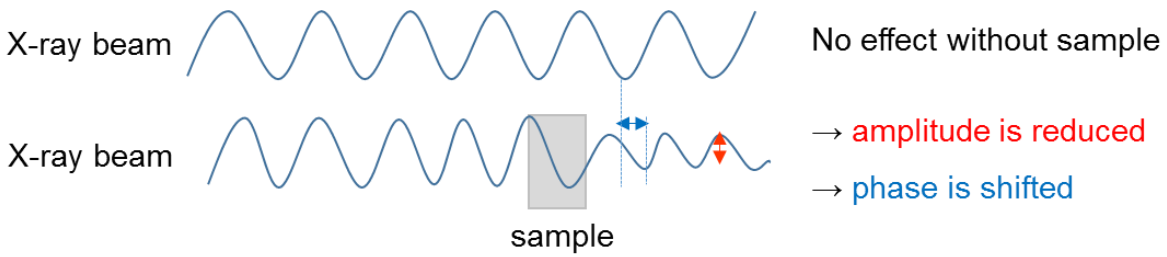

Figure II.10 – Illustration of the effect of a sample placed in a beam. The amplitude is reduced, this is related to β and the phase is shifted, this is related to δ.

The absorption index is directly linked to the linear attenuation coefficient μ by the following expression:

$$\mu = \frac{4\pi}{\lambda}\beta \tag{II.5}$$

where λ is the wavelength of the beam. The refractive index decrement describes the wave propagation in the material. Except at X-ray energies close to the absorption edges, the refractive index is proportional to the electron density of the material [Guinier1994]:

$$\delta = \frac{r_e \rho_e \lambda^2}{2\pi} \tag{II.6}$$

where r_e is the classical radius of the electron and ρ_e the electron density. This parameter can finally be expressed as a function of the mass density ρ and the wavelength by making the approximation that the ratio electron number to atomic mass is approximately always equal to ½ [Guinier1994]. The images obtained with the refractive index δ are thus linked to the mass density of the sample:

$$\delta \approx 1.3\ 10^{-6} \rho \lambda^2 \tag{II.7}$$

with ρ the mass density expressed in g.cm^{-3} and λ the wavelength in Angstrom. In general, the phase sensitivity is much greater than the amplitude one. This is especially true for light (low *Z*) elements, but it remains true also for heavier elements. The theoretical values of the physical parameters of the material (δ and β) are calculated using the X-ray Optics software XOP [del Rio2004]. The ratio δ/β reflects the importance of phase effects compared to attenuation effects. It is plotted on the Figure II.11 as a function of the X-ray beam energy for three kinds of materials used in SOCs. One can note that this ratio increases to a value higher than 10 when hard X-rays are used for the experiment. X-ray phase imaging is a particularly relevant technique as the use of a high energy allows limiting the absorption while preserving a good

sensitivity to small details. This is the key property to obtain tomography reconstructions with a large field of view and a high spatial resolution.

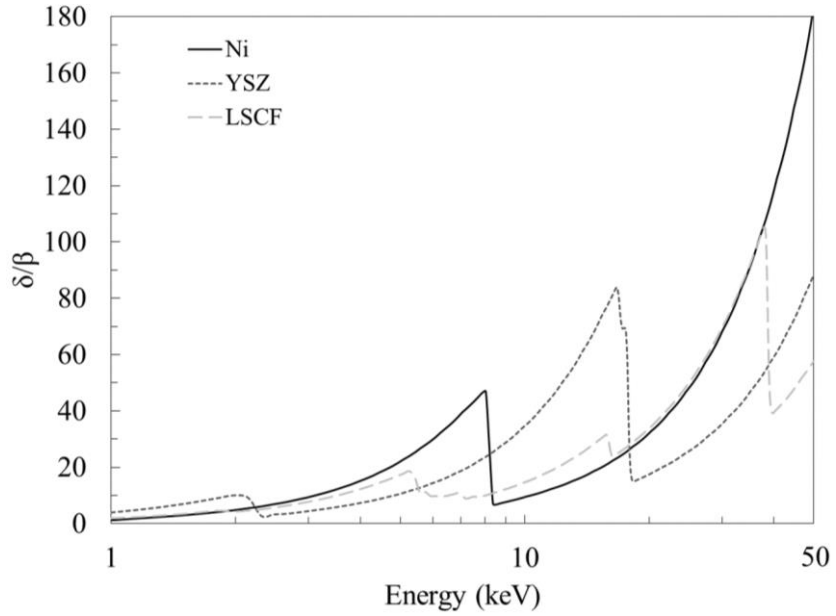

Figure II.11 – The ratio δ/β plotted as a function of the beam energy for three kinds of materials used in SOCs.

2.3 X-ray detection

The X-ray beam that passed through the sample has to be recorded as an image by a detector. As the detector is sensitive to visible light, it is necessary to use a specific component to convert the X-ray photons in visible light photons. This component is a scintillator.

2.3.1 Scintillator

The principle of the scintillator is based on the energy gap in a material. According to the Pauli principle, the electrons are distributed in several band-gaps [Ishii1991, Beauger1999, Nikl2006]. The valence band is defined as the last band partially or totally filled at 0 K whereas the conduction band corresponds to the first one that is empty. The gap between the two bands is a forbidden area for the electron. For some materials at non zero temperature, electrons are transferred in the conduction band. Materials are thus classified as insulator, conductor or semiconductor according to the number of electrons filling these bands and the gap. By adding some dopants in a material, it is possible to create intermediate energy levels in the forbidden gap [VanEijk2002, Lempicki1998, Douissard2010, Kraemer2006]. After interaction with the X-ray beam, electrons are excited to the conduction band by Compton and photoelectric effects. The relaxation of the electrons produces a characteristic wave. The presence of dopant creating intermediate energy levels in the forbidden gap allows the emission of photons that cannot be reabsorbed by the scintillator matter (since its energy is lower than the material gap). These

photons are emitted with a wavelength in the visible light so that they can be detected on a classical camera.

In order to select the best scintillator material, some key parameters can be checked. A first parameter is the ability of the scintillator material to absorb the X-rays. In that objective, a high density as well as a high atomic number are necessary since the photoelectric interaction is proportional to ρZ^4. A second main parameter is the ability of the scintillator to convert the absorbed energy to visible light. This light yield is calculated by the following equation [Lempicki1998, Nikl2006]:

$$N_{photon} = \frac{ESQ}{\beta_{mat} E_{gap}} \tag{II.8}$$

where S and Q are respectively the transfer and quantum efficiency, β_{mat} is a phenomenological constant comprised between 2 and 3, E_{gap} is the band gap of the scintillator and E the X-ray beam energy. Obviously, the scintillator has to be selected to generate photons detectable by the following sensor. Other important parameters are the luminescence decay time that should be as short as possible and the afterglow (persistence of the luminescence) which happens because of trapped electrons in the intermediate energy level [Nickl2006, Douissard2010]. Finally, the scintillator material has to be stable under the X-ray beam.

2.3.2 Detector

The photons emitted by the scintillator are recorded on a detector. Nowadays, Charge Coupled Device (CCD) camera are mainly used in the synchrotrons. At the ESRF, a specific low-noise detector with a high read-out speed (FReLoN) has been developed [Labiche2007]. This very performing camera exists in different versions integrating commercially available CCDs. It allows the recording of highly resolved 2D images in a short time. Faster image sensors based on CMOS technology are also increasingly used, at the expense of a lower degree of perfection and a low full well capacity. In general, the response of each pixel of the camera is not perfect. Indeed, the recorded data on a pixel is not a perfect Dirac pulse but a blurred signal. If the Point Spread Function (PSF) of the detector is known, this effect can be corrected by a deconvolution of the signal by the PSF.

3. 3D reconstruction by holotomography

Holotomography is taking advantage of the coherence and brilliance properties of the X-rays produced by a synchrotron. Getting the final 3D reconstruction of a sample with this technique requires several steps. The first one is to be able to analyse the data recorded by the detector. In that goal, a fine description of the beam arriving on the detector is presented in the next section. The description of the phase contrast formation is named the direct problem: it consists in calculating the recorded image(s) for a known object and known experimental conditions.

In reality it is necessary to inverse the problem to retrieve the sample electron density. The specificity of the solution used for SOC electrodes is especially detailed in the following section. Finally, the process to build the 3D volume from the 2D projections is explained.

3.1 Phase contrast imaging

As presented in the previous section, the X-ray beam going through the sample is affected by two phenomena. The first one is a reduction of the wave amplitude and the second one is a phase shift of the wave. These effects are included in the complex refractive index n which can be written in each space position as following:

$$n(x,y,z) = 1 - \delta(x,y,z) + i\beta(x,y,z) \tag{II.9}$$

where $\delta(x,y,z)$ is the refractive index decrement and $\beta(x,y,z)$ the absorption index. The projections of these parameters, respectively $B(\mathbf{x})$ and $\varphi(\mathbf{x})$, will affect the image formation as absorption and phase contrasts respectively:

$$B(\mathbf{x}) = \frac{2\pi}{\lambda}\int \beta(x,y,z)dz \tag{II.10}$$

$$\varphi(\mathbf{x}) = -\frac{2\pi}{\lambda}\int \delta(x,y,z)dz \tag{II.11}$$

where $\boldsymbol{x} = (x,y)$ is the spatial coordinate in the plan orthogonal to the beam propagation direction.

3.1.1 Intensity recorded on the detector

To take into account absorption and phase shift of the X-ray beam after the sample, a transmission function is introduced with the following expression:

$$T(\mathbf{x}) = e^{-B(\mathbf{x})}e^{i\varphi(\mathbf{x})} \tag{II.12}$$

So, the X-ray wave after the sample u_0 is expressed by a multiplication of the transmission function with the incident beam u_{inc}:

$$u_0(\mathbf{x}) = T(\mathbf{x})u_{inc}(\mathbf{x}) \tag{II.13}$$

It should be noted that the propagation inside the object itself is neglected in this expression, a good approximation in the case of hard X-rays.

If a detector is placed just after the sample, the signal recorded on it is the following intensity:

$$I_0(\mathbf{x}) = |u_0(\mathbf{x})|^2 = |T(\mathbf{x})u_{inc}(\mathbf{x})|^2 = I_{inc}(\mathbf{x})e^{-2B(\mathbf{x})} \tag{II.14}$$

The parameter I_{inc} is the intensity of the incident beam. This expression corresponds to the classical Beer-Lambert law used in attenuation tomography. One can notice that the phase

information disappears from the intensity recorded on the detector. Several techniques exist to retrieve this phase information.

3.1.2 Phase contrast imaging techniques

Different methods have been developed to exploit the phase shift for imaging. Each of them has advantages and drawbacks related to stability or restrictions on the set-up. Three main techniques with different phase sensitivities are presented hereafter.

3.1.2.1 Crystal interferometry

A first solution is the crystal interferometry imaging technique [Bonse1965] that measures directly the phase shift $\varphi(\mathbf{x})$ by comparison with a reference beam. For this method, a set-up is built with three successive single crystals. The first one is used to split the X-ray beam in two. A part of the beam is used as a reference whereas the second part is deviated on the sample with a second crystal. The two beams are recombined in a third crystal before reaching the detector. The intensity recorded on the detector is directly proportional to the cosines of the phase shift [Momose1995a, Momose1995b]. Despite an interesting potential for the phase shift analysis [Momose1996], the complexity of the set-up as well as its stability limit severely the application of this technique [Coan2006].

3.1.2.2 Analyser based imaging

Analyser based imaging (ABI) is a second group of techniques which is sensitive to the derivative of the phase. For this method, a first crystal is used as a monochromator upstream of the sample. A second analyser crystal is placed between the sample and the detector in Bragg condition. The diffracted Bragg intensity corresponds to a rocking curve when the angle of the crystal is moved around the maximum position. As the sample is changing the refraction angle, it is possible to retrieve the phase gradient from the following expression [Bushuev2001]:

$$\Delta\alpha = -\frac{\lambda}{2\pi}\frac{\partial\varphi}{\partial \mathrm{x}} \qquad \text{(II.15)}$$

By rotating the sample and by considering several angles for the analyser crystal, it is possible to retrieve the phase from this imaging technique [Foerster1980]. The set-up is simpler than the previous technique and the stability requirements are less severe. This is why this technique is much more used in characterization [Davis1996, Bravin2003, Pavlov2004, Coan2005].

Requirements on stability and monochromaticity (related to the diffraction by perfect crystals) remain important drawbacks of analyser based imaging. Therefore, alternative techniques sensitive to the derivative of the phase have attracted a lot of momentum recently: grating based imaging [David2002, Momose2003, Weitkamp2005] and speckle based imaging

[Morgan2012, Zanette2014]. These techniques are much more robust and compatible with a broader bandwidth of the radiation. Therefore, they can be applied with specific laboratory sources.

A common drawback of the phase contrast techniques mentioned above is their rather low spatial resolution of a few microns at the best. This limitation is related to the interaction of the beam with the object (crystal or grating) placed downstream of the sample to induce phase contrast.

3.1.2.3 Propagation based imaging

A third solution to convert the phase shift in detectable intensity variations is propagation based imaging [Snigirev1995, Cloetens1996]. This technique is, in first approximation, sensitive to the second derivative of the phase as it is measuring the edge enhanced phase contrast. For a long time, Fresnel diffraction was considered as an artefact in absorption tomography or ABI. However, it is an interesting solution to retrieve the phase. The phase of the incident beam is modified along the edge or inside the sample at the interfaces between the material phases or porosities. If the beam propagates after the sample over a distance *D*, a radiograph consisting of absorption and interference fringes is recorded on the detector. These fringes are due to Fresnel diffraction (free space propagation). In the following section, the direct problem of the beam propagation after a sample is presented in detail. By inverting this approach, it is possible to obtain the phase, and hence, when combined with tomography, the sample electron density.

3.1.3 Free space propagation

The X-ray wave of the beam at a distance *D* after the sample, $u_D(\mathbf{x})$, is described by the convolution of the wave function just after the sample at the distance *D=0*, $u_0(\mathbf{x})$, with a propagation function $P_D(\mathbf{x})$ as expressed here [Goodman1996, Born2005]:

$$u_D(\mathbf{x}) = P_D(\mathbf{x}) * u_0(\mathbf{x}) \tag{II.16}$$

It is important to know the expression of the propagation function to be able to retrieve the phase. The propagator can be expressed in the Fourier or real space.

3.1.3.1 Fourier space approach

It is easier to express the propagation function in the Fourier space. For that, equation (II.16) has to be expressed in the frequency domain, as a function of the frequency coordinate **f**, conjugate to the spatial coordinate **x**. Reminding that a convolution in the real space corresponds to a multiplication in the Fourier space, the wave function is then given by:

$$\tilde{u}_D(\mathbf{f}) = \widetilde{P_D}(\mathbf{f}).\tilde{u}_0(\mathbf{f}) \tag{II.17}$$

where the functions $\tilde{u}_D, \widetilde{P_D}, \tilde{u}_0$ are the Fourier transform of respectively the functions u_D, P_D, u_0. The wave function after the sample is expressed in the Fourier space by the equation (II.18) and the inverse Fourier transform is given by equation (II.19).

$$\tilde{u}_0(\mathbf{f}) = \int u_0(\mathbf{x}) e^{-i2\pi \mathbf{x}.\mathbf{f}} d\mathbf{x} \tag{II.18}$$

$$u_0(\mathbf{x}) = \int \tilde{u}_0(\mathbf{f}) e^{i2\pi \mathbf{x}.\mathbf{f}} d\mathbf{f} \tag{II.19}$$

At a distance *D*, the wave function is the multiplication of a plane wave at *D=0* with a phase factor expressed $e^{ik_z D}$with the wavevector $k = (k_x, k_y, k_z)$ [Cloetens1999a]

$$u_D(\mathbf{x}) = \int \tilde{u}_0(\mathbf{f})\, e^{i\frac{2\pi}{\lambda}\sqrt{1-(\lambda f_x)^2-(\lambda f_y)^2}D} e^{i2\pi \mathbf{x}.\mathbf{f}} d\mathbf{f} \tag{II.20}$$

In the Fourier space, this expression is given by the following equation:

$$\tilde{u}_D(\mathbf{f}) = \tilde{u}_0(\mathbf{f})\, e^{i\frac{2\pi}{\lambda}\sqrt{1-(\lambda f_x)^2-(\lambda f_y)^2}D} \tag{II.21}$$

The angle of the wavevector with respect to the propagation direction *z* can be considered small as the dimension of the sample is much more important than the wavelength [Cloetens1999a]. Thus, the following approximation can be done:

$$|\sin\theta| \approx |\theta| = \lambda|\mathbf{f}|, |\theta| \ll 1 \tag{II.22}$$

Doing a Taylor expansion at the first order of the square root gives:

$$\tilde{u}_D(\mathbf{f}) = \tilde{u}_0(\mathbf{f})\, e^{i\frac{2\pi D}{\lambda}}\, e^{-i\pi\lambda D|\mathbf{f}|^2} \tag{II.23}$$

This expression is valid if the second order term is negligible, it means:

$$\frac{D\lambda^3|\mathbf{f}|_{max}^4}{8} \ll 1 \tag{II.24}$$

Due to the small wavelength compared to the spatial resolution (~$1/|\mathbf{f}|_{max}$), this will generally be the case.

In the equation (II.23) and disregarding an unimportant constant phase term $e^{i\frac{2\pi D}{\lambda}}$, the Fourier transform of the propagator can be recognized as:

$$\tilde{P}_D(\mathbf{f}) = e^{-i\pi\lambda D|\mathbf{f}|^2} \tag{II.25}$$

This last expression can be used for the estimation of the intensity in the direct problem. Indeed, in the Fourier domain, the amplitude corresponds to the product of the propagator with the wave function after the sample. The intensity is then trivially calculated as the square of the amplitude in real space.

3.1.3.2 Real space approach

The propagation function can also be expressed in real space even if it is more complex. If the wave after the sample is considered as a distribution of secondary sources, the wave function can be linearized thanks to the Rayleigh-Sommerfield diffraction integral [Goodman1996, Born2005]:

$$u_D(\mathbf{x}) = \frac{1}{i\lambda}\int u_0(\mathbf{x_0})\frac{e^{ik|\mathbf{r}|}cos\theta}{|\mathbf{r}|}d\mathbf{x_0} \tag{II.26}$$

The integration is done in the diffraction plane located at a distance *D* from the object. The parameter $|\mathbf{r}|$ is the length of the wave propagation between the object and the diffraction plane and θ is the angle made by $\boldsymbol{r}$ with the propagation direction. For hard X-rays, the angle θ is small, thus the cosine term can be approximated by one and the wave propagation length in the denominator is approximated by the distance *D* [Cloetens1999a]. By doing a Taylor expansion of the expression in the exponential, the term $|\mathbf{r}|$ can be approximated by:

$$|r| = D\left[1 + \frac{1}{2}\left(\frac{x-x_0}{D}\right)^2 + \frac{1}{2}\left(\frac{y-y_0}{D}\right)^2\right] \tag{II.27}$$

This is the Fresnel approximation. It is valid if the second order term is negligible, it means:

$$D^3 \gg max\frac{\pi}{4\lambda}[(x-x_0)^2 + (y-y_0)^2]^2 \tag{II.28}$$

This approximation seems difficult to fulfil with the small wavelength of the hard X-rays but this condition stays valid for a zone close to the point (*x*, *y*). The wave function in the diffraction plane at distance *D* can be expressed by:

$$u_D(\mathbf{x}) = \frac{e^{ikD}}{i\lambda D}\int u_0(\mathbf{x_0})e^{i\frac{\pi}{\lambda D}[(x-x_0)^2+(y-y_0)^2]}d\mathbf{x_0} \tag{II.29}$$

The propagator function in the real space can be deduced from the previous equation as:

$$P_D(\mathbf{x}) = \frac{1}{i\lambda D}e^{i\frac{\pi}{\lambda D}|\mathbf{x}|^2} \tag{II.30}$$

It should be noted that the Fourier space approach is most appropriate in the case of relatively small distances *D*, considering equation (II.24) and expression (II.30) showing a very fast oscillation of the complex exponential for small distances. On the opposite, the real space approach is more appropriate for relatively large distances *D*, including the Fraunhofer diffraction limit, considering equation (II.28).

For imaging, the interesting quantity is the intensity recorded on the detector. The Fourier transform of the intensity can be obtained from the equations (II.14) and (II.29) as proposed by [Papoulis1974, Guigay1978]. The six integrals obtained with this calculation can be reduced to a double integral as shown by [Guigay1977]:

$$\tilde{I}_D(\mathbf{f}) = \iint T\left(\mathbf{x} - \frac{\lambda D\mathbf{f}}{2}\right) T^*\left(\mathbf{x} + \frac{\lambda D\mathbf{f}}{2}\right) e^{-i2\pi\mathbf{f}.\mathbf{x}}\, d\mathbf{x} \tag{II.31}$$

This expression is not a simple Fourier transform of the transmission function $T(\mathbf{x})$ as the two terms are dependent of the frequency $\mathbf{f}$. This expression can be considered as a plane in the 4D ambiguity function [Papoulis1974, Guigay1978, Nugent2007] expressed as:

$$A_T(\eta, \mathbf{f}) = \iint T\left(\mathbf{x} - \frac{\eta}{2}\right) T^*\left(\mathbf{x} + \frac{\eta}{2}\right) e^{-i2\pi\mathbf{f}.\mathbf{x}}\, d\mathbf{x} \tag{II.32}$$

with $\eta = \lambda D\mathbf{f}$. This expression is fundamental as it is the base for the various approximations made to retrieve the phase. It will be used in the section dedicated to the inverse problem with the Transport of Intensity Equation (TIE).

3.1.4 Effect of partial coherence

So far, the X-ray beam was considered as perfectly coherent. However, it is not the case for the real beam, hence this effect has to be considered. The source can be decomposed in several sources each completely coherent but mutually incoherent [Born2005]. The total intensity is the incoherent sum of each contribution coming from each source. The mutual intensity can be used to describe this effect:

$$J_D(\mathbf{x}_1, \mathbf{x}_2) = \sum_p u_D^{(p)}(\mathbf{x}_1) u_D^{(p)*}(\mathbf{x}_2) \tag{II.33}$$

which is the intensity obtained by the superposition of the wave coming from $\mathbf{x}_1$ and $\mathbf{x}_2$ in the plane located at a distance $l + D$ from the source. When the two points are coinciding, the classical intensity is obtained. One can introduce the degree of coherence which is the ratio between the mutual intensity and the intensity in each point:

$$\gamma^c(\mathbf{x}_1, \mathbf{x}_2) = \frac{J(\mathbf{x}_1, \mathbf{x}_2)}{\sqrt{I(\mathbf{x}_1) I(\mathbf{x}_2)}} \tag{II.34}$$

This parameter describes the coherence between the two points. It is equal to one when the points are coherent and zero in the case of total incoherence. In the plane located just after the object, the mutual intensity can be expressed by:

$$J_0(\mathbf{x}_1, \mathbf{x}_2) = J_{inc}(\mathbf{x}_1, \mathbf{x}_2) T(\mathbf{x}_1) T^*(\mathbf{x}_2) \tag{II.35}$$

By analogy with what was done before, the Fourier transform of the intensity can be expressed by [Guigay1978]:

$$\tilde{I}_D(\mathbf{f}) = \int J_0\left(\mathbf{x} - \frac{\lambda D\mathbf{f}}{2}, \mathbf{x} + \frac{\lambda D\mathbf{f}}{2}\right) e^{-i2\pi\mathbf{f}.\mathbf{x}}\, d\mathbf{x} \tag{II.36}$$

The calculation of the intensity is easier in the Fourier space as it is a multiplication by a factor which is only dependent on the difference between $\mathbf{x}_1$ and $\mathbf{x}_2$.

3.1.5 Effect of detector

As was the case for partial coherence, the effect of the detector can be taken into account. Indeed, if all the non-uniformities and non-linearities are considered already corrected, the detector response is not a perfect Dirac but a Point Spread Function (PSF). It means that some blur is introduced in the intensity recorded by the detector. This effect is described by a convolution of the intensity with the PSF of the detector [Cloetens1999a]. This expression is equivalent to a multiplication in the Fourier space:

$$\tilde{I}_{det}^{rec}(\mathbf{f}) = \tilde{R}(\mathbf{f}).\tilde{I}_{det}(\mathbf{f}) \tag{II.37}$$

3.1.6 Summary of the direct problem

Finally, one can notice that the intensity recorded on the detector is a succession of multiplications in respectively the real and Fourier space. The incident wave is first multiplied with the transmission function in the real space. The Fourier transform of this expression is then propagated by multiplication with the propagator at a distance *D*. The ideal intensity is then calculated as the square modulus of the wave in the real space. The partial coherence effect as well as the detector effect are corrected in Fourier space by multiplication with respectively the modulus of the degree of coherence and the detector transfer function. At the end, the intensity recorded on the detector can be expressed as follows:

$$I_D(\mathbf{x}) = \mathcal{F}^{-1}\left[\tilde{R}(\mathbf{f})|\tilde{\gamma}^c(\lambda D\mathbf{f})|\mathcal{F}\left[\left|\mathcal{F}^{-1}\{\tilde{P}_D\mathcal{F}[Tu_{inc}]\}\right|^2\right](\mathbf{f})\right](\mathbf{x}) \tag{II.38}$$

From the direct problem, four Fourier transforms are necessary to obtain the final intensity. To achieve a 3D reconstruction, it is the inverse problem that must be solved. This is usually done in a two steps procedure: first the phase of the transmission function is retrieved from the recorded intensities and secondly the electron density is tomographically reconstructed from a large number of phase projections. Therefore, the inverse problem has to be solved: retrieving the unknown phase from the intensity recorded on the detector. The inverse problem method used for SOC samples is presented in the following section.

3.1.7 Transport of Intensity Equation

A lot of methods have been proposed in the literature to solve the inverse problem. They can commonly be divided in two classes and, to be efficient, make use of a linearization of the non-linear relationship given by equation (II.38). The Contrast Transfer Function (CTF) approach [Guigay1977, Cloetens1996, Cloetens1999b, Turner2004] is based on a linearization of the problem with respect to the object functions $B(\mathbf{x})$ and $\varphi(\mathbf{x})$. Therefore, it is valid for objects showing weak absorption and a slowly varying phase. The CTF approach is extensively used

in holotomography of biological samples, but it is not appropriate for SOC samples due to the relatively strong absorption and fast changes of the phase. The Transport of Intensity Equation (TIE) approach [Teage1983, Gureyev1995, Paganin1998, Turner2004], on the other hand, is based on a linearization of the propagator of equation (II.25) with respect to the distance *D*. Therefore, it is valid for small propagation distances only, but theoretically without restrictions on the absorption. In this section, only the TIE is detailed as it is the approach yielding best results for SOC samples. Except for truly weak objects, the first guess of the phase obtained by the linearized methods will have to be iteratively improved to overcome the assumptions initially made.

The TIE is obtained by starting from the equation (II.31) which is the Fourier transform of the intensity under Fresnel diffraction. By considering only a small distance *D* between the object and the detector [Turner2004], the following Taylor expansion can be made:

$$T\left(\mathbf{x}+\frac{\lambda D\mathbf{f}}{2}\right)=T(\mathbf{x})+\frac{1}{2}\lambda Df\ \frac{\partial T(\mathbf{x})}{\partial \mathbf{x}} \tag{II.39}$$

By introducing this last expression in the equation (II.31), the following expression is obtained:

$$I_D(\mathbf{x})=I_0(\mathbf{x})-\frac{\lambda D}{2\pi}\frac{\partial}{\partial \mathbf{x}}\left[I_0(\mathbf{x})\frac{\partial \varphi(\mathbf{x})}{\partial \mathbf{x}}\right] \tag{II.40}$$

As the assumption $\lambda D|\mathbf{f}|_{max}^2 \ll 1$ is considered, the final expression of the TIE is obtained:

$$-\frac{2\pi}{\lambda}\frac{\partial I_0}{\partial z}=\frac{\partial}{\partial \mathbf{x}}\left[I_0(\mathbf{x})\frac{\partial \varphi(\mathbf{x})}{\partial \mathbf{x}}\right] \tag{II.41}$$

This final expression is a linear relation between the phase and the intensity obtained by doing the approximation of small propagation distances. In the absence of absorption ($I_0(\mathbf{x})=constant$) the intensity variation recorded at a small distance is thus simply proportional to the second derivative of the phase. In the absorbing case ($I_0(\mathbf{x})\neq constant$), the solution of equation (II.41) is not trivial, but possible using different methods [Gureyev1995]. A full TIE solution, without assuming a relationship between absorption and phase, will be sensitive to noise due to the small distance and weak contrast conditions.

3.1.8 Paganin's approach

The phase retrieval approach used for the SOC samples is based on a method using the TIE and considering the object as homogeneous, it means a constant ratio δ/β [Paganin2002]. The demonstration is based on the TIE. The Beer-Lambert law is a good approximation for the intensity in the plane located just after the object:

$$I_0(\mathbf{x})=I_{inc}e^{-\mu T_h(\mathbf{x})} \tag{II.42}$$

with $T_h(\mathbf{x})$ the local thickness of the object.

If the object is sufficiently thin, the phase is directly proportional to the thickness function as:

$$\varphi(\mathbf{x}) = -\frac{2\pi}{\lambda}\delta\, T_h(\mathbf{x}) \tag{II.43}$$

By introducing the two last equations in expression (II.41), a linear relation for $e^{-\mu T_h(\mathbf{x})}$ is obtained:

$$\frac{\partial I_0(\mathbf{x})}{\partial z} = -\frac{\delta}{\mu} I_{inc} \frac{\partial^2}{\partial \mathbf{x}^2} \cdot e^{-\mu T_h(\mathbf{x})} \tag{II.44}$$

By considering small distances between the object and the image planes, the following approximation can be done:

$$\frac{\partial I_0(\mathbf{x})}{\partial z} \approx \frac{I_D(\mathbf{x}) - I_{inc} e^{-\mu T_h(\mathbf{x})}}{D} \tag{II.45}$$

By introducing this expression in equation (II.44), the equation is:

$$\frac{I_D(\mathbf{x})}{I_{inc}} = e^{-\mu T_h(\mathbf{x})} \left[1 - \frac{\delta}{\mu} D \frac{\partial^2}{\partial \mathbf{x}^2} \cdot \right] \tag{II.46}$$

By going through the Fourier space, the thickness function can be expressed in the real space by the following equation [Paganin2002]:

$$\mu T_h(\mathbf{x}) = -ln\left(\mathcal{F}^{-1}\left\{ \frac{\mathcal{F}\{I_D(\mathbf{x})/I_{inc}\}}{\left[1 + \frac{\delta}{\beta}\lambda D \pi |\mathbf{f}|^2\right]} \right\} \right) \tag{II.47}$$

From this last equation, it is possible to obtain the phase of the object as it is directly linked to the linear attenuation coefficient:

$$\varphi(\mathbf{x}) = -\frac{\delta}{\beta}\frac{\mu}{2} T_h(\mathbf{x}) \tag{II.48}$$

By doing the approximation of homogeneous object besides small propagation distances, the Paganin's approach links the phase to the measured intensity $I_D(\mathbf{x})$ on the detector. The expression (II.47) is 'popular' both at synchrotron and laboratory sources because it allows determination of the phase from the intensity recorded in a single plane and knowledge of the δ/β ratio. The expression is similar to the one used in absorption tomography except for the presence of a low pass filter, implemented by two Fourier transformations. However, the result is necessarily a blurred version of the recorded intensity while the main goal is obtaining a high resolution 3D image of the microstructure. Therefore, this method needs to be enhanced iteratively without assumptions on the propagation distance or the homogeneity of the sample. This is done by the Conjugate Gradient Method (CGM) detailed in the following part.

3.1.9 Conjugate Gradient Method

The last relation can be used to reconstruct phase maps from a scan recorded at a single distance *D*. This method can be extended to a multiple distances approach. In this case it allows

obtaining a better signal-to-noise ratio, less 'ring artefacts' and a more constant background level. However, with this approach, the use of multiple distances does not solve the blurring problem. This is solved by an iterative procedure using the full image formation problem. The main principle of CGM is presented hereafter.

Samples with materials presenting strong absorption and a complex microstructure such as SOC electrodes are difficult to analyse by the classical phase retrieval algorithms. In fact, some artefacts remain in the reconstruction and the distinction between the different material phases can be difficult. In order to improve the image quality obtained by a linearized solution of the phase (Eq. (II.48)), an iterative method using a conjugate gradient approach (CGM) is used [Cloetens1999, Suhonen2017]. The main idea of this approach is to reduce the difference between the measured intensity on the detector I_D^{meas} and the calculated intensity I_D^{calc}. In practice the difference in a least squares sense is used. Therefore, we minimize the following cost function C(T(x)) for the *M* distances with respect to the transmission function T(x):

$$C\big(T(\mathbf{x})\big) = \frac{1}{M}\sum_{i=1}^{M}\int \left|I_D^{meas}(\mathbf{x}) - I_D^{calc}(\mathbf{x})\right|^2 d\mathbf{x} \tag{II.49}$$

The calculated intensity is obtained without approximations by the direct problem with the equation (II.38). The transmission function of the iteration $i+1$ is changed to reduce the cost function compared to the iteration i. The minimization of this expression allows an improvement of the final image. The update of the transmission function at each iteration requires four Fourier transformations according to the expression (II.50):

$$\tilde{T}^{i+1} = \tilde{T}^{i} + \frac{\eta_{conv}}{M}\sum_{j=1}^{M}\tilde{P}_j^{*}\,\mathcal{F}\left[u_j^i\mathcal{F}^{-1}\left\{\tilde{R}\left(\tilde{I}_j^{i\,meas} - \tilde{I}_j^{i\,calc}\right)\right\}\right] \tag{II.50}$$

with η_{conv} a convergence parameter. This corresponds to choosing the steepest descent direction to search for the minimum of the cost function. However, the convergence to a local minimum of such a function can be long. The speed of convergence is increased by using a non-linear conjugate gradient method that consists in following a 'conjugate' search direction. The new search direction is not simply the steepest direction, but a linear combination of the steepest direction and the old search direction according to an update rule. The update proposed by Polak-Ribiere is used in practice [Polak1969].

Still, in the case of strong absorption and phase objects such as SOC electrodes, the algorithm can converge to non-physical results appearing as artefacts after tomographic reconstruction. It is possible, at the cost of supplementary calculations at each iteration, to avoid these artefacts by adding some constraints in the CGM. A first constraint that can be used is a limitation on the maximum phase gradient in the projection. This will avoid non-physical, very fast changes of the phase from one pixel to the other. A second constraint, acting on the absorption, is often required. For example, it is possible to take into account a uniform absorption in the transmission function or a fixed absorption distribution that is not updated. The last approach is used for SOC electrodes and the absorption determined from the generalized Paganin's approach is kept during all iterations. Finally, a last constraint exists to reduce the contribution

of very bright spots that occur in the recorded intensity in the case of very porous samples such as SOC electrodes. After the phase retrieval procedure, phase projections are obtained at each scan angle. Another procedure is necessary to obtain a 3D volume. The tomographic reconstruction is described hereafter.

3.2 Tomographic reconstruction

To reconstruct a 3D volume by tomography requires to know the 2D projections of the sample at different angles of rotation. Then, the projections are put together to obtain a 3D volume. In the case of the holotomography method, it is necessary to retrieve the phase for each angle before doing this processing step. Some algorithms are developed to process the phase retrieval in the same time than the tomographic reconstruction [Bronnikov1999, Burvall2011]. In our case, the phase retrieval is always done according to the method presented in the previous section for each projection angle independently and before the tomographic reconstruction. Once the phase is extracted from the measured intensity, the tomographic reconstruction is carried out according to an analytical algorithm described hereafter.

3.2.1 Fourier slice theorem

To reconstruct a 3D volume, it is necessary to link the projections with the final object. In this part, the X-ray beam is considered as a parallel beam meaning that a line on the detector corresponds to a slice of the 3D volume (see Figure II.12). A slice of an object is represented on the Figure II.12b in the fixed coordinate (x, z) with the y-axis as the rotation axis. A coordinate system rotating with the sample is also shown on Figure II.12b. This system is turned by an angle θ compared to the system (x, z). If a line along u for an angle θ is considered, the projection of the object $o(x, z)$ can be written as:

$$P_\theta(u) = \int_{-\infty}^{+\infty} o(x, z)dv \tag{II.51}$$

By taking the Fourier transform and by doing a change of variable to go to the (x, z) system, the following expression is obtained:

$$\tilde{P}_\theta(f) = \iint o(x, z)e^{-2i\pi f.(xcos\theta+zsin\theta)}dxdz = \tilde{o}(fcos\theta, fsin\theta) \tag{II.52}$$

This relation is very important for the tomographic reconstruction. It is the slice-projection theorem, which shows that the 1D Fourier transform of the projection line at an angle θ is a line in the 2D Fourier transform of the object [Kak1988].

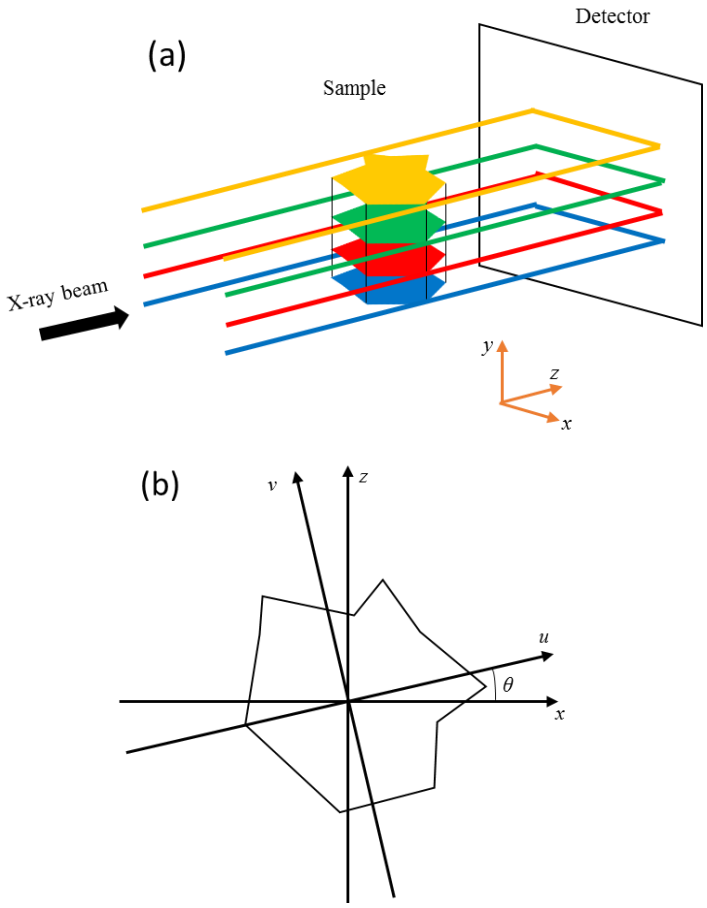

Figure II.12 – (a) Illustration of tomography using a parallel beam: each line of the detector corresponds to a slice in the sample and (b) a slice of the tomographic reconstruction in the two coordinate systems

3.2.2 Filtered back projection

The direct use of the slice-projection theorem to reconstruct the object is not straightforward and may introduce artefacts because it requires interpolating the complex function $\tilde{o}(f cos\theta, f sin\theta)$. An interesting solution is to change to the polar coordinate system for the inverse Fourier transform [Kak1988]. However, a simple backprojection leads to a convolution with a function $1/r$. This effect is illustrated on the Figure II.13 with the example of a circle. The summation of all the backprojections allows the reconstruction of the circle. Nevertheless, a halo is visible around it.

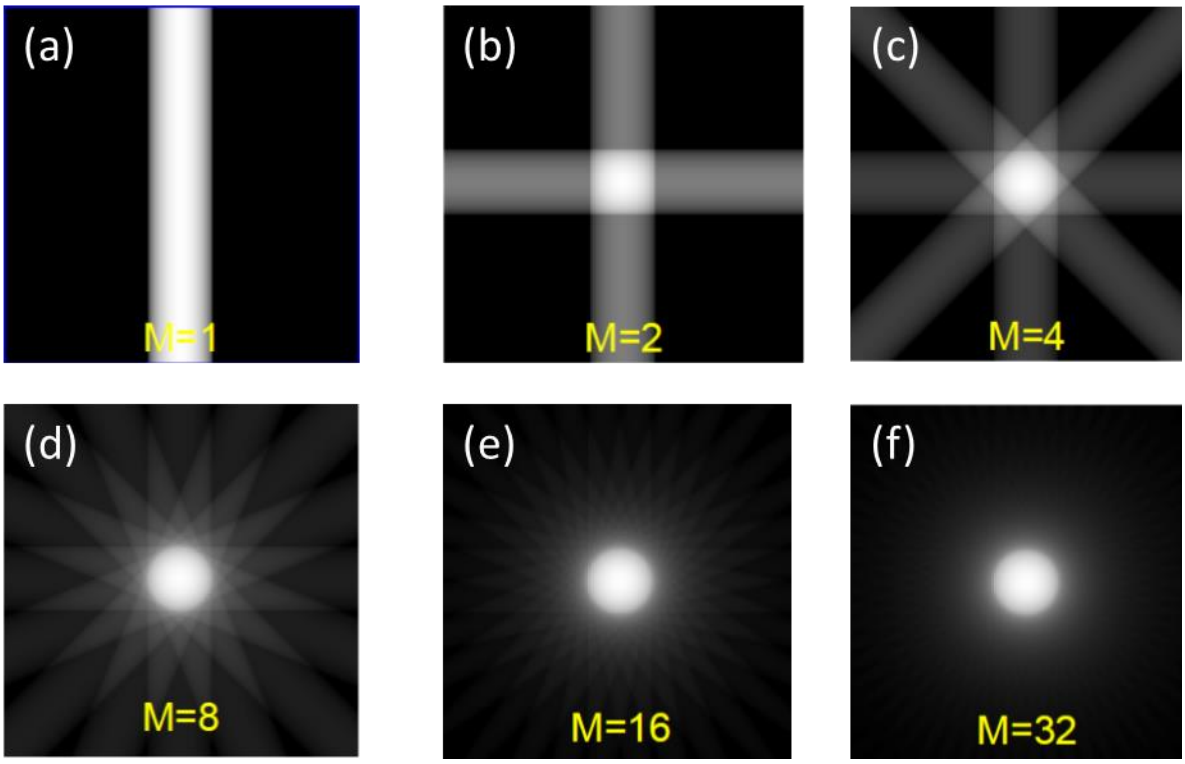

Figure II.13 – Illustration of the reconstruction of a circle by simple backprojection with (a) 1 projection, (b) 2 projections, (c) 4 projections, (d) 8 projections, (e) 16 projections and (f) 32 projections. A halo is visible around the circle on (f). Moreover, it is clear that a sufficient number of projections are necessary to obtain a clear image

A simple solution to solve this problem is to multiply the 1D Fourier transform of the projection with a filter [Bracewell1967]. The exact analytical filter is a ramp filter or the absolute value of the frequency appearing in:

$$o(x,z) = B[\tilde{p}](x,z) = \int_0^{\pi} \int_{-\infty}^{+\infty} \tilde{o}(f cos\theta, f sin\theta)|f| e^{i2\pi f(cos\theta x + sin\theta z)}\, df\, d\theta \tag{II.53}$$

As this is a high pass filter, it can increase the noise in the final volume. Therefore, a lot of different apodization filters have been developed [Ramachandran1971, Shepp1974, Kenue1979].

From Figure II.13, it is also possible to see that a certain number of projections are necessary to correctly reconstruct the object. In the frequency domain, the projections are distributed uniformly over 180°. It is not necessary to record projections between 180°-360° as it is just a mirror image of the other projections. The angular interval δ_θ between two successive projections is:

$$\delta_\theta = \frac{\pi}{N_{proj}} \text{ with } N_{proj} \text{ the number of projections} \tag{II.54}$$

To have a good sampling rate, the radial and angular resolutions in frequency space have to be the same. If the sampling interval is p_{size}, the maximum Nyquist frequency is given by

$$f_{max} = \frac{1}{2p_{size}} \tag{II.55}$$

The radius in the frequency domain corresponds to this maximum frequency [Kak1988].

The angular distance between two points at the maximum frequency value is given by:

$$d_\theta = f_{max}\delta_\theta = \frac{\pi}{2p_{size}N_{proj}} \tag{II.56}$$

For the radial distance, it is directly linked to the sampling interval and the number of pixels N_{pix}:

$$d_r = \frac{2f_{max}}{N_{pix}} = \frac{1}{N_{pix}p_{size}} \tag{II.57}$$

If the radial and angular resolutions are the same, the following relation is obtained for the number of projections that have to be recorded:

$$d_r = d_\theta \Leftrightarrow N_{proj} = \frac{\pi}{2}N_{pix} \tag{II.58}$$

In practise, this condition is not often verified to save time during a scan. This limitation is impacting the spatial resolution achievable in the 3D reconstruction. The Nyquist resolution limitation is expressed as:

$$R_{Nyquist} = \frac{\pi}{2}\, p_{size}\, \frac{N_{pixel}}{N_{proj}} \tag{II.59}$$

The parameter $R_{Nyquist}$ represents the best spatial resolution achievable in a 3D volume obtained with N_{proj} recorded on a detector of N_{pixel} and a pixel size p_{size}. This resolution is equal to 32 nm for a volume obtained at 25 nm pixel size with 2500 projections and a detector of 2048 pixels.

4. Conclusions of the chapter

This chapter is dedicated to the state-of-the-art of holotomography. This 3D reconstruction technique allows a large field of view to be obtained on SOCs compared to the other solutions. It has been shown in this chapter that phase contrast is a highly sensitive method. A conjugate gradient method based on a Paganin's approach is used for phase retrieval of SOC samples. The 3D volumes are then obtained by using an analytical algorithm for the tomographic reconstruction. The improvement of the spatial resolution and reliability of the recording process will be described in the next chapter.

Chapter III:

Enhancement of the X-ray nano-holotomography protocol

Synchrotron X-ray nano-holotomography has been presented as an interesting solution for SOC imaging. This technique allows obtaining large volumes. However, the spatial resolution can be considered limited for fine microstructures. In Villanova et al. [Villanova2013], the spatial resolution has been estimated at 80 nm. Moreover, the success of the tomographic reconstruction was uncertain due to a lack of control of the sample geometry. In this work, the new Nano-Imaging beamline ID16A has been used for the magnified holotomographic experiments. In this chapter, the new beamline as well as the improvement of the method in terms of sample preparation and recording process are presented. A special attention has been paid to the spatial resolution measurement in the final 3D volume. Finally, the microstructural properties extracted from the reconstruction are given for pristine oxygen and hydrogen electrodes.

1. Data acquisition on the new Nano-Imaging beamline ID16A-NI

Many scientific fields are interested by an improved spatial resolution in X-ray imaging [Baruchel2006, Ray2006, Carmona2008, Leppard2008, Bohic2012]. Reduction of the X-ray beam spot-size is a solution developed by the synchrotrons. At the ESRF, two parallel long beamlines have been built in that goal. The first one, ID16A-NI, is dedicated to nano-imaging at two fixed photon energies (17 keV and 33.6 keV), while the second beamline, ID16B-NA, proposes a large choice of nano-analysis techniques in a large energy range (~6-50 keV) with a larger spot-size [Martinez2016, Pacureanu2017]. The undulators of these two beamlines are located in the same straight section of the ring. They are canted symmetrically at angles of ±2.7 mrad in order to operate two independent experimental hutches at more than 165 meters from the source in a common satellite building. In the following section, the ID16A-NI set-up is described in detail.

1.1 The new Nano-Imaging beamline ID16A-NI

This new beamline has been designed to achieve the highest spatial resolution. Specific enhancements have been done to reach that goal. The main characteristics are presented in the following sections.

1.1.1 Beamline layout

The Nano-Imaging beamline is 185 meters long from the source to the sample (Figure III.1). It uses two in-air revolver undulators delivering specific harmonics for the experiments. Choosing a period of 18.3 mm, the undulators operate as single line undulators delivering an X-ray energy of 17 keV. Complementary, the 22.4 mm period delivers a 33.6 keV beam on the third harmonic. The number of optics has been reduced as much as possible to preserve the coherence of the beam. The first optical element is a multilayer monochromator located at 28

meters from the source. It consists of a single bounce multilayer coated spherical mirror to select the harmonic of the undulator with the right photon energy E. The coating consists of different stripes with different multilayer spacings to select the energy according to Bragg condition, the angle of incidence being fixed at 8 mrad. Thanks to this element and its supplementary angular deviation of 16 mrad, the separation between the two beamlines is sufficient in the satellite building. The monochromaticity of the beam is determined by the width of the undulator harmonic and the bandwidth of the multilayer monochromator. Overall it is rather modest ($\Delta E/E = 10^{-2}$). The use of a crystal monochromator could improve this characteristic but the photon flux would be severely impacted by two orders of magnitude. The spherical shape of the monochromator substrate focuses the beam in the horizontal direction onto a secondary source located at 40 meters from the source. In fact, it is necessary to reduce the horizontal size of the source as its original shape is highly elliptical (940(h) x 22(v) µm) due to the large horizontal emittance at the ESRF. In the vertical direction, the beam is not modified by any optics from the source all the way to the experimental hutch.

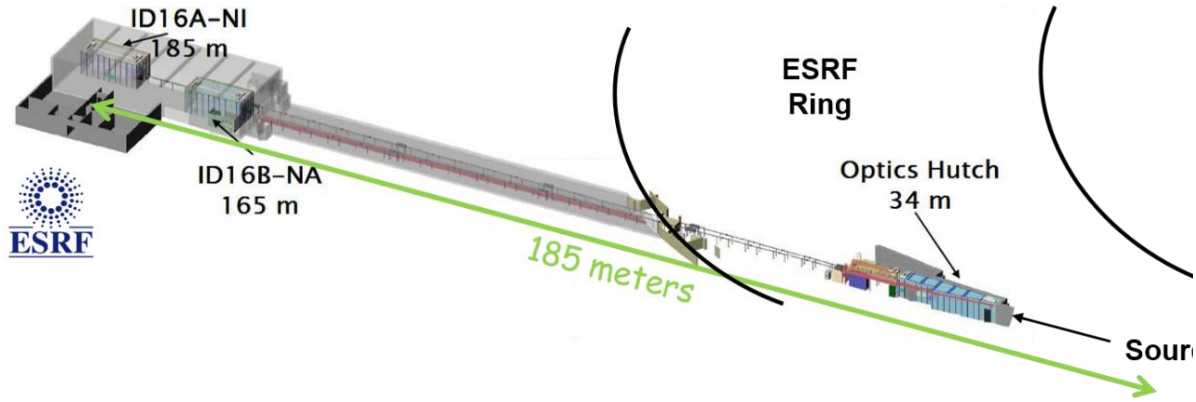

Figure III.1 – Schematic representation of the ID16 beamlines. The optics hutch is located inside the ESRF ring whereas the experimental hutches are in a satellite building at 165 m and 185 m from the source for ID16B and ID16A respectively.

The experimental hutch is located at 185 meters from the source where the beam has excellent coherence properties. Because of this long distance and the potential drift over time, it is necessary to control finely the position of the beam until the sample. To carry out this control, several Beam Position Monitors (BPMs) have been placed along the beam at pertinent positions. Some attenuators can also be put in the beam according to the sample that is scanned. All these components are mobile to limit the number of optical elements in the X-ray beam.

1.1.2 Focusing optics

On ID16A-NI, the X-ray beam is nano-focused after 185 meters thanks to Kirkpatrick-Baez (KB) mirrors [Kirkpatrick1948]. A specificity of the beamline is the design of two pairs of mirrors adapted for each available energy (17 keV and 33.6 keV). The mirrors consist of a multilayer deposited on a substrate with a specific fixed curvature. All the KB setups are made

to achieve a focus spot-size of about 14 nm [Morawe2015]. Some 'knife scans' have been performed in horizontal and vertical direction to measure the focal spot-size. They consist in scanning a sharp edge of a lithography structure through the focus while recording the X-ray fluorescence emitted by the structure. With this method, the focus was found at 23(h) x 37(v) nm² at 17 keV and 24.9(h) x 19.5(v) nm² at 33.6 keV. These values are higher than the expected one. This can be explained by some alignment and stability issues which will be solved over time, but also by the knife scan approach that always overestimates the real focus size due to the width of the lithography structure. X-ray fluorescence images of a Siemens star lithography structure are shown in Figure III.2 to illustrate the improvement of the resolution from the old beamline ID22NI to the new ID16A-NI. It is clear that the thin, 50nm wide, inner lines are better resolved with the new setup. Moreover, the asymmetry of the focal spot is observable on the second image (Figure III.2).

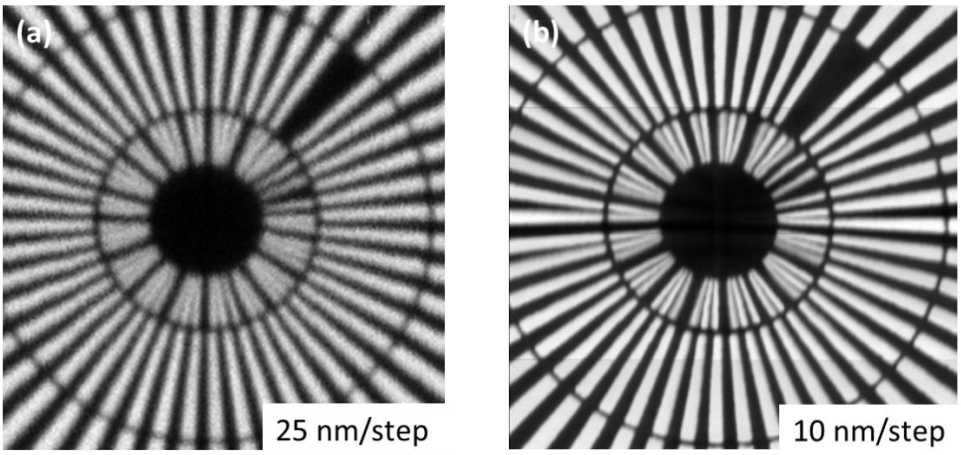

Figure III.2 – Siemens star pattern imaged by X-ray fluorescence (a) on the former Nano-Imaging endstation ID22NI and (b) on the new ID16A-NI beamline. The improvement in resolution is visible as well as the asymmetry of the focal spot.

1.1.3 Sample stage

The KB mirrors are placed inside a vessel under high vacuum, which also includes all the sample stages (Figure III.3). A fine attention has been paid to develop a sample stage with high precision motions. Indeed, the setup stability as well as the good control of the sample position during rotation are two important aspects to achieve a high resolution in tomography. The new Nano-Imaging beamline is using a lot of piezoelectric motors to reach this goal. These motors have the advantage to be small in size, to lock to a fixed position after motion and to reduce the vibrations [Uchido1996]. The precise alignment and rotation of the sample is ensured by a short range hexapod designed at the ESRF. Twelve capacitive sensors are placed around the sample near a metrology ring to check online its positioning. These sensors are converted into Cartesian coordinates to measure 5 degrees of freedom (three translations and two tilts). A feedback loop permanently controls the six piezoelectric actuators of the hexapod in order to correct the tilt or position of the sample. Thanks to this high precision equipment, the resolution

limitation due to the sample stability problem should not be very important. However, depending on the sample mounting, a drift of the sample itself with respect to the stage can still occur during the holotomography acquisition.

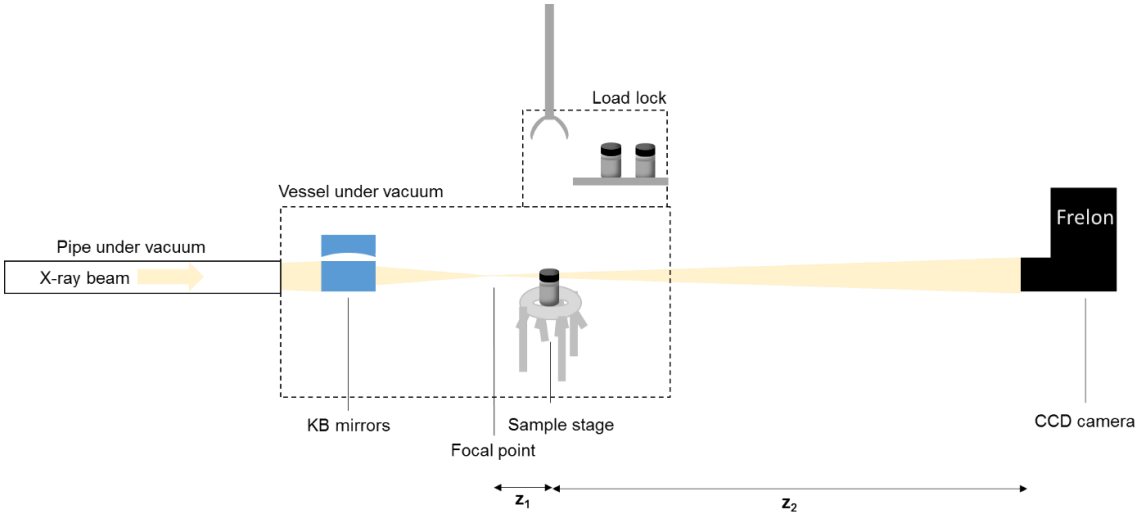

Figure III.3 – Scheme of the experimental hutch showing the KB focusing mirrors and the sample stage located in a vacuum vessel, as well as the load lock sample changer and the X-ray imaging detector.

1.1.4 Detector

The divergent X-ray beam comes out of the vessel through a large diamond window. The propagation of the wave further takes place in air. Two detectors are available for the projections recording. It should be noticed that the images are magnified on the detector as a focalised beam is used. The first available detector on ID16A-NI is using a semi-transparent scintillator allowing the beam to propagate to the second detector located downstream. The imaging sensor is a FReLoN CCD camera with 2048x2048 pixels of 24 µm, yielding an effective pixel size of 0.86 µm considering the magnification of the scintillator-CCD lens coupling. The second detector is also a FReLoN camera but with a larger number of pixels (4096x4096 pixels of 15 µm). A specifically designed lens is used to couple the scintillator to the large CCD area. It yields an effective pixel size of 1.5 µm. The pixels are usually binned (2x2) to 3 µm in order to reduce the data size and increase the recording time. The detectors are placed on motorized translation stages, with three degrees of freedom, to align them in and along the X-ray beam or to remove them from the beam.

In the parallel beam case, the pixel size of the detector can be a limiting factor for the spatial resolution in the 3D volume. Indeed, each pixel directly represents a voxel in the final reconstruction. The decrease of the pixel size of the detector can be an interesting solution to improve the image resolution. However, the decrease of the detector pixel size and resolution requires using a thinner and less efficient scintillator. This will require increasingly longer scanning times to maintain a good Signal-to-Noise Ratio (SNR). From that point of view, a compromise has to be found to preserve the SNR and to decrease as far as possible the pixel

size of the detector (and hence the voxel size of the final image). Also, due to the finite wavelength of the visible light photons, the spatial resolution of parallel beam tomography is about 500 nm at the very best, or more likely about 1 µm to preserve some detection efficiency at high energies. In our case, magnified nano-holotomography is used. As the X-ray beam is focalised by the KB mirrors, a magnified projection of the object is recorded on the detector (Figure III.3). By choosing the distance between the focal point and the sample (z_1) and the distance between the sample and the detector (z_2), the X-ray magnification (*M*) can be selected. In that case, the detector is no more limiting the resolution for the 3D volume.

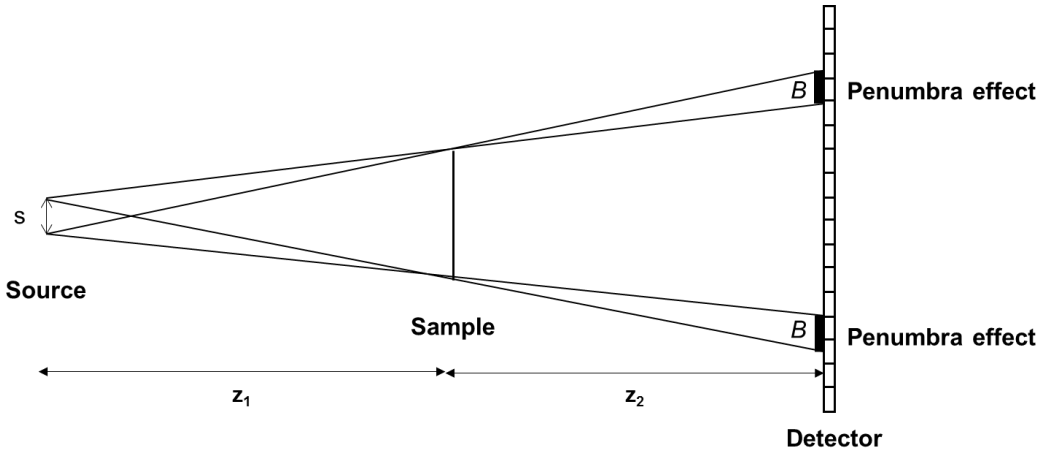

Figure III.4 - Schematic representation of the penumbra effect due to the source size.

However, the source size can be responsible of a spatial resolution degradation [Pogany1997, Arhatari2004]. As shown on Figure III.4, the width of an incoherent source causes a penumbra on the detector. This zone of shadow on the detector creates blurring in the recorded projection [Ouandji2002]. A simple geometric relation links the blurring B to the source size s and the distances between focal point, sample and detector:

$$B = s\frac{z_2}{z_1} \qquad \text{(III.1)}$$

In our case, with a source size of about 20 nm and distances $z_1 = 10.5\ mm$ and $z_2 = 1.255\ m$, a blurring of 2.4 µm is obtained. This value is smaller than the pixel size of the detector which is 3 µm. The penumbra effect is thus not impacting too much the projections.

1.1.5 Sample changer

As specified previously, the entire sample environment is under vacuum (~10^{-7} mBar). A specific load lock chamber has been designed to allow an easy sample change. The load lock is a small volume which can be isolated from the whole vessel (Figure III.3). In this way, it is not necessary to vent the complete vessel to change a sample what would take too much time. The load lock can be vented and pumped in less than one hour. A support with several positions for sample holders is available in the load lock. In this way, time is saved as the venting is not

necessary for each sample change. A pincer allows the sample to be removed from the load lock to the sample stage in the vessel and reciprocally.

1.2 The new sample preparation process

A new sample preparation process has been developed to improve the reliability of the global workflow. The studied SOC and the different steps are presented hereafter.

1.2.1 Studied cell

A commercial circular cell has been used in this work. It is a hydrogen electrode supported cell. The electrolyte and hydrogen electrode have a diameter of 50 mm whereas the oxygen electrode presents an active surface of 9.08 cm². The electrolyte is made of a dense 5 µm thick layer of 8%mol Yttria stabilized Zirconia (YSZ). The hydrogen electrode is a ceramic-metallic composite of nickel and YSZ (Ni-YSZ). Its thickness is about 260 µm. The oxygen electrode is composed of several layers. A barrier layer made of 10%mol Gadolinium doped Ceria ($Gd_{0.1}Ce_{0.9}O_{1.95}$ abbreviate GDC) is first added on the electrolyte to avoid chemical reactivity. It should be noticed that this layer is not fully dense. Then, a composite active layer of GDC and $La_{0.6}Sr_{0.4}Co_{0.2}Fe_{0.8}O_{3-\delta}$ (LSCF) is deposited. The mix of materials ensure a good matching between the thermal expansion coefficients of the cell layers. A single phase LSCF porous layer of about 18 µm thick is added to the oxygen electrode. Finally, a $La_{0.5}Sr_{0.5}CoO_3$ (LSC) layer of about 20 µm is put on the surface of the oxygen electrode to ensure current collection. All the thicknesses and compositions are summarized on the Figure III.5 obtained by SEM.

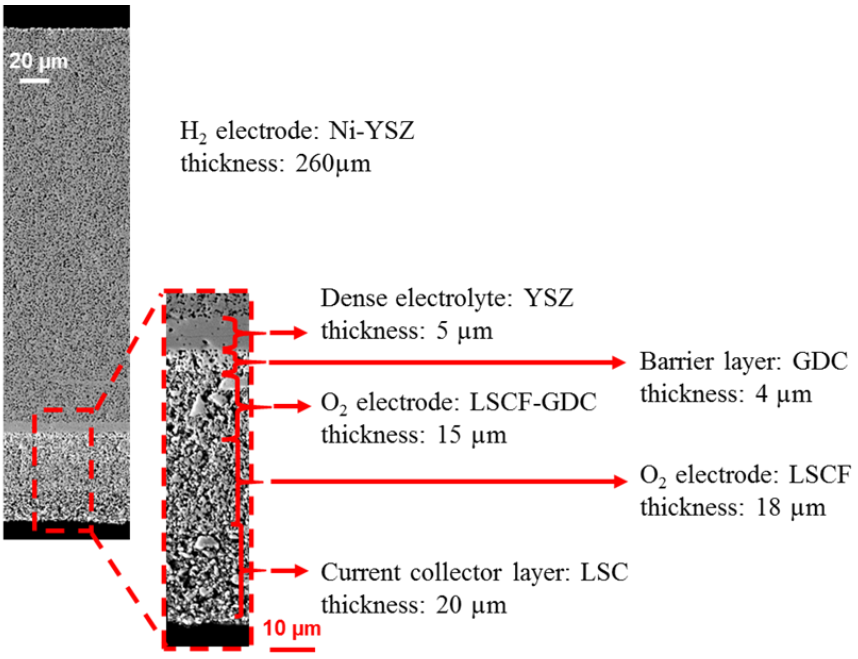

Figure III.5 - SEM cross section image obtained with Secondary Electron Detector of the studied cell. The materials and thicknesses are detailed.

1.2.2 Sample preparation requirements

The geometry of the pincer as well as the sample holder are limiting the overall size of the samples. As sample carrier, two kind of Huber pins made in brass or aluminium are used to fix the sample (Huber Diffraktionstechnik GmbH & Co. KG). The pin, with a length of 12.5 mm and a diameter of 3.15 mm, is attached to an in-house designed sample holder that is grabbed by the pincer of the sample changer. The height from the top of the Huber pin cannot exceed 7 mm. Moreover, the thickness and shape of the sample has a huge impact on the data quality and analysis. Firstly, an axisymmetric shape is the most suitable geometry for the specimen. Indeed, the sample being rotated during the tomographic scan, the cylindrical geometry has the advantage to present the same absorption whatever the angle. Secondly, for tomography, it is better to reduce the thickness of the sample to have enough signal on the detector and to reach high resolution. Moreover, the analytical tomographic reconstruction presented in chapter II is strictly speaking only valid if the width of the sample fits within the field of view of the images. However, the reconstructed 3D volume must be large enough to be representative of the complete electrode microstructure. Previously, a complex multi-steps process was used [Villanova2013, Lay2014]. It consists of an initial laser cutting of strips, which were then polished down to a thickness of 100 µm. Finally, small triangular needles were obtained by sword cutting the polished strips. The sample was then placed in a capillary and filled with a specific resin. The shape and thickness of the sample was not fully controlled and poorly adapted to the experiments.

1.2.3 Focused Ion Beam

In order to better control the localisation, geometry and size of the sample, a new preparation process has been developed. It is known that a Gallium Focused Ion Beam (FIB) setup is an interesting tool for the preparation of tomographic samples [Shearing2009, Shearing2010b] or for material characterisation in conjunction with a SEM [Phaneuf1999, Munroe2009]. Nevertheless, this equipment leads to a maximum sample dimension of 10-20 µm if a reasonable process time is considered [Bleuet2013]. A new category of Plasma-FIB (PFIB) using Xenon ions have been developed during the last decades. This tool is about 60 times faster than a conventional Ga-FIB [Kwakman2011]. This increase in the milling speed is due to the larger size of the Xenon ions compared to Gallium and the higher current available on the PFIB.

1.2.4 FIB milling

For all the samples studied, a Plasma-FIB Vion (FEI™) using an inductively coupled plasma source of Xenon ions has been employed. On this equipment, no SEM is available but the ion beam can be used at low current to image the sample. First of all, a piece of cell fixed on a

support is placed on a 5-axis motorized stage. Once the chamber of the PFIB under vacuum, the beam is focused and the eucentric height is identified. This position corresponds to the location where the imaged part of the sample is always the same whatever the rotation and the tilt. After these preliminary adjustments, a clean and flat region of interest is chosen at the surface of the electrode. It should be noticed that it is easy to select the position of the sample. In that way, if the inlet and outlet of the cell are well identified, it is possible to prepare a sample in these areas.

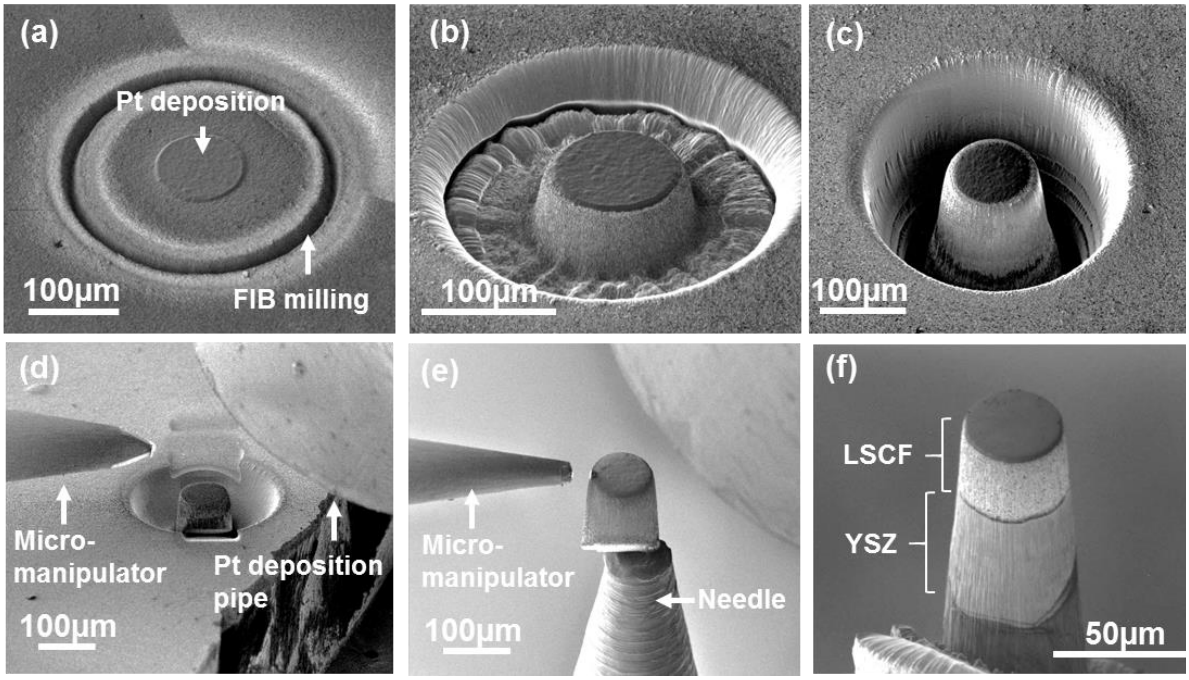

Figure III.6 – Sample preparation by PFIB. (a) Pt deposition and start of the FIB milling, (b) Sample after a first concentric circle milling, (c) sample at the end of the FIB milling, (d) sample removed from the cell with the micro-manipulator, (e) sample fixed on the needle and (f) final sample with a clean and undamaged surface

The first step for the preparation is the deposition of a circular platinum protective layer with a thickness of about 2-5 µm and a diameter close to the required final sample dimension. The deposition is obtained by the decomposition under the ion beam of a carbonate gas mixed with Pt. This layer protects the top of the sample of potential degradation throughout the whole FIB milling process. To be able to remove the sample by the lift-out process, a sufficiently large ring is initially milled around the Pt deposition (Figure III.6a). Indeed, the width and the depth of the FIB milling will have a huge impact on the size of the final sample [Lombardo2012]. In our case, with our lift-out technique and a reasonable FIB milling time, the maximum sample height is about 100 µm. This value is smaller than the H_2 electrode thickness. For the samples of the cermet at the interface with the electrolyte, the milling has been done from the O_2 electrode side. To be sure to obtain a sufficiently large representative volume of the cermet, a part of the oxygen electrode has been removed with sandpaper. As no precision is required during this process step, the highest available current on the PFIB is used for the milling (1.3 µA at 30 kV). Concentric rings are milled one after the other to obtain the final required milling

depth and to avoid too much sputtered material (Figure III.6b and Figure III.6c). The complete process is taking about 3-4 hours.

1.2.5 Lift-out process

The second part of the sample preparation is the lift-out process. The sample is removed from the cell and placed on a needle adapted for the tomographic sample holder [Lombardo2012, Chen2014]. For this step, a micromanipulator located in the PFIB chamber is used to handle the sample. The micromanipulator is first approached close to the sample (Figure III.6d). A small Pt deposition is done to weld the arm with the sample. Then, the cylinder is cut from the cell with the ion beam. At this time, it can be lift out of the cell and fixed to the needle with a Pt weld. Finally, the first weld between the micromanipulator and the sample is cut and the arm is removed from the chamber (Figure III.6e).

Once strongly fixed on the needle, the diameter of the sample is reduced to the required value. A width of about 50 µm is a good compromise for the tomographic experiments and the representativeness of the microstructural parameters. For this purpose, a low current (59 nA) is used to obtain a smooth and undamaged surface (Figure III.6f). Thanks to the PFIB equipment, the final sample has a close to perfect axisymmetric geometry which is well adapted for tomographic scans. Indeed, the absorption in the projection is the same whatever the angle of the tomographic acquisition.

Once the sample has been prepared by PFIB, the needle is inserted in a Huber pin and fixed to the ID16A sample holder with silver lacquer. It is important to perfectly stabilize the sample to avoid any unwanted shivers during holotomographic scans. The sample is then ready to be characterized on ID16A-NI.

1.3 The new data acquisition process and 3D reconstruction

Before starting the experiment, some parameters have to be chosen. One of them is the beam energy. For SOCs which are made of strongly absorbent materials, it is better to work at 33.6 keV. For a sample of 50 µm thickness, the beam transmission is about 80% at this energy, it would be 50% at 17 keV. Furthermore, the phase shifts are reduced roughly by a factor two making the phase retrieval easier. All the data presented in this manuscript have been obtained at this high X-ray beam energy. The other steps for the data acquisition and 3D reconstruction are presented in the developments.

1.3.1 Magnification

As presented in the previous sections, the X-ray beam is focused by KB mirrors. The projections recorded on the detector are thus magnified (Figure III.7). The magnification

depends on the distance between the focal plane and the sample (z_1) and the distance between the sample and the detector (z_2). In our experiments, the distance $z_1 + z_2$ between the focal point and the detector is kept constant. The pixel size of the projection can thus be chosen by changing the sample location between these two positions. The pixel size of the projection is obtained by the following relation:

$$p_{size} = \frac{p_{detector}}{M} = \frac{p_{detector} \cdot z_1}{z_1 + z_2} \qquad \text{(III.2)}$$

Smaller pixels in the image allow a finer description of the microstructure to be reached but the field of view is smaller. It appears that a pixel size of 25 nm is a good compromise between a fine microstructural characterization of the SOC electrodes and a large final 3D volume ($51.2 \times \pi \times 25.6^2$ µm^3) which is representative of the whole electrode.

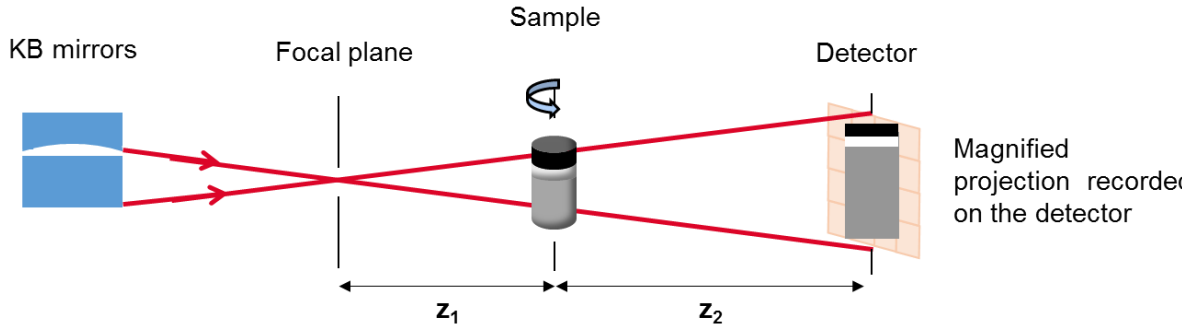

Figure III.7 – Set-up geometry

1.3.2 Acquired data

For a classical holotomographic acquisition, about 2000 projections are collected over 180° at four different sample distances. The rotation is ensured by a step-by-step scanning process. Although this way is slower compared to a continuous scan, it guarantees a high stability of the sample at each angle. With the current setup, it turned out that a continuous scan creates too much heat and vibrations to be compatible with high resolution imaging. Moreover, a waiting time of about 500 milliseconds is respected after each angular step before recording a projection to ensure a good stabilization of the motors. All these procedures improve the spatial resolution of the final 3D volume.

Before and after each tomographic scan at a given distance, flat field images are recorded without sample in the beam. No intermediate flat field images are recorded during the tomographic scan to avoid repositioning errors. Dark images without X-ray illumination are recorded at the end of each scan. The flat field and dark images are used to correct the non-linearities of the detector [Cloetens1999a] and to correct for the non-homogeneous illumination. The corrected intensity is obtained with the following equation:

$$I_{corr} = \frac{I - dark}{flat - dark} \qquad \text{(III.3)}$$

While this correction is not perfect, it improves the quality of images. Strictly speaking, equation (III.3) is only correct at zero propagation distance and with a perfect detector point spread function, see equation (II.14). In the presence of propagation, it is an approximation because the non-homogeneous incident wave 'mixes' with the object transmission function in a more complex way as seen in equation (II.38). Flat field images must be recorded regularly to take into account the beam drift over time.

1.3.3 Shift correction

As explained previously, for the phase retrieval, it is necessary to record scans at different sample positions. Four distances appear as a good compromise to avoid missing spatial frequencies information without increasing too much the tomographic time [Zabler2005]. The projections recorded at different sample positions present a different magnification. Before the phase retrieval processing, all the projections are rescaled at the best pixel size (it means the smaller pixel size). As some misalignment necessarily exists between the different planes, a horizontal and vertical shift correction is done. To limit the processing time, projections of the four distances at regular angle (every 100 projections for example) are compared by a correlation-based method. Then, a polynomial function is determined for the shift correction of all the projections.

1.3.4 Iterative Conjugate Gradient Method for SOCs

The phase retrieval for the SOC samples is done by using an iterative Conjugate Gradient Method (CGM) which has been introduced in the previous chapter. An illustration of the interest of the CGM and the relevance of the constraints is presented on the Figure III.8 for a Ni-YSZ porous electrode. The first slice corresponds to a result obtained by using only the linear method (Paganin multi-distances approach) without iterations and constraints. Even if the low frequencies are roughly right, it is not possible to identify the three different material phases as shown on the histogram (Figure III.8d). The second slice was obtained with the CGM after ten iterations without using any constraints. The identification of the phases is easier, but the segmentation remains uncertain as the histogram is not very well defined (Figure III.8b and Figure III.8e). The third slice was reconstructed by using CGM and constraints after ten iterations. The constraints consisted in slow change in the phase, imposed amplitude and limitation of bright spots. The visual result is good as well as the histogram that shows three separated peaks (Figure III.8f). Another advantage of the CGM with constraints is the improvement obtained in the whole 3D reconstruction. Thanks to the constraints, some errors such as streak artefacts or ring artefacts are reduced.

The number of iterations has a huge impact on the global process time of the phase retrieval. It is interesting to limit this number as much as possible. The cost function of the CGM could be considered as a good parameter to evaluate the level of convergence and determine a stop

criterion. However, the cost function does not necessarily reflect the final image quality after tomographic reconstruction.

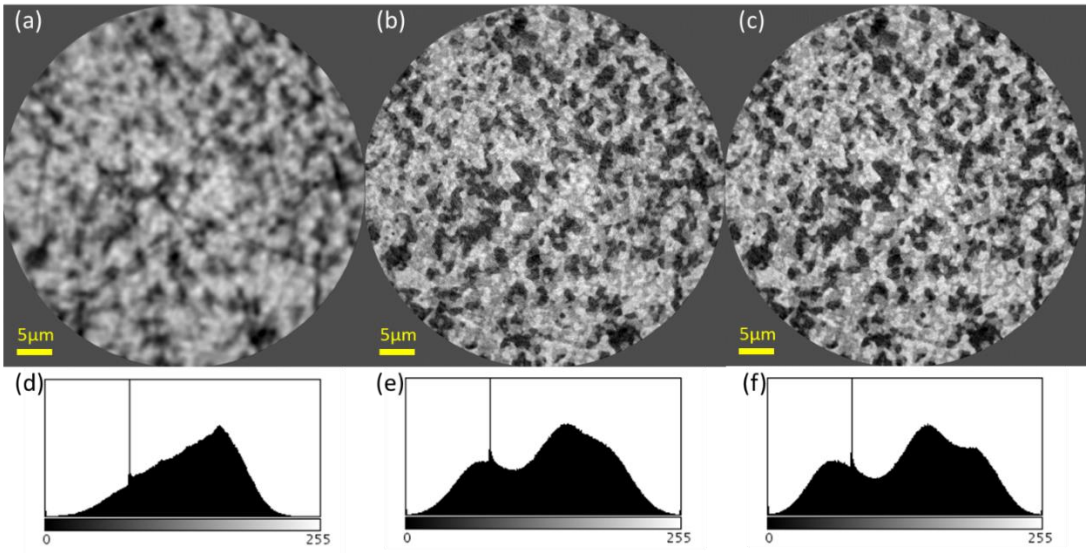

Figure III.8 - Slice taken in the middle of a 3D reconstruction and the corresponding histograms of grey levels for volumes obtained (a) and (d) without iterations, (b) and (e) with 10 iterations in CGM without constraints, (c) and (f) with 10 iterations in CGM with constraints. Black is pores, black grey is YSZ and white grey is Ni.

Another more relevant criterion describing the quality of the material phase segmentation is used. The Otsu's method [Otsu1979] allows to compute an indicator comprised between 0 and 1 that reflects the "goodness" of the segmentation. A value of 1 indicates a perfect segmentation. This criterion has been calculated on slices obtained after a different number of iterations of the CGM (Figure III.9). The main improvement in the images are obtained with the first iterations. After six iterations, the criterion is increasing slowly. It appears that 10 iterations are sufficient to converge to a good physical solution in the reconstruction. The CGM based on a multi-distances Paganin's approach seems to be very relevant for SOCs as it allows the different solid phases to be distinguished.

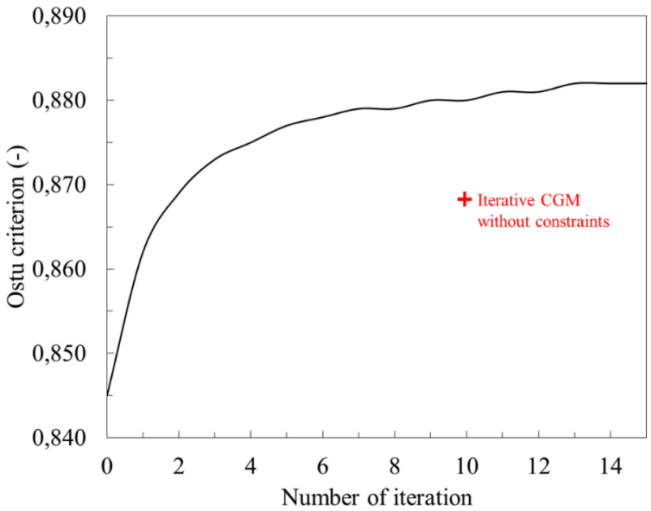

Figure III.9 – Evolution of the Otsu criterion with the number of iteration in the CGM. The red cross represents the Otsu criterion obtained using the iterative CGM without constraints. It appears than 10 iteration are sufficient to converge to an asymptotic value.

1.3.5 3D reconstruction of the hydrogen electrode with random displacement process

For the SOC samples, the phase retrieval is done with in-house codes using the GNU Octave programming environment [Eaton1997] and the public-domain image processing program ImageJ [Schneider2012]. A parallelization of calculations on a large cluster is ensured by using the resource manager OAR [OAR]. The value of the δ and β parameters of the different materials making the studied cell are summarized in the Table III.*1*. Ten iterations are done to reach a good image quality. The 3D volume is then reconstructed by using a classical filtered back projection processing that is done with the software PyHST2 [Mirone2014]. The data are then converted to 8 bits and the grey level is inverted in order to obtain the pore phase in black and solid phase in white. For the cermet electrode, the transitional grey solid phase is the YSZ and the bright white solid phase is Nickel.

Table III.1 : Values of the refractive index decrement δ and the absorption index β for the studied materials at 33.6 keV.

Material	δ	β
Ni	$1.57\ 10^{-6}$	$1.89\ 10^{-8}$
YSZ	$1.02\ 10^{-6}$	$2.38\ 10^{-8}$
GDC	$1.12\ 10^{-6}$	$1.38\ 10^{-8}$
LSCF	$1.04\ 10^{-6}$	$1.23\ 10^{-8}$
LSC	$9.98\ 10^{-7}$	$1.26\ 10^{-8}$

Unfortunately, the reconstructed volumes present strong ring-like artefacts, especially in the middle of slices (Figure III.10a). Each ring is related to a wrong signal reception or acquisition of a given pixel of the 2D CCD camera. As the bad information is always localised on the same pixel, it results in a ring in the 3D tomographic data set [Ketcham2001, Vidal2005, Boin2006]. Different causes can explain this artefact. The fault can be due for example to a defect on the mirrors, the scintillator or a non-uniform pixel response on the CCD camera and it is not sufficiently corrected by the flat field procedure. In our case, we think that the main origin of the artefacts is the failure of the flat field due to the mixing of the incoming wave and the object. Two methods have been developed in the literature to solve the ring artefacts. The first one is based on image processing after the data acquisition. Several algorithms have been proposed to correct the rings from the sinogram [Raven1998, Boin2006, Yousuf2010, Rashid2012] or the slices [Sijbers2004, Kyriakou2009, Lyckegaard2011, Jha2014]. These methods are powerful but they require time after the reconstruction and it is not possible to separate perfectly the artefacts from the real object features. Moreover, the spatial resolution is often degraded in the volume. The second method consists of moving the detector or the sample during the scan [Davis1997, Doran2001, Jenneson2002, Zhu2013]. In that way, the faulty signal is not always localised on the same pixel during the recording of the projections. This method requires a good control of the movement. However, no complex extra-processing is necessary after the acquisition.

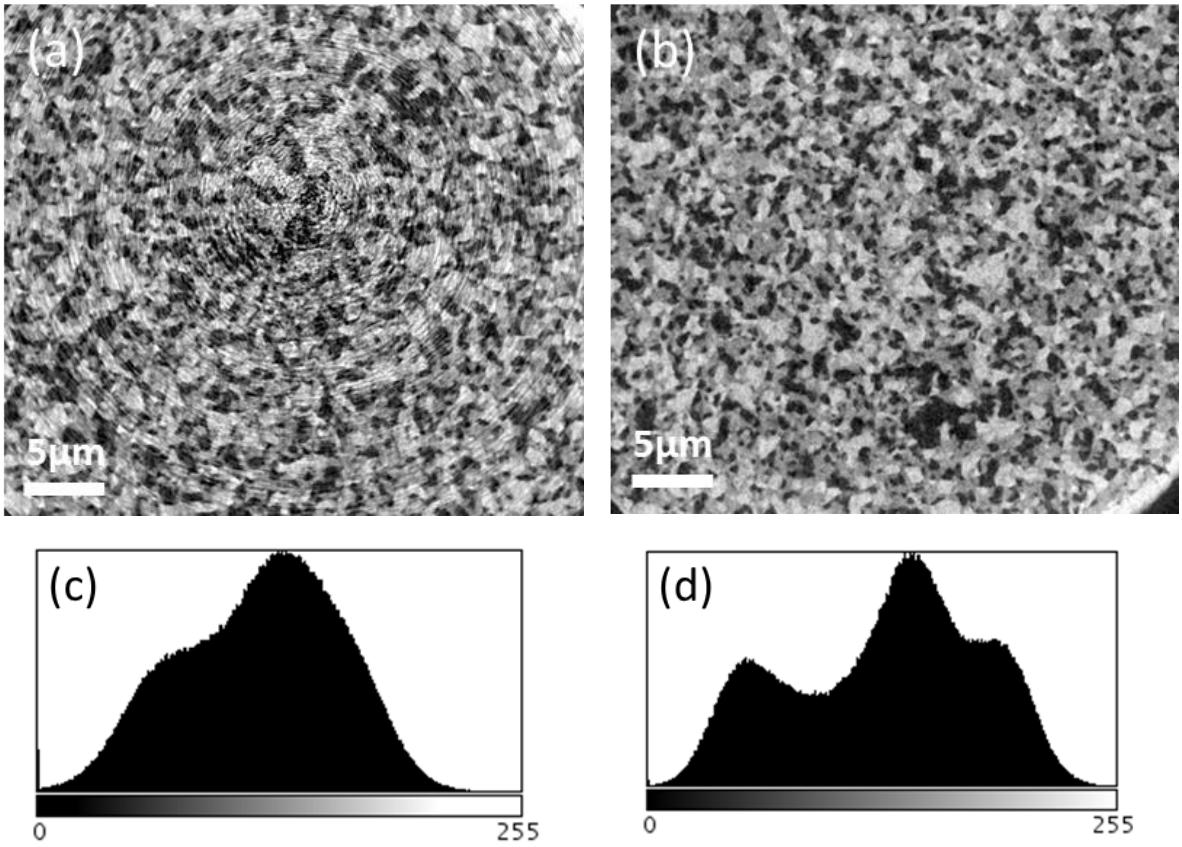

Figure III.10 – Slices extracted from a 3D reconstruction of a cermet electrode and associated histograms for (a) and (c) a reconstruction obtained without random motion, (b) and (d) a volume obtained with the random motion process. It is clear that the ring artefacts disturb the phase separation on the histogram (c). The random displacement process allows removing these artefacts and identifying the three phases.

For the SOC samples, a method based on the random displacement of the sample during the scan has been developed. Moving the sample is the best way to randomize the 'noise' introduced by the mixing of incident wave and sample. Moving the detector would only induce a translation of the recorded images, and hence, would only correct errors introduced by the detector. Before the recording of a projection at an angle, the sample is moved in the x-axis and y-axis of a random motion. This displacement is limited between ±12 pixels in both directions. This is sufficient to spread the wrong signal over a sufficient number of pixels without impacting too much the holotomographic scan time. The lateral displacement with the piezo-motors is done simultaneously with the incremental rotation and takes about the same time. The exact position of the sample for each angle is saved in a dedicated file. This file is used during the shift correction of the projections to also correct the random displacement: the opposite displacement as the one imposed during the scan is applied to the magnified projections. The phase maps obtained at the end of the phase retrieval are thus aligned. In that way, the data processing is not impacted by this change in the data acquisition. It should be noted that the random displacement approach is not compatible with a continuous tomography scan and it should be considered as an advantage of the step-by-step scan.

On the Figure III.10a, a slice of a cermet electrode obtained without random displacement is shown. Strong ring like artefacts are visible in the middle of the slice. They are not continuous like the usual rings and their size is similar to the sample features. It is clear on the histogram (Figure III.10c) that the segmentation of the three different phases is not possible in that case. A slice of the same electrode obtained with the random motion is presented on Figure III.10b. The image is free of ring artefacts. Indeed, the rings are averaged in the background noise. On the histogram, three peaks are visible allowing a segmentation of the volume (Figure III.10d). The huge improvement of the image quality confirms that the interpretation of the origin of the artefacts is correct and that an efficient experimental solution has been found. However, a full theoretical justification does not exist yet.

It is important to check that no blurring is induced by the random motion in the final reconstruction. To this end, a comparison of phase maps with forward projections appears relevant. The forward projections are obtained by using the 3D reconstructed volume to go to 2D projections. It is implemented in the same software PyHST2. The forward projections can be different from the initial phase maps as they are obtained from a 3D volume which includes all the projections information. A correlation based method has been used to compare phase maps and forward projections. The small misalignment named “jitter” is given in horizontal and vertical direction on Figure III.11. The jitter amounts to few nanometres in both directions. It can be concluded from these results that the random motion is perfectly taken into account in the reconstruction procedure. No significant residual misalignments due to this motion are detectable.

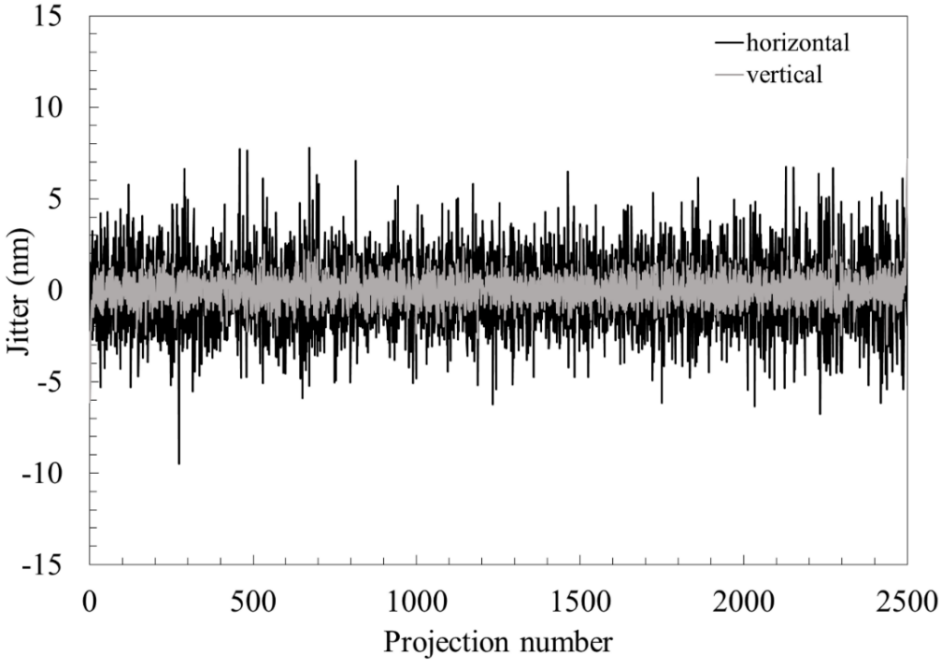

Figure III.11 – Residual movements in the 3D reconstruction obtained with the random displacement process. The jitters are smaller than 5 nm, they cannot be ascribed to the random movement.

1.3.6 Reconstruction of the oxygen electrode

Now that the hydrogen electrode has been reconstructed with success, the same acquisition process is used for the oxygen electrode. A pristine LSCF layer has been imaged by nano-holotomography. A slice and a zoom-in extracted from the whole reconstruction are presented on Figure III.12a and Figure III.12b. It can be noticed that the microstructure is fine. The solid phase is perfectly distinguishable from the porosity as shown on the histogram (Figure III.12c). This 3D volume will be used for the microstructural parameters extraction.

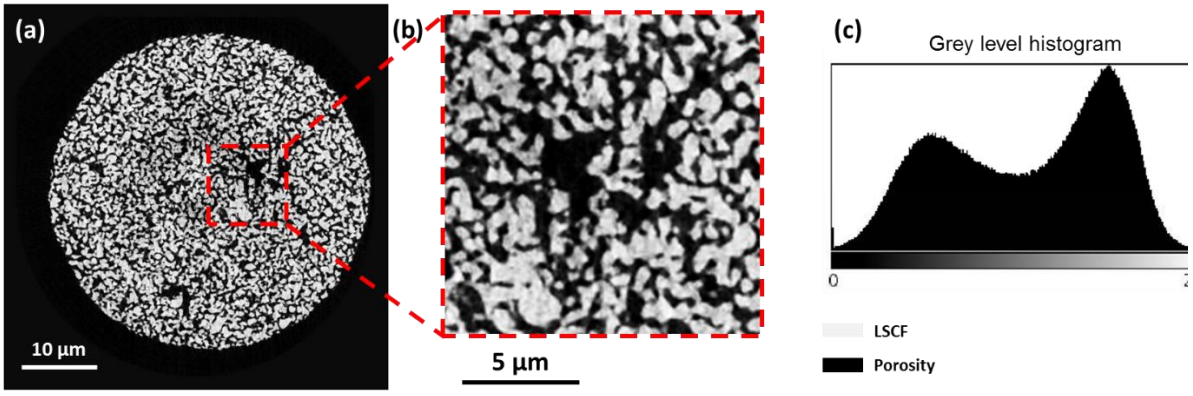

Figure III.12 – Reconstruction of LSCF layer. (a) Slice extracted from the 3D volume, (b) zoom in of the slice and (c) the associated histogram. White phase is solid phase and black phase is porosity.

The composite layer made of LSCF and GDC has also been imaged. Unfortunately the solid phases are not identifiable (Figure III.13). This problem can be explained by the δ and β parameters of materials which are close to each other (see Table III.1). It seems that holotomography is not the best imaging method for this kind of composite layer for the moment. The sensitivity to small density changes needs to be further improved in the presence of huge density jumps related to the porosity.

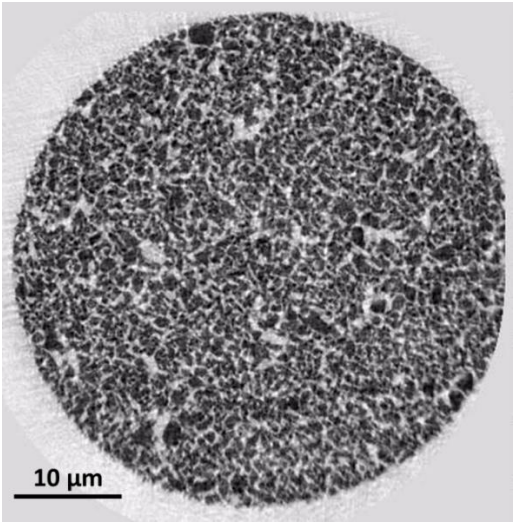

Figure III.13 – Slice extracted from a 3D reconstruction obtained by nano-holotomography of a LSCF-GDC electrode. The two solid phases cannot be satisfactorily distinguished (white=porosity, black=solid phases).

2. Image analysis and microstructural quantification on pristine electrodes

The 3D reconstruction of pristine oxygen and hydrogen electrodes have been obtained by magnified nano-holotomography. Thanks to a new acquisition process, the different phases are identifiable in the volumes. A specific attention has been paid to the spatial resolution estimation of these volumes. The value will be compared with the 80 nm obtained in [Villanova2013] with the same reconstruction method. Moreover, the importance of this parameter for the fine microstructural characterisation is shown in the following section. A quick reminder is also given of the tools used at CEA for the 3D analysis of the electrodes. Some morphological properties are compared with the ones obtained from 2D SEM images. Finally, all the required properties for the models are summarized at the end of this section.

2.1 Evaluation of the spatial resolution

A common mistake in the 3D volume analysis is the mix between the spatial resolution and the voxel size. On the one hand, the spatial resolution depicts the width of the image of a point (point spread function) or the minimum distance between two distinguishable points in the image. This parameter can be affected by the magnified pixel size, but not only. It also depends on the beam size at the focal plane and the sample vibrations for example. On the other hand, the voxel size is the smallest unit of the 3D image. This value is tuneable and it can be reduced without changing the spatial resolution. If the voxel size is increased beyond the spatial resolution, the latter will be impacted due to incorrect sampling. The spatial resolution in the final 3D volume is important for the analysis.

Several methods are proposed in the literature to estimate the spatial resolution [Cardone2005, Holler2014, Robisch2016]. A simple solution is to look at the edges between the different phases. Indeed, the number of voxels included in the grey level distribution across a boundary between two phases is directly linked to the spatial resolution. The edge profile is fitted by a function based on a hyperbolic tangent to obtain the resolution. Grey scale line profiles have been measured within the LSCF electrode 3D volume in the three space directions for the polar, azimuthal and axial orientations as depicted in Figure III.14. The grey level distributions as a function of the position across the edge between LSCF and void is shown in Figure III.14d. The transition zone contains two voxels of 25 nm for all orientations, which indicates that the spatial resolution of the 3D electrode reconstruction is almost 50 nm. The same measure has been done within the Ni-YSZ reconstruction. The grey level distribution is also presented on Figure III.14d. Again, the edge contains two voxels of 25 nm. The spatial resolution of our reconstructions can thus be estimated at 50 nm. With the chosen pixel size at 25 nm, it is normal to not achieve higher spatial resolution since at least two voxels are the lower limit for the spatial resolution [Osten2016].

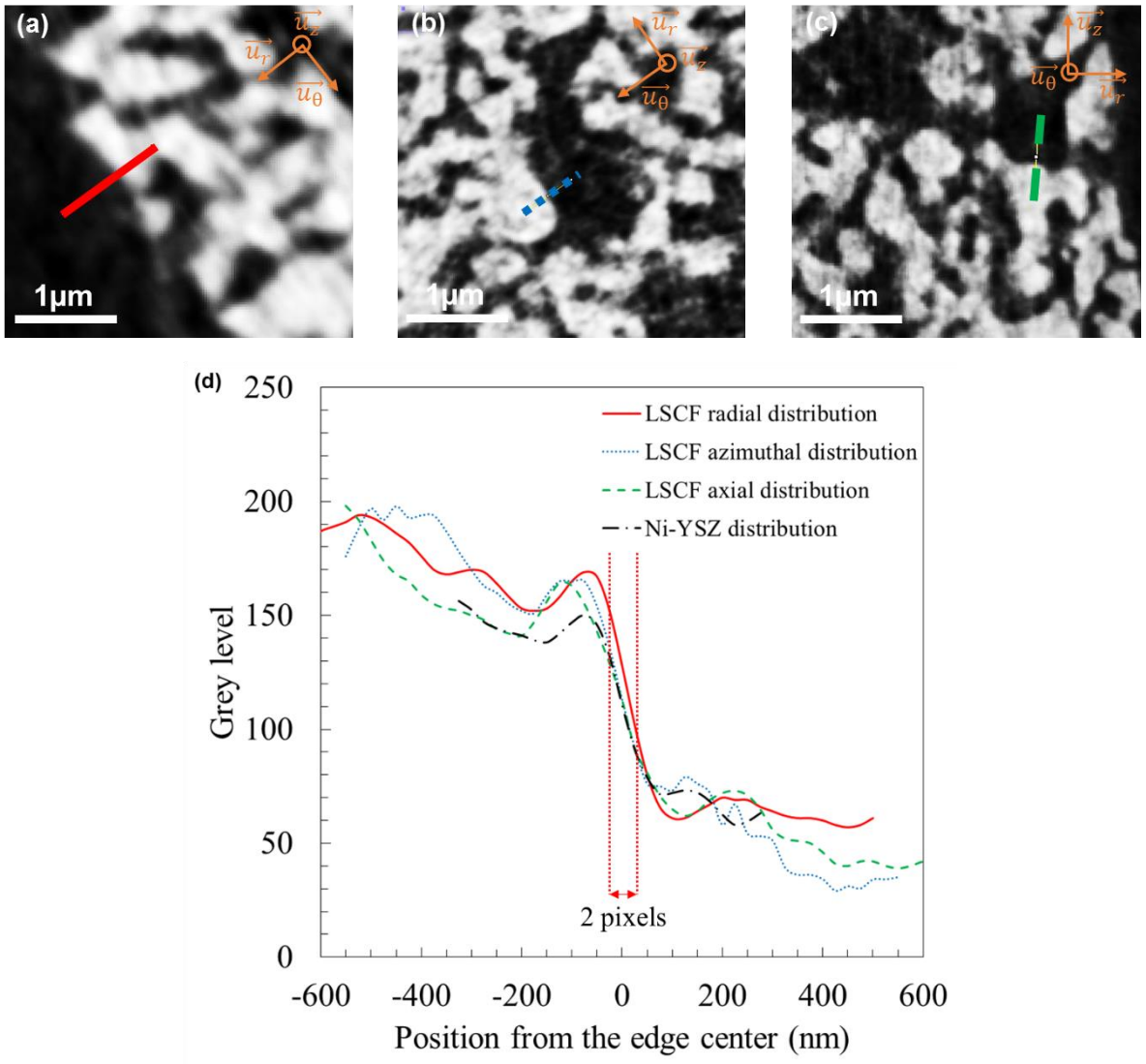

Figure III.14 – Estimation of the resolution: (a) zoom in of the region where the red line profile in (d) has been plotted for LSCF radial resolution, (b) for LSCF azimuthal resolution (blue dot line), (c) for LSCF axial resolution (green dash line), (d) Grey level plotted as a function of the position in the line profiles for LSCF and Ni-YSZ electrodes. A spatial resolution of about 2 pixels (50 nm) is achieved for both electrodes.

The high spatial resolution value is important for the determination of the microstructural properties. It has been shown by Joos et al. [Joos2012] that 10-15 voxels are necessary on the particle diameter to determine accurately the specific surface area. In [Usseglio2015], the theoretical value of the specific surface area is reached at 10 voxels on the particle diameter for a synthetic microstructure. The spatial resolution of 50 nm obtained on our 3D reconstruction of both electrodes allows a fine analysis of microstructure that presents characteristic lengths of around 0.5 µm.

2.2 Three dimensional analysis

To extract the main morphological and physical properties from the 3D volumes obtained on ID16A-NI, a series of image processing and data analysis steps are necessary. They are presented hereafter.

2.2.1 Volume segmentation

The first step of the process is an anisotropic diffusion filtering of the volume [Perona1990, Villanova2013]. The main goal of this step is to enhance the peak separation on the histogram. The filter is smoothing the voxels with a close grey level inside the material phases whereas the contrast at boundaries is enhanced. This is an iterative process done on the full 3D volume. Thanks to this step, the segmentation of each phase is made easier. An automated segmentation method is used for the identification of the phases. The approach is based on the Otsu's method [Otsu1979], which determines the best threshold value to obtain the highest between-class variance. This method is adapted for a two or three phases volume; thus it can be used for both kinds of electrode obtained by holotomography. However, in the case of a three phases volume, it is necessary to correct the segmented volume at the interface between porosity and the brightest solid phase [Usseglio2015]. Indeed, a transition zone considered as intermediate grey level solid phase appears at this interface [Holzer2011] due to the finite spatial resolution and the finite voxel size. It is thus important to correct this non-real border. It is done by an in-house code dividing these voxels between the two other phases.

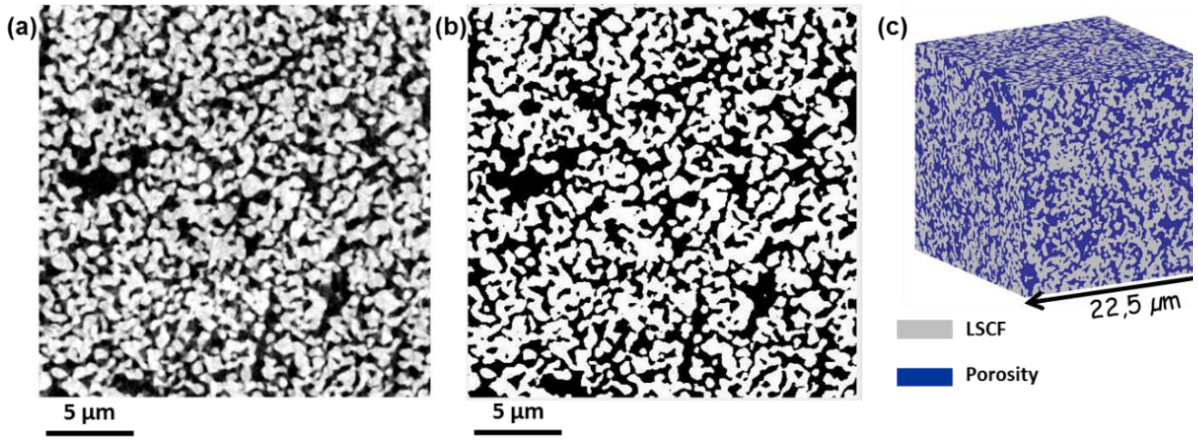

Figure III.15 – Analysed oxygen electrode 3D volume: (a) slice extracted from the raw volume, (b) same slice after segmentation and (c) 3D rendering volume. (black/blue=porosity, white/grey=LSCF)

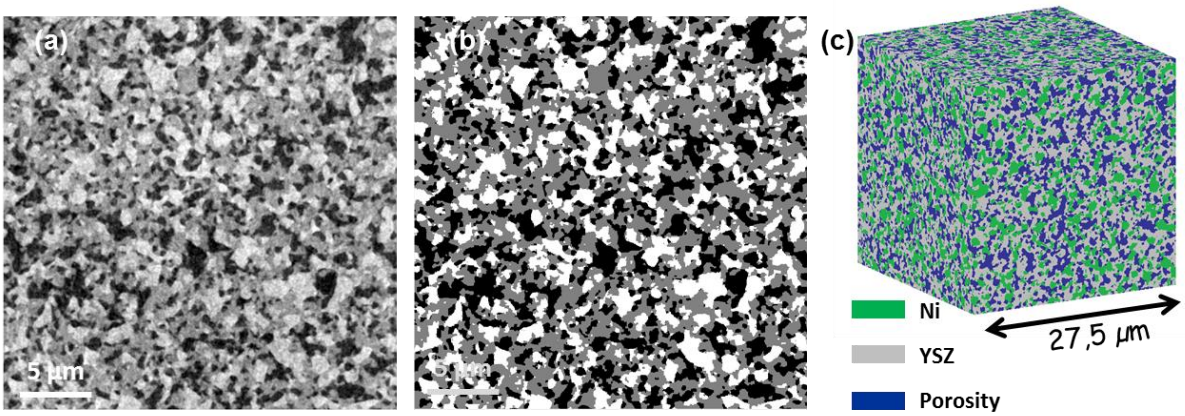

Figure III.16 - Analysed hydrogen electrode 3D volume: (a) slice extracted from the raw volume, (b) same slice after segmentation and (c) 3D rendering volume. (black/blue=porosity, grey=YSZ, white/green=Ni)

On Figure III.15 and Figure III.16, slices and 3D visualisations of oxygen and hydrogen electrodes microstructures are shown. The slices are extracted from the analysed volume. They are taken at the same position in the reconstruction before and after segmentation. The phases are similar in both images. It shows that the thresholds have been well chosen for the segmentation. Now that each phase is identified, the main morphological properties can be extracted from the volumes.

2.2.2 Volume fractions

Before the volume analysis, the voxel size is increased by binning the voxels eight by eight from 25 nm to the physical image resolution of 50 nm. The decrease of the number of elements in the volume limits the computation time for the morphological and microstructural properties without altering the quality of the recorded image too much. The percolation of the phases is then calculated. It appears that the phases are almost totally continuous as the percolating ratio is higher than 98% for each phase. The volume fraction is determined by counting the number of voxels corresponding to each phase. For the LSCF electrode, the solid phase represents 55.4% of the volume, the remainder being the porosity. In the hydrogen electrode, YSZ holds 43.7% of the volume with a ratio of solid phase of about 60%. SEM images of the cermet have also been made. By thresholding these images, the volume fractions have been estimated. It has been found that the volume fractions are 42.5% for YSZ, 32.5% for Ni and 25.0% for porosity respectively. These values are close to the ones found by holotomography. The differences can be explained by the inhomogeneity over the cell thickness (Figure III.19). This validates our segmentation process.

2.2.3 Mean particle diameter and specific surface area

The mean particle diameter and the specific surface area of each phase are computed from the geometrical covariogram and the covariance function [Haas1967]. The first tool allows the specific surface area to be determined. The geometrical covariogram K is the intersection of a volume V with the same volume shifted by a distance h (Eq. (III.4) for calculation in x direction). The differentiation of K at the origin presents an interesting property. Indeed, this derivative is directly proportional to the specific surface area of the studied phase (Eq. (III.5)) [Usseglio2014]. This method has the advantage to be independent from the voxelization of the volume. No correction factor is necessary contrary to the specific surface area that can be calculated by counting the voxel surface at the interface between the phases [Rajon2002, Laurencin2012, Usseglio2014].

$$K(h) = \iiint k(x,y,z) \times k(x+h,y,z)dV \tag{III.4}$$

$$with\ k(x,y,z) = \begin{cases} 1\ if\ (x,y,z) belongs\ to\ the\ studied\ phase \\ 0\ if\ (x,y,z) does\ not\ belong\ to\ the\ studied\ phase \end{cases}$$

$$S_p = \frac{S_{area}}{V_{phase}} = -\frac{4}{V_{phase}} \times \left.\frac{dK(h)}{dh}\right|_{h=0} \tag{III.5}$$

The mean particle diameter is determined from the covariance function. This function represents the probability of two points separated by a distance h to be part of the same phase (Eq (III.6)) [Haas1967, Usseglio2014]. This property is directly related to the geometrical covariogram. The covariance is starting from the volume fraction ε of the phase and tends toward an asymptotic value of ε^2. The distance h at which the covariance function reaches its asymptotic value corresponds to a representative dimension of the phase. This calculation is done in the three space directions and the mean particle diameter corresponds to the mean of these values.

$$C(h) = P(x \in phase\ and\ (x+h) \in phase) \tag{III.6}$$

In the literature, several other solutions for the particle size measurement are proposed [Gelb1999, Holzer2011b, Ender2012]. It is also interesting to plot the Particle Size Distribution (PSD) of each phase to look if different particle diameters appear on the distribution. This effect is visible for example in Usseglio et al. [Usseglio2014] for porosity in a support of a cermet electrode, which presents two peaks (due to the use of pore-former). This method consists in evaluation the probability than a voxel belongs to the largest sphere. It should be noticed that the PSD gives a smaller value of the mean particle diameter than the covariance function as it is considering spherical particles [Holzer2011b, Usseglio2014].

2.2.4 Triple Phase Boundary length

Another very important property of the three phases electrodes is the Triple Phase Boundary length (TPB). It corresponds to the line where the ionic, electronic and gas phases meet each other. These lines play a major role in the electrode performance as the electrochemical reactions take place there. The length is calculated by counting the voxel's edges in contact with the three different phases [Vivet2011, Holzer2011b, Usseglio2014]. However, the TPB is overestimated with this method as it is considering cubic voxels. A correction factor of 1.455 has been proposed by Wilson et al. [Wilson2010] to take into account this problem. All the TPB presented in this work are corrected with this factor and are measured only on the percolating phases (as they are the electrochemically active phases).

2.2.5 Tortuosity factor

Finally, the last determined property is τ_{phase}, the tortuosity factor of the phase. The tortuosity factor includes the geometrical tortuosity as well as a constriction parameter. The geometrical tortuosity is the ratio of the effective length and the shortest length as illustrated on Figure III.17a [Kishimoto2011]. The constriction corresponds to the bottleneck effect between two particles as illustrated in Figure III.17b [Holzer2013].

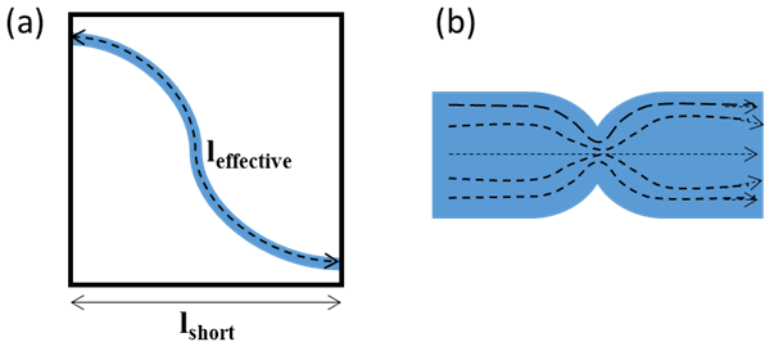

Figure III.17 - Schematic representation of (a) the geometrical tortuosity and (b) the tortuosity due to the bottleneck

This parameter is deduced from the computation of the effective diffusion coefficient D_{phase}^{eff} which is determined by using a classical homogenization technique [Kanno2011, Laurencin2012, Usseglio2014, Laurencin2015]. Once the effective diffusivity determined, it is possible to express the tortuosity factor with the relation:

$$\tau_{phase} = \varepsilon_{phase} \frac{D_{phase}}{D_{phase}^{eff}} \quad \text{(III.7)}$$

2.2.6 Summary of the microstructural properties

All the microstructural and morphological properties presented before have been computed for the oxygen and hydrogen electrodes. The Ni-YSZ electrode 3D volume (27.5x27.5x27.5 μm^3) has been divided into eight independent iso-volumes for the calculations of the properties to estimate the error whereas the whole LSCF electrode has directly been analysed as the volume is smaller (22.5x22.5x22.5 μm^3). The data are summarized in Table III.2 and Table III.3.

Table III.2 : Microstructural properties calculated on the hydrogen reference electrode 3D volume.

Properties	Phase	Hydrogen reference electrode
Percolated volume fraction (-)	Porosity YSZ Ni	0.28 ± 0.014 0.436 ± 0.003 0.262 ± 0.013
Mean particle diameter (µm) with covariance	Porosity YSZ Ni	0.96 ± 0.06 0.60 ± 0.00 1.01 ± 0.03
Mean particle diameter (µm) with PSD	Porosity YSZ Ni	0.416 0.368 0.480
Specific surface area (μm^{-1})	Porosity YSZ Ni	2.48 ± 0.07 3.62 ± 0.03 2.09 ± 0.09
Tortuosity factor (-)	Porosity YSZ Ni	8.46 2.27 7.45
TPB length density (μm^{-2})		4.75 ± 0.08

Table III.3 : Microstructural properties calculated on the oxygen reference electrode 3D volume.

Properties	Phase	Oxygen reference electrode
Percolated volume fraction (-)	Porosity LSCF	0.444 0.556
Mean particle diameter (µm) with covariance	Porosity LSCF	0.5 0.45
Mean particle diameter (µm) with PSD	Porosity LSCF	0.390 0.448
Tortuosity factor (-)	Porosity LSCF	2.05 2.03
Specific surface area (μm^{-1})		3.38

To be representative of the whole electrode, it is necessary to analyse a sufficiently large volume. This is named the Representative Volume Element (RVE). The RVE is different

according to the microstructure and the analysed properties [Harris2015a, Harris2015b, Laurencin2012, Usseglio2014]. An estimation of the RVE has been done for the two kinds of electrodes by looking at the volume fraction of the porosity. The evolution of the mean value of the pore volume fraction as a function of the volume size is plotted on Figure III.18. The minimum and maximum value as well as the standard deviation of the independent iso-volumes are also presented on this Figure. The standard deviation becomes negligible for the LSCF electrode from a volume with an edge of 8 µm. This dimension can be considered as the RVE of this electrode. For the Ni-YSZ porous electrode, the RVE is around $15 \times 15 \times 15$ µm^3. It can be noticed that the domain size corresponds to about 15 times the mean particle diameter. This result is consistent with the rule proposed in [Harris2015a, Harris2015b, Metcalfe2010]. Since the analysed 3D volumes are larger than the RVE, the uncertainty in the computed microstructural parameters should be very low.

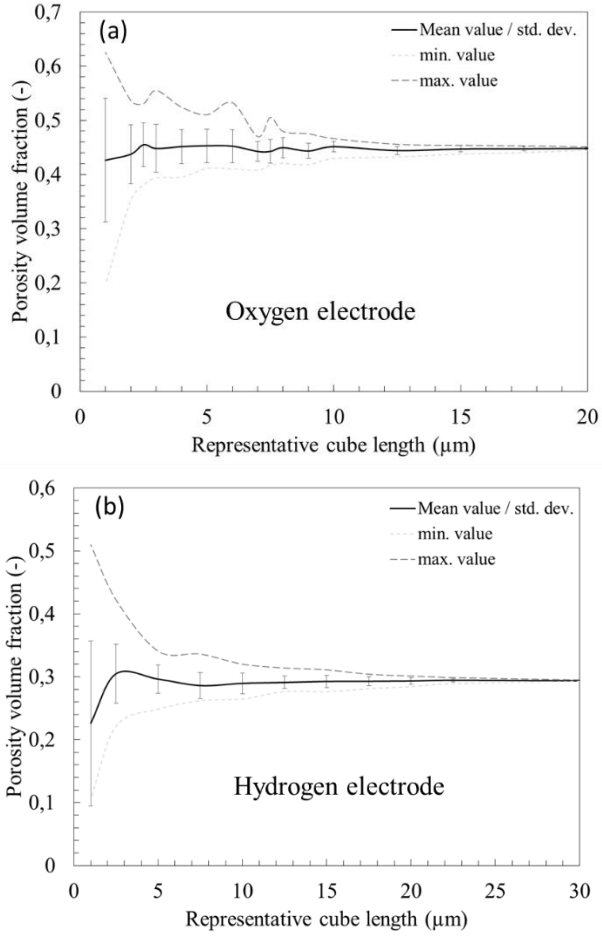

Figure III.18 – Estimation of the Representative Volume Element from the porosity volume fraction for (a) the oxygen electrode and (b) the hydrogen electrode. The RVE can be estimated around 8 µm for the LSCF and 15 µm for the Ni-YSZ.

Nevertheless, it has been observed on SEM images that the microstructure is not homogeneous over the entire electrode thickness. Indeed, in Figure III.19, some small differences are visible according to the area. These differences can be explained by the manufacturing of the electrode.

As the electrode is made by successive layer deposition, the microstructure is not perfectly homogeneous. This can explain a standard deviation in the measured morphological properties such as the volume fraction.

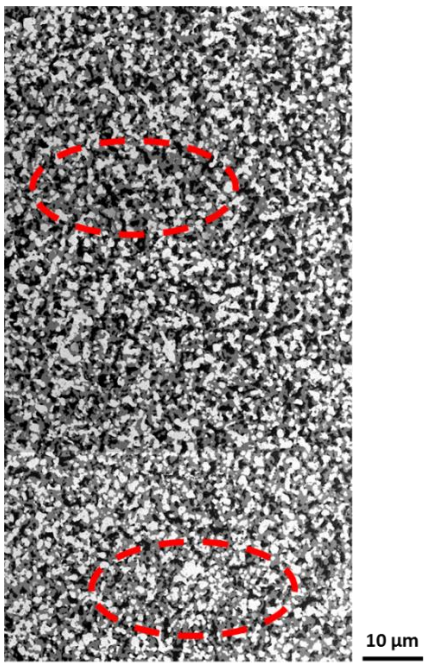

Figure III.19 – SEM image of the cermet (black=porosity, grey=YSZ, white=Ni). The red circles highlight areas with visible variation in the composition.

3. Conclusions of this chapter

In this chapter, the improvements of the nano-holotomographic measurements have been presented. The implementation of a new beamline dedicated to the nano-imaging is of great interest to improve the 3D reconstructions quality. It offers a high X-ray energy option of 33.6 keV well adapted to absorbing SOC materials. The reliability of the global process for holotomography has been improved. This enhancement is possible thanks to a new sample preparation method. Indeed, a Focused Ion Beam using Xenon ions has been used. The sample geometry and size are now perfectly controlled. Moreover, the holotomographic acquisition and reconstruction have also been improved. By doing a random motion during the scan all ring like artefacts are eliminated. They originate from the complex mixing between the inhomogeneous incident wave and the object. A phase retrieval procedure based on a multi-distance Paganin's method, followed by 10-15 constrained CGM iterations, was shown to give consistently good results.

A second milestone is the improvement of the spatial resolution. A specific attention has been paid to this measurement. It has been shown in this chapter that the spatial resolution of holotomographic reconstructions has been improved from 80 nm to 50 nm. This improvement seems modest, but together with the increased reliability it allows systematic studies of the evolution of the fine electrode microstructures. Moreover, the 3D volumes are large and representative of the whole electrode microstructure, as shown by the calculated RVEs.

Finally, classical tools developed at CEA for the 3D analysis of the microstructural and morphological properties are used for pristine electrodes. These values are in agreement with the ones obtained from SEM images. As the characterization tool is now ready, the microstructural investigation can be led to investigate the microstructure evolution on aged samples.

Chapter IV:

Long-term electrochemical tests and post-mortem characterizations

As detailed in the previous chapter, the X-ray nano-holotomography experimental protocol has been adapted for SOC microstructural characterization. This protocol has been used to investigate the electrode microstructural evolution upon operation. For this purpose, a set of long-term tests has been performed in the objective to identify the operating parameters affecting the electrochemical degradation.

In this chapter, the experimental set-up is described from the test bench main features to the start-up and shut-down procedures. Then, the electrochemical long-term tests are presented by starting with the initial performances, the selected test conditions for ageing and the degradation rates. The most striking results, which can be inferred from the regular electrochemical measurements carried out on aged cells, are detailed hereafter. Finally, the fine post-mortem characterizations are reported to highlight the effect of the operating parameter on the electrode microstructural evolution.

1. Experimental set-up description

1.1 Test bench

The electrochemical tests have been performed on test bench dedicated to the electrochemical assessment of single cell. As depicted on Figure IV.1, the test bench presents a geometry with a radial co-flow configuration. The set-up is adapted to operate in fuel cell or electrolysis mode.

The cell housings are made of Crofer22APU without coating. Despite the possible chromium poisoning, the metallic supports present several interesting advantages for the long-term testing. First of all, the metallic set-up is able to withstand thermal cycles without any large cell degradation. More precisely, it has been checked the accumulation of more than 25 thermal cycles does not lead to any fatal electrolyte failure or crack in the glass seal. Only a degradation of 2 mV per cycle (measured at 0.5 A/cm², FU=60%) has been found that would be related to a slight electrode deterioration and/or a damage of the electrode current collection [Rinaldi2015]. Furthermore, as shown on Figure IV.1, the metallic housing allows connecting easily the power supply to the set-up. It is worth noting that dry air was used for all the experiments in order to limit the issue related to the Cr release from the metallic interconnect [Fergus2005, Shuler2012]. Indeed, in this condition, the degradation induced by the Cr electrode poisoning is expected to be rather negligible over an operating period of more than 2000 hours [Ghezel2013].

In the test bench, the gas and electrical distributions are ensured by gold and nickel grids of 100 mesh.cm^{-2} at the oxygen and hydrogen electrode sides, respectively. As shown in Figure IV.1, weights corresponding to an applied pressure of 400 g.cm^{-2} have been put for the experiments on the oxygen support to improve the electrical contacts between the grids and the electrodes. The cell voltage is measured by gold wires that are welded on the gold grid or the metallic support for the O_2 and H_2 electrode respectively. The thermal control of the experiment is guaranteed by a thermocouple located close to the cell in the hydrogen gas outlet. A second measurement is done in the furnace near the set-up.

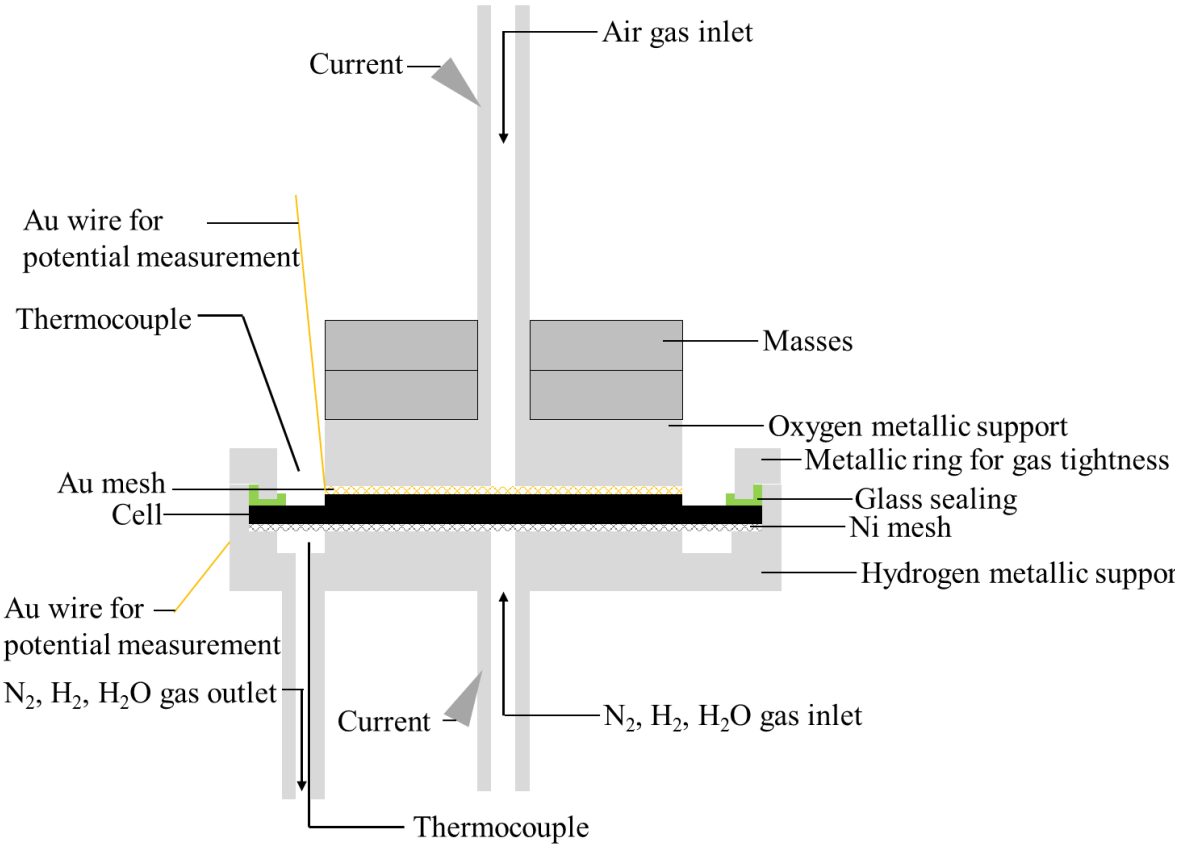

Figure IV.1 – Schematic representation of the experimental set-up near the cell

For both electrodes, the gases are introduced in the centre and are distributed with a radial co-flow configuration on the cell active area of 9 cm^2. Mass flow controllers are used for the gas delivery. The oxygen electrode is fed with dry air which is released in the furnace at the exit of the cell. At the hydrogen electrode side, N_2 and H_2 are available for gas distribution. The gas tightness of the hydrogen compartment is ensured by a glass-ceramic seal deposited all around the cell edge. The steam is produced by a bubbler (Figure IV.2) which is a common equipment in literature [Aaberg1998, Park2010, Hauch2011, Zhang2013b]. It consists of a porous element inside a metallic container filled of water. The carrier gas is introduced by the bottom of the tank and small bubbles are distributed in the porous element. The proportion of steam in the gas flow is controlled by the humidifier temperature. Thermocouples allow the water and vapour phases temperatures to be controlled. A pressure sensor is added on the humidifier to follow the inhomogeneity in the steam flow. To limit this effect, a buffer volume is connected to the bubbler (Figure IV.2). The gas inlet pipe is heated up to 110°C until the cell support to avoid water condensation. At the cell outlet, a condenser allows water to be recovered and weighed. The gases are carried away in an air vent.

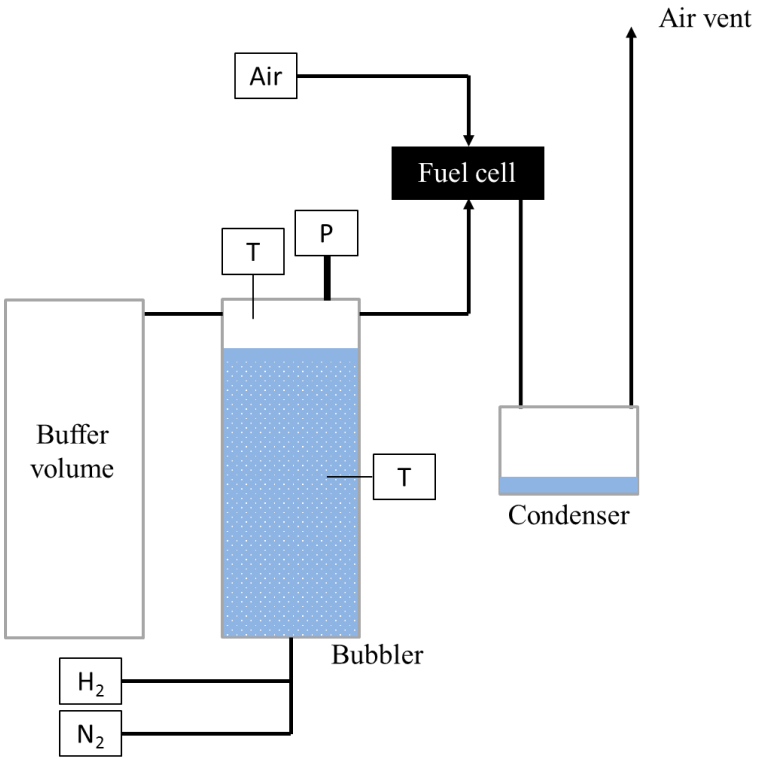

Figure IV.2 – Schematic representation of the complete test bench

On the test bench, the temperature and gas flow rate are driven with the supervision software RSView®. All the data are automatically saved for each seconds. In addition, supervision allows the automation of procedures such as heating or Ni reduction. Security procedures can also be defined in case of alarms.

1.2 Electrochemical performance measurements

Two kinds of measurement have been done to evaluate the cell performances. The first one is the polarisation curve and the second one is the Electrochemical Impedance Spectroscopy (EIS). The specificities related to both the device and the conditions used for the measurements are detailed hereafter.

1.2.1 Polarisation curve

The polarisation curve consists in plotting the current density as a function of the cell potential. A potentiostat/galvanostat (Autolab PGSTAT-302N) equipped with a FRA2 module and a 20 amps current booster has been used during the experiments. The i-U curves have been measured in galvanostatic mode with a sweep rate of 10 or 20 $mA.s^{-1}$. This sweep rate is a good compromise between a fast enough data acquisition and a sufficiently low scanning rate to consider the stationary conditions to be fulfilled.

1.2.2 Electrochemical Impedance Spectra (EIS)

The EIS is a technique used to separate and identify in the frequency domain the contributions coming from the electrochemical and transport processes occurring in the cell. It is based on the measurement of the system response to a small periodic perturbation in current *i* or voltage *U* [Barsoukov2005, Nechache2014]. The cell linear impedance *Z(f)=U/i* is then evaluated for different frequencies *f* of the applied signal.

For the tested cells, the data have been recorded in galvanostatic mode. It means that an alternative current perturbation i_{ac} is imposed on the operating direct current density i_{dc}. The cell voltage response is then recorded to evaluate the impedance *Z(f)*. The same device than the one used for the polarisation curve measurements was employed for the EIS acquisition, while the NOVA software was used as interface with the equipment. The half-amplitude of the sinusoidal current density perturbation has been chosen at ±22 $mA.cm^{-2}$ and a frequency range comprised between 10^5 Hz and 10^{-2} Hz has been investigated. One can note that the amplitude of the applied signal was adapted to fulfil the small perturbation assumption in order to obtain a linear response of the system. Before starting the electrochemical characterization, the system was stabilized 2 minutes at the direct current density i_{dc} considered for the EIS data acquisition.

1.3 Start-up and shutdown procedure

The same starting-up procedure has been defined and followed for all the tested cells. The temperature is initially increased to 900°C for the sealing pre-treatment with a rate of $1^{\circ}C.min^{-1}$ to limit the thermal gradient inside the cell. During the heating up, the O_2 and H_2 electrodes are swept under air and nitrogen respectively with flows of 0.5 $NL.h^{-1}$. After 30 minutes at 900°C, the temperature is reduced to 860°C for a 90 minutes' step in order to finalise the thermal treatment of the glass seal. The cell is lastly cooled down to 800°C for the next start-up phase.

Before starting the electrochemical experiments, it is required to reduce the nickel oxide of the cermet into Ni. This procedure is carried out at 800°C by replacing step by step the nitrogen gas flow by hydrogen according to the protocol given in Figure IV.3. Once under pure hydrogen, the cermet is maintained under this highly reducing condition during 2 hours to complete the full Ni reduction. The cell voltage is usually stabilized after the treatment and can be compared to the expected Open Circuit Voltage (OCV) which is a good indicator of both the full cermet reduction and the gas tightness of the hydrogen compartment. For all the experiments, a difference of less than 8% was obtained between the experimental and theoretical OCV meaning that the Ni contained in the cermet was fully reduced and the H_2 hydrogen compartment was fully gas tight (cf. Table IV.1).

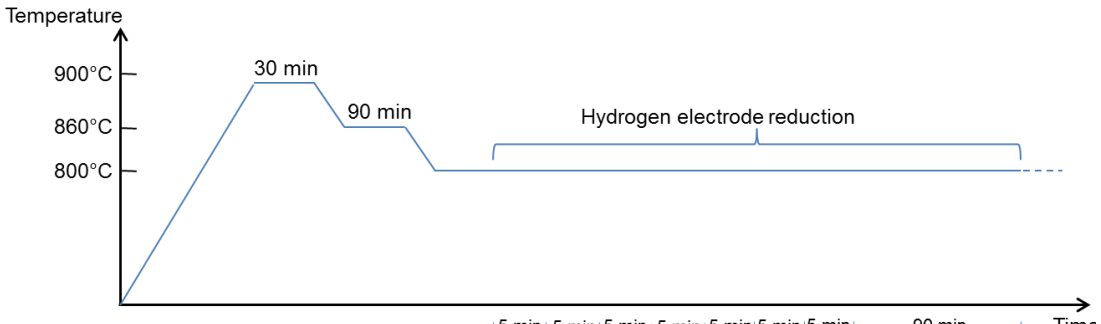

		5 min	5 min	5 min	5 min	5 min	5 min	5 min	90 min
Hydrogen electrode									
N_2 (10^{-6} mol.s^{-1})	6.2	49.6	43.4	37.2	24.8	12.4	0.0	0.0	0.0
H_2 (10^{-6} mol.s^{-1})	0.0	0.0	6.2	12.4	24.8	37.2	49.6	63.6	63.6
Oxygen electrode									
Air (10^{-6} mol.s^{-1})	6.2	49.6	49.6	49.6	49.6	49.6	49.6	63.6	280.1

Figure IV.3 – Starting-up procedures for the cells including glass sealing treatment and hydrogen electrode reduction.

Note that all the experiments were started with the humidifier emptied of water. If steam was required for the durability test, the container was filled with water only after the hydrogen electrode reduction step. The bubbler temperature was then increased to obtain the required ratio of H_2/H_2O.

When the long-term test was completed, the cell was cooled down to room temperature at a rate of -1°C.min^{-1}. Anodic and cathodic gas flows were lowered to 2 NL.h^{-1} by keeping an air sweeping condition for the O_2 electrode whereas a mixture of nitrogen and hydrogen with a N_2/H_2 ratio of 97/3 was used at the hydrogen electrode side. Thanks to this shutdown procedure, all the cells were retrieved without any mechanical damage or oxidation of the cermet. The cells were finally removed from the support by cutting the border with a diamond pen.

2. Electrochemical degradation tests

A series of long-term tests have been performed on the studied cell. The initial performances have been systematically obtained in identical conditions to check the cell reproducibility. The durability test conditions have been selected to highlight the main impacting parameters. The degradation rates are reported in the next section. An analysis of the cell polarisation curves measured during the ageing test is then proposed. Finally, a tentative analysis of impedance diagrams is presented.

2.1 Initial performances

The initial performances of the tested cells should be similar as they come from the same manufacturing batch. For all the tested cell, a polarisation curve was recorded at 800°C under dry hydrogen and air. The gas flows were 3.16 NL.h^{-1} and 22.6 NL.h^{-1} at the H_2 and O_2

electrode respectively. In Figure IV.4, a typical cell polarisation curve is presented. As a general matter, the characteristics of the i-U curve given in Figure IV.4 is found to be consistent with the ones expected for this kind of cells [Wuillemin2014]. This result allows validating the start-up protocol (heating, cermet reduction…) and the experimental set-up regarding the test performance. Moreover, the cells exhibit quite good performances meaning that they are well representative of the current best SOEC/SOFC technology.

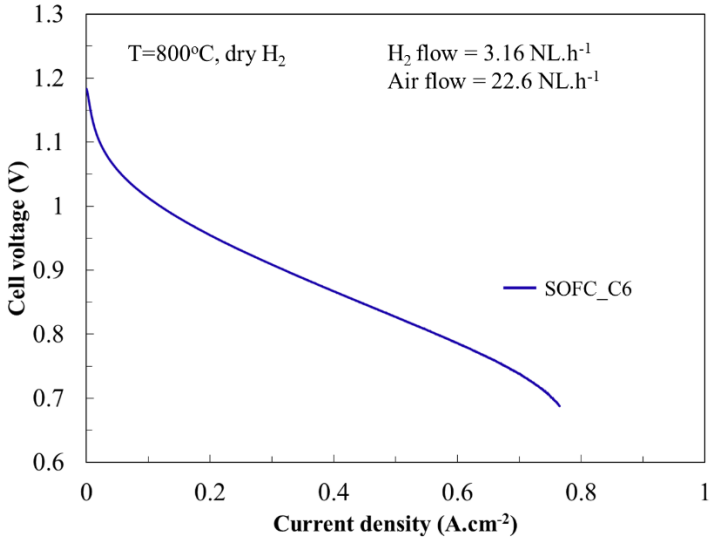

Figure IV.4 – Initial polarization curve in fuel cell mode of cell SOFC_C6 after cermet reduction at 800°C.

More precisely, the OCVs for the 6 tested cells are given in *Table IV.1*. As already stated, they are close to the theoretical value of 1.186 V (at 800°C for dry H_2 with 0.5% of residual steam) indicating a good cermet reduction and gas tightness of the anodic sealing. It can be mentioned that the cells from SOEC_C1 to SOFC_4 present a lower OCV than SOFC_5 and SOFC_6. That lower values are explained by a higher residual humidity in the inlet gas circuit (bubbler and buffer volume). By looking at the potential measured at 0.5 A.cm^{-2}, it can be seen that all the cells give a similar result (*Table IV.1*). The standard deviation on these measurements is about 8 mV. The ohmic resistance R_s given in *Table IV.1* correspond to the electrolyte and contact resistance measured with EIS at 0.5 A.cm^{-2}. The cells SOFC_C5 and SOFC_C6 have a higher ohmic resistance that can be explained by a lower mass pressure was applied in these cases (330 g.cm^{-2} instead of 400 g.cm^{-2}). All these results are consistent and validate the test bench reproducibility.

Table IV.1- Initial performances measures at 800°C under dry hydrogen for the tested cells.

Cell	OCV (V)	U (V) (@0.5 A.cm^{-2})	R_s (Ω.cm^2)
SOEC_C1	1.134	0.847	0.136
SOEC_C2	1.094	0.832	0.134
SOEC_C3	1.109	0.836	0.140
SOFC_C4	1.093	0.843	0.135
SOFC_C5	1.183	0.827	0.180
SOFC_C6	1.183	0.827	0.192

2.2 Durability tests

2.2.1 Test conditions

A set of long-term durability tests have been performed with different operating conditions. The experimental parameters have been selected to understand their effect on the degradation. All the experimental conditions are summarized in Table IV.2. The polarisation mode chosen for the ageing is indicated in the name of the sample. The green colours are related to cells tested in electrolysis whereas the blue colours refer to fuel cell mode. Tests have been performed in galvanostatic condition at current densities varying between -0.5 $A.cm^{-2}$ and -0.75 $A.cm^{-2}$ in electrolysis and 0.5 $A.cm^{-2}$ and 0.67 $A.cm^{-2}$ in fuel cell mode. The temperature has been mainly set at 850°C to enhance thermally activated mechanisms liable to produce cell degradation. One test was performed at 750°C to identify the effect of this parameter on durability and microstructural evolutions.

Table IV.2 – Overview of tested cells operating conditions and ageing time

Test name	Temp. (°C)	H_2/H_2O	SC/FU (%)	*j* ($A.cm^{-2}$)	Ageing time (h)
SOEC_C1	850	50/50	60	-0.5	1500
SOEC_C2	850	50/50	60	-0.5	2000
SOEC_C3	850	50/50	60	-0.75	2400
SOFC_C4	850	50/50	60	+0.5	1000
SOFC_C5	850	100/0	80	+0.66	1200
SOFC_C6	750	100/0	60	+0.5	9000

For all tested cells, the air flow at the O_2 electrode has been adapted to keep an air conversion rate of 20%. This low value has been chosen to limit the oxygen partial pressure gradient along the cell radius. For the hydrogen electrode, four tests have been performed with a gas composition ratio H_2/H_2O=50/50 and flow rates of 6.32 $NL.h^{-1}$ (C1, C2 and C4) or 9.48 $NL.h^{-1}$ (C3). This ratio allows the same OCV to be reached whatever the polarisation selected for the ageing. In other words, the effect of electrolysis or fuel cell mode can be directly compared at this composition. The two other tests were operated under dry hydrogen with a flow rate of 3.16 $NL.h^{-1}$. It should be noticed that all the experiments have been done over more than thousand hours.

2.2.2 Long-term tests

On Figure IV.5, the cell voltage evolution over time is plotted for the cells aged with a ratio H_2/H_2O=50/50. The initial points are different as the operating conditions changed according to the cells. It can be noticed that the curves are oscillating with an amplitude of about 20 mV in electrolysis and 5 mV in fuel cell mode during the test. This effect is directly linked to the humidifier which generates a non-perfectly continuous steam flow. This phenomenon has also

been seen in other studies using bubbler or evaporator [Schefold2012, Schefold2015, Shimada2016]. A transient period of about 200h can be observed before a linear evolution of the cell overpotential. For all these cells, the overpotential evolution over time is found to be limited after the transient period.

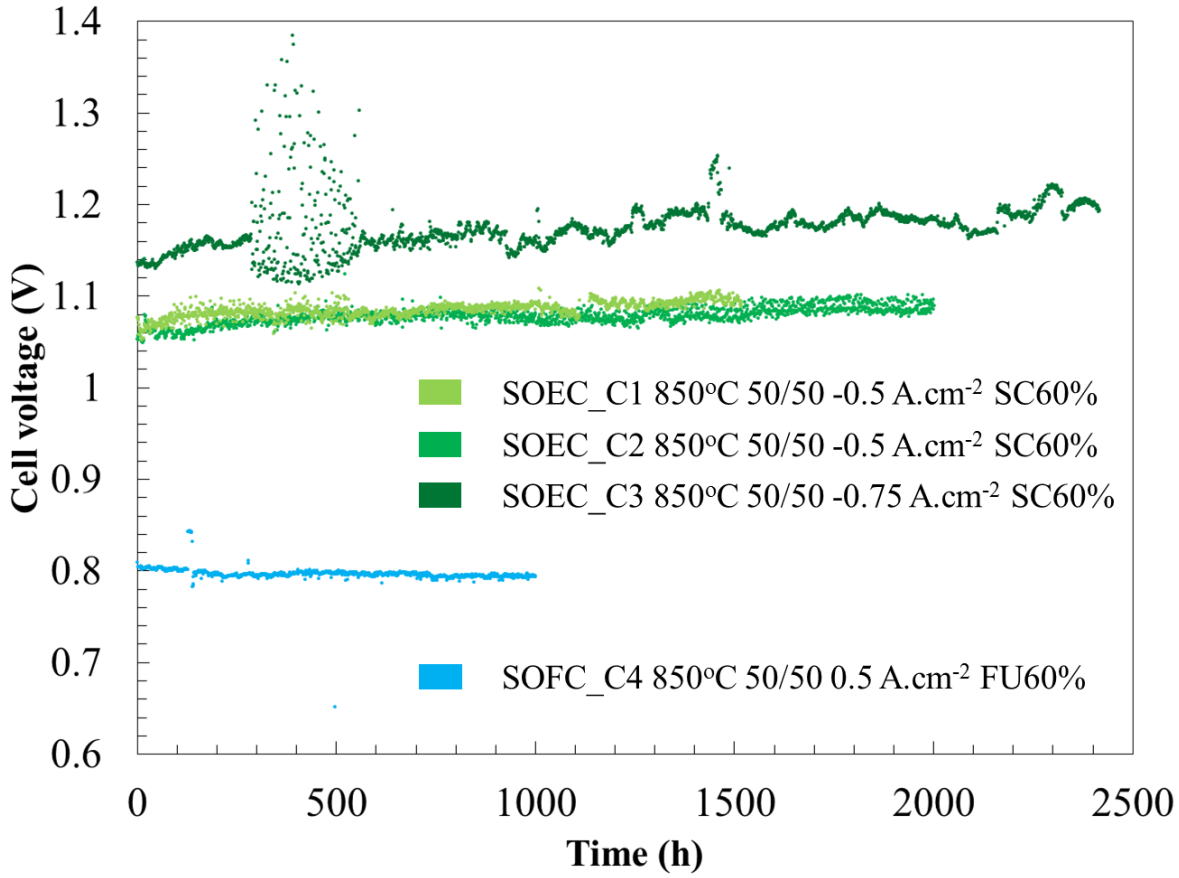

Figure IV.5 – Cell voltage evolution over time for durability tests performed under H_2/H_2O=50/50.

Other tests were performed in fuel cell mode under dry hydrogen atmosphere. Their cell voltage evolutions are shown on Figure IV.6 with the cell SOFC_C4 previously presented. The cell SOFC_C5 presents a high degradation that can tentatively be attributed to the severe operating conditions chosen in that case (FU 80%). The last test SOFC_C6 was done in collaboration with Bertrand Morel. This cell was aged at lower temperature (750°C) and during more than one year (9000h). Some test interruptions are visible but they are not detrimental for the cell life. A period of 300h at 80% FU is also observable after 1000h of ageing. It can be noticed that the cell voltage evolution is not critically evolving during 9000h. The other tests stopped after a shorter duration should thus be representative of the cell degradation over this long period of around 1 year.

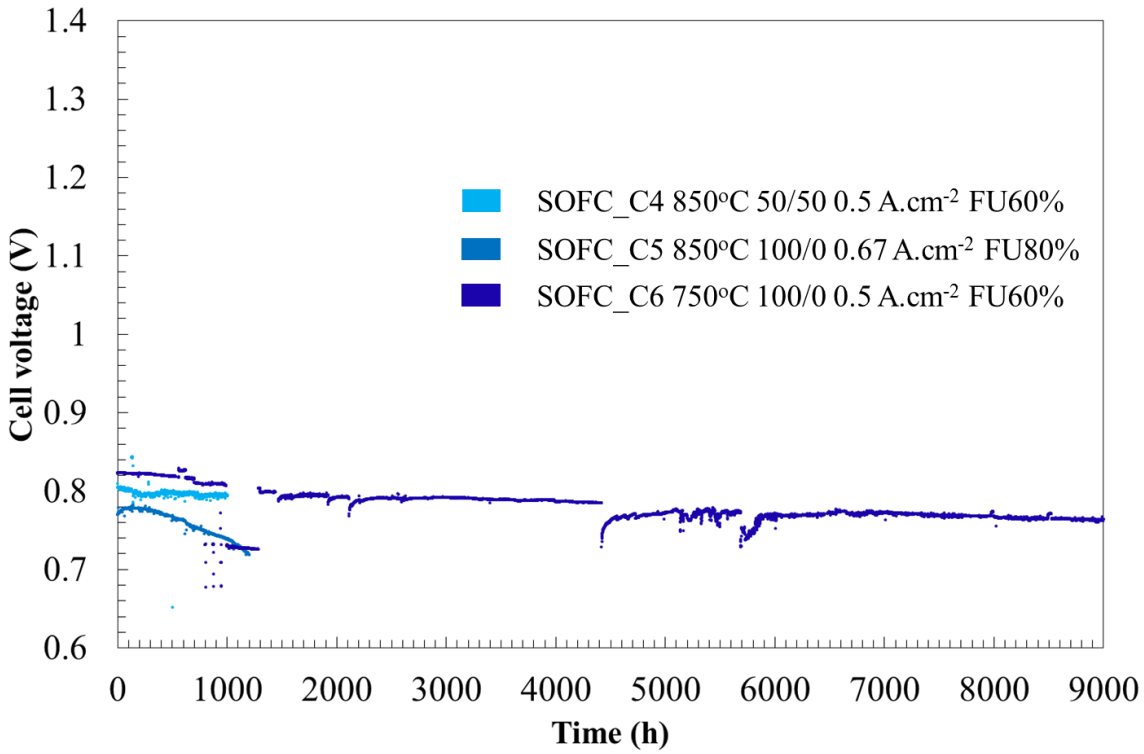

Figure IV.6 – Cell voltage evolution over time for durability tests in fuel cell mode.

2.2.3 Degradation rate results

For all the tested cells, the degradation rates have been measured after the transient period of ~200 hrs that is to say on the linear parts of the curve. The data are all summarised in Table IV.3. Note that for the cell SOFC_C6, two values of degradation rates are given. Indeed, two periods are visible on the curve plotted in Figure IV.6. The first one lasted 2000h whereas the second one went to the end of the test with a lower degradation rate.

The uncertainties given for the degradation rates stem from the noise on the recorded raw data (see Figure IV.5 and Figure IV.6). It can be noticed that the degradation rates are very limited and are among the best results published in the literature, especially in SOEC mode [Schefold2015, The2015, Trofimenko2015].

Table IV.3 – Degradation rates measured on the total curve or linear part for the tested cells.

Test name	Degradation rate (mV.kh^{-1})	Degradation rate (%.kh^{-1})
SOEC_C1	9.7 ±2.0	0.90 ±0.2
SOEC_C2	8.8 ±1.0	0.84 ±0.1
SOEC_C3	15.8 ±3.0	1.39 ±0.3
SOFC_C4	3.5 ±1.0	0.43 ±0.1
SOFC_C5	57.2 ±2.0	6.96 ±0.2
SOFC_C6	(1) 13.5 ±0.5 (2) 4.1 ±1.0	(1) 1.64 ±0.1 (2) 0.50 ±0.1

From the degradation rate measurements, some discussions are possible on the "apparent" degradation of cells. The term "apparent" is specified to do the difference with the intrinsic cells degradation. The following statements can be inferred from the degradations rates given in Table IV.3:

- SOEC_C1 and SOEC_C2 are operated in the same operating conditions (-0.5 $A.cm^{-2}$). As expected, their degradations rates are found to be similar. It can thus be concluded that the durability tests are reproducible.

- The test performed in electrolysis at -0.75 $A.cm^{-2}$ (SOEC_C3) presents a higher cell voltage increase. In other words, it appears that the "apparent" degradation in electrolysis mode is more pronounced with a higher current density. This result is consistent and confirmed by many studies already reported in fuel cell mode [Hagen2006, Zhang2013, Sun2015].

- The cell SOFC_C4 was tested in fuel cell mode with comparable test conditions than cell SOEC_C1 and SOEC_C2 in terms of temperature, inlet gas compositions and current density. It is found that the "apparent" degradation is significantly lower in fuel cell mode than in electrolysis mode. This statement indicates that an operation under electrolysis current is liable to induce larger degradation in the cell layers. This result is found to be in good agreement with the study of Zhang et al. [Zhang2013] dedicated to the durability evaluation of reversible solid oxide cells.

- As expected, the cell SOFC_C5 aged with the most severe operating conditions, that is to say at the highest fuel utilisations (80%), exhibits the highest degradation rate. As for the effect of current density parameter, this result means that the highest is the fuel utilisation, the highest would be the "apparent" degradation rate. This statement has been already reported in many studies performed in fuel cell mode [Koch2006, Yokokawa2008]. Nevertheless, in our case, it is suspected that the very high degradation rates measured at 80% could be related to a non-homogeneous gas distribution on the electrode surface. Indeed, in this case, some part of the cell surface could be operated at fuel utilisation approaching or even exceeding 100%. This local high fuel utilisation is assumed to accelerate the material degradation, and hence, should explain the rather big performance loss reported in Table IV.3 for SOFC_C5.

- The last durability experiment SOFC_C6 presents a rather low degradation rate over a period of more than 1 year. It worth reminding that this test was performed at a lower temperature than the others (i.e. 750°C instead of 850°C). However, despite a lower operating temperature, the "apparent" degradation rate is found to be slightly higher to the one obtained in similar conditions but at higher temperature (see degradation rate for SOFC_C4 operated at 850°C, $0.5A.cm^{-2}$ and FU=60%). This unexpected result has been already reported by other authors [Hagen2006, Diethelm2013, Fang2015, Kotisaari2016] and is still not understood.

All these results have shown effects of operating parameters on the "apparent" degradation. It is necessary to use other characterization techniques to analyse more finely the "intrinsic" cell degradation. The analysis of the polarisation curves and electrochemical impedance spectra is proposed hereafter.

2.3 Analysis of polarisation curves

Besides the overpotential evolution over time, regular electrochemical characterizations have been performed during the long-term tests. In particular, the polarisation curves of cells have been measured after different ageing time. For the experiments done with a ratio H_2/H_2O of 50/50, the i-U curves have been plotted in fuel cell and electrolysis mode whatever the ageing conditions. The effect of the operating parameters can thus be compared.

The polarisation curves before and after 1000h ageing of cell SOFC_C4 are presented on Figure IV.7a. A first observation is a higher apparent degradation in electrolysis than in fuel cell mode. To illustrate this tendency, the potential evolution at ±0.5 A.cm^{-2} is highlighted on Figure IV.7a. The cell voltage evolution is about three times higher in electrolysis compared to fuel cell mode. The same curves for SOEC_C2 aged in electrolysis are presented on Figure IV.7b. Similar observations can be done with a factor three between the degradation rates in both modes. The difference between the cell voltage evolution upon ageing measured in fuel cell and electrolysis could come from this non-symmetric behaviour.

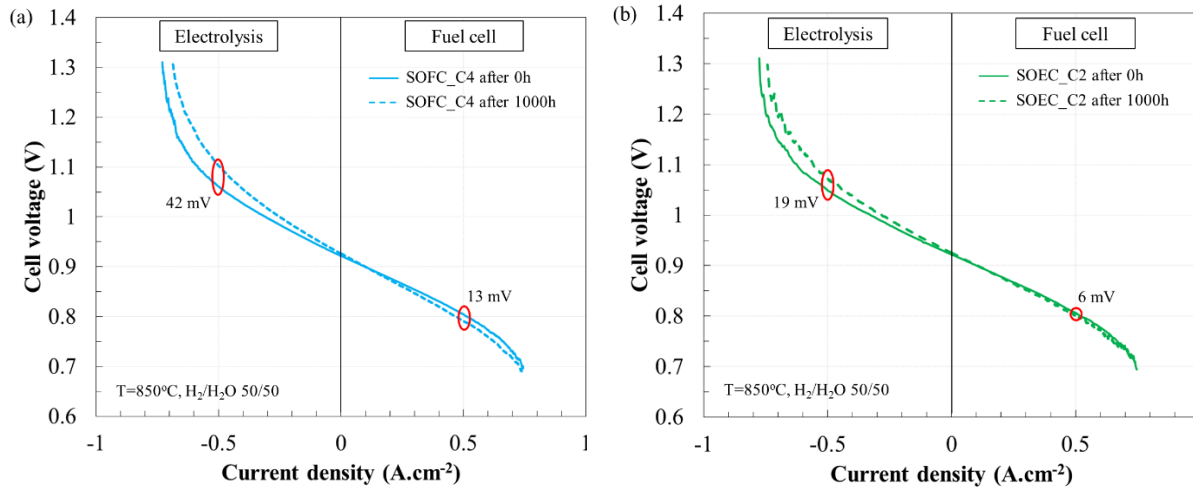

Figure IV.7 – Polarisation curves in both modes after 0h (continuous line) and 1000h (dashed line) for (a) SOFC_C4 and (b) SOEC_C2. The degradations at ±0.5 A.cm^{-2} are detailed on the graphs (red circles).

The effect of current density on the degradation can also be studied with the polarisation curves. They have been are plotted on Figure IV.8 for SOEC_C3 at the beginning and after 2000h. At the operating current density (-0.75 A.cm^{-2}), the degradation rate is found to be close to the value obtained from the overpotential evolution over time (15.8 mV.kh^{-1} vs 18 mV.kh^{-1}). At the "classical" current density of -0.5 A.cm^{-2}, the degradation rate is estimated at about 9 mV.kh^{-1}. This value is consistent with the ones obtained for SOEC_C1 and SOEC_C2 aged in the same conditions (8.8 mV.kh^{-1} and 9.7 mV.kh^{-1}). Comparing these tests, it comes that the degradation tends to be the same whatever the current density during the long-term test. In other words, the intrinsic degradation of cells would be similar whatever the operating current density.

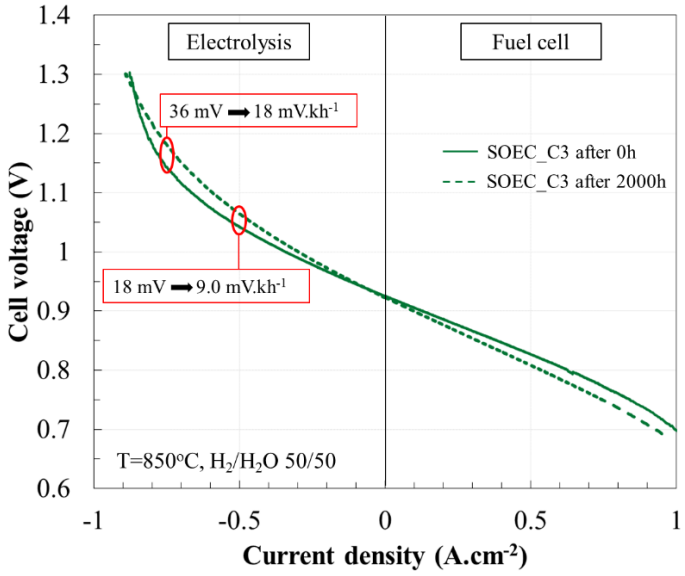

Figure IV.8 – Polarisation curves for SOEC_C3 after 0h (continuous line) and 2000h (dashed line). The degradation rates at -0.75 A.cm^{-2} and -0.5 A.cm^{-2} are detailed on the graph.

2.4 Analysis of Electrochemical Impedance Spectra

As for the polarisation curve, regular EIS have been recorded during the durability tests at a direct current density i_{dc} of ±0.5 A.cm^{-2} with gas composition ratio H_2/H_2O=50/50. Unfortunately, the steam flow instability does not allow well shaped spectra to be plotted. EIS recorded before ageing at i_{dc}=+0.5 A.cm^{-2} between SOEC_C2 and SOFC_C6 are compared on Figure IV.9. The spectra obtained with dry hydrogen is clearly better defined than the one recorded under humidified gas at the H_2 electrode. In the following the analysis of EIS are thus limited to qualitative observations in the high frequency range.

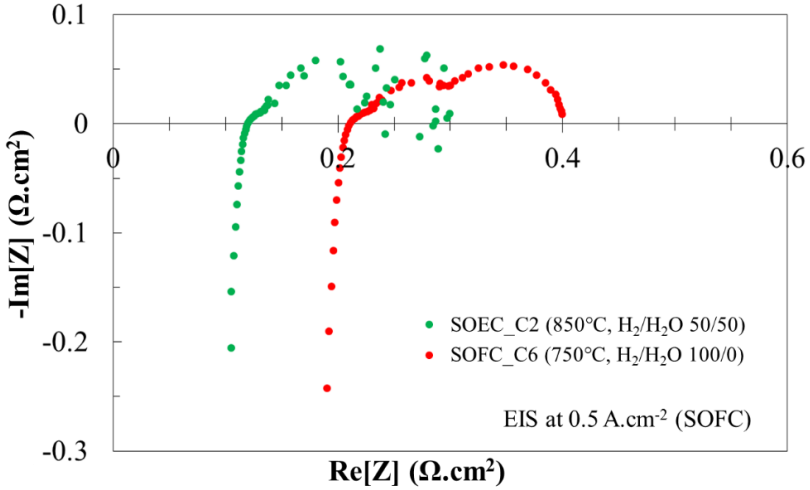

Figure IV.9 – Initial EIS at i_{dc}=+0.5 A.cm^{-2} (SOFC) for cells SOEC_C2 (green) and SOFC_C6 (red). The spectrum obtained under dry hydrogen is better defined.

Despite the poor quality of EIS, a qualitative observation can be done for cell tested with H_2/H_2O=50/50. On Figure IV.10, a comparison between EIS recorded before and after ageing of cell SOFC_C4 in both polarisations is proposed. Figure IV.10a corresponds to the fuel cell mode. It is difficult to see any clear evolution. Indeed, the shift after operation of the high frequency intercept with the real axis could be ascribed to an increase of the electrolyte

resistance or to an artefact (due to the convolution of the high frequency semi-circle with the inductance induced by the wires). On Figure IV.10b, the spectra recorded in electrolysis mode are proposed. There is a visible increase of the contribution at the beginning of the spectra corresponding to the high frequencies which are usually attributed to a charge transfer process [Jiang1999b]. In our case, the charge transfer process seems to be affected by the 1000h operation.

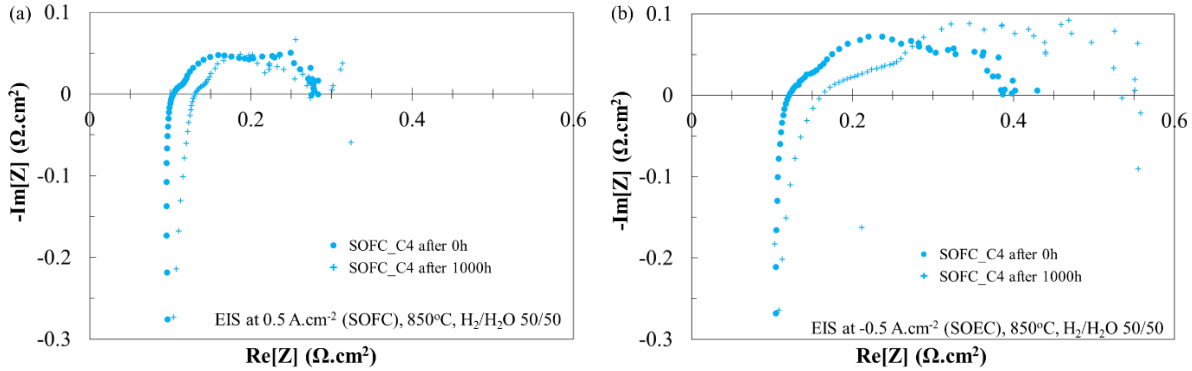

Figure IV.10 – Electrochemical Impedance Spectra of SOFC_C1 after 0h (dot) and 1000h (cross) (a) at 0.5 A.cm^{-2} and (b) at -0.5 A.cm^{-2}. There is a clear increase of the high frequency contribution in SOEC mode.

The same EIS are shown on Figure IV.11 for a cell aged in electrolysis (SOEC_C2). Here again, hardly any difference can be found in SOFC mode whereas there is a clear increase of the high frequency contribution for spectra recorded in SOEC mode. From these observations, it can be suggested that degradation phenomenon impacting a charge transfer mechanism would be more visible in electrolysis mode. In other words, it would become more critical for electrolysis reactions.

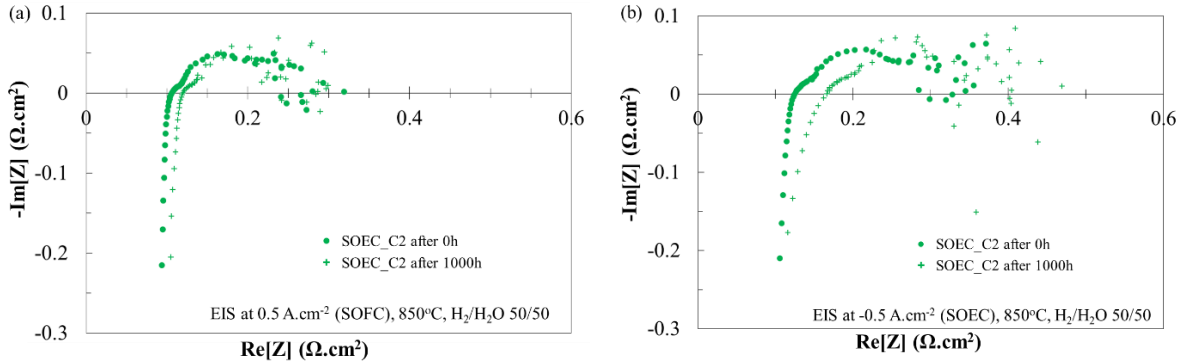

Figure IV.11 - Electrochemical Impedance Spectra of SOEC_C2 after 0h and 1000h (a) at 0.5 A.cm^{-2} and (b) at -0.5 A.cm^{-2}. There is a clear increase of the high frequency contribution in SOEC mode.

3. Post-mortem characterization

In addition to the electrochemical performances monitored during durability tests, fine characterizations of electrodes are essential. The first post-mortem observations of electrodes have been done by Scanning Electron Microscopy (SEM). Some interesting information on the nickel agglomeration mechanisms can be extracted from these 2D images. To take the analysis one step further, 3D nano-holotomographic reconstructions of aged cells have been performed. A summary of the available volumes is given before comparing the relevant microstructural parameters of each cell.

3.1 Scanning Electron Microscopy

Polish cross sections of pristine and aged cells have been prepared for SEM observations. As a general matter, the observations have not revealed any striking cell deteriorations such an electrode delamination, a massive Cr re-deposition in the O_2 electrode or an extensive Ni agglomeration. More precisely, no delamination of the O_2 electrode was found even in electrolysis mode operated at high current density (cell SOEC_3). Moreover, it has been checked that the Cr re-deposition was restricted to the LSC contact layer even after a test duration of 9000 hrs (SOFC_C6). Since the O_2 electrode active layers (LSCF-CGO/LSCF) were protected from Cr pollution, the mechanism should not be involved in the electrochemical degradation. All these statements are in good agreement with the low degradation rates reported in the previous section.

Regarding the objective of the study, a focus on the Ni-YSZ electrode is detailed hereafter. A special attention has been paid to identify the most relevant conditions to distinguish the Ni, YSZ and pores phases on the micrographs. For this purpose, the electrode was embedded in an epoxy resin (Epofix®). The observations were realised in Secondary Electrons (SE) mode at a low acceleration voltage (0.5 kV). In addition, the working distance between the sample and the SE detector was lowered to 2-3 mm. This work has been done in collaboration with Sergii Pylypko.

As already discussed in the previous chapter, it is reminded that observations of the pristine cell have revealed a rather homogenous distribution of YSZ, Ni and pores in the cermet (see Figure III.16) even if some zones appear to be enriched in Ni or YSZ. It is reminded that such inhomogeneity is liable to a slight scattering in the data extracted from reconstructed volume which are restricted to around $25^2 x \pi x 50\ \mu m^3$. This remark underlines the necessity to have 3D volumes as large as possible reinforcing the relevance of the X-ray holotomography compared to other techniques.

It has been stated by many authors that the cermet particles re-agglomerate under operation (see Chapter I). The global view of the cermet for the fresh and a tested hydrogen electrodes in both electrolysis (SOEC_C2) and fuel cell modes (SOFC_C4 and SOFC_C6) are presented in Figure IV.12. On the polished cross section micrographs, it can be remarked that the nickel

phase mean diameter seems to be modified after long-term operation. Nevertheless, the differences that could arise between the different aged samples, cannot be easily quantified. Moreover, the analysis of the 2D microstructural evolution is not straightforward. A more sensitive tool taking into account the complex 3D structure of the cermet is thus necessary. In this study, nano-holotomographic reconstructions have been performed on Ni-YSZ electrodes to reveal this degradation phenomenon. The results are detailed in the following section.

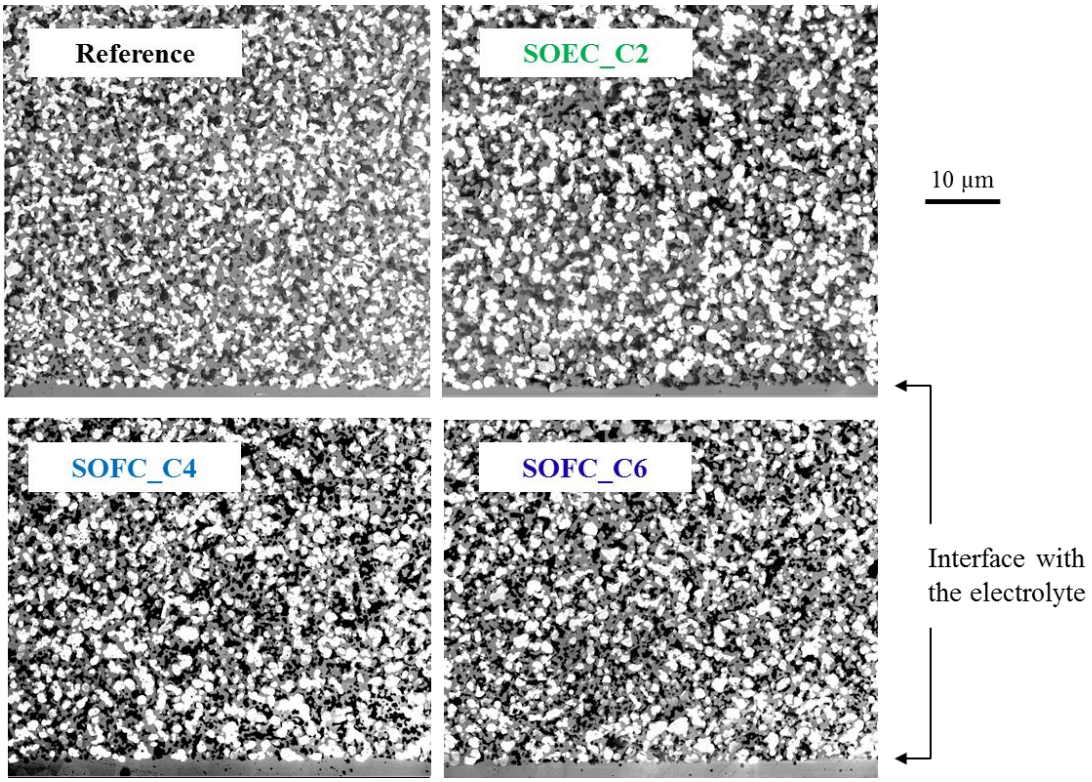

Figure IV.12 – SEM images of cermet for reference and aged cells at the interface with electrolyte. Ni is white, YSZ is grey and porosities are black. (Secondary Electron detector at Working Distance 2-3 mm and tension 0.5 kV). Changes of Ni phase is observable on aged samples.

As discussed in the first chapter, some authors have reported a Ni volatilisation in operation leading to a Ni depletion or enrichment at the interface with the electrolyte. Some authors have even observed after operation a thin electrode layer in contact with the electrolyte for which Ni has been completely removed by volatilization and redepositing [Matsui2012, The2015, Mogensen2016]. However, in our case, the careful inspection of the interfaces of all the samples has not revealed any significant modifications whatever the duration of the test or the polarisation modes. This statement can be checked on Figure IV.13 that compares the cermet microstructure in the vicinity of the electrolyte interface for the fresh and tested cells. Even after 9000h of operation, it is clear that no major Ni depletion has occurred. It can be inferred from these observations that the long distance transport of Ni under vapour species should not be involved in the nickel coarsening for the studied cells. In our case, the nickel agglomeration would be rather controlled by short distance mechanisms such as Ni surface or bulk diffusion. As a consequence, the underlying mechanism of Ni transport seems to be dependent on the

cermet microstructure and/or the chemical nature of the components (purity of materials, adhesion between Ni and YSZ, etc…).

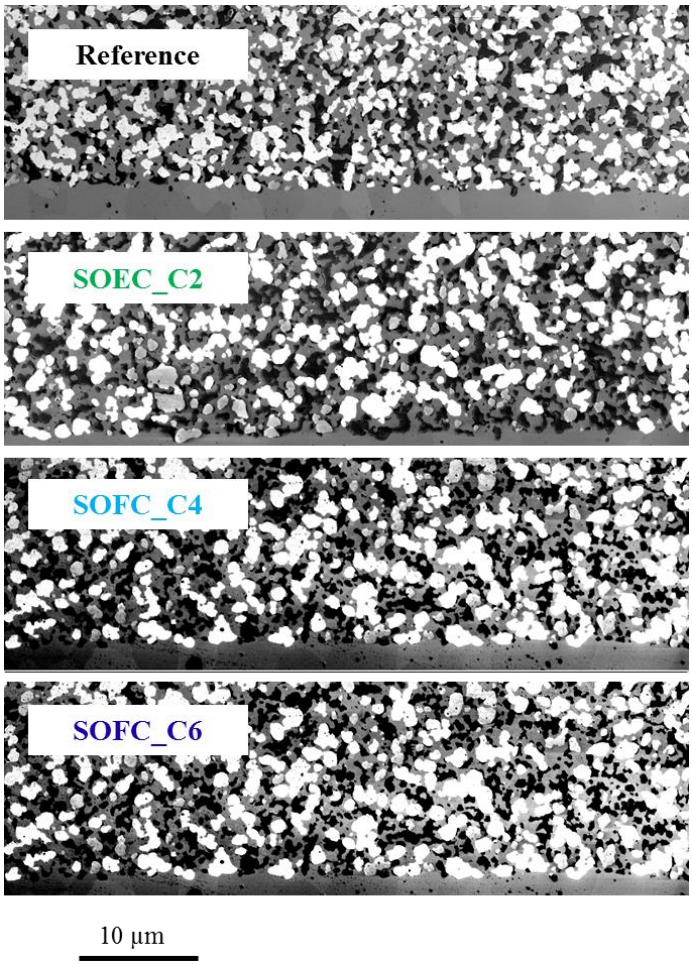

Figure IV.13 – Zoom-in of the SEM cross section micrographs on the Ni-YSZ/YSZ interface of fresh (reference) and aged samples. Ni is white, YSZ is grey and porosities are black (Secondary Electron detector at Working Distance 2-3 mm and tension 0.5 kV). No Ni depletion is observed on aged samples.

3.2 3D tomographic reconstructions

The aged cells have been characterized by nano-holotomography with the same method developed for the pristine samples (see Chapter III). The study is focused on the cermet to measure the nickel agglomeration that has been detected by SEM. The summary of all the reconstructions is presented in the following section. Then, the evolutions of the cermet microstructural properties due to Ni coarsening are discussed with the long-term operating parameters.

3.2.1 3D reconstructions

Thanks to the new sample preparation by PFIB, the location of the tomography specimen can be easily chosen. Taking advantage of the method, four different localisations have been studied (Figure IV.14). Some samples have been extracted from the bulk of the hydrogen electrode that means close to the free surface. Others have been taken in the electrochemically

active layer at the interface with the electrolyte. In addition to these two positions in the cermet thickness, samples have been cut at the gas inlet and outlet. Therefore, the effects such as the steam partial pressure change along the cell radius can be studied with these samples.

	SOEC	SOFC
Inlet	P_{H2O} high & P_{H2} low	P_{H2O} low & P_{H2} high
Outlet	P_{H2O} low & P_{H2} high	P_{H2O} high & P_{H2} low

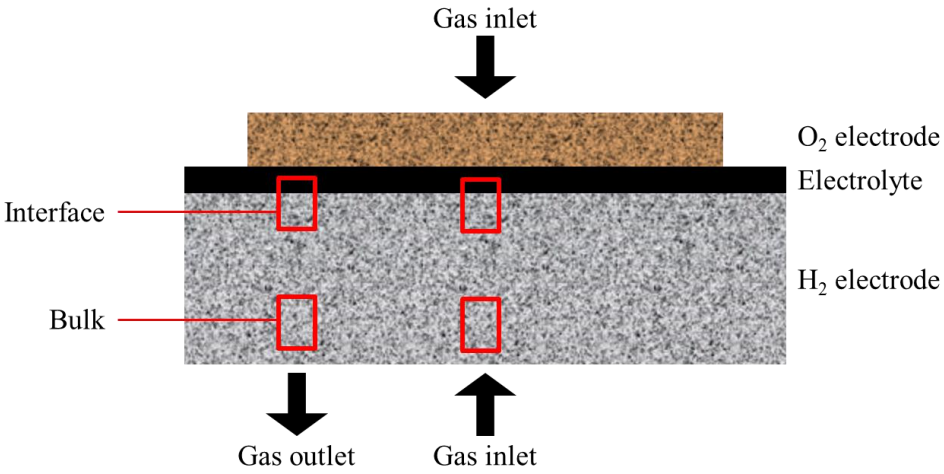

Figure IV.14 – Schematic representation of the tomographic sample localisations (red rectangles) in the hydrogen electrode.

The 3D volumes available for microstructural analysis are summarized in Table IV.4. Thanks to this large amount of data, the effect of the operating parameters on the degradation can be analysed. The main interesting results are described hereafter whereas the whole dataset is detailed in Appendix 1.

Table IV.4 – Summary of 3D volume reconstructions

	Bulk		**Interface**	
	Inlet	**Outlet**	**Inlet**	**Outlet**
Reference	☺		☺	
SOEC_C1	☺			
SOEC_C2	☺		☺	☺
SOEC_C3			☺	☺
SOFC_C4		☺	☺	☺
SOFC_C5		☺		
SOFC_C6			☺	☺

3.2.2 Effect of localisation in the thickness

The analysis of the 3D volumes has revealed some slight morphological differences in the thickness of the cermet substrate. Indeed, on fresh samples, it has been found that the microstructure is finer at the interface of the electrolyte with higher density of TPBs (i.e. 5.25 μm^{-2} at the interface *versus* 4.75 μm^{-2} in the bulk) and lower nickel particles size (i.e. 0.9 µm at the interface *versus* 1.01 µm in the bulk). Although the cermet does not have a functional layer, that gradient in the microstructure should allow enhancing the electrochemical efficiency of the active layer. It is consistent with the SEM images where some inhomogeneities due to the cell manufacturing have been observed in the hydrogen electrode layer (Figure III.19).

3.2.3 Effect of current density

The effect of current density can be analysed comparing the cell SOEC_C3 and SOEC_C2 which have been operated in similar conditions of temperature, air and steam conversion rates except for the current density (at -0.75 $A.cm^{-2}$ instead of -0.5 $A.cm^{-2}$ respectively). The evolution of the density of TPBs is shown on Figure IV.15 for samples taken at the interface with the electrolyte and gas outlet. A significant decrease of the TPBs is observed after ageing. However, despite a longer ageing time and higher current density, SOEC_C3 is not more degraded than SOEC_C2. This tendency is found with all other microstructural parameters such as mean particle diameters. As a consequence, in our operating conditions, there seems to be no effect of the current density on the Ni coarsening. This operating parameter can thus be considered as a non-impacting factor on the nickel agglomeration. This result is consistent with the polarisation curves. Indeed, while the "apparent" degradation is higher with a higher current density, the "intrinsic" degradation is similar.

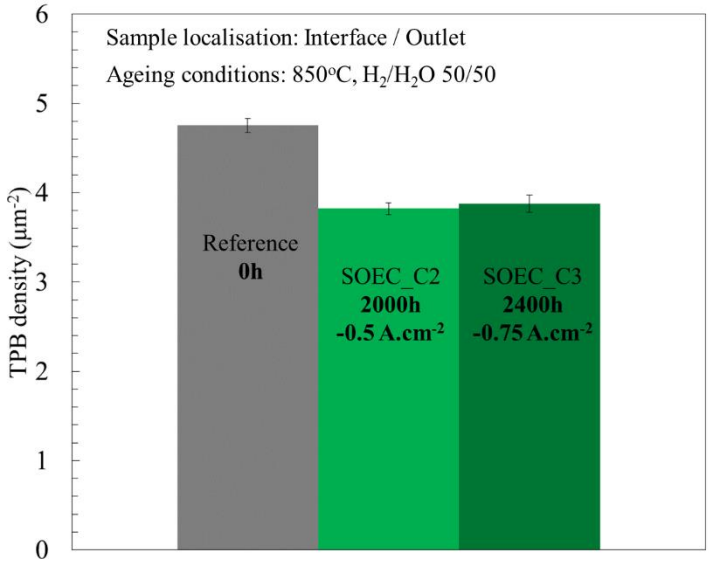

Figure IV.15 – TPB density for cells tested with different current densities. No effect of this operating parameter on the degradation.

3.2.4 Effect of steam partial pressure

It is classically expected that a high steam partial pressure in the hydrogen electrode could promote nickel agglomeration [Jiang2003, Holzer2011, Pihlatie2011]. To analyse this possibility, reconstructions at the interface with the electrolyte have been compared for the inlet and outlet areas of SOEC_C2 and SOEC_C3. The difference on density of TPBs is shown in Figure IV.16. Despite a significant difference in the steam content lower at the cell outlet for these tests performed in electrolysis mode at a high conversion rate, there is no clear difference between the densities of TPBs. The same observation can be done on the nickel particle diameter which varies between 1.06 µm and 1.09 µm. This observation tends to indicate that, with our cells and in our operating conditions, the water partial pressure is not a first order degradation parameter for nickel coarsening. That result is consistent with the hypothesis of a Ni agglomeration mechanism that would not be based on the vaporisation of Ni under gaseous hydroxides $Ni(OH)_2(g)$ (cf. section 3.1 of this chapter). Indeed, this mechanism requires water molecules, and hence, is expected to be very sensitive to the steam partial pressure. In our case, the Ni coarsening would rather be controlled by sintering phenomena with mass transfer on the surface or in the bulk of the metallic particles.

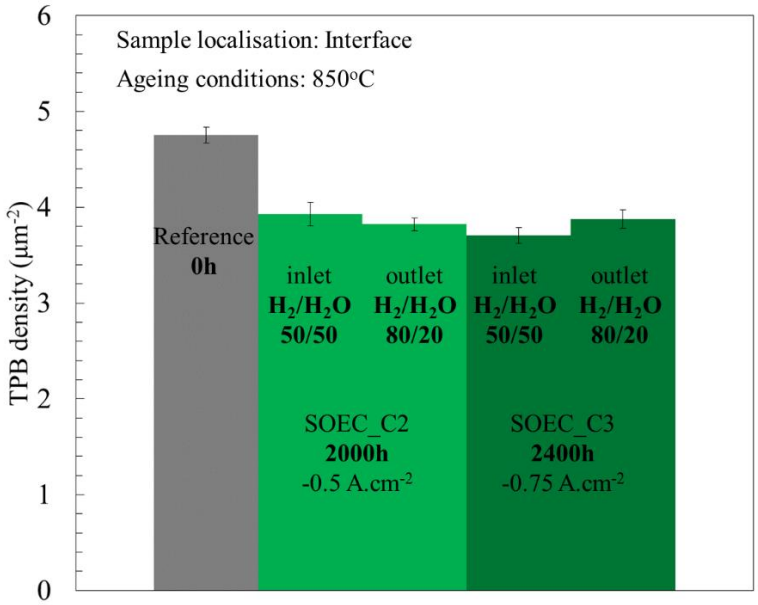

Figure IV.16 - TPB density at gas inlet and outlet for 2 aged cells. The water partial pressure is different according to the localisation. Nevertheless, no effect of this operating parameter is visible on the degradation.

3.2.5 Effect of polarisation

Thanks to the selected operating conditions for the long-term tests, the effect of polarisation can also be studied. For this purpose, properties extracted for the reconstructions of samples taken in SOFC_C4 and SOEC_C2 have been compared. In Figure IV.17a and Figure IV.17b the densities of TPBs and the mean particle diameters at the interface with the electrolyte for the gas inlet are provided. The decrease in active TPBs in the cell aged in fuel cell mode is slightly higher than in the one aged in electrolysis although the ageing time in fuel cell mode

was limited to 1000h whereas it reached 2000h in electrolysis mode. However, no significant difference is detected between the nickel particle diameter of the same two samples (Figure IV.17b), indicating that polarisation would have no clear effect on Ni coarsening. In that way, the polarisation cannot be considered as a major parameter for Ni coarsening. This result is quite logical since the Ni mass transfer involved in the sintering of metallic particles does not be dependent on the electrical field.

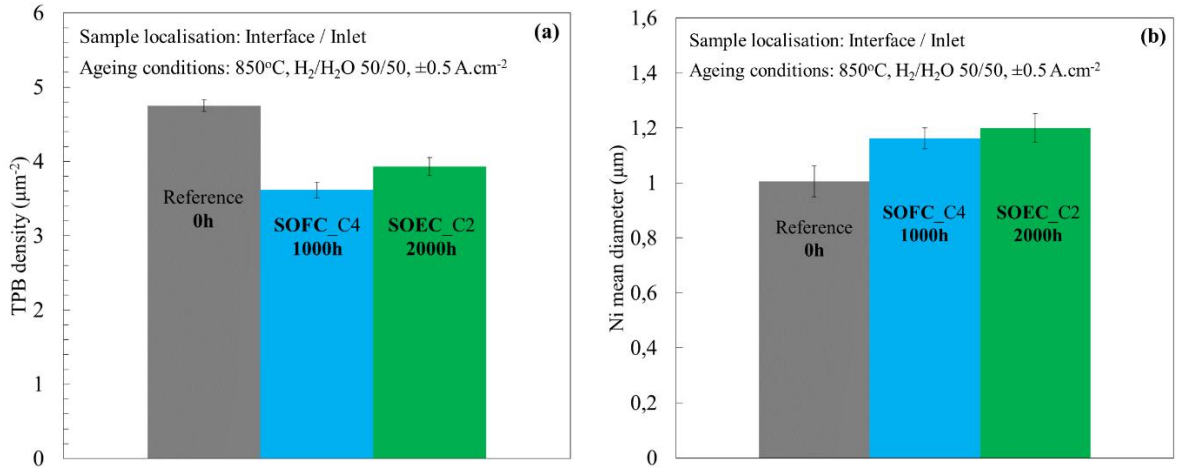

Figure IV.17 – Effect of polarisation on the degradation. (a) TPB density for cells aged in fuel cell (blue) and electrolysis (green). (b) Ni mean diameter for same aged cells. The effect of polarisation is not clear on the microstructural evolution.

3.2.6 Effect of time and temperature

Conversely to the electrical field or the current density, it is generally accepted that the time and temperature are two parameters affecting the sintering process of metallic particles. Any increase in operating time or temperature should result in an increase of the Ni coarsening in the cermet. In the following sections, the YSZ, porosity and nickel phases evolutions over time and temperature are detailed assuming that all the cells tested either in fuel cell or electrolysis mode can be considered together.

3.2.6.1 YSZ phase and porosity

The microstructure of the YSZ ceramic skeleton has been analysed in the reconstructions of aged cells. The mean YSZ particle diameter obtained with the covariance function is presented on Figure IV.18 for cells tested over 9000h at temperatures of 850°C and 750°C. It is clear that the grain size stays stable over time in our test conditions. That result is consistent with the Particle Size Distribution (PSD) which is not evolving between samples. In other words, as expected the ceramic backbone does not suffer any microstructural evolution at 750°C and 850°C. The mean size of porosities shows also a relative stable behaviour over time. As a conclusion, it can be stated that both, the ceramic and porosities, remain constant during all the durability tests.

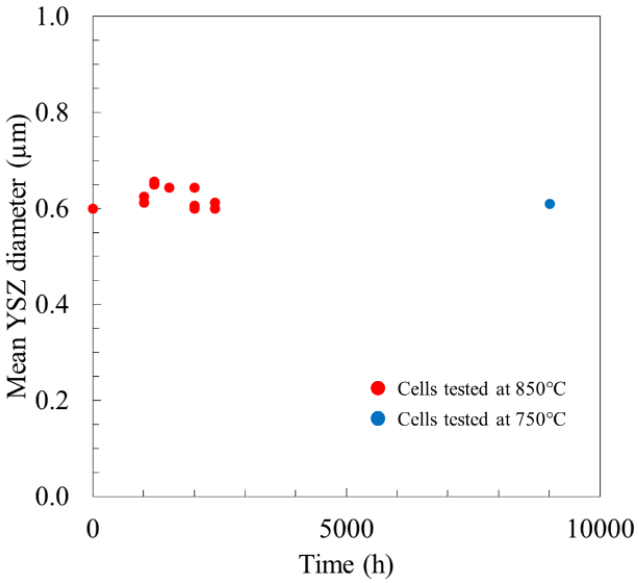

Figure IV.18 – Evolution over time of YSZ mean particle diameter measured with covariance function on all the 3D reconstruction.

3.2.6.2 Nickel phase

The Ni particle growth has been quantified in the aged cells thanks to the 3D reconstructions. On Figure IV.19, the percentage evolution of the Ni mean particle diameters is plotted over time for data measured in the bulk of all the tests. All these results can be gathered on the same graph and analysed all together as it has been shown previously that, in our case, the current density, the water partial pressure and the polarisation are not first order parameters for nickel coarsening. It is worth noting that all the data are consistent to each other and follow the same trend over time.

On this figure, data from Tanasini et al. [Tanasini2009] have also been reported as the cell and temperature (850°C) are identical. As shown in Figure IV.19, the data from Tanasini et al. [Tanasini2009] are in very good agreement with our measures as they are in perfect line with the Ni evolution found in the present study. This result allows validating all the protocol from the electrochemical test and the 3D reconstruction to the data analysis.

Apart from validation, the plot in Figure IV.19 highlights a significant increase in the Ni particle diameter at 850°C. Indeed, there is a clear increase by more than 30% after 2000h of the particle diameter at 850°C. This agglomeration is much more limited at 750°C as the Ni only growth by 13% after 9000h of operation. Therefore, the Ni coarsening is found to be strongly thermally activated. This temperature behaviour is obviously consistent with a classical sintering process. However, such a high impact of temperature could indicate a more complicated mechanism with a potential role of the ceramic backbone that is suspected by many authors to limit or even inhibit the Ni agglomeration at low temperature.

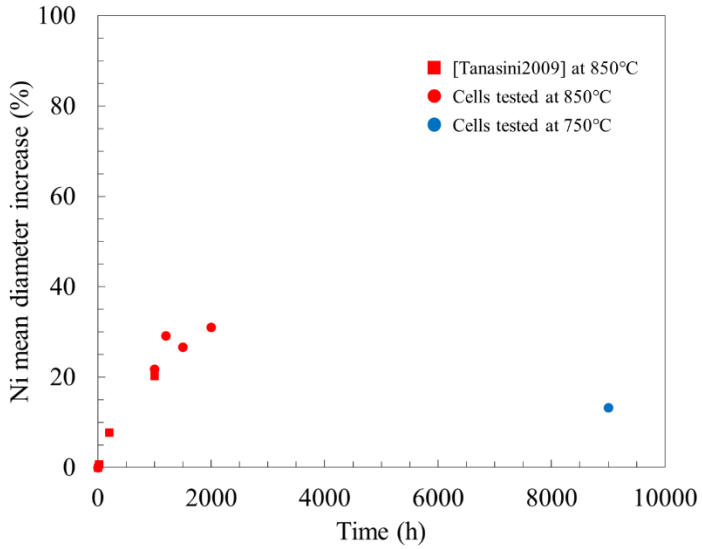

Figure IV.19 – Evolution of nickel mean diameter over time for aged cells at 850°C (red dot) and 750°C (blue dot). The diameters have been measured on samples extracted from the bulk. Data from [Tanasini2009] performed on similar cells have been added (red squares).

In order to analyse the change of nickel mean particle diameter, the size distribution can be observed. On Figure IV.20, the nickel PSD is given for a pristine and a 2000h aged cell (SOEC_C2). There is a clear decrease in the frequency of the smallest particles due to the nickel agglomeration leading to a rearrangement of the smallest particles to the biggest ones. In other words, the distribution is shifted towards larger particle sizes what is consistent with the measurement of the mean diameter performed with the covariance function.

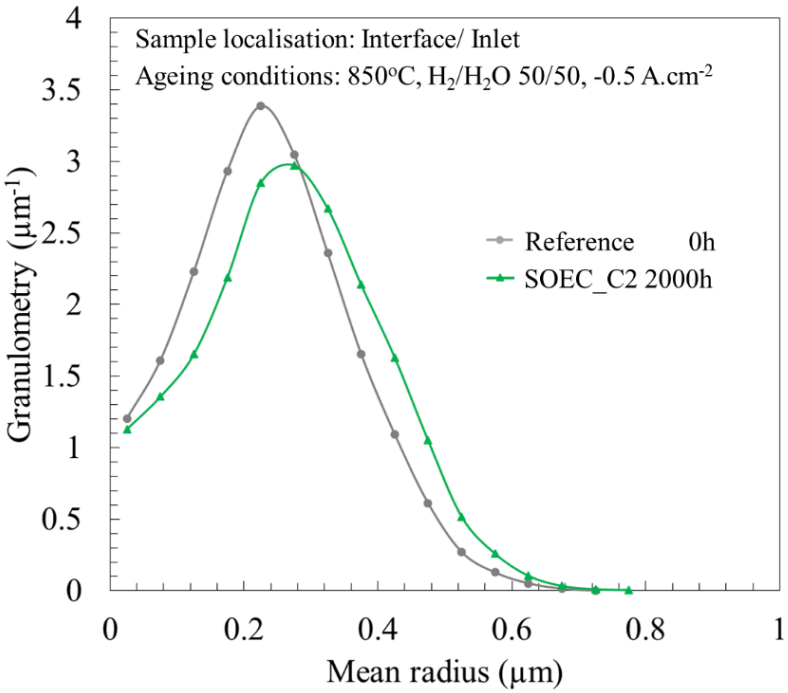

Figure IV.20 – Ni Particle Size Distribution (PSD) for pristine and aged sample in electrolysis.

In order to better understand the nickel agglomeration mechanism, the evolution of specific surface areas of nickel with gas and YSZ have been analysed. On Figure IV.21, the evolution of $S_p^{Ni/gas}$ is plotted as a function of time. A strong decrease is highlighted at 850°C whereas

the evolution is more limited at 750°C. In the same time, it is found that the specific surface area between nickel and YSZ is quasi stable over time (for example, the decrease percentage is only 3.5% after 1000 hours at 850°C for SOFC_C4). In other words, the metal-ceramic interface does not change significantly with time whereas the surface in contact with the gas phase is strongly affected by the Ni coarsening. This statement indicates that Ni phase sintering in the cermet mainly results from the rearrangement of particles in contact with gas while the others seem to be strongly attached to the YSZ backbone. Such behaviour is rather logical knowing that the interfacial energy between Ni and gas is expected to be much lower than the one between Ni and YSZ. This result has been suspected by many authors who have reported a probable inhibition effect of the YSZ on the nickel agglomeration [Jiang1999b, Jiang2003, Zhu2003, Tu2004, Jia2006, Pihlatie2011]. In this study, the precise analysis of the tomographic reconstructions has allowed to highlight the crucial role of the YSZ network on the Ni sintering in the cermet.

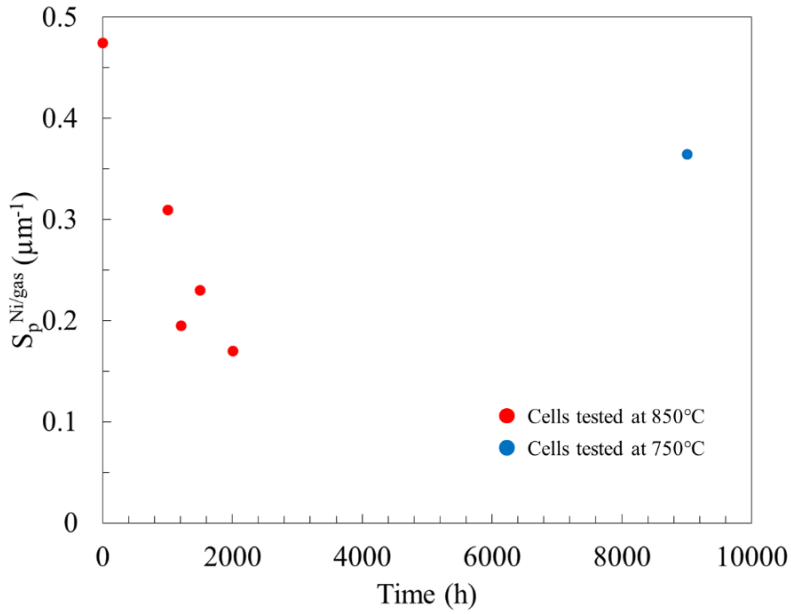

Figure IV.21 – Evolution of the specific surface area between nickel and gas phases at 850°C (red dot) and 750°C (blue dot).

The evolution of the nickel phase microstructure is expected to strongly affect the cells performances as it is convolved with a decrease of the density of TPBs. Indeed, the evolution of the density of electrochemically active sites over time is presented on Figure IV.22 with the data extracted from the same cells than Figure IV.19. The decrease of TPBs density is pronounced at 850°C whereas it is limited at lower temperature. These evolutions are coherent with the previously reported Ni particle growth. Therefore, the decrease of the TPBs density appears to be clearly linked to the Ni coarsening upon operation. Temperature appears to be a major controlling parameter.

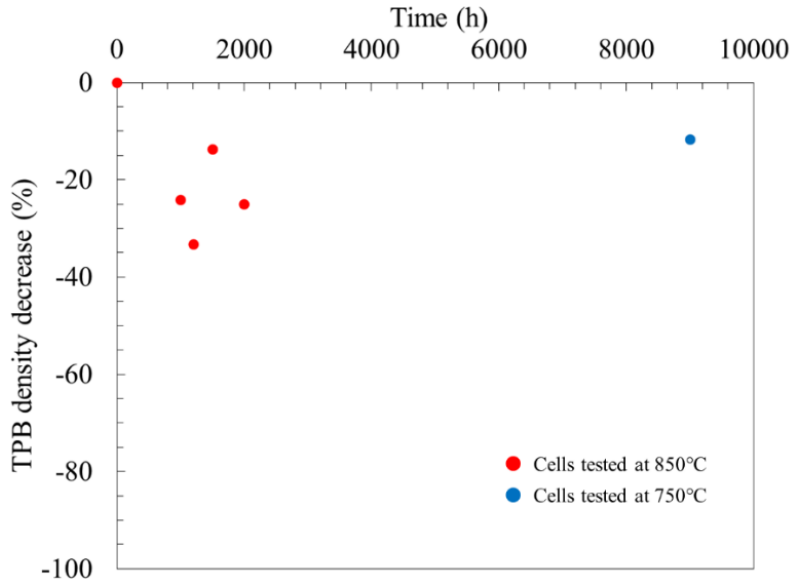

Figure IV.22 - Evolution of Triple Phase Boundary density over time for aged cells at 850°C (red dot) and 750°C (blue dot). The TPB densities have been measured on samples extracted from the bulk.

4. Conclusions of this chapter

The experimental set-up detailed in this chapter was used to perform six different durability tests in galvanostatic mode over periods of more than 1000h. The effect of operating conditions on cell degradation has been highlighted by changing the polarisation, the current density and the temperature between the experiments. The degradations measured on cell voltage evolutions are in the state-of-the-art of the literature for both polarisations. It appears that the degradation rate is higher in electrolysis than in fuel cell mode for similar operating conditions. A higher current density also leads to a higher "apparent" degradation of the cell.

Regular electrochemical measurements of the cell performances have been done during the long-term tests. The analysis of the i-U curves revealed that the current density would not affect the "intrinsic" degradation of cells when the performances are compared in the same operating conditions. However, the analysis of the polarisation curves in fuel cell and electrolysis modes allow explaining only a part of the degradation rate difference between SOFC and SOEC. It is found that the electrolysis operating conditions seem to highlight the cell degradation. Despite the poor shape of Electrochemical Impedance Spectra, a qualitative analysis showed the increase of a high frequency contribution whatever the ageing conditions.

To go further in the analysis of degradation, several post-mortem characterizations have been done. Polish cross-sections of the cermet have been observed by SEM. No nickel depletion was detected on the 2D images but a coarsening of the Ni particle was evidenced. This observation would indicate a short distance agglomeration mechanism for nickel such as surface or bulk diffusion (while, in our case, the Ni vaporisation/redisposition is not involved in the Ni microstructural evolution). As SEM images are limited to highlight the complex microstructural evolutions of the cermet, X-ray nano-holotomography has been performed on aged samples as for the pristine cell to extract the main morphological parameters.

From the 3D analysis, it has been found that the current density is not enhancing the nickel agglomeration what is consistent with the polarisation curves. Moreover, the steam partial pressure and polarisation appears like secondary order parameters for the nickel coarsening. However, time and temperature are strongly affecting the nickel phase evolution. Indeed, the nickel particle size growth reaches about 30% after 2000h of operation at 850°C whereas it is only 13% after 9000h at 750°C. This change was also shown to affect the density of electrochemically active sites directly impacting the cell performances. The significant effect of the YSZ skeleton on the nickel agglomeration has also been shown analysing the evolution of Ni specific surface area with gas and ceramic phases. While the interface with YSZ area is only slowly decreasing over time, a clear diminution of the Ni surface with the porosities is measured. That result confirms inhibiting effect of YSZ on the nickel agglomeration discussed in the literature.

Now that the microstructural parameter evolving over time have been identified, it would be interesting to use these evolutions in a modelling approach. The contribution of nickel agglomeration on the performance losses could thus be evaluated. This multi-scale modelling approach is presented in the next chapter. All the microstructural properties obtained on the cells will be used as input data for the simulations.

Chapter V:

Numerical tools for degradation study

As presented in the previous chapters, the main morphological properties of the H_2 and O_2 electrodes have been obtained by X-ray nano-holotomography. Moreover, the microstructural evolutions of the H_2 electrode have been carefully analysed for aged cells in different operating conditions. In complementarity with the electrochemical and post-mortem characterizations, the electrode and cell modelling must ensure a better understanding of the underlying mechanisms of SOC operation and degradation. Besides, the simulations can be used to quantify the contribution of a specific degradation phenomenon on the total cell voltage loss measured experimentally.

In this chapter, a description of the multi-scale modelling approach used in this work is proposed. The main features of numerical tool developed at different scales are reminded hereafter with a special emphasis on the essential links between microscopic and macroscopic models. The model was initially calibrated on one experimental i-U curve obtained before ageing to determine some missing kinetic parameters. Then, it was validated by comparing the simulation results with other experimental polarisation curves measured for different gas composition, polarisation or temperatures. The second and third sections of this chapter are specifically dedicated to the model calibration and validation. Finally, the simulation was used to analyse the degradation mechanism. For this purpose, a model for nickel agglomeration was proposed and implemented in the model. The updated numerical tool was employed to quantify the contribution of Ni coarsening on the cell performances losses. The modelling and simulations of degradation due to Nickel agglomeration are detailed in the last section of the chapter.

1. Model structure

A complete multi-scale and multi-physics modelling framework has been developed at CEA. It is based on micro-models describing the operation at the electrode level and a macro-model for the global cell response. These two scales are connected to each other. The parameters allowing the link between micro and macro simulations are presented in the overview of the modelling approach in the subsection 1.1, whereas the specificities of the models are detailed in subsequent subsections (see section 1.2 and 1.3).

1.1 Overview of the modelling approach

The complete modelling framework is a combination of micro-models describing the electrodes operation [Lay2013, Usseglio2014] and macro-models illustrating the cell response under SOFC [Morel2005, Laurencin2008] and SOEC mode [Laurencin2011]. This multi-scale approach is relevant to explain finely the experimental results. Indeed, the micro-model can be used to analyse the co-limiting elementary steps in the electrodes whereas the cell-model allows the simulation of macroscopic operating parameters such as current densities, overpotentials, gas compositions, etc. In this modelling approach, the knowledge of the electrodes morphological properties is essential to reduce the number of unknown parameters.

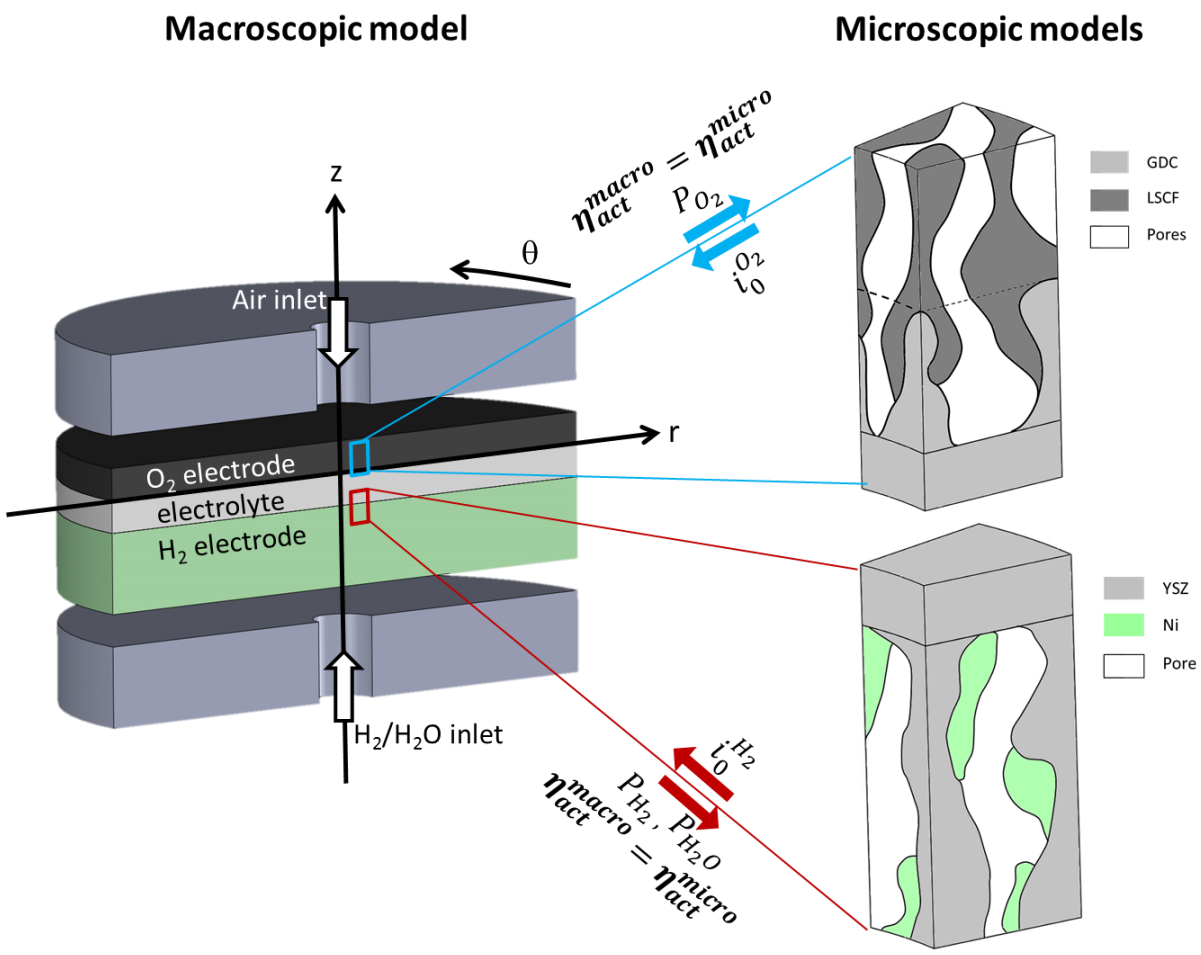

Figure V.1 – Overview of the modelling structure with macro-model for the complete cell and micro-models dedicated to each electrode.

As illustrated in Figure V.1, the micro and macro scale models are connected in such way that the activation overpotentials calculated at the electrode level are equal to the ones computed at the cell level. In this objective, these overpotentials are expressed in the macroscopic model through exchange current densities i_0 which include all the phenomena occurring in the electrode active layers. In other words, the parameter i_0 encompasses the elementary reaction process convoluted with the mass and charge transfers in the electrode active layers which are taken into account at the micro-scale level. As shown in equations (V.1) and (V.2), the exchange current density depends on the temperature and the partial pressures in the neighbourhood of the active sites which are reduced in the macro cell model at the electrode/electrolyte interfaces. These partial pressures calculated with the macro-model are used as boundary conditions in the electrode models as illustrated in Figure V.1.

$$i_0^{H_2} = i_{00}^{H_2} \left(P_{H_2}\right)^{\alpha} \left(P_{H_2O}\right)^{\beta} e^{-\frac{E_a^{H_2}}{RT}} \tag{V.1}$$

$$i_0^{O_2} = i_{00}^{O_2} \left(P_{O_2}\right)^{\gamma} e^{-\frac{E_a^{O_2}}{RT}} \tag{V.2}$$

The parameters $E_a^{H_2}$ and $E_a^{O_2}$ are the activation energies for each electrode. The exponents α, β and γ on the partial pressures are numerically determined with the micro-models to reach a match between the activation overpotentials of macro and micro models. To identify the exponent and the activation energies for the exchange current density laws, a large range of partial pressure and temperature has been investigated. A least square method has been used to find the best fit between the simulated exchange current densities and the evolution laws (V.1) and (V.2). The result obtained with micro-models for both electrodes are given in Table V.1.

Table V.1- Exponents and activation energies used for the expression of the exchange current density of both electrodes according to the partial pressures and temperature.

	Hydrogen electrode			**Oxygen electrode**	
Polarisation	**α**	**β**	$E_a^{H_2}$**(kJ.mol^{-1})**	**γ**	$E_a^{O_2}$ **(kJ.mol^{-1})**
SOFC	0.09	0.57	115	0.34	120*
SOEC	0.07	0.61		0.15	

* Data extracted from literature [Costamagna1998b, Nagata2001]

For the hydrogen electrode, the exponent values are in good agreement with experimental data available in the literature. Indeed, in fuel cell mode, Jiang et al. [Jiang 1999] have found $\alpha = 0.1$ and $\beta = 0.5$. Similar values have been reported in [Bieberle2001, Kanno2011] ($\alpha = 0.11$ and $\beta = 0.67$). The activation energy on the exchange current density identified in this work is also given in Table V.1. This result is consistent with the reported activation energy of this electrode in the literature [Costamagna1998b, Nagata2001, Usseglio2014].

For the oxygen electrode, the determined exponent is also in the range of the published data. For example, Costamagna et al. [Costamagna1998b] have proposed to take 0.25 for the exponent γ whereas Yonekura et al. [Yonekura2011] have found 0.3. The activation energy for the exchange current density of the oxygen electrode has been set to 120 kJ.mol^{-1} according to data from the literature [Costamagna2004, Hernadez2005, Bernadet2016].

1.2 Micro-model

The micro-scale modelling approach describes the electrochemical reactions taking place at the H_2 and O_2 electrodes. It is a 1D model considering a slice of isothermal electrode. To estimate the different mass and charge transport phenomena, the microstructural properties of the ionic and electronic conducting phases and porosity are essential input parameters. The main information on the kinetic rates for both electrodes are reminded in the following sections. It should be noticed that the micro-model aims at calculating the activation overpotential of each electrode to be used in the macro-scale model.

1.2.1 Hydrogen electrode

The morphology of the studied hydrogen electrode is relatively homogeneous in all the thickness and does not present a specific microstructure for the active layer. It has been checked

that the reaction can extend in the depth of the electrode over a distance of about 15 µm. It has been assumed that the electrochemical reaction mechanism is controlled by a charge transfer at TPBs in both polarisations (see Figure V.2). This kinetic is consequently expressed by a Bulter-Volmer formalism as shown in Eq. (V.3). The rate v_{ct} depends on the density of TPBs ζ_{TPB}, the gas partial pressures in the functional layer and the electrode potential $E(z)$.

$$v_{ct}(z) = \zeta_{TPB}\left(k_{ox}e^{\frac{\alpha_{ox}2\mathcal{F}E(z)}{RT}}P_{H_2}(z) - k_{red}e^{\frac{-\alpha_{red}2\mathcal{F}E(z)}{RT}}P_{H_2O}(z)\right) \quad \text{(V.3)}$$

$$\text{with} \qquad k_{ox} = k_{ox}^0 \times e^{-\frac{E_a^{ct}}{RT}} \quad \text{(V.4)}$$

$$\text{and} \qquad K_e^{ct} = \frac{k_{ox}}{k_{red}} \quad \text{(V.5)}$$

The parameters α_{ox} and α_{red} are the symmetry factors of the reaction ($\alpha_{ox} + \alpha_{red} = 1$). The charge transfer reaction being thermally activated, the kinetic constant can be expressed through an Arrhenius law (Eq. (V.4)). The kinetic constants k_{ox} and k_{red} are linked each other through a thermodynamic equilibrium constant of the charge transfer reaction K_e^{ct} (Eq. (V.5)). The pre-exponential constant k_{ox}^0 has been adjusted to the experimental data during the models calibration at 800°C.

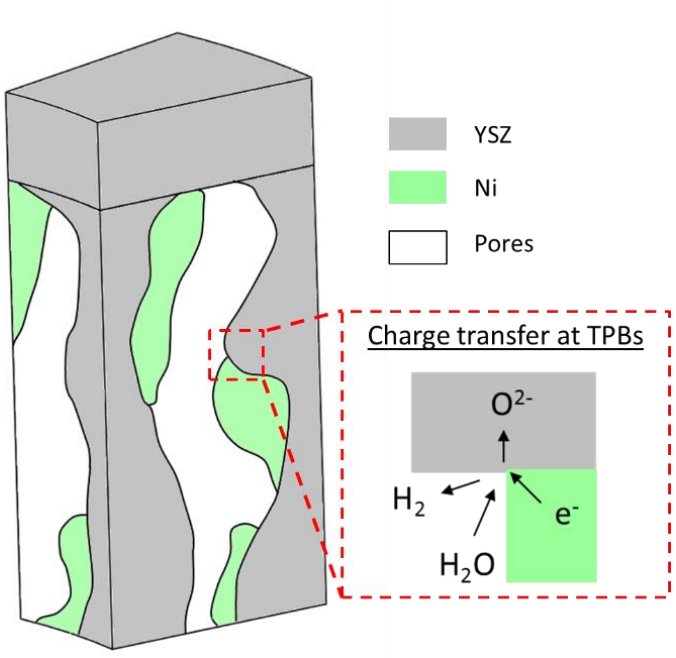

Figure V.2 – Schematic representation of the electrochemical reaction mechanism in electrolysis mode for the hydrogen electrode.

1.2.2 Oxygen electrode

As shown in Figure V.3, the oxygen electrode of the studied cells presents a bilayer structure with a LSCF-GDC composite associated to a pure LSCF coating. It is reminded that the LSCF compound is a MIEC that means it presents an ionic and electronic conductivity. It was necessary in the present work to enrich the numerical tool with a module dedicated to this kind

of material. The main characteristics of this micro-model are reminded hereafter. A complete description of this model can be found in [Laurencin2015b, Hubert2016].

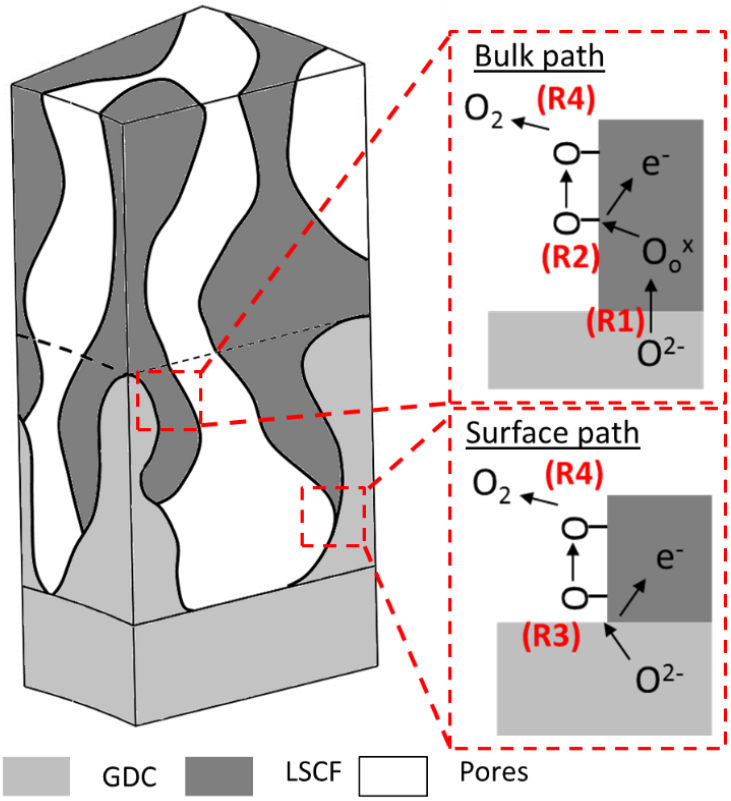

Figure V.3 - Schematic representation of the electrochemical reaction mechanisms in electrolysis mode for the oxygen electrode.

Four reactions are taking place in the oxygen electrode that can be split in two parallel reactive pathways (see Figure V.3). In anodic polarisation (i.e. in electrolysis mode), the bulk path consists of an ionic transfer of oxygen from the electrolyte material (R1 on Figure V.3) into the MIEC. It is followed by the oxygen excorporation from the LSCF lattice onto the surface of the material (R2 on Figure V.3). In parallel to this reactive pathway, the surface path corresponds to a direct oxidation at the Gas/MIEC/Electrolyte TPBs yielding adsorbed oxygen atoms on the surface of the electrode particles (R3 on Figure V.3). . Finally, a last step of oxygen desorption which belongs to both path allows producing dioxygen gas molecule in the porosities (R4 on Figure V.3). In order to compare the prevalence of each reactive pathway, the ratio of surface path to bulk path has been plotted for a single phase LSCF electrode (Figure V.4).

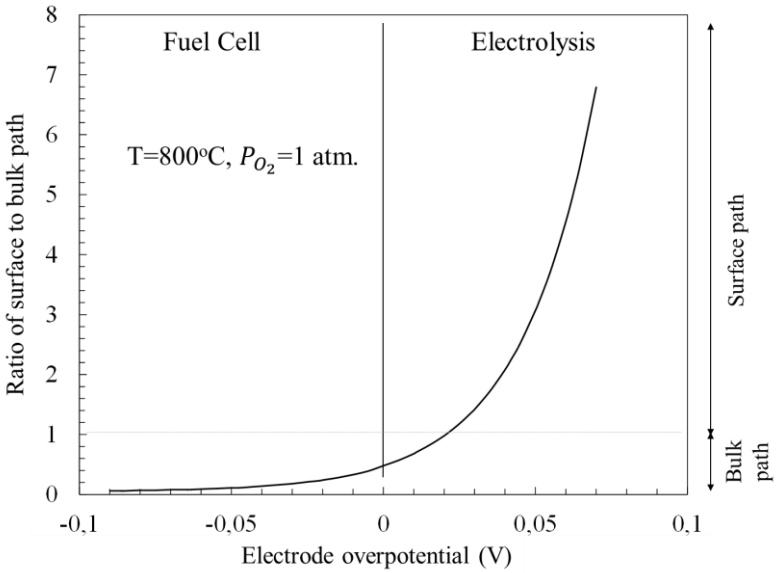

Figure V.4 – Kinetic rate ratio of surface path (TPBs) to bulk bath (MIEC surface) for a LSCF electrode of 23 µm thick. [Laurencin2015b]

In fuel cell mode, the ratio is found to be much smaller than the unity. It means that the bulk path contribution is much higher than the surface one. In other words, the reactions of adsorption, incorporation into LSCF followed by the oxygen bulk transfer are governing the electrode operation. This result is in good agreement with literature [Adler1996, Baumann2006, Grunbaum2009]. In electrolysis mode, it can be noticed that the ratio of surface to bulk path is increasing sharply above one. It means that at low overpotential the prevailing reactive pathway is still the bulk path whereas the surface one becomes predominant at higher polarisation. This change of reactive pathway can be attributed to the fast ionic transfer. Indeed, the MIEC is fed with oxygens atoms up to its maximum concentration under anodic polarisation resulting in a limitation of the bulk path. Then, only the reactivity at TPBs can occur.

It is worth mentioning that the specific LSCF-GDC/LSCF electrode bi-layer structure has been taken into account in the simulation. The ratio of surface to bulk path for this electrode is shown on Figure V.5. It can be observed that the ratio is higher than one whatever the polarisation. It means that the charge transfer at TPBs, which can extend in the whole thickness of the composite layer, governs the electrode response in electrolysis and fuel cell modes.

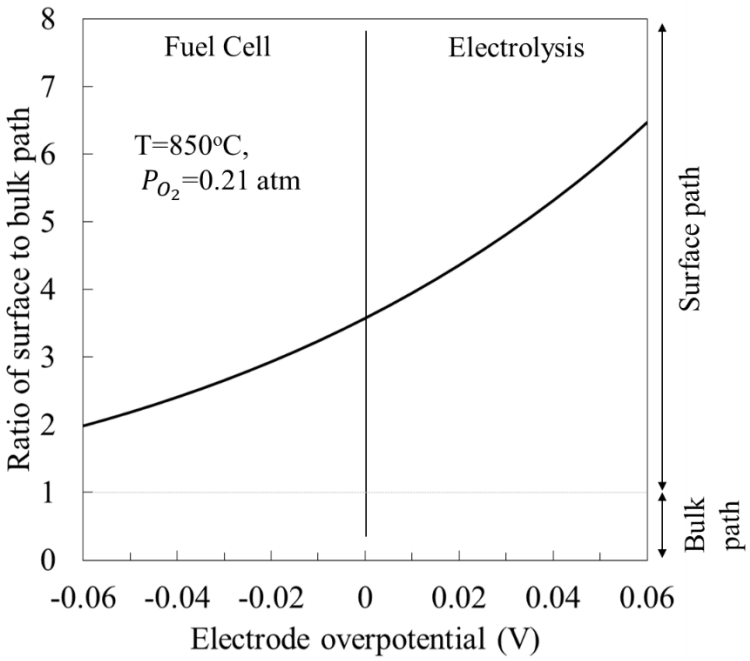

Figure V.5 - Kinetic rate ratio of surface path (TPBs) to bulk bath (MIEC surface) for the studied LSCF-GDC and LSCF electrode.

1.3 Macro-model

The 2D macro-scale model allows simulating the complete cell (Figure V.1) with the functional layer being restricted to the interface between electrodes and electrolyte. The asymmetrical condition has been considered for the simulations in order to describe the radial geometry of the cell and the co-flow configuration for the gas distribution on the electrodes. With this model, the local current density, gas composition, ohmic losses or overpotentials can be determined. The gas transport in the porous electrodes is described in the frame of the Dusty Gas Model (DGM). It takes into account the molecular as well as the Knudsen diffusion. The mass transport is strongly impacted by the electrodes microstructure [Lanzi1990, Berg2012, Holzer2013b].

The cell voltage is calculated in the macro-model through the determination of each irreversible contribution. The ohmic losses includes (i) the contact resistance extracted from the EIS characterizations of the pristine cell at different temperatures, (ii) the electronic resistance of the electrodes and (iii) the ionic resistance of the electrolyte. The concentration overpotentials are evaluated with the change in gas composition at the electrode/electrolyte interfaces that arises under operation. This contribution is affected by the transport of species in the electrode thickness and by the consumption/production of gaseous species along the cell radius. Finally, the activation overpotential encompasses all the reactive mechanisms occurring in the electrode active layer. It is calculated through the exchange current density. This parameter is determined with the electrode micro-scale model.

2. Model calibration

The modelling of SOC performances requires several input data. Thanks to the approach used in this work, most of them are known. The microstructural parameters of the electrodes are necessary to calculate the mass and charge transport as well as the kinetic rates. The characterization of electrodes done by nano-holotomography supplies most of these required data. Indeed, the main microstructural properties have been extracted from the 3D reconstructions excepted for the LSCF-GDC composite layer (see chapter III). In this case, the phase volume fractions and the mean pore radius have been estimated by SEM images analysis whereas the others parameters have been taken in the literature for similar composites [Wilson2010, Usseglio2014]. The values used for the simulations for this layer are summarized in the Table V.2.

Table V.2 : LSCF-GDC microstructural parameters used in the simulations.

Properties	**Phase**	**LSCF-GDC electrode**
Volume fraction (-)	Porosity	0.44
	GDC	0.33
	LSCF	0.23
Interfacial Specific surface area (μm^{-1})	LSCF/Gas	1.7*
	LSCF/GDC	2.0*
Tortuosity factor (-)	Porosity	2.1*
	GDC	3.5*
	LSCF	8.5*
TPB density (μm^{-2})		2.0*

* Properties that have been estimated through similar composite reconstruction in the literature [Wilson2010, Usseglio2014].

The physical properties in terms of conductivities and diffusivities for the ionic, electronic and gas phases are also required to compute the transport of the different species. These set of data are available in the literature. The thermodynamic data such as the standard electrode potential or the coverage rates at equilibrium used in the simulations are also coming from published data. The last set of unknown parameters in the model are the kinetic constants of reactions. For the hydrogen electrode, the kinetic constant of oxidation at TPBs have to be determined. There is three kinetic constant (TPBs, incorporation and adsorption) that have to be identified for the oxygen electrode. All these kinetic parameters have been adjusted on only one experimental polarisation curve recorded in fuel cell mode. The determination of the kinetic constants for both electrodes are detailed hereafter. The result of the calibration is presented in the last section.

2.1 Adjustment of kinetic constants

The kinetic constants of the reactions taking place in both electrodes have been adjusted on a single i-U curve. The polarisation curve recorded in fuel cell mode at 800°C for cell SOFC_C4 before ageing has been used for the adjustment. The gas compositions were H_2/H_2O=96.5/3.5

and O_2/N_2=21/79 at the H_2 and O_2 electrode. The respective gas flows were 3.92 10^{-5} mol.s^{-1} and 2.8 10^{-4} mol.s^{-1}. It should be noticed that it is the only experimental data used for the calibration. The reaction mechanisms being thermally activated, the micro-scale modelling allows estimating an activation energy for the kinetic constants. These steps are detailed hereafter for H_2 and O_2 electrode respectively.

2.1.1 Hydrogen electrode: determination of k_{ox}^0

As previously introduced, the electrochemical reaction is described by a charge transfer at TPBs as expressed in Eq. (V.3). Since the forward and backward kinetic constants are linked each other through a thermodynamic equilibrium constant (see Eq. (V.5)), only one needs to be adjusted. Moreover, the charge transfer reaction being thermally activated, the kinetic constant can be expressed through an Arrhenius law with a pre-exponential factor k_{ox}^0 and an activation energy for the charge transfer E_a^{ct} (see Eq. (V.4)). On Ni-8YSZ material, the activation energy for the charge transfer at TPBs has been reported at 201 kJ.mol^{-1} in the literature [Bessler2007]. This value has been used in the micro-model so that only the pre-exponential factor k_{ox}^0 remains to be identified. The model calibration on the experimental reference polarisation curve has led to identify a pre-exponential factor k_{ox}^0 equal to 140 mol.s^{-1}.m^{-1}.

2.1.2 Oxygen electrode: determination of k_{ox}^0, k_{TPB}^0 and k_{ads}^0

Compared to the hydrogen electrode, more reaction mechanisms are considered for the oxygen electrode. The adjustment of the kinetic constant related to the four reaction steps is thus more complicated. It should be noticed that the ionic transfer (Reaction R1) has been considered to be non-limiting in the simulations. The three other kinetic rates have been calibrated to reach the exchange current density evaluated with the experimental data while keeping a reasonable ratio of surface to bulk path as shown on Figure V.5.

To take into account the thermal activation of the reaction steps, it has been chosen to fix a common activation energy for all the four kinetic constants which results in a global electrode activation energy of 120 kJ.mol^{-1} [Costamagna2004, Hernadez2005, Bernadet2016]. In that way, the surface to bulk path is kept identical for each operating temperatures. This activation energy is about 159 kJ.mol^{-1}. The associated pre-exponential factors for each kinetic constant are summarized in Table V.3.

Table V.3 : Pre-exponential factors for the kinetic constants of the oxygen electrode reactive mechanisms.

Kinetic constant		
k_{ox}^0	Reaction R2	9.95 10^9 m^8.mol^{-3}.s^{-1}
k_{TPB}^0	Reaction R3	2.03 10^9 m^3.mol^{-1}.s^{-1}
k_{ads}^0	Reaction R4	1.24 10^{10} m^2.mol^{-1}.atm^{-1}.s^{-1}

2.2 Result of the calibration

The result of the calibration is shown on Figure V.6. As expected, a good agreement between the simulation and the experimental data has been achieved by fitting the model missing parameters. It should be noticed that the model perfectly describes the cell response at low and high current density.

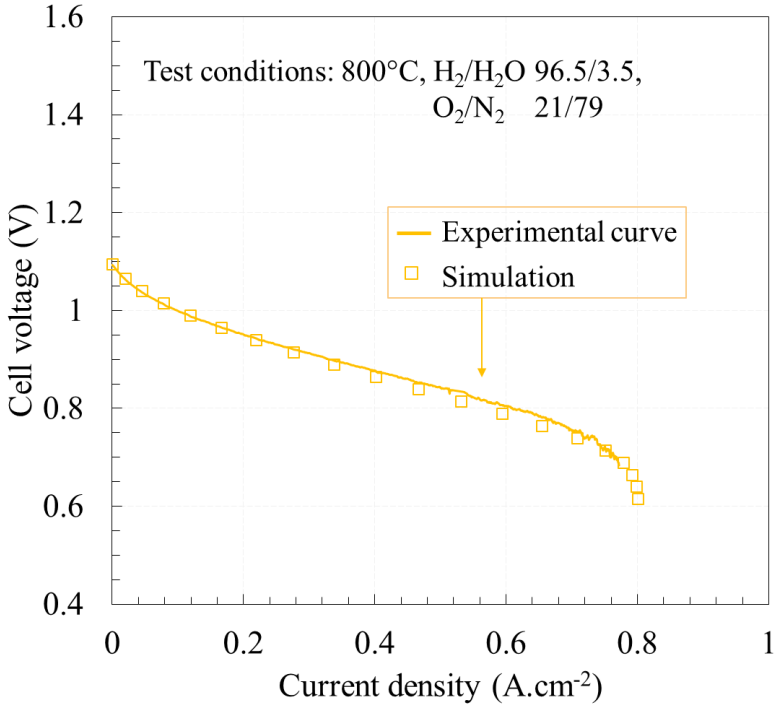

Figure V.6 – Experimental and simulated polarization curves for pristine cell at 800°C in fuel cell mode. Gas flows were 3.92 10^{-5} mol.s^{-1} and 2.8 10^{-4} mol.s^{-1} for H_2 and O_2 electrode respectively.

3. Model validation with all experimental initial performances

Once the model has been calibrated on the reference experimental curve, its validation has to be done with other experimental data. In that goal, polarisation curves recorded in different test conditions have been used. The agreement between experimental curves and simulated ones will allow to validate the modelling approach. The comparison is detailed hereafter.

3.1 Validation with different operating conditions

The model has firstly been used with other data recorded at 800°C but with different operating conditions than the calibration curve. In particular, the gas compositions, inlet flow rates and operating mode have been changed. The comparison between the experimental and simulated polarisation curves are presented on Figure V.7 (a) and (b).

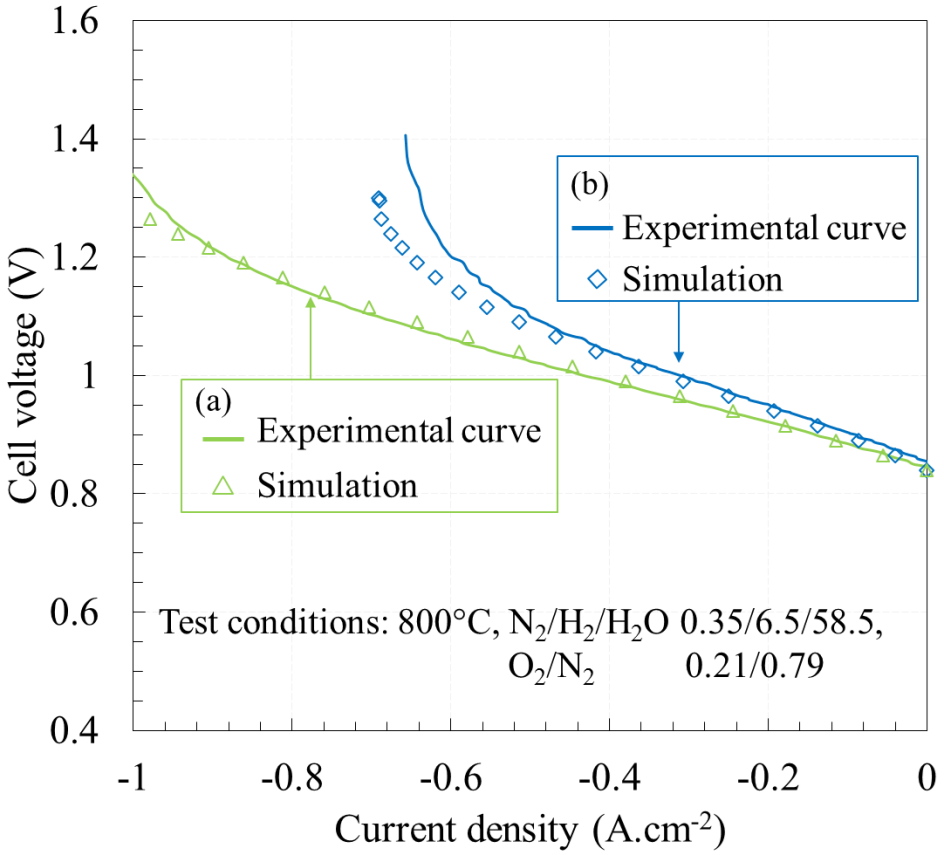

Figure V.7 - Experimental and simulated polarization curves for pristine cells at 800°C in electrolysis mode. Gas flows were (a) 4.31 10^{-5} mol.s^{-1} and 8.62 10^{-5} mol.s^{-1} for H_2 and O_2 electrode respectively, (b) 2.15 10^{-5} mol.s^{-1} and 4.31 10^{-5} mol.s^{-1} for H_2 and O_2 electrode respectively

These test results are extracted from the work of Lucile Bernadet [Bernadet2016] done on a different test bench with the same cells. The cell performance has been measured in electrolysis mode with a mixture $H_2/H_2O/N_2$=6.5/58.5/35 at the hydrogen electrode and air at the oxygen electrode. For the data (a), the gas flow is 18.5 NmL.min^{-1}.cm^{-2} at the H_2 electrode and twice this value at the other side. The experimental curve (b) has been obtained in the same conditions but gas flows divided by two. As can be observed on Figure V.7, there is a good agreement between the experiments and the simulation for these curves. A slight difference is observed on the limiting current of the test with low flow rate (b). This mismatch could be due to experimental difficulty to measure the limiting current at high steam conversion rate. It could also be related to the choice of a simple charge transfer reaction as reactive mechanism in the hydrogen electrode.

The modelling approach validation has been also performed at other temperatures. On Figure V.8, experimental and simulated data are shown at 750°C and 850°C in both polarizations for test done with a ratio H_2/H_2O=50/50. The O_2 electrode is fed with air. These test conditions are equivalent to the ones of tests SOEC_C1, SOEC_C2 and SOFC_C4. There is a perfect match between the experimental data and the simulations at high temperature. The difference is more pronounced at 750°C for data obtained in fuel cell mode. Nevertheless, the simulation has

shown a good agreement with the experiments. The modelling approach is thus validated to describe the cell performance in different operating conditions. In particular, the dissymmetric behavior of the polarisation curve can be explained thanks to the simulation. This result is presented hereafter.

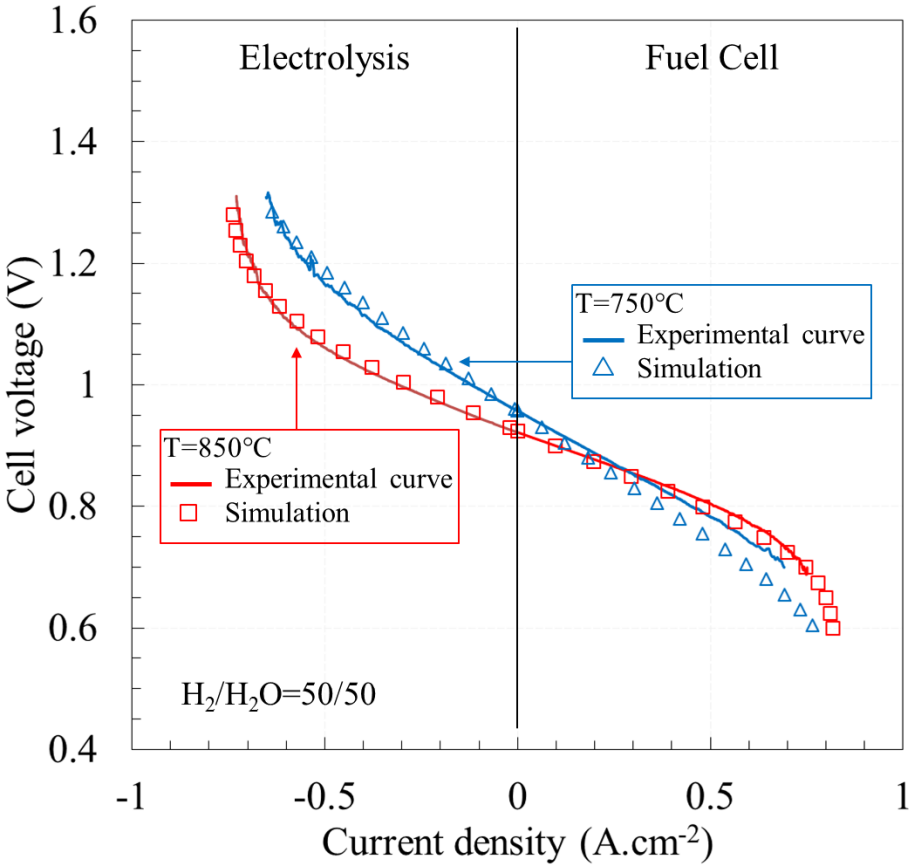

Figure V.8 – Experimental and simulated polarization curves for pristine cells at H_2/H_2O=50/50, O_2/N_2=21/79 and different temperatures. Gas flows were 7.84 10^{-5} mol.s^{-1} and 2.8 10^{-4} mol.s^{-1} for H_2 and O_2 electrode respectively.

3.2 Dissymmetry of the polarisation curve

The polarisation curves present an asymmetry between the fuel cell and the electrolysis mode. This phenomenon is illustrated on Figure V.9 for data recorded at 850°C and a ratio H_2/H_2O=50/50. There is a clear difference between SOFC and SOEC curves at high current density as shown by the symmetrical curve plotted on the graph. As the simulation is able to reproduce this behaviour, the numerical tool can be used to explain the dissymmetry.

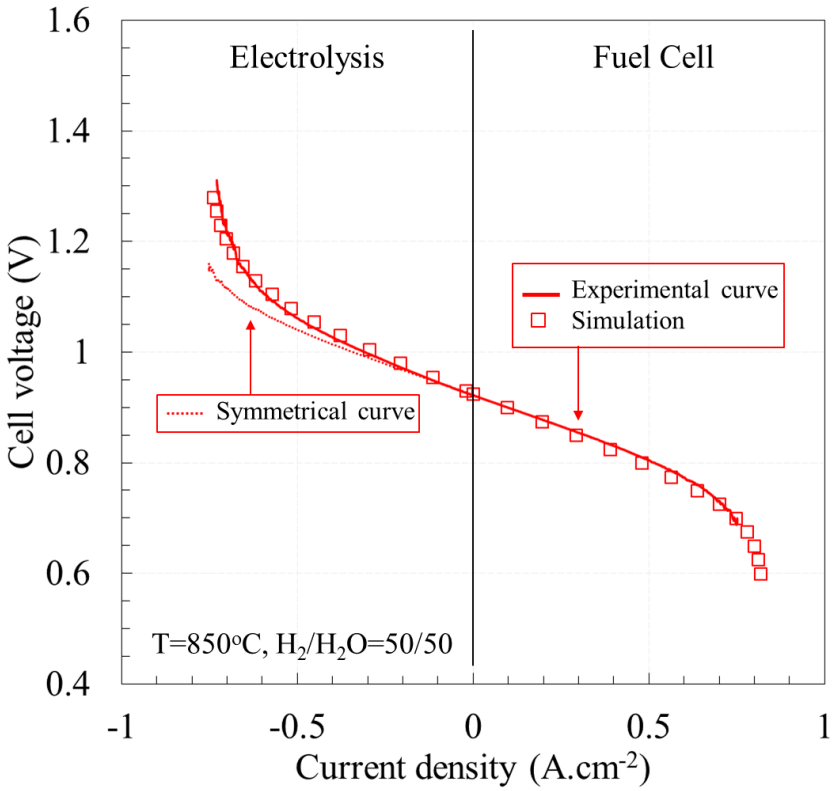

Figure V.9 – Experimental and simulated polarisation curves for a pristine cell at 850°C, H_2/H_2O=50/50. The dissymmetry is highlighted by the symmetrical fuel cell curve reported in electrolysis mode. Gas flows were 7.84 10^{-5} mol.s^{-1} and 2.8 10^{-4} mol.s^{-1} for H_2 and O_2 electrode respectively.

In order to better understand this phenomenon, the overpotential evolutions expressed as a function of the current density can be analysed in these operating conditions. On Figure V.10, the activation and concentration overpotentials are reported for both electrodes. These values have been obtained for the complete cell at 850°C and for a gas composition of H_2/H_2O=50/50:

(i) Overpotential at the oxygen electrode: it can be observed that the concentration overpotentials of the oxygen electrode are extremely limited whatever the current densities. This is due to the low thickness, the relatively large porosity size of this electrode and also because of the low O_2 conversion rates (due to high air inlet flow rate send at the O_2 electrode). Besides, it can be also remarked that the activation overpotentials for this electrode increase with increasing the current density and present quite similar values in both operating modes. As a matter of fact, it can be claimed that the voltage losses at the O_2 electrode are not involved in the asymmetry of the polarization curve between the SOFC and SOEC modes.

(ii) Overpotentials at the hydrogen electrode: the concentration overpotentials at the hydrogen electrode exponentially increases steeply for high current densities because of fuel or steam depletion (due to high fuel utilization and steam conversion rates). These overpotentials represent the main part of the voltage losses in both operating modes. As they exhibits a non-symmetrical behavior as shown in Figure V.6, it can be stated that they are mainly responsible of the dissymmetry of the polarisation curve. In addition, it can be also noticed that the activation overpotentials at the H_2 electrode do not exhibit similar values in both operating

modes. Therefore, in a less extent, they are also involved in the dissymmetry of the polarization curve. A much deeper analysis of these overpotentials can be done thanks to the models:

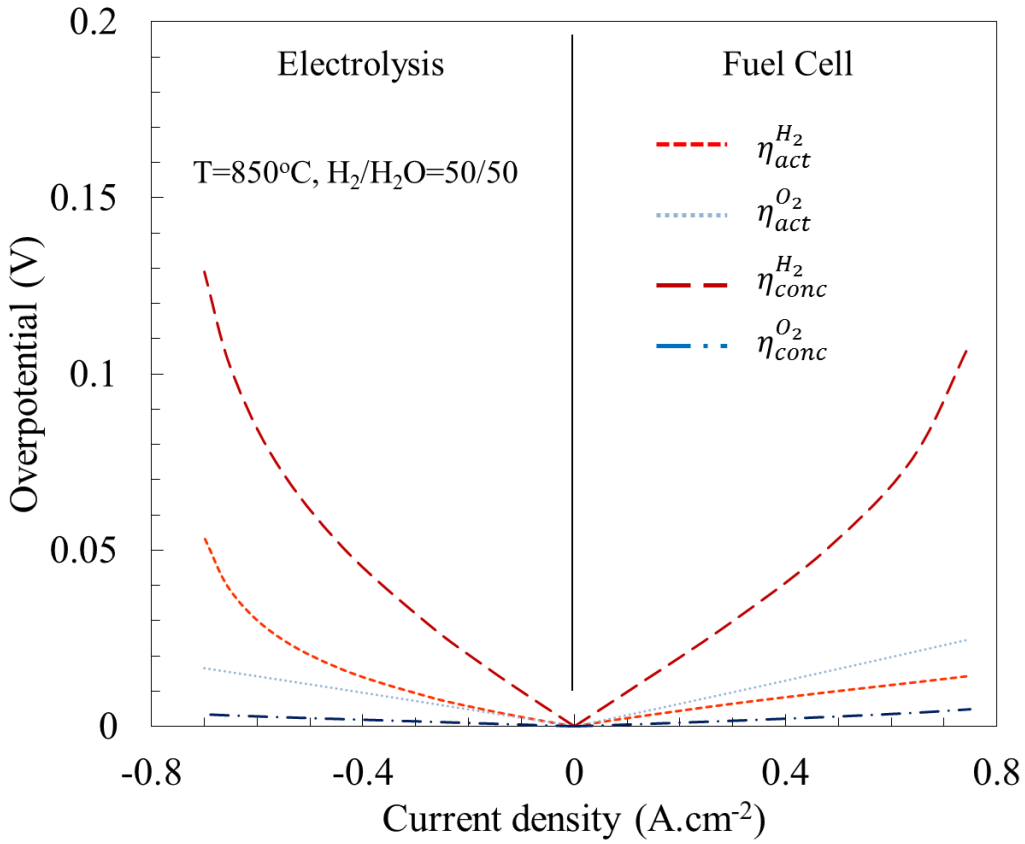

Figure V.10 – Activation and concentration overpotentials obtained with the modelling approach at 850°C, H_2/H_2O=50/50 and air. Gas flows were 7.84 10^{-5} mol.s^{-1} and 2.8 10^{-4} mol.s^{-1} for H_2 and O_2 electrode respectively.

As stated, the concentration overpotential at the H_2 electrode side plays a major role in the asymmetry of the polarisation curve. This effect is related to the gas diffusion in the hydrogen electrode. Indeed, the effective diffusion coefficient for steam is higher than the one for hydrogen in the model. This difference cannot be attributed to the molecular diffusion as the binary diffusion coefficient of H_2O in H_2 and H_2 in H_2O are the same. The dissymmetry is in fact explained by the higher Knudsen diffusion coefficient for H_2O than the one for H_2. Therefore, under electrolysis current, the Knudsen transport limits the mass transfer, which has to supply the electroactive site by steam, and hence, leads to the high concentration overpotentials observed in Figure V.10. This result is in good agreement with the high sensitivity of the model with the pore radius of H_2 electrode introduced for the simulation. Indeed, the Knudsen diffusion coefficient is directly proportional to this parameter.

In addition to the concentration overpotential dissymmetry, the activation overpotential is also contributing to the dissymmetry. It is calculated by the exchange current density law previously presented. The exponent value found for the water partial pressure dependence in this equation is higher than the one for the hydrogen partial pressure (0.61 to 0.07). In electrolysis mode, the exchange current density is lower at high current density as there is less water and thus the

activation overpotential is higher. This is the opposite in fuel cell mode. That dependence on water partial pressure explains the dissymmetry of this overpotential.

All these statements are fully consistent with the results reported in [Njodzefon2012, Njodzefon2013].

4. Modelling, simulation and analysis of SOC degradation

The modelling approach being calibrated and validated to simulate the initial performances, it can be used to explain the degradation. In particular, the fine 3D analysis of the microstructure evolution in the hydrogen electrode can be introduced in the model. In that goal, it is necessary to select a Ni agglomeration law that would be implemented in the modeling approach. A first section is dedicated to the presentation of the best model describing the Ni agglomeration and the decrease of TPB density. Then, these laws are used in the simulation to quantify the contribution of Ni coarsening in the total degradation rates.

4.1 Ni agglomeration law

From the 3D microstructural analyses of the aged cells, it has been observed that the Ni mean particle diameter is clearly increasing upon operation. This evolution is directly connected with the decrease of electrochemically active sites density. This loss in active TPBs lengths is impacting the cell performances. This degradation mechanism is suspected to be significant in the cell voltage losses. In the literature, several laws have been proposed to explain the Ni agglomeration. They can be classified into a physically-based law related to sintering of metallic particles [Simwonis2000, Vassen2001, Faes2009, Chen2011b, Pihlatie2011, Chen2016, Kennouche2016] and a phenomenological approach based on the geometric agglomeration of spheres [Faes2009, Tanasini2009, Nelson2012, Gao2014]. The phenomenological law, usually named as the "capacitor" model in the literature, is given in equation (V.6).

$$r_{Ni} = (r_{Ni}^{max} - r_{Ni}^{0})\left(1 - e^{-k_{Capa}\,t}\right) + r_{Ni}^{0} \qquad \text{(V.6)}$$

The parameters r_{Ni}^{0} and r_{Ni}^{max} are respectively the initial and maximal Ni particle radius and k_{Capa} is the rate constant of the process. Two effects are taken into account in this law. The first one is the mass transport from small particles to bigger ones. The second effect is related to the inhibition of the YSZ backbone on the nickel agglomeration. On Figure V.11, the "capacitor" model is plotted for Ni mean particle diameter obtained at different temperatures. On this figure, data from literature [Jiang2003, Tanasini2009] obtained on similar cells have been added to the post-mortem analyses done in this work. It should be noticed that this law fits accurately the Ni diameter evolution over time. Nevertheless, the asymptotic bounds seem to be reached rashly. While no data are available after long time of operation at 850°C, it appears very restrictive to consider that the Ni diameter evolution is stopped after 2000h. This condition can be discussed by inspecting the time constant of the process $t_s = 1/k_{Capa}$. This

time constant is about 1200 hours for nickel coarsening obtained at 850°C with the data reported on Figure V.11. However, it was estimated at 445 hours by [Tanasini2009] with the same data measured on cells aged until 1000h. By adding new data obtained at the same temperature, the time constant has been pushed back to a higher value. In other words, it seems that the asymptotic value is reached later and later by increasing the duration of the long-term tests. This law could appear too much restrictive to model the Ni agglomeration at 850°C even for very long-term tests.

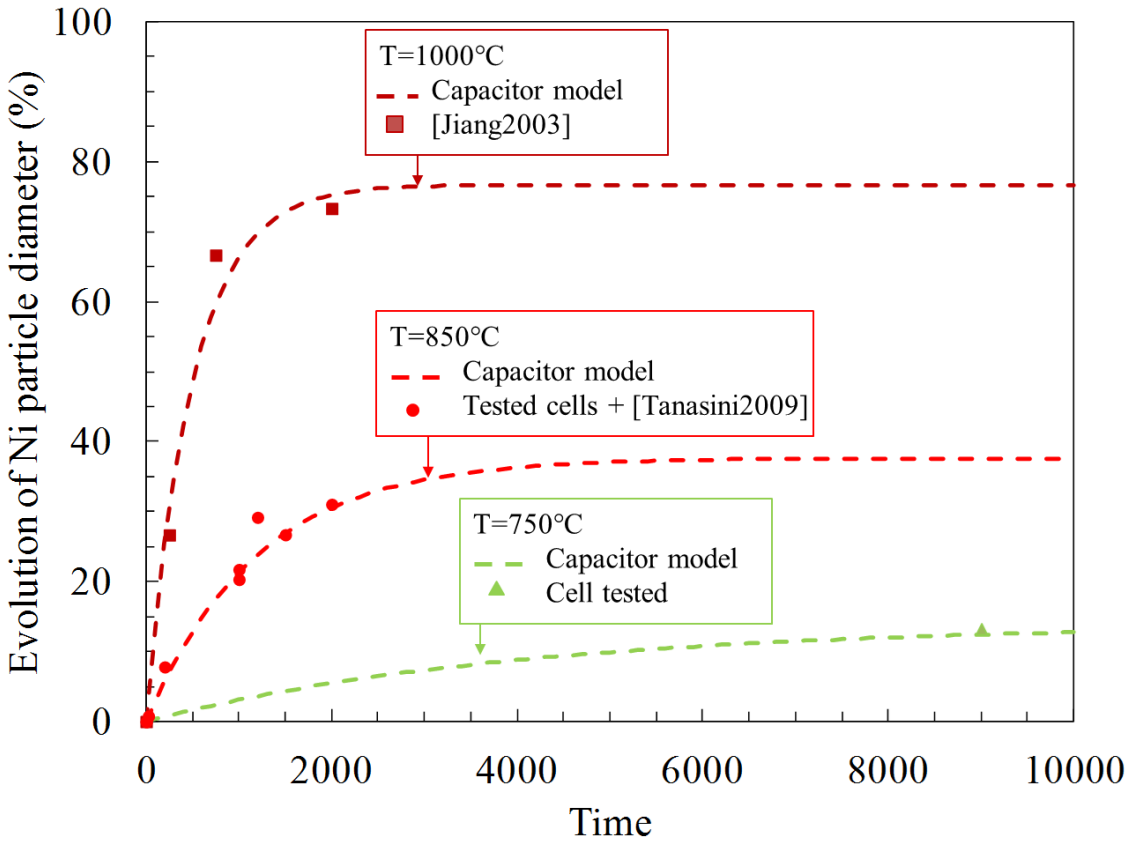

Figure V.11 – Experimental evolution of Ni particle diameter fitted by the capacitor model at different temperatures.

Another possibility to describe the nickel agglomeration is the use of a standard power-law model. It results from the physically-based modelling of the sintering of two metallic particles. The value of the exponent reflects the nature of the mass transfer phenomena involved in the sintering mechanism such as bulk or surface diffusion. This model, which is given by equation (V.7), relates the Ni particle radius to the operating time.

$$r_{Ni}{}^{n} - r_{Ni}^{0}{}^{n} = k_{pow} \times t \tag{V.7}$$

$$\text{with} \quad k_{pow} = k_{pow}^{0} \times e^{-\frac{E_a^{Ni}}{RT}} \tag{V.8}$$

The parameter k_{pow} is the rate constant of the process. The sintering mechanism being thermally activated, the parameter k_{pow} can be expressed by an Arrhenius law as shown in equation (V.8). The value of the exponent *n* is characteristic of the predominant mass transport

mechanism involved in the agglomeration process. Evaporation-condensation corresponds to low exponent $n = 2 - 3$ whereas higher values are related to surface or bulk diffusion processes [Tsyganov2007, Pihlatie2011]. In the literature, some authors [Vassen2001, Chen2016, Kennouche2016] used $n = 4$ to fit data obtained at temperature equal or above 1000°C. They found a rather good agreement of their models with experimental data.

A least square method has been used with our data of Ni particle diameter obtained at 850°C to identify the best fit between the experimental points and the model. An exponent *n* ranging between 7 and 9 gives the best result. As an illustration on Figure V.12, the agglomeration law calculated with $n = 8$ is plotted for the different temperatures. It should be noticed that $n = 7$ is regarded as surface diffusion mechanism for coarsening [Pihlatie2011]. In [Adda1978], the exponent $n = 7$ is related to a surface diffusion mechanism for small particles of about one micrometer or less. It is the case in the studied hydrogen electrode. This high exponent value related to a surface diffusion mechanism is also consistent with the SEM characterizations previously presented (see Chapter IV, section 3.1). Indeed, an exponent around 2-3 related to an evaporation mechanism for the agglomeration is not expected since no Nickel depletion has been observed. The high exponent introduced in the model could be also related to the specific cermet architecture. Indeed, as already mentioned in the previous chapter, the YSZ backbone of the hydrogen electrode prevents the Ni phase from a massive agglomeration. To take into consideration this inhibiting effect of YSZ, a high exponent value is required in the power law model to enhance the asymptotic behaviour of the particle size evolution over the time.

In addition to the exponent value determination, the activation energy of the sintering process has been evaluated with the data presented on Figure V.12. The parameter E_a^{Ni} has been found equal to about 376 kJ.mol^{-1}. In [Kennouche2016], the activation energy for the Nickel agglomeration process in SOC is found between 225 kJ.mol^{-1} and 266 kJ.mol^{-1}. This range of values is high compared to the classical activation energies reported in the literature for the sintering of Nickel particles [Elliot1968]. This apparent discrepancy could be once again due to the YSZ inhibiting effect on Ni sintering. The adhesion between Ni and YSZ being probable strongly thermally activated, it could explain the higher activation for the Ni coarsening in the cermet. Moreover, it has to be mentioned that the scattering in the activation energies is important as it is comprised between 109 kJ.mol^{-1} and 335 kJ.mol^{-1}. These variations are related to the different test conditions such as the particle diameter or the gas composition for the experiments.

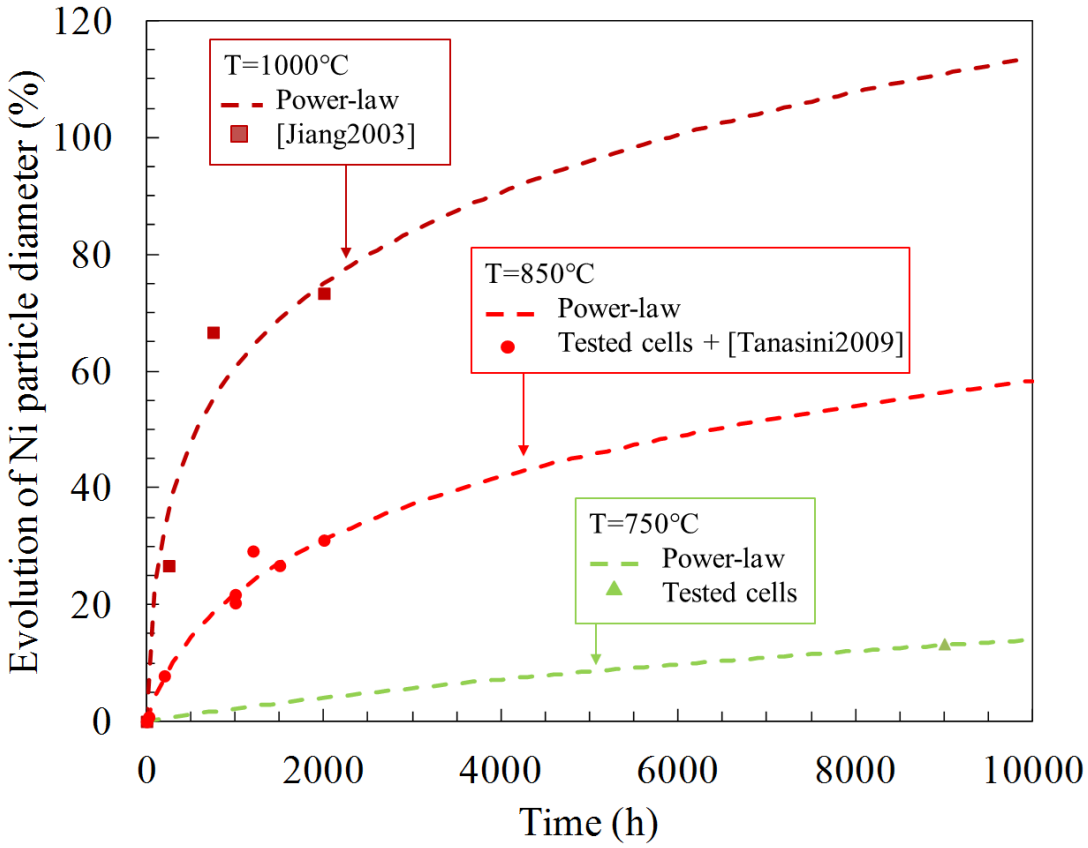

Figure V.12 - Experimental evolution of Ni particle diameter fitted by the power-law model with an exponent equal to 8 at different temperatures.

Besides the identification of the best agglomeration law for the experimental results, the same work has been carried out for the decrease in the density of active TPBs. There are many less studies dedicated to this parameter in the literature. In [Faes2009], a capacitor model similar to the one which describes the nickel particle size evolution has been used. In [Kennouche2016], the density of TPB is related to the particle size by using a geometrical sphere-packing model. In this work, the evolution of the TPB density over time is described by a power-law similar to the one used to describe the growth of the nickel particle diameter:

$$l_{TPB}^{0}{}^{n} - l_{TPB}{}^{n} = k_{pow\_tpb} \times t \qquad \text{(V.9)}$$

The exponent has also been set to 8 in this model. On Figure V.13, the curves of the power-law model are plotted with the experimental results obtained at 750°C and 850°C. The decrease of the active sites is well described by the simulation.

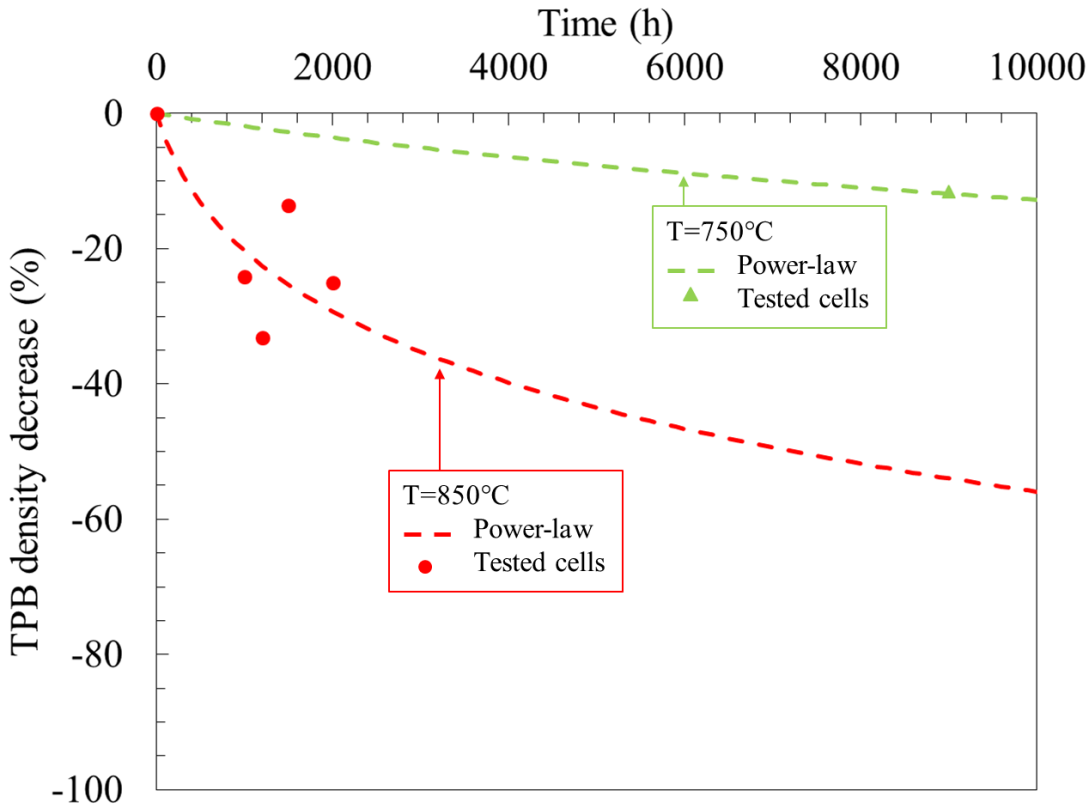

Figure V.13 - Experimental evolution of TPB density fitted by a power-law model with an exponent equal to 8 at different temperatures.

4.2 Contribution of Ni agglomeration on the degradation

From the multi-scale modelling approach, it is possible to study the contribution of nickel agglomeration on the total degradation measured on long-term operations. In that goal, the law of TPB density evolution upon operation has been implemented in the micro-model to determine the new exchange current density. The dependence with the partial pressure and the temperature have been kept as for the reference case. The contribution of nickel coarsening on the performances is detailed for the different tests hereafter.

For the test performed in fuel cell mode at $i = 0.5$ A.cm^{-2}, T=850°C and a ratio H_2/H_2O=50/50 (SOFC_C4), it has been found with the model that the deterioration of the exchange current density is about 10% after 1000h. This change is impacting the activation overpotential calculated for the complete cell. The contribution of nickel agglomeration can thus be estimated from the loss of performance obtained with the modelling approach. On Figure V.14, the cell voltage increase from experiment and simulation are presented over time. It can be seen that the nickel agglomeration is explaining a part of the measured degradation. After 1000h, the cell voltage is decreasing of 1.1 mV according to the simulation. This value corresponds to about 32% of the total degradation rate obtained with the experiment.

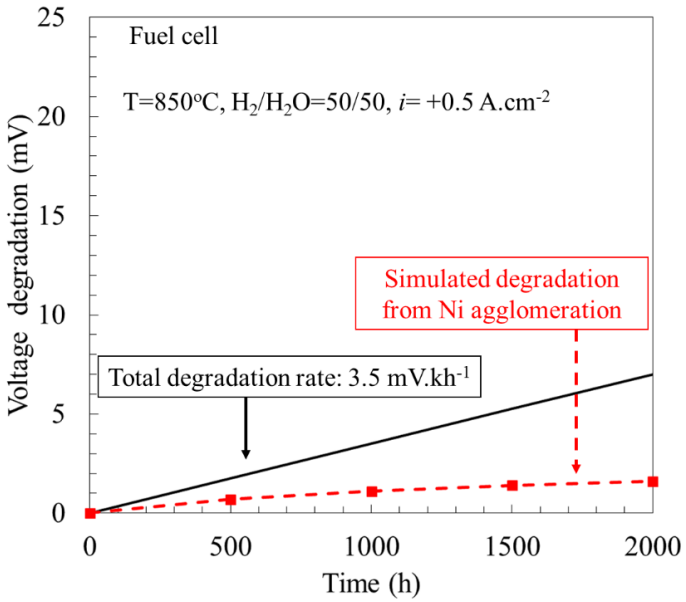

Figure V.14 – Experimental degradation rate and simulated contribution from the Ni agglomeration.

For the cell aged in electrolysis mode at $i = -0.5$ A.cm^{-2}, T=850°C and H_2/H_2O=50/50 (SOEC_C1 and SOEC_C2), the exchange current density is found to decrease in the same order than fuel cell mode after 1000h. This new value can be introduced in the model to reach the degradation contribution of Ni agglomeration in electrolysis. On Figure V.15, the cell voltage increase from experiment and simulation are presented as a function of time. After 1000h, the simulation gives a degradation of 2.4 mV whereas it is 3.5 mV after 2000h. These values are higher than in fuel cell mode. This difference can be explained by the asymmetric response of the cell according to the polarization. However, the nickel agglomeration is found to be responsible of about 19-26% of the experimentally measured degradation rate. In electrolysis, the nickel coarsening is found to represent a smaller part of the total degradation compared to the fuel cell mode. This difference is mainly explained by the higher experimental degradation rate recorded in electrolysis mode.

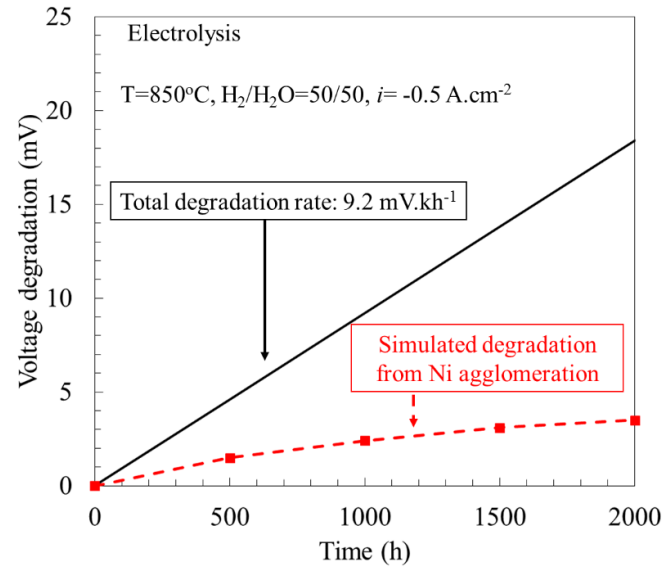

Figure V.15 - Experimental degradation rate and simulated contribution from the Ni agglomeration.

For the test done in fuel cell mode at 750°C under dry hydrogen, the exchange current density decrease is limited to 6% after 9000h of operation. The cell performance evolution has been simulated in these conditions to evaluate the contribution of the nickel agglomeration on the cell degradation. A loss of about 2.2 mV is obtained after 9000h of operation with the simulation what represents about 6% of the experimental degradation.

5. Conclusions of this chapter

The modeling approach used in this work has been presented in this chapter. It is based on models developed at the electrode as well as the cell level. They are strongly connected through the "apparent" electrode exchange current densities that take into account the limitation due to the electrochemical reaction at the macroscopic scale. To complete this approach, it has been required to develop a micro-model for the MIEC materials as used in the studied O_2 electrode.

The determination of the unknown kinetic parameters of the model has been performed by fitting the simulations on an experimental polarisation curve recorded in fuel cell mode at 800°C under dry hydrogen. Once calibrated, all the simulations have been performed without changing any input parameter in the models. With the global approach, we were able to simulate the effect of the gas composition, flows or temperature on the cell performances. Moreover, the dissymmetry of the polarizations curves in fuel cell and electrolysis mode has been mainly explained by the Knudsen diffusion in the H_2 electrode, and in a less extent, by the activation overpotential of the hydrogen electrode.

The models have been used to evaluate the contribution of the nickel agglomeration on the loss of performances measured experimentally. In that goal, evolution laws for the nickel particle diameter and TPB density upon operation have been fitted on the experimental data. It appears that a power-law with an exponent of about 7-9 is well adapted to describe the Ni coarsening. Then, the fitted relation of TPBs density over time has been implemented in the model to quantify the impact of Ni agglomeration on cell performances. It was found that this phenomenon represents about 32% in fuel cell mode and 26% in electrolysis mode of the experimentally measured degradation after 1000h at 850°C. Some other causes can be found to be responsible of the remaining degradation. They are discussed in the last chapter.

Chapter VI:

Discussion

The approach based on electrochemical testing, 3D electrode characterizations and modelling has been successfully applied to investigate the contribution of Nickel agglomeration on the SOC performances. In this chapter, the main results are summarized and discussed in the light of other published data. Based on this discussion, some outlooks for further studies and developments are suggested. In particular, the X-ray holotomography contribution to SOC electrode characterization is detailed and future progresses for the imaging technique are proposed. The 3D volume allowed the quantification of electrode microstructural properties that are essential for the modelling. The potential improvements of the numerical tool are discussed in regard to the statements achieved in this work. The contribution of Nickel agglomeration on experimental degradation rates has been evaluated with the model. The results obtained with this method are detailed and discussed hereafter to explain some observations reported in the literature. It is also highlighted in this chapter that new developments still remain required to understand more deeply the global response and degradation of a SOC. Nevertheless, as presented in the last section, the approach used in this work appears to be fully relevant to extend the analysis to other degradation phenomena or even applications.

1. Contribution of the tomography to SOC electrode characterization

An important achievement of this work is the adaptation of X-ray holotomography for the fine characterization of SOC electrodes. The advantage of nano-holotomography compared to other tomographic techniques (i.e. FIB-SEM and X-ray absorption tomography) has been highlighted in chapter II. It allows reaching a large field of view while keeping a sufficient high spatial resolution in the 3D reconstructions. The state-of-the-art of the phase contrast imaging has been detailed in the same chapter. Then, the modifications brought to the technique to adapt experimental protocols to SOC materials specificities have been described in the chapter III. The reliability of the global process has been especially improved thanks to a new sample preparation and an original acquisition technique. A Xenon P-FIB has been used to extract cylindrical samples from SOC electrodes. This equipment allows to easily control the sample location and its final shape. Moreover, the P-FIB is faster than conventional FIB working with Ga ions so that larger samples can be prepared in less time. The new Nano-Imaging ID16A beamline and acquisition process also contributes to enhance the global quality of the reconstructions obtained by X-ray nano-holotomography as shown in the third chapter. The data acquisition is based on the random displacement of the sample during the scan to compensate wavefront inhomogeneities. Without this method to record the projections, the 3D volumes are unusable because of strong ring artefacts. Finally, 3D reconstructions of both hydrogen and oxygen electrodes have been successfully obtained. The main physical and morphological properties of a pristine cell have been extracted from these volumes with specific tools available at the laboratory.

It should be noticed that the LSCF-GDC composite layer of the oxygen electrode was not reconstructed by holotomography. Indeed, the two ceramic phases could not be distinguished in the 3D image after the phase retrieval process. As illustrated on Figure V.16 for a slice taken

in the 3D reconstruction, the contrast in grey level between LSCF and GDC is very poor and is clearly insufficient to proceed to the image thresholding. This difficulty is probably related to the absorption consideration in the phase retrieval process.

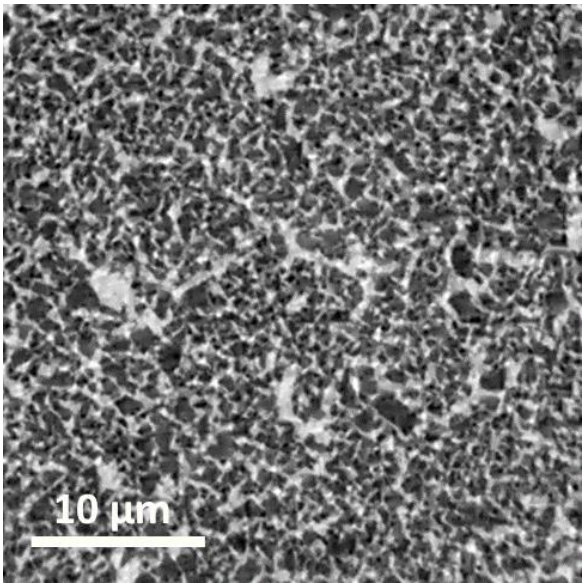

Figure V.16 – View of a slice extracted from a 3D reconstruction obtained by nano-holotomography of a LSCF-GDC electrode. The two solid phases cannot be satisfactorily distinguished (white=porosity, black=solid phases).

For this composite ceramic layer, the use of other imaging techniques could be more appropriate. SEM imaging is known to give a good contrast between the two ceramic phases. The tomographic method based on FIB-SEM appears as one relevant technique to separate LSCF from GDC in the reconstruction. A first work presenting a 3D volume obtained by FIB-SEM on similar electrode has been published recently [Kim2017]. Another way to characterize these materials over large volumes could be the X-ray ptychography. The experimental set-up is shown on Figure V.17a. The sample is scanned in the orthogonal plan to the X-ray beam. Diffraction patterns are recorded over 180° to reach a 3D volume. This technique presents a high potential with an improved resolution and a high material phase sensitivity [Da silva2015]. It allows the reconstruction of 3D electron density maps without any assumptions as weak phase object or negligible absorption [Dierolf2010]. An alternative method is the Near Field Ptychography (NFP) which also gives access to the microstructure as shown in [Stockmar2015]. The experimental set-up for this technique is similar to holotomography as shown on Figure V.17b. Several Fresnel diffraction patterns are recorded for different transverse shifts of the sample. This acquisition process is repeated at different angles to reach a 3D volume. These techniques should give access to large 3D volumes of the LSCF-GDC composite oxygen electrode that could be segmented. It would be fully complementary with the nano-holotomography method.

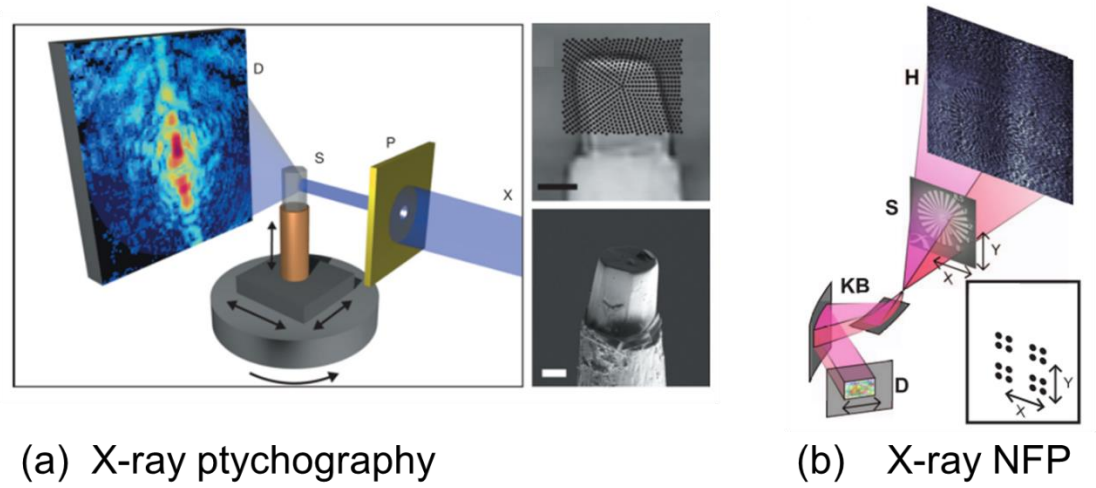

Figure V.17 – Schematic of the experimental set-up used for (a) X-ray Ptychography (extracted from [Dierolf2010]) and (b) X-ray Near Field Ptychography (extracted from [Stockmar2015])

In the work, a special attention has been given to evaluate accurately the spatial resolution of the reconstructions. The measurement has been done directly on the 3D volumes obtained by nano-holotomography by measuring the grey-level profile at the interface between two phases. A spatial resolution of 50 nm has been obtained as shown in chapter III. Other methods can be used to evaluate this parameter as shown by [Holler2014]. In particular, the development of the Fourier Shell Correlation (FSC) [Van Heel2005] appears interesting to refine the assessment of the spatial resolution on 3D volumes. The use of a such method could limit the confusion often found on the determination of this parameter in the literature. For instance, the spatial resolution of 3D reconstructions is sometimes claimed without evidence [Cronin2013]. Some authors have also assessed the spatial resolution on 2D well defined objects and assumed that it is representative for the SOC electrode 3D images [Vila-Comamala2012, Nakajo2016].

The resolution of 50 nm obtained in this work has been strongly validated and appeared to be sufficient to describe accurately the electrodes microstructure. Indeed, it has been shown in the literature that about 10-15 voxels per particle diameter are required to describe accurately the microstructure [Joos2012, Villanova2013]. However, an improvement of this parameter will be necessary when finer microstructure and especially smaller morphological evolutions will be studied. In this objective, the X-ray ptychography appears as a promising imaging technique to enhance the spatial resolution [Da silva2015].

2. Modelling of a SOC in its initial state

The determination of the electrodes microstructure properties can be computed on the 3D reconstructions obtained by X-ray nano-holotomography. As detailed in chapter V, microstructural parameters are essential for the SOC multi scale models. Indeed, the knowledge of these data is mandatory to limit the number of unknown parameters in the simulations. The

physical and thermodynamic data being taken in the literature, the kinetic constants were the last unknown parameters to be adjusted on an experimental curve. This model calibration step has been detailed in chapter V as well as the "top-down" and "bottom-up" links used between the micro and macro-scale models. At the microscopic level, it is assumed that the H_2 electrode mechanism is controlled by a charge transfer at TPBs whereas a new model for the O_2 electrode dedicated to the MIEC materials has been proposed and implemented in the multi-scale approach. It has been shown that the improved numerical tool is able to simulate accurately the cell polarisation curves in different conditions of temperature, gas composition, flow rates or even operating mode in fuel cell or electrolysis modes. Thanks to the simulations, the dissymmetry of the polarisation curve, which was experimentally measured between the two operating modes, has been explained and assigned to a difference in the concentration and activation overpotentials arising at the hydrogen electrode.

In chapter I, it has been shown that the reactive pathway in the hydrogen electrode is described by a series of elementary steps [Bessler2007, Vogler2009]. In fuel cell mode, it is nowadays widely acknowledged that the charge transfer reaction at TPBs is the rate-limiting step of the global process. Under electrolysis conditions, the global reactive pathway could be more complex. Indeed, in addition to the charge transfer, it seems that a gas-solid interaction could also affect the cell response [Grondin2011, Dasari2013]. Therefore, it could be necessary to consider in the electrochemical reactive pathway a co-limitation of the charge transfer with an adsorption step of water molecules at the Nickel surface. This additional step could be easily added to the micro-model of the hydrogen electrode. Nevertheless, as done for the MIEC oxygen electrode [Laurencin2015b], this amelioration of the Ni-YSZ model for cathodic polarisation will require a specific experimental validation on symmetrical cells with a three electrodes set-up.

With this supplementary reaction implemented in the model, it is expected that the dissymmetry between fuel cell and electrolysis operating mode will be increased. Indeed, the electrode activation overpotential should be increased in cathodic polarisation when taking into account this additional limiting step. However, it is worth underlying that the global cell polarisation curve should not be strongly different from the one currently simulated since the cathode activation overpotential only represents a minor contribution to the total cell voltage increase. Despite this expected minor impact on the i-U curve, the integration of this limiting step should be of most importance for electrode microstructural optimisation. Indeed, the optimum microstructure is expected to be different if TPBs or the Ni specific surface area are the main affecting parameter in the reactive mechanism. Finally, this supplementary step could also be essential to investigate some critical operating conditions more sensitive to the reactive pathway.

3. Modelling of SOC degradation

Aside from the description of the initial cell behaviour, the modelling approach is also useful to investigate the contribution of a given degradation mechanism on the global performance. In that goal, a set of long-term tests have been carried out as presented in chapter IV. All the

durability tests have been performed during more than 1000h and the measured degradation rates have been found to range within the state-of-the-art values reported for both fuel cell and electrolysis modes. From a technological point of view, it has been observed that the degradation rates in fuel cell are lower than the ones obtained in electrolysis mode. Moreover, a higher current density leads to a higher "apparent" degradation of the cell whereas the "intrinsic" degradation seems to remain unaffected.

The cells have been characterized by post-mortem analyses. The 2D SEM images revealed that no Nickel depletion has occurred in the cermet whatever the operating conditions. Therefore, in our case, it can be stated that the evaporation-condensation of the Nickel phase is not the mechanism governing the agglomeration. In complementarity with SEM observations, the pristine and aged Ni-YSZ electrodes have been analysed by X-ray nano-holotomography. The reconstructions and their analyses are given in the chapter IV. It has been found that current density is not involved in the Ni particles coarsening. Moreover, steam partial pressure and polarisation appeared as second order parameters whereas time and temperature are controlling parameters strongly affecting the Ni particle size as well as the TPB density.

In this work, the progressive evolution from small particles to bigger ones has been observed over time. The rearrangement of the Nickel phase was found to be directly linked to the decrease of the TPBs density. This significant decrease of electrochemically active sites being expected to lower the cell performances. It has also been shown that the YSZ backbone plays a major role on the Nickel agglomeration mechanism. Indeed, it has been highlighted that the specific surface area between Nickel and gas is decreasing over time whereas the one between the Nickel and YSZ stays stable. This result confirms the expected inhibition effect of the ceramic phase that prevents the Ni phase from a massive agglomeration at the SOFC/SOEC operating temperatures. It should be also noticed that the decrease of the nickel specific surface area in contact with porosity is expected to contribute to the performance degradation by limiting the adsorption of water molecules. This could be more accurately described with the simulation tool by adding an adsorption step in the H_2 electrode model.

The Nickel agglomeration mechanism has been modelled in chapter V. In the literature, two constitutive laws are classically used to fit the experimental results. The first one, a "capacitor" law, is based on a pure geometrical approach. After an initial stage, it assumes that the Ni coarsening can be completely inhibited by the YSZ backbone. This model was found to describe correctly the experimental data obtained in this work. However, its asymptotic behaviour yielding to a maximal bound for the Ni particle size appears to be too restrictive. Indeed, it has been shown that the characteristic time constant for Nickel coarsening is pushed back to higher values as soon as supplementary experimental results obtained for longer ageing time are added to the set of data. The second model for Ni agglomeration mechanism is based on a physical approach. Assuming the sintering of two spherical particles, the growth of the Ni phase size over time can be expressed thanks to a power-law model. It has been found that this model is also able to describe accurately our experimental results with an exponent value comprised between 7 and 9. This is a rather high value for this type of law. Nevertheless, it is consistent with a sintering mechanism which would be based on Ni surface diffusion. Moreover, the high exponent also reflects the inhibiting effect of the YSZ backbone. Indeed, a

high exponent of the power law model is required to describe the asymptotic behaviour of the Ni particle size plotted as a function of time. From this analysis, it appears that both the "capacitor" and "power law" models are able to fit our data. It has been shown that the first one corresponds to a lower bound for Ni agglomeration since it provides data that underestimates the Ni particle size after very long operation time. Conversely, the power law model could lead to overestimate the Ni coarsening. From that point of view, additional very long-term tests (more than 4000h) could be performed to clarify the evolution of the Nickel particle radius over time.

Finally, the TPB density evolution over time has been modelled using a similar power-law as shown in chapter V. The TPB decrease is directly affecting the cell performances as highlighted with the simulation results. Some authors choose to link the TPB evolution to the Ni particle agglomeration law by using a geometrical sphere-packing model [Kennouche2016]. The identification of an accurate morphological law for this degradation mechanism would allow describing better its evolution.

4. Performances degradation over time

The models of the Nickel agglomeration and of the TPB density decrease have been introduced in the cell performance simulation tool as shown in chapter V. The contribution of Ni coarsening on the global cell degradation has been quantified for the long-term tests presented in chapter IV. The durability experiments performed at 850°C under a composition ratio H_2/H_2O=50/50 presented a degradation rate of 3.5 $mV.kh^{-1}$ in fuel cell mode and 9.2 $mV.kh^{-1}$ in electrolysis. The simulation revealed that the Ni coarsening of the H_2 electrode can explain around 30% of the total degradation rate measured in fuel cell mode after 1000h. This contribution would be reduced to about 25% for the cells aged in electrolysis mode.

Up to now, the modelling approach has only been used to quantify the Nickel agglomeration contribution on the total degradation rates in experimental conditions studied. As the model has been validated, it can be used to investigate other operating points or ageing time using interpolation or even extrapolation. The cell voltage losses due to the Nickel agglomeration has been computed for a cell aged in electrolysis mode after 1000h, 10000h and 17500h (2 years). These two long durations are representative of a real industrial application. On Figure V.18, the cell voltage degradations are shown for a cell operated at T_{ageing}=750°C and 850°C. The resulting cell voltage loss has also been assessed with the model at two different temperatures $T_{assessment}$ after the simulation of the long-term test (performed at T_{ageing})

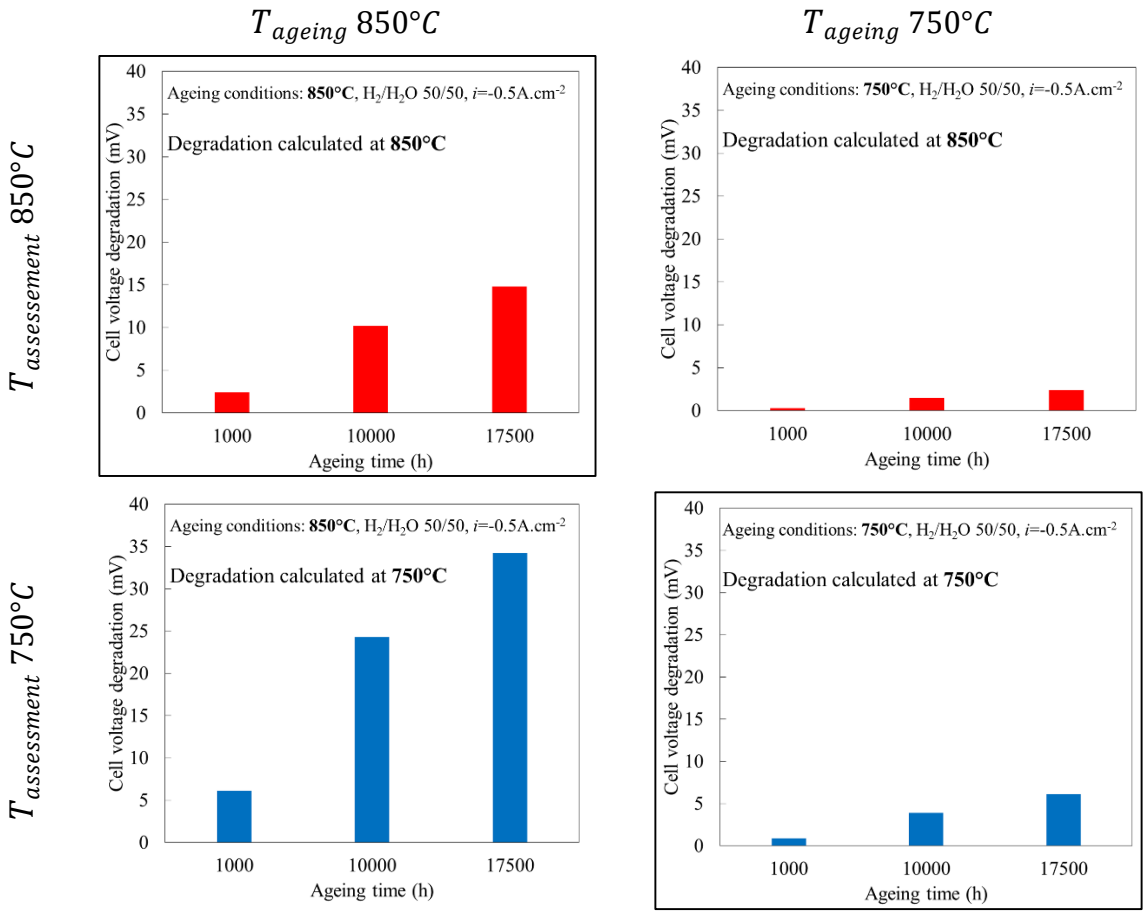

Figure V.18 – Simulated degradation due to Nickel agglomeration over time for two different operating conditions T_{ageing} and estimated at two different temperatures $T_{assessment}$.

By comparing the diagrams horizontally, it can be observed that the degradation is expected to be significantly higher for the cell aged at the highest operating temperature. This result is consistent with the microstructural analysis done in this work. Moreover, it appears that the temperature to assess the degradation rate would strongly affect the results as shown comparing the diagrams vertically on Figure V.17. Indeed, for a given ageing temperature, the cell degradation rate is found to be lower when "estimated" at 850°C rather than 750°C. This statement is explained because the electrode activation overpotential is lower at high temperature. This analysis could explain the surprising results reported in the literature telling that the degradation rate would be lowered at higher temperature [Hagen2006, Hauch2006, Diethelm2013, Fang2015, Kotisaari2016].

However, it can be noticed that the Nickel agglomeration contributes only for a part of the total degradation rate. Moreover, this mechanism is not sensitive to the polarisation mode, and hence, cannot explain the higher degradation rates recorded in electrolysis mode compared to the fuel cell mode (with similar condition of cell ageing). The remaining part of the total degradation must be attributed to other degradation mechanisms. For the hydrogen electrode, as described in chapter I, the second most critical degradation mechanism in terms of criticality is pollutant poisoning. These pollutants would come from raw materials, glass seal or even

from the gas. To detect these impurities, an equipment with a high chemical sensitivity is required as well as a high resolution since poisoning is expected to be located near the TPBs. The oxygen electrode and the electrolyte can also participate to the total degradation rate. Their contributions are discussed in the following section.

5. Oxygen electrode degradation

The electrolyte and the oxygen electrode could also take part to the degradation measured after the long-term tests. In this work, the pristine O_2 electrode in LSCF has been characterized by X-ray nano-holotomography as presented in chapter III. The main microstructural parameters have been extracted from the 3D reconstruction. The electrode morphology has been studied after ageing by SEM imaging on cross sectional samples. No evolutions were detected, this result being in good agreement with [Lay2013b, Wang2016] who shown the stability of LSCF in classical operating conditions for SOCs.

In addition to the 3D reconstructions of the hydrogen electrode, the GDC/YSZ interface has also been imaged by nano-holotomography. Even though the contrast is low between YSZ and GDC layers as shown on Figure V.19, a new phase has been detected inside the porosities of the GDC close to the electrolyte for the cells aged in electrolysis mode.

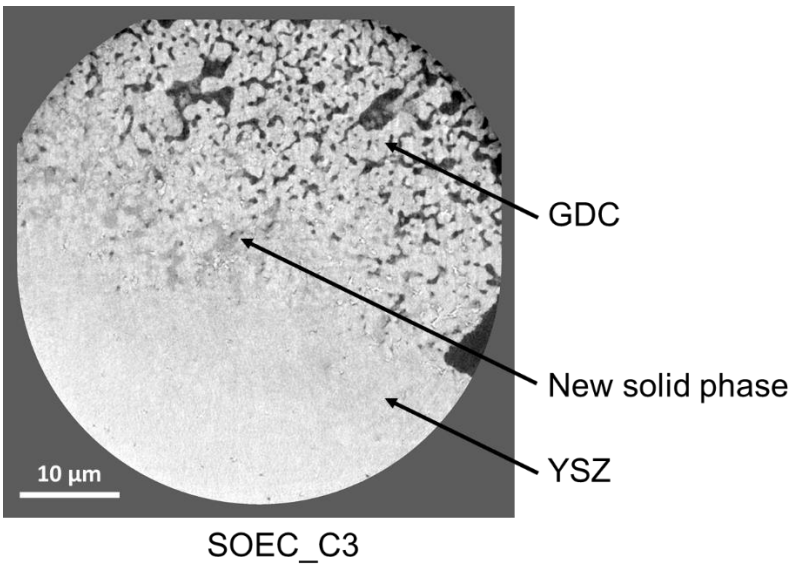

Figure V.19 – Slice extracted from a 3D reconstruction of SOEC_C3 showing the GDC/YSZ interface. A new solid phase is observable in the GDC porosities.

Supplementary characterizations of this interface have been performed by SEM-EDX in collaboration with Sergii Pylypko. A higher contrast between the different phases was obtained using Secondary Electron detector (SE) at Working Distance (WD) comprised from 12 to 18 mm and tension (EHT) of 4 kV. To perform elemental analysis of phases using EDX, WD was decreased to 8 mm and EHT was fixed at 15 kV. The SEM and EDX analyses are presented on Figure V.20 for the pristine and aged cells in both polarisations.

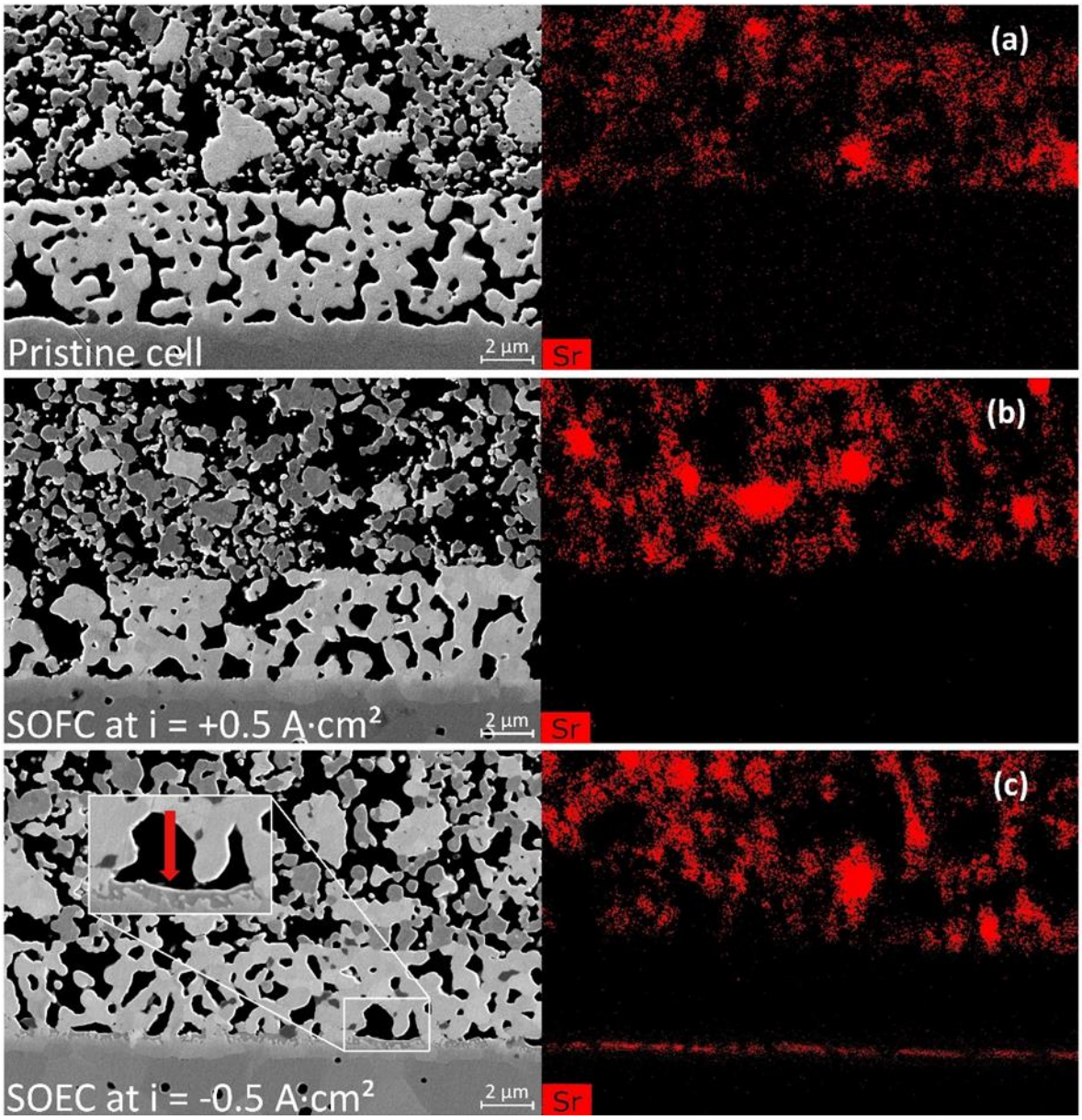

Figure V.20 - SEM-EDX images taken at GDC/YSZ interface complemented by Sr chemical maps (a) for pristine cell, (b) for SOFC_C4 and (c) for SOEC_C1

In the pristine cell, the bright grey level corresponds to GDC, the dark grey levels to the YSZ and LSCF phases whereas the porosity appears in black. No additional solid phase is observed in the reference cell. For the cell aged in fuel cell mode, the observations are quite similar. Only a small amount of a secondary phase is observed at the interface with the electrolyte. Conversely, the cell aged in electrolysis mode exhibits clearly additional new solid phase. It is found all along the GDC/YSZ interface resulting in a quasi-continuous layer inside the porosities of the GDC barrier layer. The same locations have been analysed by EDX and the resulting Sr chemical maps are shown in Figure V.20. For the cell operated in electrolysis mode, it reveals that the new solid phase contains a high quantity of Sr. As a consequence, it can be stated that the layer formed during operation is probably made of $SrZrO_3$ and due to the reaction between the Sr coming from LSCF and Zr coming from the electrolyte [Wang2014].

It should be noticed that the observation of this new solid phase in the cells aged in electrolysis mode can be directly correlated with the presence of nano-porosities in the electrolyte. As shown on Figure V.21, a clear line of porosities located at the grain boundaries of the electrolyte is observed by SEM for these samples. This kind of degradation has already been detected by several authors [Tietz2013, The2015]. The formation of the nano-porosities could be due to Zr^{4+} ions diffusion to the interface with the oxygen electrode [The2015].

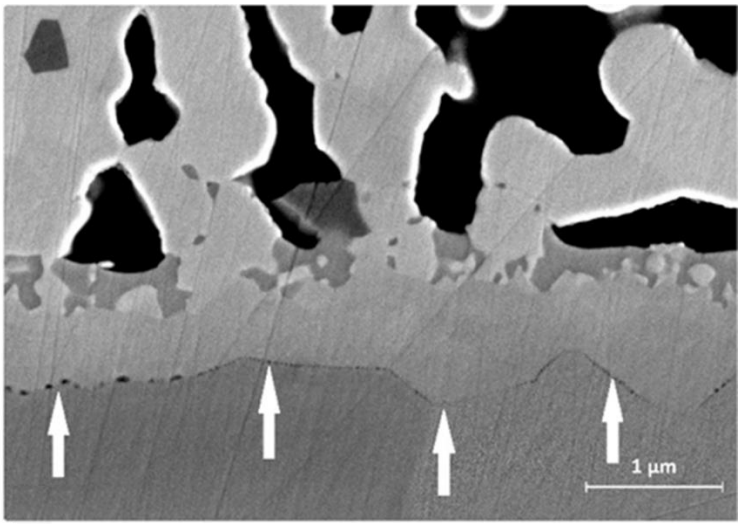

Figure V.21 – SEM image at the interface GDC/YSZ for SOEC_C1. The white arrows highlight the line of nano-pores observed at grain boundaries in the electrolyte.

These preliminary results on the oxygen electrode degradation require deeper characterizations. It could be interesting to clearly identify the crystallographic phase of the reactive layer. Moreover, the modelling approach could be used to propose a mechanism for this degradation and also quantify its contribution to the global degradation. However, these first observations could allow proposing another contribution to the degradation measured experimentally. It should especially affect the cell performances in electrolysis mode and explain the difference measured between fuel cell and electrolysis degradation rates.

6. General aspect of the proposed methodology

The approach used in this work was based on an integrated methodology coupling electrochemical experiments, post-test characterizations and multi-scale modelling. In the present study, it has been shown that such methodology was relevant to study the degradation of SOCs. Indeed, by improving the three aspects of the approach, it has been possible to propose a better understanding of the underlying mechanisms that link the performances and the microstructure to the degradation rates. New results on the Nickel agglomeration have been obtained as shown in chapter V.

This approach could be extended to other cases. A cell using classical materials with good performances and stability over time has been used in this work. It is worth mentioning that SOC manufacturing routes allow obtaining a large variety of electrode microstructures. Therefore, some commercial SOCs present an optimized microstructure with the H_2 electrode composed of a bilayer [Tietz2002, Laurencin2012, Villanova2013]. With some specific

analysis, the proposed methodology could be adapted for the different microstructures of SOCs. The method could also be extended to other materials. For instance, Nickelates are nowadays considered as promising oxygen electrode for SOCs [Mauvy2003, Lalanne2008, Sun2010, Chen2015]. Their analysis would require the development of a new micro-model for this kind of electrode to use the approach. Finally, the method could also be adapted for different operating conditions as co-electrolysis or operation under pressure [Aicart2014, Bernadet2015]. It requires adjusting and calibrating the simulation parameters to these new electrochemical conditions.

7. Conclusions of this chapter

In this chapter, the main results obtained in this work have been summarized and put into perspective against the literature. In particular, the possible improvement for the imaging of SOCs have been discussed. New techniques such as X-ray Ptychography or X-ray Near-Field Ptychography seem relevant to characterize materials with improved contrasts and high spatial resolution. More specific methods to measure the spatial resolution should also be developed and shared to avoid any confusion in the literature.

The modelling approach used in this work has allowed describing accurately the cell performances. This numerical tool could be further improved by adding a co-limiting step related to the adsorption of steam on the Ni surface which is suspected to happen and to be somewhat limiting in electrolysis mode. For the degradation, very long-term tests over 4000h would allow refining the fit of the power-law coarsening model for Nickel agglomeration.

The contribution of the Nickel coarsening on the degradation has been evaluated in different conditions with the numerical tool. It was found to explain 25% to 30% of the overall degradation rate. In addition, the simulations highlighted the effect of the temperatures at which the degradation is occurring and measured. The lower activation overpotential at higher temperature could explain some results from the literature where the highest degradation rates are surprisingly reported for the lower operating temperature.

As the degradation rates measured experimentally cannot be fully explained by the Nickel agglomeration contribution, some preliminary observation of the electrolyte and oxygen electrodes have been made. They revealed other degradation mechanisms such as nano-porosities or material reactivity that are specific of the electrolysis operation. These preliminary observations open a new filed of investigations to study the underlying degradation mechanism. Finally, the genericity of the approach used in this work could allow using it to study other microstructure, materials or operating conditions.

Conclusions

This work aimed to investigate the links between the microstructure, the performances and the degradation of high temperature solid oxide cells operated in fuel cell and electrolysis modes. Indeed, the durability of these electrochemical devices is still insufficient regarding the competitiveness and the economic viability of the technology. Therefore, the SOCs durability constitutes nowadays a major issue that remains to be solved. The deep understanding of the degradation mechanisms is thus essential in order to propose relevant solutions and recommendations to limit the deterioration of SOC performances upon operation. In that perspective, an integrated approach coupling long-term durability tests, 3D electrode characterizations based an advance X-ray tomography method and a multi-scale modelling framework has been used to investigate the SOCs degradation operated in both fuel cell and electrolysis modes.

First of all, a review on the state-of-the-art of high temperature Solid Oxide Cells (SOCs) has been made. Based on this bibliography review, it has been shown that the durability of SOCs has been significantly improved during the last years even if their degradation mechanisms are not precisely understood. Among the different causes of the performance loss, it was found that Nickel agglomeration in the hydrogen electrode shows a high level of criticality. Such a statement led us to focus the present work mainly on this problematic. Nevertheless, some improvements in the global approach were required before studying the Ni coarsening mechanism.

First improvements were related to the 3D electrode characterizations. In order to improve the global quality of the reconstructions, the complete protocol for nano-holotomography has been modified and adapted to the SOCs materials. In particular, a specific sample preparation method has been developed using a Xenon Plasma-FIB. This equipment allows maintaining a full control on the shape, the size and the localization where the sample is taken from the cell. It is worth noting that the final cylindrical shape obtained with this tool is especially well adapted to tomography experiments. The samples have been imaged on the new Nano-Imaging ID16A beamline at the ESRF. This new beamline has been designed to obtain three-dimensional reconstructions with a large field of view while maintaining a high spatial resolution. A new acquisition method, using random displacements during the tomography scan, has been implemented in the process to achieve 3D reconstructions that are free of artefacts. A phase retrieval procedure based on a multi-distance Paganin's method, followed by 10-15 constrained CGM iterations, was shown to give consistently good results. The spatial resolution has been estimated at 50 nm by grey-level edge measurements; sufficient to describe accurately the microstructures of both hydrogen and oxygen electrodes. All the different materials present in the electrodes could be identified and segmented, except for the LSCF-GDC mixture of composite oxygen electrodes.

A second milestone was the achievement of relevant durability experiments. A set of long-term tests ($t \geq 1000h$) has been carried out in different operating conditions. Degradation rates ranging within the state-of-the-art values ($0.4 \leq r_{deg}\ (\%.kh^{-1}) \leq 7$) have been obtained in fuel cell and electrolysis modes. While the ageing conditions have been confirmed to affect the

measured degradation rates, fine post-test characterizations were required to analyse the intrinsic permanent degradation. Post-mortem analyses were especially dedicated to the identification of the Nickel agglomeration. High Resolution SEM observations of cell polished cross sections have revealed that no Nickel depletion occurs in the hydrogen electrode in our operating conditions. Furthermore, the H_2 electrodes of aged cells have been reconstructed by nano-holotomography. As expected, the measurement on the 3D volumes of the cermet morphological parameters has shown a clear reorganization of small Ni particles to bigger ones. It has been found that the Ni coarsening is highly sensitive to the operating temperature and time. However, the analyses have also revealed that the current density is not affecting the Nickel coarsening, whereas, the steam partial pressure and the polarisation can be considered as second order parameters for this degradation mechanism. Finally, the suspected inhibition effect of the YSZ backbone, that prevents the Nickel from a massive agglomeration, has been emphasized by the microstructural analyses of the specific surface areas.

The data extracted from the 3D volumes have been fitted by a Ni coarsening power law model that was implemented in an in-house multi-scale modelling framework. Beforehand, it has been mandatory to enrich the numerical tool with a new module describing the studied oxygen electrode made of a Mixed Ionic Electronic Conductor operated in fuel cell and electrolysis modes. The global completed modelling approach has been calibrated on a single experimental curve recorded at 800°C in fuel cell mode. Then, simulations have been performed in different operating conditions (gas flows, composition and temperature) and compared to experimental polarisation curves. A good agreement has been obtained with these data allowing the validation of the model.

Once the model validated, it has been chosen to describe the Nickel agglomeration with a physics-based power law model related to the sintering of metallic particles. The exponents allowing to fit accurately the experimental data were found to range around 7-9. These rather high values for such power law model are consistent with a surface diffusion mechanism for small particles. It is also suspected that the high exponent of the agglomeration model reflects the inhibiting effect of the YSZ backbone, and hence, could be related to the specific cermet architecture.

With this completed modelling framework, the contribution of the Nickel agglomeration to the total degradation rate measured experimentally has been evaluated. It has been found that the microstructural change in the H_2 electrode explains about 30% of the total degradation in fuel cell mode and about 20-25% in electrolysis mode at 850°C after 1000-2000h. Moreover, thanks to the modelling approach, it has been highlighted that the temperature for the assessment of the degradation plays also a role on the result. Indeed, due to the low activation overpotential at high temperature, it is possible to measure higher degradation rates at lower temperature while the intrinsic degradation of electrodes is less pronounced. This result could explain some surprising results reported in the literature.

Finally, the results of this work have been discussed in the light of the recent literature. It appears that this approach based on electrochemical tests, characterization and modelling is relevant to study SOCs and has allowed bringing new elements of comprehension. It could be extended to other microstructure, cell materials or operating conditions. Moreover, some

improvements are possible for each section of the approach. Promising imaging techniques such as X-ray ptychography are developed with higher spatial resolution and possibly better phase sensitivity. The modelling approach could be refined by adding elementary reaction steps in the micro-models and could be enlarged for taking into account pressurized conditions or co-electrolysis operation. The Nickel agglomeration being only a part of the total degradation, other mechanisms should be investigated and quantified such as poisoning of the hydrogen electrode. Electrolyte and O_2 electrode should also be characterized more thoroughly since preliminary results showed significant changes in these layers, especially for cells aged in electrolysis mode.

Bibliography

[Aarberg1998] R. J. Aaberg, R. Tunold, M. Mogensen, R. W. Berg, R. Ødegaård, "Morphological Changes at the Interface of the Nickel-Yttria Stabilized Zirconia Point Electrode", Journal of The Electrochemical Society 145(7) (1998) 2244-2252
[Ackmann2003] T. Ackmann, L. G. J. De Haart, W. Lehnert, D. Stolten, "Modeling of mass and heat transport in planar substrate type SOFCs", Journal of the Electrochemical Society 150(6) (2003) A783-A789
[Adda1978] Y. Adda, J. M. Dupouy, J. Philibert, Y. Quere, "Elements de métallurgie physique, Volume 4 : Diffusion Transformation", CEA Editor (1978) 991
[Adijanto2011] L. Adijanto, R. Küngas, F. Bidrawn, R. J. Gorte, J. M. Vohs, "Stability and performance of infiltrated La 0.8 Sr 0.2 Co x Fe 1− x O 3 electrodes with and without Sm 0.2 Ce 0.8 O 1.9 interlayers", Journal of Power Sources 196(14) (2011) 5797-5802
[Adler1996] S. B. Adler, J. A. Lane, B. C. H. Steele, "Electrode kinetics of porous mixed-conducting oxygen electrodes", Journal of the Electrochemical Society 143(11) (1996) 3554-3564
[Adler2010] S. B. Adler, W. G. Bessler, "Elementary kinetic modeling of SOFC electrode reactions", Handbook of Fuel Cells—Fundamentals, Technology and Applications, ed. W. Vielstich, H. A. Gasteiger, A. Lamm, H. Yokokawa, John Wiley & Sons, Chichester, UK (2010) vol. 5
[Aguiar2002] P. Aguiar, D. Chadwick, L. Kershenbaum, "Modelling of an indirect internal reforming solid oxide fuel cell", Chemical Engineering Science 57(10) (2002) 1665-1677
[Aicart2014] J. Aicart, J. Laurencin, M. Petitjean, L. Dessemond, "Experimental Validation of Two-Dimensional H2O and CO2 Co-Electrolysis Modeling", Fuel Cells 14(3) (2014) 430-447
[Anderson2006] A. B. Anderson, E. Vayner, "Hydrogen oxidation and proton transport at the Ni–zirconia interface in solid oxide fuel cell anodes: Quantum chemical predictions", Solid State Ionics 177(15) (2006) 1355-1359
[Andersson2010] M. Andersson, J. Yuan, B. Sundén, "Review on modeling development for multiscale chemical reactions coupled transport phenomena in solid oxide fuel cells", Applied Energy 87(5) (2010) 1461-1476
[Ardigo2011] M. R. Ardigò, A. Perron, L. Combemale, O. Heintz, G. Caboche, S. Chevalier, "Interface reactivity study between La 0.6 Sr 0.4 Co 0.2 Fe 0.8 O 3− δ (LSCF) cathode material and metallic interconnect for fuel cell", Journal of Power Sources 196(4) (2011) 2037-2045
[Arhatari2004] B. D. Arhatari, A. P. Mancuso, A. G. Peele, K. A. Nugent, "Phase contrast radiography: image modeling and optimization", Review of scientific instruments 75(12) (2004) 5271-5276
[Autissier2004] N. Autissier, D. Larrain, J. Van Herle, D. Favrat, "CFD simulation tool for solid oxide fuel cells", Journal of Power Sources 131(1) (2004) 313-319
[Barsoukov2005] E. Barsoukov, J. Ross Macdonald, eds. “Impedance spectroscopy: theory, experiment, and applications”, John Wiley & Sons (2005)
[Baruchel2006] J. Baruchel, J.-Y. Buffiere, P. Cloetens, M. Di Michiel, E. Ferrie, W. Ludwig, E. Maire, L. Salvo, "Advances in synchrotron radiation microtomography", Scripta Materialia 55(1) (2006) 41-46
[Baumann2006] F. S. Baumann, J. Fleig, H.-U. Habermeier, J. Maier, "Impedance spectroscopic study on well-defined (La, Sr)(Co, Fe) O 3− δ model electrodes", Solid State Ionics 177(11) (2006) 1071-1081
[Beauger1999] C. Beauger, “Elaboration, caractérisation et modélisation des phénomènes de luminescence du monoaluminate de strontium dopé à l’europium et au dysprosium SrAl2O4”, Thesis Chemical and Process Engineering, Ecole Nationale Supérieure des Mines de Saint-Etienne (1999)

[Berg2012] C. F. Berg, "Re-examining Archie's law: Conductance description by tortuosity and constriction", Physical Review E 86(4) (2012) 046314
[Bernadet2015] L. Bernadet, G. Gousseau, A. Chatroux, J. Laurencin, F. Mauvy, M. Reytier, "Influence of pressure on solid oxide electrolysis cells investigated by experimental and modeling approach", International Journal of Hydrogen Energy 40(38) (2015) 12918-12928
[Bernadet2016] L. Bernadet, "Etude de l'effet de la pression sur l'électrolyse de l'eau à haute température", Thesis manuscript, Université de Bordeaux (2016)
[Bessiere1996] M. Bessière, "Introduction au rayonnement synchrotron et à ses avantages", Le Journal de Physique IV 6(C4) (1996) 511-535
[Bessler2005] W. G. Bessler, "A new computational approach for SOFC impedance from detailed electrochemical reaction–diffusion models", Solid State Ionics 176(11) (2005) 997-1011
[Bessler2007] W. G. Bessler, S. Gewies, M. Vogler, "A new framework for physically based modeling of solid oxide fuel cells", Electrochimica Acta 53(4) (2007) 1782-1800
[Bieberle2001] A. Bieberle, L. P. Meier, L. J. Gauckler, "The electrochemistry of Ni pattern anodes used as solid oxide fuel cell model electrodes", Journal of the Electrochemical Society 148(6) (2001) A646-A656
[Bieberle2002] A. Bieberle, L. J. Gauckler, "State-space modeling of the anodic SOFC system Ni, H 2–H 2 O| YSZ", Solid State Ionics 146(1) (2002) 23-41
[Bleuet2013] P. Bleuet, G. Audoit, J.-P. Barnes, J. Bertheau, Y. Dabin, H. Dansas, J.-M. Fabbri, B. Florin, P. Gergaud, A. Grenier, G. Haberfehlner, E. Lay, J. Laurencin, R. Serra, J. Villanova, "Specifications for Hard Condensed Matter Specimens for Three-Dimensional High-Resolution Tomographies", Microsc. Microanal. 19(3) (2013) 726-739
[Blum2005] L. Blum, W. A. Meulenberg, H. Nabielek, R. Steinberger-Wilckens, "Worldwide SOFC technology overview and benchmark", International Journal of Applied Ceramic Technology 2(6) (2005) 482-492
[Blum2013] L. Blum, U. Packbier, I. C. Vinke, L. G. J. de Haart, "Long-Term Testing of SOFC Stacks at Forschungszentrum Jülich", Fuel Cells 13(4) (2013) 646-653
[Bohic2012] S. Bohic, M. Cotte, M. Salomé, B. Fayard, M. Kuehbacher, P. Cloetens, G. Martinez-Criado, R. Tucoulou, J. Susini, "Biomedical applications of the ESRF synchrotron-based microspectroscopy platform", Journal of structural biology 177(2) (2012) 248-258
[Boin2006] M. Boin, A. Haibel, "Compensation of ring artefacts in synchrotron tomographic images", Optics Express 14(25) (2006) 12071-12075
[Bonse1965] U. Bonse, M. Hart, "An X-ray interferometer," Appl. Phys. Lett. 6(8) (1965) 155–156
[Borglum2015] B. P. Borglum, H. Ghezel-Ayagh, "Development of Solid Oxide Fuel Cells at Versa Power Systems and FuelCell Energy", ECS Transactions 68(1) (2015) 89-94
[Born2005] M. Born, E. Wolf, "Principle of Optics", 7th ed. Pergamon Press, Oxford, New York, (2005)
[Bracewell1967] R.N. Bracewell, A.C. Riddle, "Inversion of fan-beam scans in radio astronomy", The Astrophysical Journal 150 (1967) 427–434
[Brandon2004] N. P. Brandon, A. Blake, D. Corcoran, D. Cumming, A. Duckett, K. El-Koury, D. Haigh, C. Kidd, R. Leah, G. Lewis, C. Matthews, "Development of metal supported solid oxide fuel cells for operation at 500–600 C", Journal of Electrochemical Energy Conversion and Storage 1(1) (2004) 61-65
[Bravin2003] A. Bravin, "Exploiting the x-ray refraction contrast with an analyser: the state of the art," J. Phys. D Appl. Phys. 36 (2003) A24–A29
[Brisse2008] A. Brisse, J. Schefold, M. Zahid, "High temperature water electrolysis in solid oxide cells", International Journal of Hydrogen Energy 33(20) (2008) 5375-5382

[Bronnikov1999] A.V. Bronnikov, "Reconstruction formulas in phase-contrast tomography", Optics Communications 171(4) (1999) 239-244
[Brus2014] G. Brus, K. Miyawaki, H. Iwai, M. Saito, H. Yoshida, "Tortuosity of an SOFC anode estimated from saturation currents and a mass transport model in comparison with a real micro-structure", Solid State Ionics 265 (2014) 13-21
[Bucher2011] E. Bucher, W. Sitte, "Long-term stability of the oxygen exchange properties of (La, Sr) 1− z (Co, Fe) O 3− δ in dry and wet atmospheres", Solid State Ionics, 192(1) (2011) 480-482
[Burvall2011] A. Burvall, U. Lundström, P.A.C. Takman, D.H. Larsson, H.M. Hertz. "Phase retrieval in X-ray phase-contrast imaging suitable for tomography", Optics express 19(11) (2011) 10359-10376
[Bushuev2001] V. A. Bushuev, A. P. Petrakov, "X-ray phase contrast of laser-heated air space", Crystallography Reports 46(2) (2001) 171-175
[Cai2012] Z. Cai, M. Kubicek, J. Fleig, B. Yildiz, "Chemical Heterogeneities on La0. 6Sr0. 4CoO3− δ Thin Films• Correlations to Cathode Surface Activity and Stability", Chem. Mater. 24(6) (2012) 1116-1127
[Cardone2005] G. Cardone, K. Grünewald, A. C. Steven, "A resolution criterion for electron tomography based on cross-validation", Journal of structural biology 151(2) (2005) 117-129
[Carmona2008] A. Carmona, P. Cloetens, G. Devès, S. Bohic, R. Ortega, "Nano-imaging of trace metals by synchrotron X-ray fluorescence into dopaminergic single cells and neurite-like processes", Journal of Analytical Atomic Spectrometry 23(8) (2008) 1083-1088
[Carraro2012] T. Carraro, J. Joos, B. Rüger, A. Weber, E. Ivers-Tiffée, "3D finite element model for reconstructed mixed-conducting cathodes: I. Performance quantification", Electrochimica Acta 77 (2012) 315-323
[Chen2003] X. J. Chen, K. A. Khor, S. H. Chan, "Identification of O 2 reduction processes at yttria stabilized zirconia| doped lanthanum manganite interface", Journal of Power Sources 123(1) (2003) 17-25
[Chen2010] X. Chen, Y. Zhen, J. Li, S. P. Jiang, "Chromium deposition and poisoning in dry and humidified air at (La 0.8 Sr 0.2) 0.9 MnO 3+ δ cathodes of solid oxide fuel cells", International Journal of Hydrogen Energy 35(6) (2010) 2477-2485
[Chen2011] K. Chen, S. P. Jiang, "Failure mechanism of (La, Sr) MnO 3 oxygen electrodes of solid oxide electrolysis cells", International Journal of Hydrogen Energy 36(17) (2011) 10541-10549
[Chen2011b] H. Y. Chen, H. C. Yu, J. S. Cronin, J. R. Wilson, S. A. Barnett, K. Thornton, "Simulation of coarsening in three-phase solid oxide fuel cell anodes", Journal of Power Sources 196(3) (2011) 1333-1337
[Chen2014] Y.K. Chen-Wiegart, F.E. Camino, J. Wang, "Sample Preparation of Energy Materials for X-ray Nanotomography with Micromanipulation", ChemPhysChem 15(8) (2014) 1587-1591
[Chen2015] Y. Chen, W. Zhou, D. Ding, M. Liu, F. Ciucci, M. Tade, Z. Shao, "Advances in cathode materials for solid oxide fuel cells: complex oxides without alkaline earth metal elements", Advanced Energy Materials 5(18) (2015)
[Chen2016] Y. C. K. Chen-Wiegart, D. Kennouche, J. S. Cronin, S. A. Barnett, J. Wang, "Effect of Ni content on the morphological evolution of Ni-YSZ solid oxide fuel cell electrodes", Applied Physics Letters 108(8) (2016) 083903
[Cloetens1996] P. Cloetens, R. Barrett, J. Baruchel, J.-P. Guigay, M. Schlenker, “Phase objects in synchrotron radiation hard x-ray imaging” J. Phys. D. Appl. Phys. 29(1) (1996) 133–146
[Cloetens1999a] P. Cloetens, “Contribution to Phase Contrast Imaging, Reconstruction and Tomography with Hard Synchrotron Radiation Principles, Implementation and Applications,” Thesis (1999)

[Cloetens1999b] P. Cloetens, W. Ludwig, J. Baruchel, D. Van Dyck, J. Van Landuyt, J. P. Guigay, M. Schlenker, "Holotomography: Quantitative phase tomography with micrometer resolution using hard synchrotron radiation x rays", Applied physics letters 75(19) (1999) 2912-2914
[Coan2005] P. Coan, E. Pagot, S. Fiedler, P. Cloetens, J. Baruchel, A. Bravin, "Phase-contrast X-ray imaging combining free space propagation and bragg diffraction," J. Synchrotron Radiat. 12(2) (2005) 241–245
[Coan2006] P. Coan, "DEVELOPMENT AND APPLICATION OF THE ANALYZER-BASED IMAG- ING TECHNIQUE WITH HARD SYNCHROTRON RADIATION", Thesis Biological Physics. European Synchrotron Radiation Facility (ESRF) (2006)
[Coffey2003] G. W. Coffey, L. R. Pederson, P. C. Rieke, "Competition between bulk and surface pathways in mixed ionic electronic conducting oxygen electrodes", Journal of the Electrochemical Society 150(8) (2003) A1139-A1151
[Costamagna1998] P. Costamagna, P. Costa, V. Antonucci, "Micro-modelling of solid oxide fuel cell electrodes", Electrochimica Acta 43(3) (1998) 375-394
[Costamagna1998b] P. Costamagna, K. Honegger, "Modeling of solid oxide heat exchanger integrated stacks and simulation at high fuel utilization", Journal of the Electrochemical Society 145(11) (1998) 3995-4007
[Costamagna2004] P. Costamagna, A. Selimovic, M. Del Borghi, G. Agnew, "Electrochemical model of the integrated planar solid oxide fuel cell (IP-SOFC)", Chemical Engineering Journal 102(1) (2004) 61-69
[Cronin2013] J. S. Cronin, Y. K. Chen-Wiegart, J. Wang, S. A. Barnett, "Three-dimensional reconstruction and analysis of an entire solid oxide fuel cell by full-field transmission X-ray microscopy", Journal of Power Sources 233 (2013) 174-179
[Da silva2015] J. C. da Silva, K. Mader, M. Holler, D. Haberthür, A. Diaz, M. Guizar-Sicairos, W. C. Cheng, Y. Shu, J. Raabe, A. Menzel, J. A. van Bokhoven, "Assessment of the 3 D Pore Structure and Individual Components of Preshaped Catalyst Bodies by X-Ray Imaging", ChemCatChem 7(3) (2015) 413-416
[Dasari2013] H. P. Dasari, S.-Y. Park, J. Kim, J.-H. Lee, B.-K. Kim, H.-J. Je, H.-W. Lee, K. J. Yoon, "Electrochemical characterization of Ni–yttria stabilized zirconia electrode for hydrogen production in solid oxide electrolysis cells", Journal of Power Sources 240 (2013) 721-728
[David2002] C. David, B. Nöhammer, H. H. Solak, E. Ziegler, "Differential x-ray phase contrast imaging using a shearing interferometer", Applied Physics Letters 81(17) (2002) 3287-3289
[Davis1996] T. J. Davis, "X-ray diffraction imaging using perfect crystals", Journal of X-ray Science and Technology, 6(4) (1996) 317-342
[Davis1997] G. R. Davis, J. C. Elliott, "X-ray microtomography scanner using time-delay integration for elimination of ring artefacts in the reconstructed image", Nuclear Instruments and Methods in Physics Research Section A: Accelerators, Spectrometers, Detectors and Associated Equipment 394(1) (1997) 157-162
[del Rio2004] M. S. del Río, R. J. Dejus. "XOP 2.1—A New Version of the X-ray Optics Software Toolkit", in AIP Conference Proceedings, edited by Tony Warwick, Joachim Stöhr, Howard A. Padmore, and John Arthur, 705(1) (2004) 784-787
[Delaforce2007] P. M. Delaforce, J. A. Yeomans, N. C. Filkin, G. J. Wright, R. C. Thomson, "Effect of NiO on the Phase Stability and Microstructure of Yttria-Stabilized Zirconia", Journal of the American Ceramic Society 90(3) (2007) 918-924
[Déportes1994] C. Déportes, M. Duclot, P. Fabry, J. Fouletier, A. Hammou, M. Kleitz, E. Siebert, J. L. Souquet, "Electrochimie des solides:«les applications de l'électrochimie des solides»", Press universitaire de Grenoble (1994) 343-428

[Deseure2005] J. Deseure, Y. Bultel, L. Dessemond, E. Siebert, "Modelling of dc and ac responses of a planar mixed conducting oxygen electrode", Solid State Ionics 176(3) (2005) 235-244
[Dierolf2010] M. Dierolf, A. Menzel, P. Thibault, P. Schneider, C. M. Kewish, R. Wepf, O. Bunk, F. Pfeiffer, "Ptychographic X-ray computed tomography at the nanoscale", Nature 467(7314) (2010) 436-439
[Diethelm2013] S. Diethelm, J. Van Herle, D. Montinaro, O. Bucheli, "Electrolysis and Co-Electrolysis Performance of SOE Short Stacks", Fuel Cells 13(4) (2013) 631-637
[Doran2001] S. J. Doran, K. K. Koerkamp, M. A. Bero, P. Jenneson, E. J. Morton, W. B. Gilboy, "A CCD-based optical CT scanner for high-resolution 3D imaging of radiation dose distributions: equipment specifications, optical simulations and preliminary results", Physics in medicine and biology 46(12) (2001) 3191-3213
[Doucet2011] J. Doucet, J. Baruchel, "Rayonnement synchrotron et applications", Les Techniques de l'Ingénieur P2700 (2011) 1-30
[Drousissard2010] P.A. Douissard, A. Cecilia, T. Martin, V. Chevalier, M. Couchaud, T. Baumbach, K. Dupré, M. Kühbacher, A. Rack, "A novel epitaxially grown LSO-based thin-film scintillator for micro-imaging using hard synchrotron radiation.," J. Synchrotron Radiat. 17(5) (2010) 571–83
[Eaton1997] J. W. Eaton, D. Bateman, S. Hauberg, "Gnu octave", Network theory Ltd. Bristol, UK, (1997)
[Ebbesen2010] S. D. Ebbesen, M. Mogensen, "Exceptional durability of solid oxide cells", Electrochemical and Solid-State Letters 13(9) (2010) B106-B108
[Elliot1968] A. G. Elliot, Z. A. Munir, "The sintering of nickel/aluminium spheres to nickel plates", Journal of Materials Science 3(2) (1968) 150-157
[Ender2012] M. Ender, J. Joos, T. Carraro, E. Ivers-Tiffée, "Quantitative characterization of LiFePO4 cathodes reconstructed by FIB/SEM tomography", Journal of The Electrochemical Society 159(7) (2012) A972-A980
[Enrico2014] A. Enrico, P. Costamagna, "Model of infiltrated La 1− x Sr x Co 1− y Fe y O 3− δ cathodes for intermediate temperature solid oxide fuel cells", Journal of Power Sources 272 (2014) 1106-1121
[Faes2009] A. Faes, A. Hessler-Wyser, D. Presvytes, C. G. Vayenas, "Nickel–zirconia anode degradation and triple phase boundary quantification from microstructural analysis", Fuel cells 9(6) (2009) 841-851
[Fang2015] Q. Fang, L. Blum, N. H. Menzler, "Performance and Degradation of Solid Oxide Electrolysis Cells in Stack", Journal of The Electrochemical Society 162(8) (2015) F907-F912
[Fergus2005] J. W. Fergus, "Metallic interconnects for solid oxide fuel cells", Materials Science and Engineering A397(1) (2005) 271-283
[Ferguson1996] J. R. Ferguson, J. M. Fiard, R. Herbin, "Three-dimensional numerical simulation for various geometries of solid oxide fuel cells", Journal of Power Sources 58(2) (1996) 109-122
[Fleig2007] J. Fleig, R. Merkle, J. Maier, "The p (O 2) dependence of oxygen surface coverage and exchange current density of mixed conducting oxide electrodes: model considerations", Physical Chemistry Chemical Physics 9(21) (2007) 2713-2723
[Foerster1980] E. Förster, K. Goetz, P. Zaumseil, "Double crystal diffractometry for the characterization of targets for laser fusion experiments", Kristall und Technik 15(8) (1980) 937-945
[Gao2014] S. Gao, J. Li, Z. Lin, "Theoretical model for surface diffusion driven Ni-particle agglomeration in anode of solid oxide fuel cell", Journal of Power Sources 255 (2014) 144-150

[Gao2016] Z. Gao, L. V. Mogni, E. C. Miller, J. G. Railsback, S. A. Barnett, "A perspective on low-temperature solid oxide fuel cells", Energy & Environmental Science 9(5) (2016) 1602-1644
[Gelb1999] L. D. Gelb, K. E. Gubbins, "Pore size distributions in porous glasses: a computer simulation study", Langmuir 15(2) (1999) 305-308
[Ghezel2013] H. Ghezel-Ayagh, "Advances in SOFC Development at FuelCell Energy ", 14th Annual SECA Workshop Pittsburgh (2013)
[Gong2014] M. Gong, R. S. Gemmen, D. S. Mebane, K. Gerdes, X. Liu, "Simulation of surface-potential driven ORR kinetics on SOFC cathode with parallel reaction pathways", Journal of The Electrochemical Society 161(3) (2014) F344-F353
[Goodman1996] J.W. Goodman, "Introduction to Fourier Optics", McGraw-Hill, San Francisco, (1996)
[Goodwin2009] D. G. Goodwin, H Zhu, A M. Colclasure, R. J. Kee, "Modeling electrochemical oxidation of hydrogen on Ni–YSZ pattern anodes", Journal of The Electrochemical Society 156(9) (2009) B1004-B1021
[Grondin2011] D. Grondin, J. Deseure, P. Ozil, J-P. Chabriat, B. Grondin-Perez, A. Brisse, "Computing approach of cathodic process within solid oxide electrolysis cell: Experiments and continuum model validation", Journal of Power Sources 196(22) (2011) 9561-9567
[Grosjean2006] A. Grosjean, O. Sanséau, V. Radmilovic, A. Thorel, "Reactivity and diffusion between La 0.8 Sr 0.2 MnO 3 and ZrO 2 at interfaces in SOFC cores by TEM analyses on FIB samples", Solid State Ionics 177(19) (2006) 1977-1980
[Grunbaum2009] N. Grunbaum, L. Dessemond, J. Fouletier, F. Prado, L. Mogni, A. Caneiro, "Rate limiting steps of the porous La 0.6 Sr 0.4 Co 0.8 Fe 0.2 O 3− δ electrode material", Solid State Ionics 180(28) (2009) 1448-1452
[Guan2016] Y. Guan, X. Dong, L. Zhang, G. Liu, Z. Liang, S. Chen, L. Chen, X. Zhang, Y. Xiong, H. Wang, Y. Tian, "Effects of nickel oxide impurities on the microstructure and electrical properties of a nickel–yttria-stabilized zirconia anode", International Journal of Hydrogen Energy (2016) 1-11
[Guigay1977] J.P. Guigay, "Fourier-transform analysis of Fresnel diffraction patterns and in-line holograms," Optik 49(1) (1977) 121-125
[Guigay1978] J.P. Guigay, "The ambiguity function in diffraction and isoplanatic imaging by partially coherent beams," Opt. Commun. 26(2) (1978) 136-138
[Guinier1994] A. Guinier, "X-ray diffraction in crystals, imperfect crystals and amorphous bodies", Courier Dover Publications (1994)
[Gureyev1995] T.E. Gureyev, A. Roberts, K. A. Nugent, "Phase retrieval with the transport-of-intensity equation: matrix solution with use of Zernike polynomials", JOSA A12(9) (1995) 1932-1941
[Haas1967] A. Haas, G. Matheron, J. Serra, "Morphologie mathématique et ganulométries en place", Extrait des Annales des Mines (1967)
[Haering2005] C. Haering, A. Roosen, H. Schichl, "Degradation of the electrical conductivity in stabilised zirconia system: Part I: yttria-stabilised zirconia", Solid State Ionics 176(3) (2005) 261-268
[Hagen2006] A. Hagen, R. Barfod, P. V. Hendriksen, Y.-L. Liu, S. Ramousse, "Degradation of anode supported SOFCs as a function of temperature and current load", Journal of The Electrochemical Society 153(6) (2006) A1165-A1171
[Hajimolana2011] S. A. Hajimolana, M. A. Hussain, W. M. Ashri Wan Daud, M. Soroush, A. Shamiri, "Mathematical modeling of solid oxide fuel cells: A review", Renewable and Sustainable Energy Reviews 15(4) (2011) 1893-1917

[Harris2015a] W. M. Harris, W. K. S. Chiu, "Determining the representative volume element size for three-dimensional microstructural material characterization. Part 1: Predictive models", Journal of Power Sources 282 (2015) 552-561
[Harris2015b] W. M. Harris, W. K. S. Chiu, "Determining the representative volume element size for three-dimensional microstructural material characterization. Part 2: Application to experimental data", Journal of Power Sources 282 (2015) 622-629
[Hassmann2001] K. Hassmann, "SOFC Power Plants, the Siemens-Westinghouse Approach", Fuel Cells 1(1) (2001) 78-84
[Hatae2015] T. Hatae, K. Sato, T. Somekawa, Y. Matsuzaki, S. Amaha, M. Yoshikawa, Y. Mugikura, K. Miyara, T. Oshima, S. Taniguchi, K. Sasaki, "Durability Assessment of SOFC Stacks with Several Types of Structures for Thermal Cycles during Their Lifetimes on Residential Use", ECS Transactions 68(1) (2015) 2209-2216
[Hauch2006] A. Hauch, S. H. Jensen, S. Ramousse, M. Mogensen, "Performance and durability of solid oxide electrolysis cells", Journal of The Electrochemical Society 153(9) (2006) A1741-A1747
[Hauch2008] A. Hauch, S. D. Ebbesen, S. H. Jensen, M. Mogensen, "Solid oxide electrolysis cells: microstructure and degradation of the Ni/yttria-stabilized zirconia electrode", Journal of The Electrochemical Society 155(11) (2008) B1184-B1193
[Hauch2011] A. Hauch, M. Mogensen, A. Hagen, "Ni/YSZ electrode degradation studied by impedance spectroscopy—Effect of p (H 2 O)", Solid State Ionics 192(1) (2011) 547-551
[Hernandez2005] E. Hernández-Pacheco, M. D. Mann, P. N. Hutton, D. Singh, K. E. Martin, "A cell-level model for a solid oxide fuel cell operated with syngas from a gasification process", International Journal of Hydrogen Energy 30(11) (2005) 1221-1233
[Hilpert1996] K. Hilpert, D. Das, M. Miller, D. H. Peck, R. Weiss, "Chromium vapor species over solid oxide fuel cell interconnect materials and their potential for degradation processes", Journal of The Electrochemical Society 143(11) (1996) 3642-3647
[Hino2004] R. Hino, K. Haga, H. Aita, K. Sekita, "38. R&D on hydrogen production by high-temperature electrolysis of steam", Nuclear Engineering and Design 233(1) (2004) 363-375
[Hjalmarsson2013] P. Hjalmarsson, X. Sun, Y. L. Liu, M. Chen, "Influence of the oxygen electrode and inter-diffusion barrier on the degradation of solid oxide electrolysis cells", Journal of Power Sources 223 (2013) 349-357
[Holler2014] M. Holler, A. Diaz, M. Guizar-Sicairos, P. Karvinen, E. Färm, E. Härkönen, M. Ritala, A. Menzel, J. Raabe, O. Bunk, "X-ray ptychographic computed tomography at 16 nm isotropic 3D resolution", Sci. Rep 4(3857) (2014) 10-1038
[Holm2006] E.A. Holm, P.M. Duxbury, “Three-dimensional materials science,” Scr. Mater. 54 (2006) 1035–1040
[Holzer2011] L. Holzer, B. Iwanschitz, T. Hocker, B. Münch, M. Prestat, D. Wiedenmann, U. Vogt, P. Holtappels, J. Sfeir, A. Mai, T. Graule, "Microstructure degradation of cermet anodes for solid oxide fuel cells: Quantification of nickel grain growth in dry and in humid atmospheres", Journal of Power Sources 196(3) (2011) 1279-1294
[Holzer2011b] L. Holzer, B. Münch, B. Iwanschitz, M. Cantoni, Th. Graule, “Quantitative relationships between composition, particle size, triple phase boundary length and surface area in nickel-cermet anodes for Solid Oxide Fuel Cells”, Journal of power Sources 196 (2011) 7076-7089
[Holzer2013] L. Holzer, B. Iwanschitz, T. Hocker, L. Keller, O. Pecho, G. Sartoris, P. Gasser, B. Muench, "Redox cycling of Ni–YSZ anodes for solid oxide fuel cells: Influence of tortuosity, constriction and percolation factors on the effective transport properties", Journal of Power Sources 242 (2013) 179-194
[Holzer2013b] L. Holzer, D. Wiedenmann, B. Münch, L. Keller, M. Prestat, P. Gasser, I. Robertson, B. Grobéty, "The influence of constrictivity on the effective transport properties of

porous layers in electrolysis and fuel cells", Journal of Materials Science 48(7) (2013) 2934-2952
[Hubert2016] M. Hubert, J. Laurencin, P. Cloetens, J. C. Da Silva, F. Lefebvre-Joud, P. Bleuet, A. Nakajo, E. Siebert, "Role of microstructure on electrode operating mechanisms for mixed ionic electronic conductors: From synchrotron-based 3D reconstruction to electrochemical modeling", Solid State Ionics 294 (2016) 90-107
[Iosolevitch1997] A. Ioselevich, A. A. Kornyshev, W. Lehnert, "Degradation of solid oxide fuel cell anodes due to sintering of metal particles correlated percolation model", Journal of The Electrochemical Society 144(9) (1997) 3010-3019
[Ishii1991] M. Ishii, M. Kobayashi, “Single crystals for radiation detectors,” Prog. Cryst. Growth Charact. 23 (1991) 245–311
[Iwata1996] T. Iwata, "Characterization of Ni-YSZ Anode Degradation for Substrate-Type Solid Oxide Fuel Cells", Journal of The Electrochemical Society 143(5) (1996) 1521-1525
[Iwata2000] M. Iwata, T. Hikosaka, M. Morita, T. Iwanari, K. Ito, K. Onda, Y. Esaki, Y. Sakaki, S. Nagata, "Performance analysis of planar-type unit SOFC considering current and temperature distributions", Solid State Ionics 132(3) (2000) 297-308
[Izzo2008] J.R. Izzo, A.S. Joshi, K.N. Grew, W.K.S. Chiu, A. Tkachuk, S.H. Wang, W. Yun, “Nondestructive reconstruction and analysis of SOFC anodes using X-ray computed tomography at sub-50 nm resolution”, Journal of the Electrochemical Society 155 (2008) B504-B508
[Jacobson2005] N. S. Jacobson, E. J. Opila, D. L. Myers, E. H. Copland, "Thermodynamics of gas phase species in the Si–O–H system", The Journal of Chemical Thermodynamics 37(10) (2005) 1130-1137
[Jenneson2002] P. M. Jenneson, W. B. Gilboy, E. J. Morton, P. J. Gregory, "An X-ray micro-tomography system optimised for the low-dose study of living organisms", Applied radiation and isotopes 58(2) (2003) 177-181
[Jensen2001] K. V. Jensen, S. Primdahl, I. Chorkendorff, M. Mogensen, "Microstructural and chemical changes at the Ni/YSZ interface", Solid State Ionics 144(3) (2001) 197-209
[Jensen2003] K. V. Jensen, R. Wallenberg, I. Chorkendorff, M. Mogensen, "Effect of impurities on structural and electrochemical properties of the Ni–YSZ interface", Solid State Ionics 160(1) (2003) 27-37
[Jha2014] D. Jha, H. O. Sørensen, S. Dobberschütz, R. Feidenhans, S. L. S. Stipp. "Adaptive center determination for effective suppression of ring artifacts in tomography images", Applied Physics Letters 105(14) (2014) 143107
[Jia2006] L. Jia, Z. Lu, J. Miao, Z. Liu, G. Li, W. Su, "Effects of pre-calcined YSZ powders at different temperatures on Ni–YSZ anodes for SOFC", Journal of alloys and compounds 414(1) (2006) 152-157
[Jiang1999] S. P. Jiang, J. G. Love, J. P. Zhang, M. Hoang, Y. Ramprakash, A. E. Hughes, S. P. S. Badwal, "The electrochemical performance of LSM/zirconia–yttria interface as a function of a-site non-stoichiometry and cathodic current treatment", Solid State Ionics 121(1) (1999) 1-10
[Jiang1999b] S. P. Jiang, S. P. S. Badwal, "An electrode kinetics study of H 2 oxidation on Ni/Y 2 O 3–ZrO 2 cermet electrode of the solid oxide fuel cell", Solid State Ionics 123(1) (1999) 209-224
[Jiang2003] S. P. Jiang, "Sintering behavior of Ni/Y2O3-ZrO2cermet electrodes of solid oxide fuel cells", Journal of Materials Science 38(18) (2003) 3775-3782
[Jiang2006] S. P. Jiang, S. Zhang, Y. D. Zhen, "Deposition of Cr species at (La, Sr)(Co, Fe) O3 cathodes of solid oxide fuel cells", Journal of The Electrochemical Society 153(1) (2006) A127-A134

[Jiang2014] S. P. Jiang, X. Chen, "Chromium deposition and poisoning of cathodes of solid oxide fuel cells–a review", International Journal of Hydrogen Energy 39(1) (2014) 505-531
[Jiao2011] Z. Jiao, N. Takagi, N. Shikazono, N. Kasagi, "Study on local morphological changes of nickel in solid oxide fuel cell anode using porous Ni pellet electrode", Journal of Power Sources 196(3) (2011) 1019-1029
[Jiao2012] Z. Jiao, N. Shikazono, N. Kasagi, "Quantitative characterization of SOFC nickel-YSZ anode microstructure degradation based on focused-ion-beam 3D-reconstruction technique", Journal of The Electrochemical Society 159(3) (2012) B285-B291
[Joos2012] J. Joos, M. Ender, T. Carraro, A. Weber, E. Ivers-Tiffée, “Representative volume element size for accurate solid oxide fuel cell cathode reconstructions from focused ion beam tomography data”, Electrochimica Acta 82 (2012) 268-276
[Jorgensen2001] M. J. Jørgensen, M. Mogensen, "Impedance of solid oxide fuel cell LSM/YSZ composite cathodes", Journal of The Electrochemical Society 148(5) (2001) A433-A442
[Kak1988] A.C. Kak, M. Slaney, “Principle of the computerized tomographic imaging”, IEEE Press (1988)
[Kakac2007] S. Kakac, A. Pramuanjaroenkij, X. Y. Zhou, "A review of numerical modeling of solid oxide fuel cells", International Journal of Hydrogen Energy 32(7) (2007) 761-786
[Kanno2011] D. Kanno, N. Shikazono, N. Takagi, K. Matsuzaki, N. Kasagi, "Evaluation of SOFC anode polarization simulation using three-dimensional microstructures reconstructed by FIB tomography", Electrochimica Acta 56(11) (2011) 4015-4021
[Keane2012] M. Keane, M. K. Mahapatra, A. Verma, P. Singh, "LSM–YSZ interactions and anode delamination in solid oxide electrolysis cells", International Journal of Hydrogen Energy 37(22) (2012) 16776-16785
[Kendall2015] K. Kendall, M. Kendall, “High-temperature Solid Oxide Fuel Cells for the 21st Century: Fundamentals, Design and Applications” Elsevier, (2015)
[Kennouche2016] D. Kennouche, Y. K. Chen-Wiegart, C. Riscoe, J. Wang, S. A. Barnett, "Combined electrochemical and X-ray tomography study of the high temperature evolution of Nickel–Yttria Stabilized Zirconia solid oxide fuel cell anodes", Journal of Power Sources 307 (2016) 604-612
[Kenue1979] S.K. Kenue, J.F. Greenleaf, "Efficient convolution kernels for computerized tomography", Ultrasonic imaging 1(3) (1979) 232-244
[Ketcham2001] R.A. Ketcham, W.D. Carlson, "Acquisition, optimization and interpretation of X-ray computed tomographic imagery: applications to the geosciences", Computers & Geosciences 27(4) (2001) 381-400
[Kiburakaran2009] A. Kirubakaran, S. Jain, R. K. Nema, "A review on fuel cell technologies and power electronic interface", Renewable and Sustainable Energy Reviews 13(9) (2009) 2430-2440
[Kim2001] J.-D. Kim, G-D Kim, J-W Moon, Y.-I. Park, W.-H. Lee, K. Kobayashi, M. Nagai, C.-E. Kim, "Characterization of LSM–YSZ composite electrode by ac impedance spectroscopy", Solid State Ionics 143(3) (2001) 379-389
[Kim2013] J. Kim, H. I. Ji, H. P. Dasari, D. Shin, H. Song, J. H. Lee, B. K. Kim, H. J. Je, H. W. Lee, K. J. Yoon, "Degradation mechanism of electrolyte and air electrode in solid oxide electrolysis cells operating at high polarization", International Journal of Hydrogen Energy 38(3) (2013) 1225-1235
[Kim2017] Y. T. Kim, Z. Jiao, N. Shikazono, "Evaluation of La 0.6 Sr 0.4 Co 0.2 Fe 0.8 O 3-Gd 0.1 Ce 0.9 O 1.95 composite cathode with three dimensional microstructure reconstruction", Journal of Power Sources 342 (2017) 787-795
[Kirkpatrick1948] P. Kirkpatrick, A.V. Baez, "Formation of optical images by x-rays" JOSA 38(9) (1948) 766-774

[Kishimoto2011] M. Kishimoto, H. Iwai, M. Saito, H. Yoshida, "Quantitative evaluation of solid oxide fuel cell porous anode microstructure based on focused ion beam and scanning electron microscope technique and prediction of anode overpotentials", Journal of Power Sources 196(10) (2011) 4555-4563
[Kishimoto2012] H. Kishimoto, K. Yashiro, T. Shimonosono, M. E. Brito, K. Yamaji, T. Horita, H. Yokokawa, J. Mizusaki, "In situ analysis on the electrical conductivity degradation of NiO doped yttria stabilized zirconia electrolyte by micro-Raman spectroscopy", Electrochimica Acta 82 (2012) 263-267
[Knibbe2010] R. Knibbe, M. L. Traulsen, A. Hauch, S. D. Ebbesen, M. Mogensen, "Solid oxide electrolysis cells: degradation at high current densities", Journal of The Electrochemical Society 157(8) (2010) B1209-B1217
[Knibbe2011] R. Knibbe, A. Hauch, J. Hjelm, S. D. Ebbesen, M. Mogensen, "Durability of solid oxide cells." Green 1(2) (2011) 141-169
[Koch2006] S. Koch, P. V. Hendriksen, M. Mogensen, Y-L. Liu, N. Dekker, B. Rietveld, B. De Haart, F. Tietz, "Solid oxide fuel cell performance under severe operating conditions", Fuel Cells 6(2) (2006) 130-136
[Konysheva2006] E. Konysheva, H. Penkalla, E. Wessel, J. Mertens, U. Seeling, L. Singheiser, K. Hilpert, "Chromium poisoning of perovskite cathodes by the ODS alloy Cr5Fe1Y2O3 and the high chromium ferritic steel Crofer22APU", Journal of The Electrochemical Society 153(4) (2006) A765-A773
[Kotisaari2016] M. Kotisaari, O. Thomann, D. Montinaro, J. Kiviaho, "Evaluation of a SOEC stack for hydrogen and syngas production: a performance and durability analysis", 12th European SOFC & SOE Forum Lucerne (2016) A1202
[Kraemer2006] K.W. Kramer, P. Dorenbos, H.U. Gudel, and C.W.E. van Eijk, “Development and characterization of highly efficient new cerium doped rare earth halide scintillator materials,” J. Mater. Chem. 16(27) (2006) 2773
[Kreuer2003] K. D. Kreuer, "Proton-conducting oxides", Annual Review of Materials Research 33(1) (2003) 333-359
[Kwakman2011] L. Kwakman, G. Franz, M.M. Visser Taklo, A. Klumpp, P. Ramm, “Characterization and Failure Analysis of 3D Integrated Systems using a novel plasma-FIB system”, In FRONTIERS OF CHARACTERIZATION AND METROLOGY FOR NANOELECTRONICS AIP Publishing 1395(1) (2011) 269-273
[Kyriakou2009] Y. Kyriakou, D. Prell, W. A. Kalender, "Ring artifact correction for high-resolution micro CT", Physics in medicine and biology 54(17) (2009) N385-N391
[Labiche2007] J.-C. Labiche, O. Mathon, S. Pascarelli, M.A. Newton, G.G. Ferre, C. Curfs, G.B. M. Vaughan, A. Homs, and D.F. Carreiras, “The fast readout low noise camera as a versatile x-ray detector for time resolved dispersive extended x-ray absorption fine structure and diffraction studies of dynamic problems in materials science, chemistry, and catalysis,” Rev. Sci. Instrum. 78 (2007) 91301
[Laguna2010] M. A. Laguna-Bercero, J. A. Kilner, S. J. Skinner, "Performance and Characterization of (La, Sr) MnO3/YSZ and La0. 6Sr0. 4Co0. 2Fe0. 8O3 Electrodes for Solid Oxide Electrolysis Cells†", Chemistry of Materials 22(3) (2009) 1134-1141
[Laguna2011] M. A. Laguna-Bercero, R. Campana, A. Larrea, J. A. Kilner, V. M. Orera, "Electrolyte degradation in anode supported microtubular yttria stabilized zirconia-based solid oxide steam electrolysis cells at high voltages of operation", Journal of Power Sources 196(21) (2011) 8942-8947
[Laguna2011b] M. A. Laguna-Bercero, R. Campana, A. Larrea, J. A. Kilner, V. M. Orera, "Performance and Aging of Microtubular YSZ-based Solid Oxide Regenerative Fuel Cells", Fuel Cells 11(1) (2011) 116-123

[Laguna2012] M. A. Laguna-Bercero, "Recent advances in high temperature electrolysis using solid oxide fuel cells: A review", Journal of Power Sources 203 (2012) 4-16
[Lalanne2008] C. Lalanne, G. Prosperi, J-M. Bassat, F. Mauvy, S. Fourcade, P. Stevens, M. Zahid, S. Diethelm, J. Van herle, J-C. Grenier, "Neodymium-deficient nickelate oxide Nd 1.95 NiO 4+ δ as cathode material for anode-supported intermediate temperature solid oxide fuel cells", Journal of Power Sources 185(2) (2008) 1218-1224
[Lanzi1990] O. Lanzi, U. Landau, "Effect of pore structure on current and potential distributions in a porous electrode", Journal of the Electrochemical Society 137(2) (1990) 585-593
[Laurencin2008] J. Laurencin, F. Lefebvre-Joud, G. Delette, "Impact of cell design and operating conditions on the performances of SOFC fuelled with methane", Journal of Power Sources 177(2) (2008) 355-368
[Laurencin2011] J. Laurencin, D. Kane, G. Delette, J. Deseure, Florence Lefebvre-Joud, "Modelling of solid oxide steam electrolyser: impact of the operating conditions on hydrogen production", Journal of Power Sources 196(4) (2011) 2080-2093
[Laurencin2012] J. Laurencin, R. Quey, G. Delette, H. Suhonen, P. Cloetens, P. Bleuet, "Characterisation of Solid Oxide Fuel Cell Ni–8YSZ substrate by synchrotron X-ray nano-tomography: from 3D reconstruction to microstructure quantification", Journal of Power Sources 198 (2012) 182-189
[Laurencin2015] J. Laurencin, J. Mougin in: A. Godula-Jopek (Ed.), “Hydrogen production by electrolysis”, Wiley (2015) 191-272
[Laurencin2015b] J. Laurencin, M. Hubert, K. Couturier, T. Le Bihan, P. Cloetens, F. Lefebvre-Joud, E. Siebert, "Reactive Mechanisms of LSCF Single-Phase and LSCF-CGO Composite Electrodes Operated in Anodic and Cathodic Polarisations", Electrochimica Acta 174 (2015) 1299-1316
[Lay2013] E. Lay-Grindler, J. Laurencin, G. Delette, J. Aicart, M. Petitjean, L. Dessemond, "Micro modelling of solid oxide electrolysis cell: From performance to durability", International Journal of Hydrogen Energy 38(17) (2013) 6917-6929
[Lay2013b] E. Lay-Grindler, J. Laurencin, J. Villanova, I. Kieffer, F. Usseglio-Viretta, T. Le Bihan, P. Bleuet, A. Mansuy, G. Delette, "Degradation study of the La0. 6Sr0. 4Co0. 2Fe0. 8O3 solid oxide electrolysis cell (SOEC) anode after high temperature electrolysis operation", ECS Transactions 57(1) (2013) 3177-3187
[Lay2014] E. Lay-Grindler, J. Laurencin, J. Villanova, P. Cloetens, P. Bleuet, A. Mansuy, J. Mougin, G. Delette, "Degradation study by 3D reconstruction of a nickel–yttria stabilized zirconia cathode after high temperature steam electrolysis operation", Journal of Power Sources 269 (2014) 927-936
[Lee2002] J-H. Lee, H. Moon, H. W. Lee, J. Kim, J. D. Kim, K. H. Yoon, "Quantitative analysis of microstructure and its related electrical property of SOFC anode, Ni–YSZ cermet." Solid State Ionics 148 (2002) 15-26
[Lee2014] Y. H. Lee, H. Muroyama, T. Matsui, K. Eguchi, "Degradation of nickel–yttria-stabilized zirconia anode in solid oxide fuel cells under changing temperature and humidity conditions", Journal of Power Sources 262 (2014) 451-456
[Lefarth2011] A. Lefarth, B. Butz, H. Störmer, A. Utz, D. Gerthsen, "Impact of Ni on Accelerated Degradation of 8.5 Mol% Y2O3-Doped Zirconia", ECS Transactions 35(1) (2011) 1581-1586
[Lefebvre-Joud2010] F. Lefebvre-Joud, J. Mougin, L. Antoni, E. Bouyer, G. Gebel, F. Nony, "Matériaux de la filière hydrogène – Production et conversion", Les Techniques de l’Ingénieur N1205 (2010)
[Lempicki1998] A. Lempicki, J. Glodo, “Ce-doped scintillators: LSO and LuAP,” Nucl. Instruments Methods Phys. Res. A 416 (1998) 333–344

[Leonide2010] A. Leonide, B. Rüger, A. Weber, W. A. Meulenberg, E. Ivers-Tiffée, "Impedance study of alternative (La, Sr) FeO3− δ and (La, Sr)(Co, Fe) O3− δ MIEC cathode compositions", Journal of The Electrochemical Society 157(2) (2010) B234-B239
[Leppard2008] G. G. Leppard, "Nanoparticles in the environment as revealed by transmission electron microscopy: detection, characterisation and activities", Current Nanoscience 4(3) (2008) 278-301
[Leucht2011] F. Leucht, W. G. Bessler, J. Kallo, K. A. Friedrich, H. Müller-Steinhagen, "Fuel cell system modeling for solid oxide fuel cell/gas turbine hybrid power plants, Part I: Modeling and simulation framework", Journal of Power Sources 196(3) (2011) 1205-1215
[Linderoth2001] S. Linderoth, N. Bonanos, K. V. Jensen, J. B. Bilde-Sørensen, "Effect of NiO-to-Ni Transformation on Conductivity and Structure of Yttria-Stabilized ZrO2", Journal of the American Ceramic Society 84(11) (2001) 2652-2656
[Liu1998] M. Liu, , Z. Wu, "Significance of interfaces in solid-state cells with porous electrodes of mixed ionic–electronic conductors", Solid State Ionics 107(1) (1998) 105-110
[Liu1998b] M. Liu, "Equivalent Circuit Approximation to Porous Mixed-Conducting Oxygen Electrodes in Solid-State Cells", Journal of the Electrochemical Society 145(1) (1998) 142-154
[Liu2003] Y. L. Liu, S. Primdahl, M. Mogensen, "Effects of impurities on microstructure in Ni/YSZ–YSZ half-cells for SOFC", Solid State Ionics 161(1) (2003) 1-10
[Liu2005] Y. L. Liu, C. Jiao, "Microstructure degradation of an anode/electrolyte interface in SOFC studied by transmission electron microscopy", Solid State Ionics 176(5) (2005) 435-442
[Liu2012] Y. L. Liu, K. Thydén, M. Chen, A. Hagen, "Microstructure degradation of LSM-YSZ cathode in SOFCs operated at various conditions", Solid State Ionics 206 (2012) 97-103
[Lombardo2012] J.J. Lombardo, R.A. Ristau, W.M. Harris, W.K.S. Chiu, "Focused ion beam preparation of samples for X-ray nanotomography", Journal of synchrotron radiation 19(5) (2012) 789-796
[Lyckegaard2011] A. Lyckegaard, G. Johnson, P. Tafforeau. "Correction of ring artifacts in X-ray tomographic images", International Journal of Tomography and Statistics 18(F11) (2011) 1-9
[Mai2005] A. Mai, V. AC Haanappel, S. Uhlenbruck, F. Tietz, D. Stöver, "Ferrite-based perovskites as cathode materials for anode-supported solid oxide fuel cells: Part I. Variation of composition", Solid State Ionics 176(15) (2005) 1341-1350
[Mai2006] A. Mai, V. AC Haanappel, F. Tietz, D. Stöver, "Ferrite-based perovskites as cathode materials for anode-supported solid oxide fuel cells: Part II. Influence of the CGO interlayer", Solid State Ionics 177(19) (2006) 2103-2107
[Maire2001] E. Maire, J.-Y. Buffiere, L. Salvo, J. J. Blandin, W. Ludwig, J. M. Letang, "On the application of X-ray microtomography in the field of materials science", Advanced Engineering Materials 3(8) (2001) 539-546
[Margaritondo2001] G. Margaritondo, Y. Hwu, G. Tromba, "Synchrotron light: from basics to coherence and coherence-related applications." Lezioni della VI scuola nazionale di luce di sincrotrone S. Margherita di Pula, Italy (2001)
[Martinez2016] G. Martinez-Criado, J. Villanova, R. Tucoulou, D. Salomon, J-P. Suuronen, S. Labouré, C. Guilloud, V. Valls, R. Barrett, E. Gagliardini, Y. Dabin, "ID16B: a hard X-ray nanoprobe beamline at the ESRF for nano-analysis", Journal of synchrotron radiation 23(1) (2016) 344-352
[Matsui2012] T. Matsui, R. Kishida, H. Muroyama, K. Eguchi, "Comparative Study on Performance Stability of Ni–Oxide Cermet Anodes under Humidified Atmospheres in Solid Oxide Fuel Cells", Journal of The Electrochemical Society 159(8) (2012) F456-F460
[Matsui2012] T. Matsui, R. Kishida, H. Muroyama, K. Eguchi, "Comparative Study on Performance Stability of Ni–Oxide Cermet Anodes under Humidified Atmospheres in Solid Oxide Fuel Cells", Journal of The Electrochemical Society 159(8) (2012) F456-F460

[Matsuzaki2001] Y. Matsuzaki, I. Yasuda, "Dependence of SOFC cathode degradation by chromium-containing alloy on compositions of electrodes and electrolytes", Journal of The Electrochemical Society 148(2) (2001) A126-A131
[Mauvy2003] F. Mauvy, J-M. Bassat, E. Boehm, J-P. Manaud, P. Dordor, J-C. Grenier, "Oxygen electrode reaction on Nd 2 NiO 4+ δ cathode materials: impedance spectroscopy study", Solid State Ionics 158(1) (2003) 17-28
[Mekhilef2012] S. Mekhilef, R. Saidur, A. Safari, "Comparative study of different fuel cell technologies", Renewable and Sustainable Energy Reviews 16(1) (2012) 981-989
[Metcalfe2010] C. Metcalfe, O. Kesler, T. Rivard, F. Gitzhofer, N. Abatzoglou, "Connected three-phase boundary length evaluation in modeled sintered composite solid oxide fuel cell electrodes", Journal of the Electrochemical Society 157(9) (2010) B1326-B1335
[Minh1993] N. Q. Minh, "Ceramic fuel cells", Journal of the American Ceramic Society 76(3) (1993) 563-588
[Mirone2014] A. Mirone, E. Brun, E. Gouillart, P. Tafforeau, J. Kieffer, "The PyHST2 hybrid distributed code for high speed tomographic reconstruction with iterative reconstruction and a priori knowledge capabilities", Nuclear Instruments and Methods in Physics Research Section B: Beam Interactions with Materials and Atoms 324 (2014) 41–48
[Mizusaki1994] J. Mizusaki, H. Tagawa, T. Saito, T. Yamamura, K. Kamitani, K. Hirano, S. Ehara, T. Takagi, T. Hikita, M. Ippommatsu, S. Nakagawa, "Kinetic studies of the reaction at the nickel pattern electrode on YSZ in H2・H2O atmospheres", Solid State Ionics 70 (1994) 52-58
[Moçoteguy2013] P. Moçoteguy, Annabelle Brisse, "A review and comprehensive analysis of degradation mechanisms of solid oxide electrolysis cells", International Journal of Hydrogen Energy 38(36) (2013) 15887-15902
[Mogensen1996] M. Mogensen, S. Skaarup, "Kinetic and geometric aspects of solid oxide fuel cell electrodes", Solid State Ionics 86 (1996) 1151-1160
[Mogensen2002] M. Mogensen, K. V. Jensen, M. J. Jørgensen, S. Primdahl, "Progress in understanding SOFC electrodes", Solid State Ionics 150(1) (2002) 123-129
[Mogensen2016] M. B. Mogensen, A. Hauch, X. Sun, M. Chen, Y. Tao, S. D. Ebbesen, P. V. Hendriksen, "Relation between shape of Ni-particles and Ni migration in Ni-YSZ electrodes–a hypothesis", In Proceedings of the 12th European SOFC & SOE Forum, European Fuel Cell Forum, (2016)
[Mokso2007] R. Mokso, P. Cloetens, E. Maire, W. Ludwig, J-Y. Buffière, "Nanoscale zoom tomography with hard x rays using Kirkpatrick-Baez optics", Applied Physics Letters 90(14) (2007) 144104
[Momose1995a] A. Momose, “Demonstration of phase-contrast X-ray computed tomography using an X-ray interferometer,” Nucl. Instruments Methods Phys. Res. A352 (1995) 622–628
[Momose1995b] A. Momose, T. Takeda, Y. Itai, “Phase-contrast x-ray computed tomography for observing biological specimens and organic materials,” Rev. Sci. Instrum. 66(2) (1995) 1434–1436
[Momose1996] A Momose, T Takeda, Y Itai, K Hirano, “Phase–contrast X–ray computed tomography for observing biological soft tissues,” Nat. Med. 2(4) (1996) 473–475
[Momose2003] A. Momose, "Phase-sensitive imaging and phase tomography using X-ray interferometers", Optics Express 11(19) (2003) 2303-2314
[Morawe2015] C. Morawe, R. Barrett, P. Cloetens, B. Lantelme, J-Ch Peffen, A. Vivo, "Graded multilayers for figured Kirkpatrick-Baez mirrors on the new ESRF end station ID16A", In SPIE Optical Engineering Applications, International Society for Optics and Photonics, (2015) 958803-958803

[Morel2005] B. Morel, J. Laurencin, Y. Bultel, F. Lefebvre-Joud, "Anode-supported sofc model centered on the direct internal reforming", Journal of The Electrochemical Society 152(7) (2005) A1382-A1389
[Morgan2012] K. S. Morgan, D. M. Paganin, K. KW Siu, "X-ray phase imaging with a paper analyzer", Applied Physics Letters 100(12) (2012) 124102
[Mori2015] N. Mori, Y. Sato, H. Nakai, M. Iha, T. Takada, T. Konoike, "Development of a Novel Co-fired SOFC at Murata", ECS Transactions 68(1) (2015) 1871-1878
[Mukherjee2007] J. Mukherjee, S. Linic, "First-principles investigations of electrochemical oxidation of hydrogen at solid oxide fuel cell operating conditions", Journal of The Electrochemical Society 154(9) (2007) B919-B924
[Munroe2009] P. R. Munroe, "The application of focused ion beam microscopy in the material sciences" Materials characterization 60(1) (2009) 2-13
[Nagata2001] S. Nagata, A. Momma, T. Kato, Y. Kasuga, "Numerical analysis of output characteristics of tubular SOFC with internal reformer", Journal of Power Sources 101(1) (2001) 60-71
[Nakajo2016] A. Nakajo, A. P. Cocco, M. B. DeGostin, A. A. Peracchio, B. N. Cassenti, M. Cantoni, W. K. S. Chiu, "Accessible triple-phase boundary length: A performance metric to account for transport pathways in heterogeneous electrochemical materials", Journal of Power Sources 325 (2016) 786-800
[Nechache2014] A. Nechache, M. Cassir, A. Ringuedé, "Solid oxide electrolysis cell analysis by means of electrochemical impedance spectroscopy: A review", Journal of Power Sources 258 (2014) 164-181
[Nelson2012] G. J. Nelson, K. N. Grew, J. R. Izzo, J. J. Lombardo, W. M. Harris, A. Faes, A. Hessler-Wyser, J. Van herle, S. Wang, Y. S. Chu, A. V. Virkar, W. K. Chiu, "Three-dimensional microstructural changes in the Ni–YSZ solid oxide fuel cell anode during operation", Acta Materialia 60(8) (2012) 3491-3500
[Ni2007] M. Ni, M. K. H. Leung, D. Y. C. Leung, "Parametric study of solid oxide steam electrolyzer for hydrogen production", International Journal of Hydrogen Energy 32(13) (2007) 2305-2313
[Ni2008] M. Ni, M. K. H. Leung, D. Y. C. Leung, "Technological development of hydrogen production by solid oxide electrolyzer cell (SOEC)", International Journal of Hydrogen Energy 33(9) (2008) 2337-2354
[Ni2009] M. Ni, "Computational fluid dynamics modeling of a solid oxide electrolyzer cell for hydrogen production", International Journal of Hydrogen Energy 34(18) (2009) 7795-7806
[Nikl2006] M. Nikl, “Scintillation detectors for x-rays,” Meas. Sci. Technol. 17 (2006) R37–R54
[Njodzefon2012] J. C. Njodzefon, D. Klotz, A. Leonide, A. Kromp, A. Weber, E. Ivers-Tiffée, "Electrochemical studies on anode supported solid oxide electrolyzer cells", ECS Transactions 41(33) (2012) 113-122
[Njodzefon2013] J. C. Njodzefon, D. Klotz, A. Kromp, A. Weber, E. Ivers-Tiffée, "Electrochemical modeling of the current-voltage characteristics of an sofc in fuel cell and electrolyzer operation modes", Journal of The Electrochemical Society 160(4) (2013) F313-F323
[Noponen2015] M. Noponen, P. Torri, J. Göös, D. Chade, P. Hallanoro, A. Temmo, A. Koit, E. Ounpuu, "Status of Solid Oxide Fuel Cell Development at Elcogen", ECS Transactions 68(1) (2015) 151-156
[Nugent2007] K.A. Nugent, “X-ray noninterferometric phase imaging: a unified picture,” J. Opt. Soc. Am. 24(2) (2007) 536-547

[O'Brien2008] J. E. O'Brien, M. G. McKellar, C. M. Stoots, J. S. Herring, G. L. Hawkes, "Parametric study of large-scale production of syngas via high-temperature co-electrolysis", International Journal of Hydrogen Energy 34(9) (2009) 4216-4226
[OAR] OAR - a versatile resource and task manager for hpc clusters and other computing infrastructures. http://oar.imag.fr/
[Oh2012] D. Oh, D. Gostovic, E. D. Wachsman, "Mechanism of La 0.6 Sr 0.4 Co 0.2 Fe 0.8 O 3 cathode degradation", Journal of Materials Research 27(15) (2012) 1992-1999
[Orera1990] V. M. Orera, R. I. Merino, Y. Chen, R. Cases, P. J. Alonso, "Intrinsic electron and hole defects in stabilized zirconia single crystals", Physical Review B 42(16) (1990) 9782
[Orui2008] H. Orui, K. Nozawa, K. Watanabe, S. Sugita, R. Chiba, T. Komatsu, H. Arai, M. Arakawa, "Development of practical size anode-supported solid oxide fuel cells with multilayer anode structures", Journal of The Electrochemical Society 155(11) (2008) B1110-B1116
[Osten2016] W. Osten ed. "Optical inspection of Microsystems", CRC Press (2016)
[Otsu1979] N. Otsu, "A threshold selection method from gray-level histograms", IEEE transaction system (1979) 62-66
[Ouandji2002] F. Ouandji, E. Potter, W. R. Chen, H. Liu, "Impact of focal spot size on the spatial resolution of a digital x-ray imaging system for small-animal studies", In International Symposium on Biomedical Optics, International Society for Optics and Photonics (2002) 109-116
[Pacureanu2017] 24. A. Pacureanu, Y. Yang, R. Baker, R. Barrett, S. Bohic, Y. Dabin, F. Fus, E. Gagliardini, C. Guilloud, O. Hignette, M. Hubert, M. Langer, J. Meyer, Ch. Morawe, J. Morse, J.C. da Silva, R. Tucoulou Tachoueres, F. Villar, L. Weber and P. Cloetens, J. Synchrotron Rad. (2017) manuscript under preparation
[Paganin1998] D. Paganin, K.A. Nugent. "Noninterferometric phase imaging with partially coherent light", Physical review letters 80(12) (1998) 2586
[Paganin2002] D. Paganin, S. C. Mayo, T. E. Gureyev, P. R. Miller, S. W. Wilkins. "Simultaneous phase and amplitude extraction from a single defocused image of a homogeneous object", Journal of microscopy 206(1) (2002) 33-40
[Papoulis1974] A. Papoulis, "Ambiguity function in Fourier optics" J. Opt. Soc. Am. 64(6) (1974) 779-788
[Park2010] K. Park, S. Yu, J. Bae, H. Kim, Y. Ko, "Fast performance degradation of SOFC caused by cathode delamination in long-term testing", International Journal of Hydrogen Energy 35(16) (2010) 8670-8677
[Park2014] E. Park, S. Taniguchi, T. Daio, J.-T. Chou, K. Sasaki, "Comparison of chromium poisoning among solid oxide fuel cell cathode materials", Solid State Ionics 262 (2014) 421-427
[Park2014b] E. Park, S. Taniguchi, T. Daio, J.-T. Chou, K. Sasaki. "Influence of cathode polarization on the chromium deposition near the cathode/electrolyte interface of SOFC", International Journal of Hydrogen Energy 39(3) (2014) 1463-1475
[Pasaogullari2003] U. Pasaogullari, C.-Y. Wang, "Computational fluid dynamics modeling of solid oxide fuel cells", Proceedings of the SOFC-VIII 7 (2003) 1403-1412
[Pavlov2004] K. M. Pavlov, T. E. Gureyev, D. Paganin, Y. I. Nesterets, M. J. Morgan, R. A. Lewis, "Linear systems with slowly varying transfer functions and their application to x-ray phase-contrast imaging," J. Phys. D. Appl. Phys. 37(19) (2004) 2746
[Perona1990] P. Perona, J. Malik, "Scale-space and edge detection using anisotropic diffusion", IEEE Transactions on pattern analysis and machine intelligence 12(7) (1990) 629-639
[Phaneuf1999] M. W. Phaneuf, "Applications of focused ion beam microscopy to materials science specimens" Micron 30(3) (1999) 277-288

[Pihlatie2011] M. H. Pihlatie, A. Kaiser, M. Mogensen, M. Chen, "Electrical conductivity of Ni–YSZ composites: Degradation due to Ni particle growth", Solid State Ionics 189(1) (2011) 82-90
[Pogany1997] A. Pogany, D. Gao, S. W. Wilkins, "Contrast and resolution in imaging with a microfocus x-ray source", Review of Scientific Instruments 68(7) (1997) 2774-2782
[Polak1969] E. Polak, G. Ribiere, "Note sur la convergence de méthodes de directions conjuguées", Revue française d'informatique et de recherche opérationnelle, série rouge 3(1) (1969) 35-43
[Priebe2016] A. Priebe, P. Bleuet, G. Goret, J. Laurencin, D. Montinaro, J.-P. Barnes, "State-of-the-Art Three-Dimensional Chemical Characterization of Solid Oxide Fuel Cell Using Focused Ion Beam Time-of-Flight Secondary Ion Mass Spectrometry Tomography", Microscopy and Microanalysis 22(6) (2016) 1261-1269
[Quey2013] R. Quey, H. Suhonen, J. Laurencin, P. Cloetens, P. Bleuet, "Direct comparison between X-ray nanotomography and scanning electron microscopy for the microstructure characterization of a solid oxide fuel cell anode", Materials Characterization 78 (2013) 87-95
[Rajon2002] D. A. Rajon, P. W. Patton, A. P. Shah, C. J. Watchman, W. E. Bolch, "Surface area overestimation within three-dimensional digital images and its consequence for skeletal dosimetry", Medical physics 29(5) (2002) 682-693
[Ramachandran1971] G. N. Ramachandran, A. V. Lakshminarayanan "Three-dimensional reconstruction from radiographs and electron micrographs: application of convolutions instead of Fourier transforms", Proceedings of the National Academy of Sciences 68(9) (1971) 2236-2240
[Rashid2012] S. Rashid, S. Y. Lee, Md K. Hasan, "An improved method for the removal of ring artifacts in high resolution CT imaging", EURASIP Journal on Advances in Signal Processing 2012 1 (2012) 1-18
[Rashkeev2012] S. N. Rashkeev, M. V. Glazoff, "Atomic-scale mechanisms of oxygen electrode delamination in solid oxide electrolyzer cells", International Journal of Hydrogen Energy 37(2) (2012) 1280-1291
[Raven1998] C. Raven, "Numerical removal of ring artifacts in microtomography", Review of scientific instruments 69(8) (1998) 2978-2980
[Ray2006] S. C. Ray, J. W. Chiou, W. F. Pong, M-H. Tsai, "The electronic properties of nanomaterials elucidated by synchrotron radiation–based spectroscopy", Critical reviews in solid state and materials sciences 31(4) (2006) 91-110
[Recknagle2003] K. P. Recknagle, R. E. Williford, L. A. Chick, D. R. Rector, M. A. Khaleel, "Three-dimensional thermo-fluid electrochemical modeling of planar SOFC stacks", Journal of Power Sources 113(1) (2003) 109-114
[Relhy] RelHy final report, European project, https://setis.ec.europa.eu/energy-research/sites/default/files/project/docs/RelHy%20final%20report_1.pdf
[Rinaldi2015] L. Rinaldi, "Evaluation of the effect of thermal cycling on the degradation of solid oxide cells by a modelling and experimental approach", Master thesis University of Salerno (2015)
[Robisch2016] A. L. Robisch, "Phase retrieval for object and probe in the optical near-field", Dissertation (2016)
[Roentgen1986] W. C. Röntgen, “On a New Kind of Rays”, Science 3 (1896) 227–231
[Rossmeisl2008] J. Rossmeisl, W. G. Bessler, "Trends in catalytic activity for SOFC anode materials", Solid State Ionics 178(31) (2008) 1694-1700
[Rueger2007] B. Rüger, A. Weber, E. Ivers-Tiffee, "3D-modelling and performance evaluation of mixed conducting (MIEC) cathodes", ECS Transactions 7(1) (2007) 2065-2074
[Salvo2003] L. Salvo, P. Cloetens, E. Maire, S. Zabler, J. J. Blandin, J.-Y. Buffière, W. Ludwig, E. Boller, D. Bellet, C. Josserond, "X-ray micro-tomography an attractive

characterisation technique in materials science", Nuclear instruments and methods in physics research section B: Beam interactions with materials and atoms 200 (2003) 273-286
[Schefold2009] J. Schefold, A. Brisse, M. Zahid, "Electronic conduction of yttria-stabilized zirconia electrolyte in solid oxide cells operated in high temperature water electrolysis", Journal of The Electrochemical Society 156(8) (2009) B897-B904
[Schefold2012] J. Schefold, A. Brisse, F. Tietz, "Nine thousand hours of operation of a solid oxide cell in steam electrolysis mode", Journal of The Electrochemical Society 159(2) (2011) A137-A144
[Schefold2013] J. Schefold, A. Brisse, "Steam electrolysis in reversibly operated SOFC: Long-term cell testing beyond 1000 h", ECS Transactions 53(9) (2013) 53-61
[Schefold2015] J. Schefold, A. Brisse, H. Poepke, "Long-term Steam Electrolysis with Electrolyte-Supported Solid Oxide Cells", Electrochimica Acta 179 (2015) 161-168
[Schneider2012] C. A. Schneider, W. S. Rasband, K. W. Eliceiri, "NIH Image to ImageJ: 25 years of image analysis", Nature methods 9(7) (2012) 671-675
[Schouler1981] E. J. L. Schouler, M. Kleitz, E. Forest, E. Fernandez, P. Fabry, "Overpotential of H2・H2O, Ni/YSZ electrodes in steam electrolyzers", Solid State Ionics 5 (1981) 559-562
[Schuler2012] J. A. Schuler, Z. Wuillemin, A. Hessler-Wyser, C. Comminges, N. Yousfi Steiner, J. Van Herle, "Cr-poisoning in (La, Sr)(Co, Fe) O 3 cathodes after 10,000 h SOFC stack testing", Journal of Power Sources 211 (2012) 177-183
[Schwinger1949] J. Schwinger, “On the classical radiation of accelerated electrons,” Phys. Rev. 75 (1949) 1912–1925
[Setoguchi1990] T. Setoguchi, T. Inoue, H. Takebe, K. Eguchi, K. Morinaga, H. Arai, "Fabrication and evaluation of flat thick film type solid oxide fuel cell", Solid State Ionics 37(2) (1990) 217-221
[Sharma2010] V. I. Sharma, B. Yildiz, "Degradation Mechanism in La0. 8Sr0. 2CoO3 as Contact Layer on the Solid Oxide Electrolysis Cell Anode", Journal of The Electrochemical Society 157(3) (2010) B441-B448
[Shearing2009] P. R. Shearing, J. Golbert, R. J. Chater, N. P. Brandon, "3D reconstruction of SOFC anodes using a focused ion beam lift-out technique", Chemical Engineering Science 64(17) (2009) 3928-3933
[Shearing2010] P. R. Shearing, J. Gelb, J. Yi, W. K. Lee, M. Drakopoulos, N. P. Brandon, “Analysis of triple phase contact in Ni-YSZ microstructures using non-destructive X-ray tomography with synchrotron radiation”, Electrochemistry Communications 12 (2010) 1021-1024
[Shearing2010b] P. R. Shearing, J. Gelb, N. P. Brandon, "X-ray nano computerised tomography of SOFC electrodes using a focused ion beam sample-preparation technique", Journal of the European Ceramic Society 30(8) (2010) 1809-1814
[Shepp1974] L.A. Shepp, B.F. Logan, "The Fourier reconstruction of a head section", IEEE Transactions on Nuclear Science 21(3) (1974) 21-43
[Shikazono2009] N. Shikazono, Y. Sakamoto, Y. Yamaguchi, N. Kasagi, “Microstructure and polarization characteristics of anode supported tubular solid oxide fuel cell with co-precipitated and mechanically mixed Ni-YSZ anodes.” Journal of Power Sources 193(2) (2009) 530-540.
[Shimada2016] H. Shimada, T. Yamaguchi, T. Suzuki, H. Sumi, K. Hamamoto, Y. Fujishiro, "High steam utilization operation with high current density in solid oxide electrolysis cells", Journal of the Ceramic Society of Japan 124(3) (2016) 213-217
[Shimonosono2012] T. Shimonosono, H. Kishimoto, M. E. Brito, K. Yamaji, T. Horita, H. Yokokawa, "Phase transformation related electrical conductivity degradation of NiO doped YSZ", Solid State Ionics 225 (2012) 69-72
[Shin2013] E.-C. Shin, P.-A. Ahn, H.-H. Seo, J.-M. Jo, S.-D. Kim, S.-K. Woo, J. H. Yu, J. Mizusaki, J.-S. Lee, "Polarization mechanism of high temperature electrolysis in a Ni–

YSZ/YSZ/LSM solid oxide cell by parametric impedance analysis", Solid State Ionics 232 (2013) 80-96
[Shishkin2009] M. Shishkin, T. Ziegler, "Oxidation of H2, CH4, and CO molecules at the interface between Nickel and Yttria-Stabilized Zirconia: a theoretical study based on DFT", The Journal of Physical Chemistry C113(52) (2009) 21667-21678
[Sijbers2004] J. Sijbers, A. Postnov, "Reduction of ring artefacts in high resolution micro-CT reconstructions", Physics in Medicine and Biology 49(14) (2004) N247-N253
[Simner2005] S. P. Simner, M. D. Anderson, G-G. Xia, Z. Yang, Larry R. Pederson, J. W. Stevenson, "SOFC performance with Fe-Cr-Mn alloy interconnect", Journal of The Electrochemical Society 152(4) (2005) A740-A745
[Simner2006] S. P. Simner, M. D. Anderson, M. H. Engelhard, J. W. Stevenson, "Degradation Mechanisms of La–Sr–Co–Fe–O3 SOFC Cathodes", Electrochemical and Solid-State Letters 9(10) (2006) A478-A481
[Simrick2012] N. J. Simrick, A. Bieberle-Hütter, T. M. Ryll, J. A. Kilner, A. Atkinson, J. L. M. Rupp, "An investigation of the oxygen reduction reaction mechanism of La 0.6 Sr 0.4 Co 0.2 Fe 0.8 O 3 using patterned thin films", Solid State Ionics 206 (2012) 7-16
[Simwonis2000] D. Simwonis, F. Tietz, D. Stöver, "Nickel coarsening in annealed Ni/8YSZ anode substrates for solid oxide fuel cells", Solid State Ionics 132(3) (2000) 241-251
[Singhal2003] S. C. Singhal, K. Kendall, eds. "High-temperature solid oxide fuel cells: fundamentals, design and applications", Elsevier (2003)
[Skafte2016] T. L. Skafte, J. Hjelm, P. Blennow C. Graves, SOC tests database v0.72 (open-access), figshare, https://dx.doi.org/10.6084/m9.figshare.1607410 (2016)
[Snigirev1995] A. Snigirev, I. Snigireva, V. Kohn, S. Kuznetsov, I. Schelokov, “On the possibilities of x-ray phase contrast microimaging by coherent high-energy synchrotron radiation” Rev. Sci. Instrum. 66(12) (1995) 5486-5492
[Song2006] H.S. Song, W. H. Kim, S. H. Hyun, J. Moon, "Influences of starting particulate materials on microstructural evolution and electrochemical activity of LSM-YSZ composite cathode for SOFC." Journal of electroceramics 17(2-4) (2006) 759-764.
[Stempien2013] J. P. Stempien, Q. Sun, S. H. Chan, "Solid oxide electrolyzer cell modeling: A review", Journal of Power Technologies 93(4) (2013) 216
[Stevens2000] P. Stevens, F. Novel-Cattin, A. Hammou, C. Lamy, M. Cassir, "Piles à combustible", Techniques de l'ingénieur. Génie électrique 5 (2000) D3340-1
[Stockmar2015] M. Stockmar, M. Hubert, M. Dierolf, B. Enders, R. Clare, S. Allner, A. Fehringer, I. Zanette, J. Villanova, J. Laurencin, P. Cloetens, "X-ray nanotomography using near-field ptychography", Optics express 23(10) (2015) 12720-12731
[Suhonen2017] H. Suhonen, M. Hubert, P. Cloetens, “Iterative phase retrieval using conjugate gradient for propagation based x-ray imaging”, manuscript in preparation
[Sun2010] C. Sun, R. Hui, Justin Roller, "Cathode materials for solid oxide fuel cells: a review", Journal of Solid State Electrochemistry 14(7) (2010) 1125-1144
[Sun2015] X. Sun, M. Chen, Y.-L. Liu, P. V. Hendriksen, "Life Time Performance Characterization of Solid Oxide Electrolysis Cells for Hydrogen Production", ECS Transactions 68(1) (2015) 3359-3368
[Tanasini2009] P. Tanasini, M. Cannarozzo, P. Costamagna, A. Faes, J. Van Herle, A. Hessler-Wyser, C. Comninellis, "Experimental and theoretical investigation of degradation mechanisms by particle coarsening in SOFC electrodes", Fuel Cells 9(5) (2009) 740-752
[Teage1983] M.R. Teague, "Deterministic phase retrieval: a Green’s function solution." JOSA 73(11) (1983) 1434-1441
[The2015] D. The, S. Grieshammer, M. Schroeder, M. Martin, M. Al Daroukh, F. Tietz, J. Schefold, A. Brisse, "Microstructural comparison of solid oxide electrolyser cells operated for 6100 h and 9000 h", Journal of Power Sources 275 (2015) 901-911

[Tietz2002] F. Tietz, H-P. Buchkremer, D. Stöver, "Components manufacturing for solid oxide fuel cells", Solid State Ionics 152 (2002) 373-381
[Tietz2006] F. Tietz, V. A. C. Haanappel, A. Mai, J. Mertens, D. Stöver, "Performance of LSCF cathodes in cell tests", Journal of Power Sources 156(1) (2006) 20-22
[Tietz2008] F. Tietz, A. Mai, D. Stöver, "From powder properties to fuel cell performance–A holistic approach for SOFC cathode development", Solid State Ionics 179(27) (2008) 1509-1515
[Tietz2013] F. Tietz, D. Sebold, A. Brisse, J. Schefold, "Degradation phenomena in a solid oxide electrolysis cell after 9000 h of operation", Journal of Power Sources 223 (2013) 129-135
[Tomoshige2013] Y. Tomoshige, N. Mori, M. Iha, T. Takada, T. Konoike, "Development of a New Concept SOFC at Murata", ECS Transactions 57(1) (2013) 115-122
[Torabi2016] A. Torabi, J. Barton, C. Willman, H. Ghezel-Ayagh, E. Tang, M. Pastula, "Development of Solid Oxide Fuel Cells at Versa Power Systems & FuelCell Energy", ECS Transactions 72(7) (2016) 3-9
[Trofimenko2015] N. Trofimenko, M. Kusnezoff, D. Klemm, D. Schimanke, "Development of Electrolyte Supported Cells Based on a Thin 3YSZ Substrate: Through Optimized Contact Layer to High Power Density", ECS Transactions 68(1) (2015) 1933-1942
[Tsyganov2007] S. Tsyganov, J. Kästner, B. Rellinghaus, T. Kauffeldt, F. Westerhoff, D. Wolf, "Analysis of Ni nanoparticle gas phase sintering", Physical Review B75(4) (2007) 045421
[Tu2004] H. Tu, U. Stimming, "Advances, aging mechanisms and lifetime in solid-oxide fuel cells", Journal of Power Sources 127(1) (2004) 284-293
[Tucker2006] M. C. Tucker, H. Kurokawa, C. P. Jacobson, L. C. De Jonghe, S. J. Visco, "A fundamental study of chromium deposition on solid oxide fuel cell cathode materials", Journal of Power Sources 160(1) (2006) 130-138
[Tucker2010] M. C. Tucker, "Progress in metal-supported solid oxide fuel cells: A review", Journal of Power Sources 195(15) (2010) 4570-4582
[Turner2004] L.D. Turner, B. B. Dhal, J. P. Hayes, A. P. Mancuso, K. A. Nugent, D. Paterson, R. E. Scholten, C. Q. Tran, A. G. Peele, "X-ray phase imaging: Demonstration of extended conditions with homogeneous objects", Optics express 12(13) (2004) 2960-2965
[Uchino1996] K. Uchino, “Piezoelectric actuators and ultrasonic motors”, Vol. 1. Springer Science & Business Media (1996)
[Udagawa2007] J. Udagawa, P. Aguiar, N. P. Brandon, "Hydrogen production through steam electrolysis: Model-based steady state performance of a cathode-supported intermediate temperature solid oxide electrolysis cell", Journal of Power Sources 166(1) (2007) 127-136
[Uhlenbruck2009] S. Uhlenbruck, T. Moskalewicz, N. Jordan, H-J. Penkalla, H. P. Buchkremer, "Element interdiffusion at electrolyte–cathode interfaces in ceramic high-temperature fuel cells", Solid State Ionics 180(4) (2009) 418-423
[US2004] US Department of Energy, “Fuel Cell Handbook (Seventh Edition)”, Office of Fossil Energy, National Energy Technology Laboratory, Morgantown, West Virginia 265070880, (2004)
[Usseglio2014] F. Usseglio-Viretta, J. Laurencin, G. Delette, J. Villanova, P. Cloetens, D. Leguillon, "Quantitative microstructure characterization of a Ni–YSZ bi-layer coupled with simulated electrode polarisation", Journal of Power Sources 256 (2014) 394-403
[Usseglio2015] F. Usseglio-Viretta, “Optimisation des performances et de la robustesse d’un électrolyseur à hautes temperatures”, PhD Thesis, Grenoble-Alpes University, 2015
[Utz2011] A. Utz, K. V. Hansen, K. Norrman, E. Ivers-Tiffée, M. Mogensen, "Impurity features in Ni-YSZ-H 2-H 2 O electrodes", Solid State Ionics 183(1) (2011) 60-70
[Van Heel2005] M. Van Heel, M. Schatz, "Fourier shell correlation threshold criteria", Journal of structural biology 151(3) (2005) 250-262

[VanEijk2002] C.W.E. Van Eijk, “Inorganic scintillators in medical imaging,” Phys. Med. Biol. 47 (2002) R85–R106
[Vassen2001] R. Vassen, D. Simwonis, D. Stöver, "Modelling of the agglomeration of Ni-particles in anodes of solid oxide fuel cells", Journal of Materials Science 36(1) (2001) 147-151
[Vernoux2000] P. Vernoux, M. Guillodo, J. Fouletier, A. Hammou, "Alternative anode material for gradual methane reforming in solid oxide fuel cells", Solid State Ionics 135(1) (2000) 425-431
[Vidal2005] F.P. Vidal, J.M. Létang, G. Peix, P. Cloetens, "Investigation of artefact sources in synchrotron microtomography via virtual X-ray imaging", Nuclear Instruments and Methods in Physics Research Section B: Beam Interactions with Materials and Atoms 234(3) (2005) 333-348
[Vila-Comamala2012] J. Vila-Comamala, Y. Pan, J. Lombardo, W. M. Harris, W. K. Chiu, C. David, Y. Wang, "Zone-doubled Fresnel zone plates for high-resolution hard X-ray full-field transmission microscopy", Journal of Synchrotron Radiation 19(5) (2012) 705-709
[Villanova2013] V. Julie, L. Jérôme, C. Peter, B. Pierre, D. Gérard, S. Heikki, U. V. François, “3D phase mapping of solid oxide fuel cell YSZ/Ni cermet at the nanoscale by holographic X-ray nanotomography”, Journal of Power Sources 243 (2013) 841-849
[Villareal2003] I. Villarreal, C. Jacobson, A. Leming, Y. Matus, S. Visco, L. De Jonghe, "Metal-supported solid oxide fuel cells", Electrochemical and Solid-state letters 6(9) (2003) A178-A179
[Virkar2000] A. V. Virkar, J. Chen, C. W. Tanner, J.-W. Kim, "The role of electrode microstructure on activation and concentration polarizations in solid oxide fuel cells", Solid State Ionics 131(1) (2000) 189-198
[Virkar2007] A. V. Virkar, "A model for solid oxide fuel cell (SOFC) stack degradation", Journal of Power Sources 172(2) (2007) 713-724
[Virkar2010] A. V. Virkar, "Mechanism of oxygen electrode delamination in solid oxide electrolyzer cells", International Journal of Hydrogen Energy 35(18) (2010) 9527-9543
[Vivet2011] N. Vivet, S. Chupin, E. Estrade, T. Piquero, P.L. Pommier, D. Rochais, E. Bruneton, “3D microstructural characterization of a solid oxide fuel cell anode reconstructed by focused ion beam tomography”, Journal of power Sources 196 (2011) 7541-7549
[Vogler2009] M. Vogler, A. Bieberle-Hütter, L. Gauckler, J. Warnatz, W. G. Bessler, "Modelling study of surface reactions, diffusion, and spillover at a Ni/YSZ patterned anode", Journal of The Electrochemical Society 156(5) (2009) B663-B672
[Wang2011] K. Wang, D. Hissel, M. C. Péra, N. Steiner, D. Marra, M. Sorrentino, C. Pianese, M. Monteverde, P. Cardone, J. Saarinen, "A review on solid oxide fuel cell models", International Journal of Hydrogen Energy 36(12) (2011) 7212-7228
[Wang2014] F. Wang, M. E. Brito, K. Yamaji, D. H. Cho, M. Nishi, H. Kishimoto, T. Horita, H. Yokokawa, "Effect of polarization on Sr and Zr diffusion behavior in LSCF/GDC/YSZ system", Solid State Ionics 262 (2014) 454-459
[Wang2016] H. Wang, K. J. Yakal-Kremski, T. Yeh, G. M. Rupp, A. Limbeck, J. Fleig, S. A. Barnett, "Mechanisms of Performance Degradation of (La, Sr)(Co, Fe) O3-δ Solid Oxide Fuel Cell Cathodes", Journal of The Electrochemical Society 163(6) (2016) F581-F585
[Wei2015] B. Wei, K. Chen, C. C. Wang, Z. Lü, S. P. Jiang, "Cr deposition on porous La 0.6 Sr 0.4 Co 0.2 Fe 0.8 O 3− δ electrodes of solid oxide cells under open circuit condition", Solid State Ionics 281 (2015) 29-37
[Weitkamp2005] T. Weitkamp, A. Diaz, C. David, F. Pfeiffer, M. Stampanoni, P. Cloetens, E. Ziegler, "X-ray phase imaging with a grating interferometer", Optics Express 13(16) (2005) 6296-6304

[Weppner1977] W. Weppner, "Formation of intermetallic Pt-Zr compounds between Pt electrodes and ZrO2-based electrolytes, and the decomposition voltage of yttria-doped ZrO2", Journal of Electroanalytical Chemistry and Interfacial Electrochemistry 84(2) (1977) 339-350
[Wiemhoefer2002] H. D. Wiemhöfer, H. G. Bremes, U. Nigge, W. Zipprich, "Studies of ionic transport and oxygen exchange on oxide materials for electrochemical gas sensors", Solid State Ionics 150(1) (2002) 63-77
[Wilson2006] J. R. Wilson, W. Kobsiriphat, R. Mendoza, H.-Y. Chen, J. M. Hiller, D. J. Miller, K. Thornton, P. W. Voorhees, S. B. Adler, S. A. Barnett, "Three-dimensional reconstruction of a solid-oxide fuel-cell anode", Nature Materials 5(7) (2006) 541-544
[Wilson2010] J. R. Wilson, J. S. Cronin, A. T. Duong, S. Rukes, H.-Y. Chen, K. Thornton, D. R. Mumm, S. Barnett, "Effect of composition of (La 0.8 Sr 0.2 MnO 3–Y 2 O 3-stabilized ZrO 2) cathodes: Correlating three-dimensional microstructure and polarization resistance", Journal of Power Sources 195(7) (2010) 1829-1840
[Winkler2002] W. Winkler, H. Lorenz, "The design of stationary and mobile solid oxide fuel cell–gas turbine systems", Journal of Power Sources 105(2) (2002) 222-227
[Wuillemin2014] Z. Wuillemin, S. Ceschini, Y. Antonetti, C. Beetschen, S. Modena, D. Montinaro, T. Cornu, O. Bucheli, M. Bertoldi, “High-performance SOFC stacks tested under different reformate compositions”, 11th European SOFC & SOE Forum Lucerne (2014) A0901
[Yakabe2001] H. Yakabe, T. Ogiwara, M. Hishinuma, I. Yasuda, "3-D model calculation for planar SOFC", Journal of Power Sources 102(1) (2001) 144-154
[Yamamoto2000] O. Yamamoto, "Solid oxide fuel cells: fundamental aspects and prospects", Electrochimica Acta 45(15) (2000) 2423-2435
[Yokokawa2008] H. Yokokawa, H. Tu, B. Iwanschitz, A. Mai, "Fundamental mechanisms limiting solid oxide fuel cell durability", Journal of Power Sources 182(2) (2008) 400-412
[Yonekura2011] T. Yonekura, Y. Tachikawa, T. Yoshizumi, Y. Shiratori, K. Ito, K. Sasaki, "Exchange Current Density of Solid Oxide Fuel Cell Electrodes", ECS Transactions 35(1) (2011) 1007-1014
[Yousuf2010] M. A. Yousuf, M. Asaduzzaman, "An efficient ring artifact reduction method based on projection data for micro-CT images", Journal of Scientific Research 2(1) (2009) 37-45
[Yurkiv2014] V. Yurkiv, R. Costa, Z. Ilhan, A. Ansar, W. G. Bessler, "Impedance of the surface double layer of LSCF/CGO composite cathodes: an elementary kinetic model", Journal of The Electrochemical Society 161(4) (2014) F480-F492
[Zanette2014] I. Zanette, T. Zhou, A. Burvall, U. Lundström, D. H. Larsson, M. Zdora, P. Thibault, F. Pfeiffer, H. M. Hertz, "Speckle-based x-ray phase-contrast and dark-field imaging with a laboratory source", Physical Review Letters 112(25) (2014) 253903
[Zhang2012] Y. Zhang, K. Chen, C. Xia, S. P. Jiang, M. Ni, "A model for the delamination kinetics of La 0.8 Sr 0.2 MnO 3 oxygen electrodes of solid oxide electrolysis cells", International Journal of Hydrogen Energy 37(19) (2012) 13914-13920
[Zhang2013] X. Zhang, J. E. O'Brien, R. C. O'Brien, G. K. Housley, "Durability evaluation of reversible solid oxide cells", Journal of Power Sources 242 (2013) 566-574
[Zhang2013b] X. Zhang, J. E. O'Brien, R. C. O'Brien, J. J. Hartvigsen, G. Tao, G. K. Housley, "Improved durability of SOEC stacks for high temperature electrolysis", International Journal of Hydrogen Energy 38(1) (2013) 20-28
[Zhu2003] W. Z. Zhu, S. C. Deevi, "A review on the status of anode materials for solid oxide fuel cells", Materials Science and Engineering A 362(1) (2003) 228-239
[Zhu2013] Y. Zhu, M. Zhao, H. Li, P. Zhang, "Micro-CT artifacts reduction based on detector random shifting and fast data inpainting", Medical physics 40(3) (2013) 031114

Figure II.4:

[1] J.S. Cronin, J.R. Wilson, S.A. Barnett, “Impact of pore microstructure evolution on polarization resistance of Ni-Yttria-stabilized zirconia fuel cell anodes”, Journal of Power Sources 196 (2011) 2640-2643
[2] A. T. Duong, D. R. Mumm, "Microstructural optimization by tailoring particle sizes for LSM-YSZ solid oxide fuel cell composite cathodes", Journal of The Electrochemical Society 159(1) (2012) B39-B52
[3] D. Gostovic, J. R. Smith, D. P. Kundinger, K. S. Jones, E. D. Wachsman, "Three-dimensional reconstruction of porous LSCF cathodes", Electrochemical and solid-state letters 10(12) (2007) B214-B217
[4] L. Holzer, B. Münch, B. Iwanschitz, M. Cantoni, Th. Graule, “Quantitative relationships between composition, particle size, triple phase boundary length and surface area in nickel-cermet anodes for Solid Oxide Fuel Cells”, Journal of power Sources 196 (2011) 7076-7089
[5] H. Iwai, N. Shikazono, T. Matsui, , H. Teshima, M. Kishimoto, R. Kishida, D. Hayashi, K. Matsuzaki, D. Kanno, M. Saito, H. Muroyama, “Quantification of SOFC anode microstructure based on dual beam FIB-SEM technique.”, Journal of Power Sources 195(4) (2010) 955-961
[6] J. Joos, T. Carraro, A. Weber, E. Ivers-Tiffée, “Reconstruction of porous electrodes by FIB/SEM for detailed microstructure modelling”, Journal of Power Sources 196 (2011) 7302-7307
[7] J. Joos, M. Ender, T. Carraro, A. Weber, E. Ivers-Tiffée, “Representative volume element size for accurate solid oxide fuel cell cathode reconstructions from focused ion beam tomography data”, Electrochimica Acta 82 (2012) 268-276
[8] J. Joos, M. Ender, I. Rotscholl, N.H. Menzler, E. Ivers-Tiffée, “Quantification of double-layer Ni/YSZ fuel cell anodes from focused ion beam tomography data”, Journal of Power Sources 246 (2014) 819-830
[9] D. Kanno, N. Shikazono, N. Takagi, K. Matsuzaki, N. Kasagi, “Evaluation of SOFC anode polarization simulation using three-dimensional microstructures reconstructed by FIB tomography”, Electrochimica Acta 56 (2011) 4015-4021
[10] M. Kishimoto, H. Iwai, M. Saito, H. Yoshida, "Quantitative evaluation of solid oxide fuel cell porous anode microstructure based on focused ion beam and scanning electron microscope technique and prediction of anode overpotentials", Journal of Power Sources 196(10) (2011) 4555-4563
[11] M. Kishimoto, M. Lomberg, E. Ruiz-Trejo, N. P. Brandon, “Enhanced triple-phase boundary density in infiltrated electrodes for solid oxide fuel cells demonstrated by high-resolution tomography”, Journal of Power Sources 266 (2014) 291-295
[12] A. Z. Lichtner, D. Jauffrès, D. Roussel, F. Charlot, C. L. Martin, R. K. Bordia, "Dispersion, connectivity and tortuosity of hierarchical porosity composite SOFC cathodes prepared by freeze-casting", Journal of the European Ceramic Society 35(2) (2015) 585-595
[13] T. Matsui, R. Kishida, J.-Y. Kim, H. Muroyama, K. Eguchi, "Performance deterioration of Ni–YSZ anode induced by electrochemically generated steam in solid oxide fuel cells", Journal of The Electrochemical Society 157(5) (2010) B776-B781
[14] T. Matsui, J.-Y. Kim, H. Muroyama, M. Shimazu, T. Abe, M. Miyao, K. Eguchi, "Anode microstructural change upon long-term operation for the cathode-supported tubular-type SOFC", Solid State Ionics 225 (2012) 50-54
[15] K. Matsuzaki, N. Shikazono, N. Kasagi, "Three-dimensional numerical analysis of mixed ionic and electronic conducting cathode reconstructed by focused ion beam scanning electron microscope", Journal of Power Sources 196(6) (2011) 3073-3082
[16] G.J. Nelson, W.M. Harris, J.J. Lombardo, J.R. Izzo Jr, W.K.S. Chiu, P. Tanasini, M. Cantoni, J. Van Herle, C. Comninellis, J.C. Andrews, Y. Liu, P. Pianetta, Y.S. Chu, “Comparison of SOFC cathode microstructure quantified using X-ray nanotomography and focused ion beam-scanning electron microscopy”, Electrochemistry Communications 13 (2011) 586-589
[17] P. R. Shearing, J. Golbert, R. J. Chater, N. P. Brandon, “3D reconstruction of SOFC anodes using a focused ion beam lift-out technique.”, Chemical Engineering Science, 64(17) (2009) 3928-3933

[18] P. R. Shearing, Q. Cai, J. I. Golbert, V. Yufit, C. S. Adjiman, N. P. Brandon, "Microstructural analysis of a solid oxide fuel cell anode using focused ion beam techniques coupled with electrochemical simulation", Journal of Power Sources 195(15) (2010) 4804-4810
[19] N. Shikazono, D. Kanno, K. Matsuzaki, H. Teshima, S. Sumino, N. Kasagi, "Numerical assessment of SOFC anode polarization based on three-dimensional model microstructure reconstructed from FIB-SEM images", Journal of The Electrochemical Society 157(5) (2010) B665-B672
[20] H. Sumi, R. Kishida, J. Y. Kim, H. Muroyama, T. Matsui, K. Eguchi, "Correlation between microstructural and electrochemical characteristics during redox cycles for Ni–YSZ anode of SOFCs.", Journal of The Electrochemical Society 157(12) (2010) B1747-B1752
[21] N. Vivet, S. Chupin, E. Estrade, T. Piquero, P.L. Pommier, D. Rochais, E. Bruneton, "3D microstructural characterization of a solid oxide fuel cell anode reconstructed by focused ion beam tomography", Journal of power Sources 196 (2011) 7541-7549
[22] N. Vivet, S. Chupin, E. Estrade, A. Richard, S. Bonnamy, D. Rochais, E. Bruneton, "Effect of Ni content in SOFC Ni-YSZ cermets : A three-dimensional study by FIB-SEM tomography", Journal of Power Sources 196 (2011) 9989-9997
[23] E.A. Wargo, T. Kotaka, Y. Tabuchi, E.C. Kumbur, "Comparison of a focused ion beam versus nano-scale X-ray computed tomography for resolving 3-D microstructures of a porous fuel cell materials", Journal of Power Sources 241 (2013) 608-618
[24] J.R. Wislon, W. Kobsiriphat, R. Mendoza, H.Y. Chen, J.M. Hiller, D.J. Miller, K. Thorton, P.W. Voorhees, S.B. Adler, S.A. Barnett, Three-dimensional reconstruction of a solid-oxide fuel-cell anode, Nature Materials 5 (2006) 541-544
[25] J. R. Wilson, M. Gameiro, K. Mischaikow, W. Kalies, P. W. Voorhees, S. A. Barnett, "Three-dimensional analysis of solid oxide fuel cell Ni-YSZ anode interconnectivity", Microscopy and Microanalysis 15(1) (2009) 71-77
[26] J.R. Wilson, J.S. Cronin, A.T. Duong, S. Rukes, H.Y. Chen, K. Thornton, D.R. Mumm, S. Barnett, "Effect of a composition of (La0.8Sr0.2MnO3-Y2O3-stabilized ZrO2) cathodes: Correlating three-dimensional microstructure and polarization resistance", Journal of Power Sources 195 (2010) 1829-1840
[27] J. R. Wilson, J. S. Cronin, S. A. Barnett, "Linking the microstructure, performance and durability of Ni-yttria-stabilized zirconia solid oxide fuel cell anodes using three-dimensional focused ion beam–scanning electron microscopy imaging", Scripta Materialia 65(2) (2011) 67-72
[28] J. S. Cronin, Y. K. Chen-Wiegart, J. Wang, S. A. Barnett, "Three-dimensional reconstruction and analysis of an entire solid oxide fuel cell by full-field transmission X-ray microscopy", Journal of Power Sources 233 (2013) 174-179
[29] K. N. Grew, Y. S. Chu, J. Yi, A. A. Peracchio, J. R. Izzo, Y. Hwu, F. De Carlo, W. KS Chiu, "Nondestructive nanoscale 3D elemental mapping and analysis of a solid oxide fuel cell anode", Journal of the Electrochemical Society 157(6) (2010) B783-B792
[30] Y. Guan, Y. Gong, W. Li, J. Gelb, L. Zhang, G. Liu, X. Zhang, X. Song, C. Xia, Y. Xiong, H. Wang, "Quantitative analysis of micro structural and conductivity evolution of Ni-YSZ anodes during thermal cycling based on nano-computed tomography", Journal of Power Sources 196(24) (2011) 10601-10605
[31] Y. Guan, X. Dong, L. Zhang, G. Liu, Z. Liang, S. Chen, L. Chen, X. Zhang, Y. Xiong, H. Wang, Y. Tian, "Effects of nickel oxide impurities on the microstructure and electrical properties of a nickel–yttria-stabilized zirconia anode", International Journal of Hydrogen Energy (2016) 1-11
[32] J.R. Izzo, A.S. Joshi, K.N. Grew, W.K.S. Chiu, A. Tkachuk, S.H. Wang, W. Yun, "Nondestructive reconstruction and analysis of SOFC anodes using X-ray computed tomography at sub-50 nm resolution", Journal of the Electrochemical Society 155 (2008) B504-B508
[33] G. J. Nelson, K. N. Grew, J. R. Izzo, J. J. Lombardo, W. M. Harris, A. Faes, A. Hessler-Wyse, S. Wang,Y. S. Chu, a. V. Virkar, W. K. Chiu, "Three-dimensional microstructural changes in the Ni–YSZ solid oxide fuel cell anode during operation", Acta Materialia 60(8) (2012) 3491-3500
[34] P.R. Shearing, J. Gelb, J. Yi, W.K. Lee, M. Drakopoulos, N.P. Brandon, "Analysis of triple phase contact in Ni-YSZ microstructures using non-destructive X-ray tomography with synchrotron radiation", Electrochemistry Communications 12 (2010) 1021-1024

[35] P. R. Shearing, J. Gelb, N. P. Brandon, "X-ray nano computerised tomography of SOFC electrodes using a focused ion beam sample-preparation technique", Journal of the European Ceramic Society 30(8) (2010) 1809-1814
[36] P. R. Shearing, R. S. Bradley, J. Gelb, F. Tariq, P. J. Withers, N. P. Brandon, "Exploring microstructural changes associated with oxidation in Ni–YSZ SOFC electrodes using high resolution X-ray computed tomography", Solid State Ionics 216 (2012) 69-72
[37] M. Hubert, J. Laurencin, P. Cloetens, J. C. da Silva, F. Lefebvre-Joud, P. Bleuet, A. Nakajo, E. Siebert, "Role of microstructure on electrode operating mechanisms for mixed ionic electronic conductors: From synchrotron-based 3D reconstruction to electrochemical modeling", Solid State Ionics 294 (2016) 90-107
[38] J. Laurencin, R. Quey, G. Delette, H. Suhonen, P. Cloetens, P. Bleuet, "Characterisation of Solid Oxide Fuel Cell Ni–8YSZ substrate by synchrotron X-ray nano-tomography: from 3D reconstruction to microstructure quantification", Journal of Power Sources 198 (2012) 182-189
[39] E. Lay-Grindler, J. Laurencin, J. Villanova, I. Kieffer, F. Usseglio-Viretta, T. Le Bihan, P. Bleuet, A. Mansuy, G. Delette, "Degradation study of the La0. 6Sr0. 4Co0. 2Fe0. 8O3 solid oxide electrolysis cell (SOEC) anode after high temperature electrolysis operation", ECS Transactions 57(1) (2013) 3177-3187
[40] E. Lay-Grindler, J. Laurencin, J. Villanova, P. Cloetens, P. Bleuet, A. Mansuy, J. Mougin, G. Delette, "Degradation study by 3D reconstruction of a nickel–yttria stabilized zirconia cathode after high temperature steam electrolysis operation", Journal of Power Sources 269 (2014) 927-936
[41] R. Quey, H. Suhonen, J. Laurencin, P. Cloetens, P. Bleuet, "Direct comparison between X-ray nanotomography and scanning electron microscopy for the microstructure characterization of a solid oxide fuel cell anode", Materials Characterization 78 (2013) 87-95
[42] M. Stockmar, M. Hubert, M. Dierolf, B. Enders, R. Clare, S. Allner, A. Fehringer, I. Zanette, J. Villanova, J. Laurencin, P. Cloetens, "X-ray nanotomography using near-field ptychography", Optics express 23(10) (2015) 12720-12731
[43] F. Usseglio-Viretta, J. Laurencin, G. Delette, J. Villanova, P. Cloetens, D. Leguillon, "Quantitative microstructure characterization of a Ni–YSZ bi-layer coupled with simulated electrode polarisation", Journal of Power Sources 256 (2014) 394-403
[44] V. Julie, L. Jérôme, C. Peter, B. Pierre, D. Gérard, S. Heikki, U. V. François, “3D phase mapping of solid oxide fuel cell YSZ/Ni cermet at the nanoscale by holographic X-ray nanotomography”, Journal of Power Sources 243 (2013) 841-849

Appendix 1 : Results of microstructural analysis on Ni-YSZ electrodes

		Reference		SOEC_C1	SOEC_C2			SOEC_C3		SOFC_C4		SOFC_C5		SOFC_C6	
		Bulk	Inter.	Bulk/in.	Bulk/in.	Inter./in.	Inter./out.	Inter./in.	Inter./out.	Bulk/out.	Inter./in.	Bulk/out.	Inter/out.	Inter./in.	Inter./out.
Percolated volume fraction (-)	Pores	0.280 ±0.014	0.287 ±0.010	0.322 ±0.026	0.304 ±0.029	0.301 ±0.008	0.316 ±0.005	0.276 ±0.008	0.279 ±0.006	0.309 ±0.014	0.293 ±0.006	0.316 ±0.029	0.312 ±0.006	0.304 ±0.006	0.299 ±0.004
	YSZ	0.436 ±0.003	0.412 ±0.005	0.406 ±0.016	0.424 ±0.018	0.419 ±0.008	0.404 ±0.005	0.439 ±0.006	0.422 ±0.005	0.404 ±0.015	0.426 ±0.006	0.413 ±0.023	0.408 ±0.004	0.412 ±0.005	0.413 ±0.007
	Ni	0.262 ±0.013	0.282 ±0.011	0.257 ±0.044	0.255 ±0.051	0.265 ±0.001	0.267 ±0.003	0.269 ±0.008	0.283 ±0.004	0.275 ±0.032	0.266 ±0.004	0.257 ±0.031	0.265 ±0.007	0.265 ±0.005	0.268 ±0.008
Mean particle diameter (µm) with covariance	Pores	0.96 ±0.06	0.90 ±0.03	1.09 ±0.04	1.16 ±0.02	1.09 ±0.05	1.06 ±0.02	1.09 ±0.04	1.09 ±0.04	1.11 ±0.02	1.08 ±0.04	2.50 ±2.45	1.15 ±0.03	0.98 ±0.03	0.96 ±0.02
	YSZ	0.60 ±0.00	0.60 ±0.00	0.64 ±0.03	0.64 ±O.O2	0.61 ±0.02	0.60 ±0.00	0.61 ±0.02	0.60 ±0.00	0.63 ±0.03	0.61 ±0.02	0.66 ±0.03	0.65 ±0.00	0.60 ±0.00	0.61 ±0.02
	Ni	1.01 ±0.03	0.90 ±0.05	1.28 ±0.09	1.32 ±0.15	1.20 ±0.04	1.19 ±0.03	1.13 ±0.04	1.11 ±0.02	1.23 ±0.08	1.16 ±0.06	1.30 ±0.04	1.24 ±0.04	1.20 ±0.14	1.14 ±0.05
Mean particle diameter (µm) with PSD	Pores	0.416	0.436	0.446	0.452	0.444	0.456	0.432	0.438	0.488	0.448	0.610	0.492	0.424	0.420
	YSZ	0.368	0.346	0.310	0.326	0.344	0.35	0.360	0.354	0.350	0.362	0.360	0.362	0.336	0.348
	Ni	0.48	0.454	0.488	0.560	0.530	0.574	0.532	0.464	0.534	0.572	0.540	0.594	0.568	0.598
Specific surface area (μm^{-1})	Pores	2.48 ±0.07	2.33 ±0.03	2.43 ±0.07	2.39 ±0.10	2.44 ±0.02	2.46 ±0.02	2.31 ±0.03	2.31 ±0.03	2.19 ±0.03	2.34 ±0.02	2.07 ±0.07	2.30 ±0.06	2.56 ±0.02	2.53 ±0.06
	YSZ	3.62 ±0.03	3.62 ±0.02	3.90 ±0.03	3.91 ±0.07	3.66 ±0.05	3.53 ±0.05	3.70 ±0.03	3.58 ±0.02	3.44 ±0.04	3.57 ±0.03	3.44 ±0.14	3.44 ±0.07	3.71 ±0.04	3.61 ±0.03
	Ni	2.09 ±0.09	2.29 ±0.08	1.93 ±0.22	1.86 ±0.28	1.85 ±0.04	1.77 ±0.03	1.90 ±0.05	1.91 ±0.03	1.87 ±0.14	1.79 ±0.03	1.76 ±0.16	1.71 ±0.08	1.86 ±0.07	1.81 ±0.06
Interfacial surface area (μm^{-1})	Ni/Pores	0.475	0.5	0.23	0.17	0.315	0.35	0.255	0.32	0.310	0.28	0.195	0.285	0.355	0.35
	Ni/YSZ	1.615	1.79	1.70	1.69	1.535	1.42	1.645	1.59	1.560	1.51	1.565	1.425	1.505	1.42
	Pores/YSZ	2.005	1.83	2.20	2.22	2.125	2.11	2.055	1.99	1.880	2.06	1.875	2.015	2.205	2.11
Tortuosity factor (-)	Pores	8.46	4.99	4.13	4.82	5.11	4.58	6.58	6.41	4.64	5.55	4.76	4.98	5.30	5.42
	YSZ	2.27	2.45	2.64	2.49	2.42	2.49	2.28	2.34	2.48	2.32	2.44	2.43	2.47	2.43
	Ni	7.45	8.40	8.91	8.27	7.82	7.58	8.05	7.68	7.24	8.30	8.13	7.90	9.67	9.71
TPB density (μm^{-2})		4.75 ±0.08	5.25 ±0.15	4.10 ±0.63	3.56 ±0.65	3.93 ±0.12	3.82 ±0.06	3.71 ±0.08	3.88 ±0.10	3.60 ±0.42	3.61 ±0.11	3.18 ±0.36	3.39 ±0.12	4.34 ±0.16	4.20 ±0.10

Durability of Solid Oxide Cells: an experimental and modelling investigation based on synchrotron X-ray nano-tomography characterization

This work aims at better understanding and quantifying the degradation of high temperature Solid Oxide Cells. An approach based on electrochemical tests, advanced post-test characterizations and multi-scale models has been used to investigate the links between the performances, the electrodes microstructure and their degradation upon operation. In that goal, long-term durability tests have been performed over few 1000h in different operating conditions. Electrode microstructures have been reconstructed by synchrotron X-ray nano-holotomography for the pristine and aged cells. It is worth noting that a special attention has been paid to the improvement of both the protocol reliability for the tomographic experiments and the spatial resolution of the 3D reconstructed images. Thanks to the valuable 3D volumes, the Ni-YSZ microstructural properties of the H_2 electrode have been quantified for the fresh and the aged samples. Then, a physically-based model for Nickel particle agglomeration has been adjusted on the microstructural parameters obtained by the 3D analysis and implemented in an in-house multi-scale modelling framework. Beforehand, it has been necessary to enrich the available numerical tool with a specific module dedicated to the oxygen electrode made in Mixed Ionic Electronic Conducting materials. Once validated on polarisation curves, the completed model has been used to quantify the contribution of Nickel agglomeration on the total experimental degradation rates (~30%) recorded in fuel cell and electrolysis modes.

Durabilité des convertisseurs électrochimiques haute température à oxydes solides : une étude expérimentale et de modélisation basée sur la caractérisation au synchrotron par nanotomographie des rayons X

Ce travail porte sur l'étude de la dégradation des convertisseurs électrochimiques haute température à oxydes solides. Une approche couplant des tests électrochimiques, des caractérisations post-mortem fines et une modélisation multi-échelle a été mise en place afin d'établir les liens entre les performances, la microstructure des électrodes et leur dégradation en fonctionnement. Dans ce but, des essais de durabilité de quelques milliers d'heures ont été menés dans différentes conditions opératoires. La microstructure des électrodes a été reconstruite au synchrotron par nano-holotomographie des rayons X pour la cellule de référence avant et après vieillissement. Une attention particulière a été apportée à l'amélioration de la résolution spatiale et à la fiabilisation du protocole expérimental. Grâce aux volumes 3D, les propriétés microstructurales de l'électrode H_2 en Ni-YSZ ont été quantifiées pour les cellules à l'état initial et vieillies. Un modèle physique d'agglomération des particules de Nickel a ensuite été ajusté sur les analyses tridimensionnelles et intégré dans une structure de modélisation multi-échelle développée au laboratoire. Il a auparavant été nécessaire de compléter l'outil numérique avec un module spécifique dédié aux matériaux composant l'électrode à oxygène fait avec un conducteur mixte ionique-électronique. Une fois le modèle validé sur des courbes de polarisation expérimentales, il a été utilisé pour quantifier la contribution de l'agglomération du Nickel sur les pertes de performances mesurées expérimentalement (~30%) en mode pile à combustible et électrolyse.